

Propagation of planar three-dimensional buoyant hydraulic fractures

Présentée le 5 septembre 2023

Faculté de l'environnement naturel, architectural et construit
Laboratoire de géo-énergie - Chaire Gaznat en géo-énergie
Programme doctoral en mécanique

pour l'obtention du grade de Docteur ès Sciences

par

Andreas MÖRI

Acceptée sur proposition du jury

Prof. F. Gallaire, président du jury
Prof. B. T. A. Lecampion, directeur de thèse
Prof. E. Rivalta, rapporteuse
Prof. E. Detournay, rapporteur
Prof. J. M. Kolinski, rapporteur

A scientific law is a generalization based on observation.

- 1) Scientific understanding is always based on the constant repetition of events.
 - 2) Miracles are not constantly repeated.
 - 3) Therefore, there is no scientific way to understand miracles.
- David L. Ulin

To M and F
my family and friends. . .



Acknowledgement of support

Funding for this thesis came from grant #192237, entitled "Microcrack toughening of hydro-mechanically driven fractures in rocks", awarded to Prof. Brice Lecampion by the Swiss National Science Foundation and the Gaznat chair on Geo-Energy at EPFL, headed by Prof. Brice Lecampion. The support is strongly acknowledged.

Lausanne, July 17, 2023

A. Möri

Acknowledgements

Expressing my sentiments, gratitude, and emotions in these challenging times is difficult. But in the spirit of Joda: I'll do it because there is no try.

I will start with the one person without whom I would have never even started this endeavour. My supervisor, mentor, promoter, and role model: Prof B. Lecampion. Thank you for giving me the opportunity to pursue a PhD at EPFL. You made an effort from the beginning to convince me that I should do a PhD and kept strengthening my belief that I can do it effectively. We have had our ups, and we have had our downs, but life is nothing but a roller coaster, and during a PhD, the ups are exceptionally high and the downs especially deep. Even during the hard times of COVID, when I lost my focus and was at the edge of giving up, you managed to convince me that I was on the right path and show me that there are ways to go on and that it can be done. Thank you endlessly for everything you have taught me, whether scientific, social, political, or personal. To put it in the words of a famous Swiss songwriter: "We shake hands as our ways part. For me, it was a good fit!".

A special thank you goes to my dissertation committee: Professors François Gallaire, John Kolinski, Eleonora Rivalta and Emmanuel Detournay. I am honoured by your commitment to reading and listening to my research and investing your precious time to provide me with stimulating and interesting comments.

I would also like to thank Prof Dmitry Garagash for supporting me during various stages of my PhD. Thank you for the valuable insights, your support in numerical methods, and the honest feedback if something was, well, plain wrong. Your agile and genius mind points to the weakness, but it is only if we address those that we will advance. Your contributions have made sure that I continue growing as a scientist. I also thank Prof Anthony Peirce for discussing leak-off and fracture closure. Thank you for supporting my application to academic positions. I am incredibly thankful. I am very honoured to have crossed ways with Dr Alexandra Kushnir. Thank you so much for everything. For helping me to connect outside of my core research field and spreading the word. For putting me in contact with your friends and colleagues and opening many doors for me.

What would a workplace be without a team? I will list the current and former members of the GEL laboratory in which I pursued my PhD, but be easy on me if I miss someone! My

Acknowledgements

first thanks go to the former PhD students Fatima and Federico. Thanks for telling me what I was getting into and keeping my spirit up during my master's thesis. Thank you so much for not scaring me off while nonetheless being honest. Many thanks also go to Garry and Thomas for their insights into the experimental work, apéros, and dinners, keeping the spirit up. I would also not want to miss the discussions with Dong, your sharp mind keeps impressing me, and I am glad to have shared some part of my way with you. Thank you, Haseeb, for supporting me when I familiarized myself with PyFrac and Dmitry Nikolskiy for your humour and good vibes. Guanyi, I will see you soon in the US, and I hope we will find the time to stay in touch. Thank you for sometimes reminding me that too much Swissness is harmful to the mind of a PhD student. Thanks for your realistic and direct personality. You have a flair for putting things in context I admire. I would also like to thank Dmitry Loginov, although your adventure was not crowned by success, I was happy to spend time with you. I would have so much to say about the current team members, but I will stick to the most prominent features inspiring me. Maalek, thanks for your unique take on efficiency, something I should learn from you. Emil, thanks for sharing mushroom secrets, discussing how bread can change lives, and so much more. You are persistent in science but always there for a joke and to talk about daily life. Thanks for this escape at some times. Many thanks also to Ankit for becoming my running buddy. I have let you down in the past weeks, but the schedule is ready. I hope you are too. Regina, thank you for lifting the spirit, whether with chocolate, sweets, serious talk or simply by stepping by and telling me not to forget to smile. You have brought some joy to the lab; I am thankful for this. Mohsen, thanks for your Paris-inspired clothes, your sweets (I gained at least a pound a day when they were there), your tea and your investment in social activities. El abuelo Tristaños, we explored the maps of the world and argued about Swiss politics and systems, and I abusively used your ReCIRCLE plastics. Thanks for taking my mind off research so many times. It had my best ideas during these breaks. Thank you also for listening to me when I was explaining something new I found and just needed someone to tell me if I made a fundamental mistake. We do not always understand what the other does, but we manage to listen and comment. Thank you so much for this. To Dominique, who has always been there for me, listened to my complaints, lifted my spirits, and encouraged and empowered me. To my lab mate Alexis, whit our unsynchronized working hours. It has been a pleasure to see your incredible mind work. Thanks for exercising my Spanish, your uncomplicated mind, and your calmness.

One team member deserves a paragraph to himself. Thanks for everything Carlo, my work wife. We have spent over fifty hours in traffic together, of whom more than half with fever and shaking. We were quarantined like a couple but managed to make it work. No divorce here! How great is that? Thank you endlessly for our detailed discussions and your help with sketches and figures (even if it ended in verbal battles sometimes). Your scientific rigour and commitment to understanding are fascinating. I learned immensely from you, and I sincerely hope our work-wife relationship survives the upcoming separation.

I do not want to miss thanking my family, my parents B. and H.-R., my brother B. and his

Acknowledgements

girlfriend L. My family-in-law, M. and F., and S. and T. with the so-sweet E. Thanks for all the time we have spent together. For your trying to understand what I do, whether it was successful or failed. Thanks for listening and supporting me in hard times. And for sharing the joy if something went well.

I could not have done it without my friends. Clemente, Candelaria, Antoine, Federica, Davide, Roxane, Stephan, Jean and all the others. Thanks for the moments we have shared. A special thanks also to the PolyDoc gang: Annie, I was so lucky to meet you! Thanks for all the discussions and the time we could spend together. And sorry for my use of your native English as my grammar check. You always lifted the spirit, and we just had so much fun. I also want to address my thank you to Didi (keep on cycling), Romain, Ayush, Nick, Rita, and Manuel, to Harsha, Michelle, Navid, Jinhui, and the rest of the EGU gang. I also want to thank my friends outside of the academic world. You kept my feet on the ground and pulled me back into the real world when my mind drifted away. Thanks to Schöggi, Schäni, Domi, Ivä, Küsu, Phipu, Risto, Tanja, Florin, Raphael, Anne, and Kili. May it be by watching sports, listening to shanty bands, playing cards or board games, you all supported me during all these years, and you deserve a thank you. So here it comes: Thank you!

A special thank goes to my referee buddy, best man, and emotional support Schneemo. Thanks for all our trips, convincing me that one should be proud of himself, and talking about whatever for no reason. It is always a pleasure to spend time with you, watch sports, blow the whistle, or get beaten at Super Mario Smash Bros.

I thanked many people but kept the most important one for the end. M., I don't know what to say or how to thank you, such that it would come close to everything you did and still do for me. Anyway, no words could explain how I feel about you, and they would never be capable of describing your support. When I am down, your footprints are in the sand. I do not know if it is your lips or beautiful eyes, but you are the best person ever. You supported me when I was standing in the rain and cheered with me when something went well. You are always there for me, and one day more. There are still so many stories to be written in our life, where the one with F. is only the next chapter. I am still like blank paper, so let us continue writing our story. Because you and I, the two of us, will take it on with the rest of the world for the longest time.

Zweisimmen, May 29, 2023

A. M.

Abstract

Hydraulic fractures are driven by an internal fluid pressure exceeding the minimum compressive stress, propagating in a direction perpendicular to the latter. This class of tensile fractures has gained interest over the last fifty years due to the development of multiple engineering applications. The most-known industrial applications are well-stimulation treatments by hydraulic fracturing used in the petroleum industry to enhance the permeability of tight reservoirs. Other industrial applications include in-situ stress measurement techniques and stimulations of geothermal systems. Natural occurrences include magmatic intrusions and the ascent of geothermal fluids in subduction zones.

In sedimentary basins, the minimum compressive stress is usually horizontal and increases with depth, such that hydraulic fractures grow along vertical planes. A buoyant force emerges as the fracturing fluid is subjected to a hydrostatic pressure gradient different from the stress gradient in the solid. This buoyant force elongates the fracture in the direction of gravitational acceleration, and the propagation can become self-sustained without additional fluid released. For fluids lighter than the surrounding material, this favors an upward growth towards possibly environmentally sensitive upper aquifers. When and how such a buoyancy effect impacts three-dimensional hydraulic fracture growth remains quantitatively unexplored. It is notably unclear how the dominant energy dissipation mechanism (viscous flow or fracture creation) will affect the partition between horizontal and vertical growth.

This thesis investigates the impact of gravitational effects on the emergence, propagation, and arrest of planar three-dimensional hydraulic fractures using scaling, semi-analytical, and numerical methods. We study the process using linear elastic hydraulic fracture mechanics and consider continuous and finite volume releases from a point source. First, we analyze the behavior of finite-volume axisymmetric hydraulic fractures in the absence of buoyant forces. In impermeable media, we show that the arrested shape is independent of the release history. For a permeable solid, the arrested fracture characteristics are a function of fluid leak-off, fracture toughness, and release history. Second, we investigate buoyant hydraulic fracture propagation under continuous fluid releases in impermeable media. A family of solutions that depends on a single dimensionless number emerges. This dimensionless number combines the properties of the solid (density, elasticity, fracture resistance), the fracturing fluid (density, viscosity), and the fluid release rate. Third, we confirm that the emergence of self-sustained buoyant hydraulic fractures in impermeable media is independent of the release history. The release history governs, however, to the first order how the fracture propagation evolves (the partition between horizontal and vertical growth, ascent rate). We further demonstrate that

Abstract

fluid mass loss and stress barriers are the most efficient mechanisms to arrest buoyant fractures at depth. We additionally argue why a pulsating behavior may occur even if the fluid release is continuous.

Keywords: Hydraulic fracture, buoyant hydraulic fractures, self-sustained buoyant growth, fracture arrest, fluid leak-off, solidification of magmatic intrusion, stress barriers, fracture toughness variations, dike intrusions

Résumé

Les fractures hydrauliques sont des fractures par tension actionnées par une pression de fluide interne supérieure à la contrainte minimale de compression. Elles ont fait l'objet d'un intérêt croissant au cours des cinquante dernières années en raison du développement de multiples applications en ingénierie. Les applications industrielles les plus connues sont les traitements de stimulation de puits par fracturation hydraulique utilisés dans l'industrie pétrolière afin d'augmenter la perméabilité des réservoirs compacts. D'autres applications industrielles comprennent les techniques de mesure des contraintes in-situ et la stimulation des systèmes géothermiques. Les intrusions magmatiques et la remontée des fluides géothermiques dans les zones de subduction sont des exemples de fracturation hydraulique naturelle.

Dans le cas des bassins sédimentaires, la contrainte minimale de compression est généralement horizontale et augmente avec la profondeur, de sorte que les fractures hydrauliques se développent dans des plans verticaux. Une poussée d'Archimède émerge car le fluide de fracturation est soumis à un gradient de pression hydrostatique différent du gradient des contraintes. Cette poussée étend la fracture dans la direction de l'accélération gravitaire ce qui peut engendrer une propagation auto-entretenu sans injection supplémentaire de fluide. Pour les fluides avec une densité inférieure à la roche, la poussée d'Archimède favorise la remontée des fluides vers des aquifères supérieures, potentiellement vulnérables. La question de quand et comment les effets gravitaires influencent quantitativement la propagation des fractures hydrauliques tridimensionnelles reste ouverte. Notamment, le rôle de l'effet de dissipation d'énergie dominant (flux visqueux ou création des surfaces) sur la partition entre la croissance verticale et horizontale n'est pas encore clarifié.

Cette thèse explore les effets gravitaires pour comprendre la création, la propagation et l'arrêt des fractures hydrauliques tridimensionnelles planaires. Nous étudions le processus à l'aide de la mécanique élastique linéaire des fractures hydrauliques et en considérant des injections continues et à volume fini à partir d'une source ponctuelle. En premier, nous clarifions le comportement des fractures hydrauliques axisymétriques d'un volume fini injecté en négligeant les effets gravitaires. Pour les milieux imperméables, nous démontrons que la géométrie à l'arrêt est indépendante de l'historique d'injection. Si le solide est perméable, les caractéristiques de la fracture à l'arrêt dépendent de la perte de fluide dans l'environnement, de la ténacité, et du taux d'injections. En deuxième, nous étudions la propagation des fractures hydrauliques gouvernées par la poussée d'Archimède dans le cas d'une injection continue dans un milieu imperméable. La solution est une famille de solutions dépendant d'un seul nombre adimensionnel. Ce nombre adimensionnel combine les propriétés du solide (densité,

Résumé

élasticité, ténacité), du fluide injecté (densité, viscosité), et le taux d'injections. En troisième, nous confirmons que la formation de fractures hydrauliques auto-entretenues gouvernées par la poussée d'Archimède dans des milieux imperméables est indépendante de l'historique d'injection. Ce dernier affecte toutefois la partition entre la croissance verticale et horizontale en première ordre. Nous démontrons également que la perte de fluide dans le milieu environnant, la solidification du fluide, et les barrières de contraintes sont les mécanismes les plus efficaces permettant d'arrêter les fractures gouvernées par la poussée d'Archimède et qu'un comportement pulsant peut se produire même à taux d'injection constant.

Mots-clés : Fracture hydraulique, fractures hydrauliques gouvernées par la poussée d'Archimède, propagation auto-entretenu des fractures hydrauliques gouvernées par la poussée d'Archimède, arrêt de fracture, échange de fluide avec l'environnement, solidification d'une intrusion magmatique, barrières de contraintes, variations de ténacité, intrusions de dykes

Zusammenfassung

Hydraulische Risse werden durch einen inneren Flüssigkeitsdruck, welcher die Mindestdruckspannung übersteigt, angetrieben und wachsen rechtwinklig dazu. Diese Klasse von Zugrissen hat durch die Entwicklung zahlreicher technischer Anwendungen in den letzten fünfzig Jahren kontinuierlich an Aufmerksamkeit gewonnen. Die bekannteste industrielle Anwendung ist das Einpressen von Flüssigkeiten in Bohrlöchern zur Erzeugung von hydraulischen Rissen. Diese Technik wird in der Erdölindustrie eingesetzt, um die Durchlässigkeit von dichten Lagerstätten zu erhöhen. Weitere industrielle Anwendungen sind Verfahren zur Bestimmung des Spannungsfeldes in geologischen Formationen und das Weiten und Erzeugen von Rissen zur Förderung des Wärmetransports in geothermischen Systemen. Zu den natürlichen Beispielen hydraulischer Risse gehören magmatische Intrusionen und das Aufsteigen geothermischer Flüssigkeiten in Subduktionszonen.

In Sedimentbecken ist die minimale Druckspannung in der Regel horizontal und nimmt mit der Tiefe zu, so dass sich die hydraulischen Risse in vertikalen Ebenen ausbilden. Dadurch entsteht eine Auftriebskraft, da die risstreibende Flüssigkeit einem hydrostatischen Druck ausgesetzt ist, welcher sich vom Spannungsgradienten des umschließenden Gesteins unterscheidet. Diese Auftriebskraft zieht den Riss entlang des Gravitationsfeldes in die Länge und es kann ein selbsterhaltendes Wachstum entstehen, welches keine zusätzliche Flüssigkeitszufuhr erfordert. Bei Flüssigkeiten mit einer geringeren Dichte als die des umgebenden Materials ist dieses Wachstum aufwärtsgerichtet, so dass der Riss möglicherweise ökologisch empfindliche, höhergelegene Grundwasserleiter erreicht. Ob überhaupt und, falls ja, in wie fern, die Auftriebskraft die Ausbreitung von dreidimensionalen planaren Rissen beeinflusst, konnte bisher nicht quantitativ erörtert werden. Unter anderem ist unklar, wie der dominierende Mechanismus zur Energieumwandlung (viskose Strömung oder Rissflächenbildung) sich auf die Trennung zwischen horizontalem und vertikalem Wachstum auswirkt.

Diese Dissertation untersucht mittels dimensionaler und semi-analytischer Methoden und numerischen Simulationen die Effekte der Schwerkraft, um die Entstehung, Ausbreitung und das Anhalten von dreidimensionalen, planaren, hydraulischen Rissen zu verstehen. Wir untersuchen den Prozess mithilfe der Mechanik linear-elastischer hydraulischer Risse und betrachten dabei fortlaufende und endliche Einpressungen von Flüssigkeiten aus einer Punktquelle. Erstens klären wir das Verhalten von axialsymmetrischen hydraulischen Rissen endlichen Volumens und vernachlässigen dabei die Schwerkraft. Für undurchlässige Gesteine zeigen wir, dass die Geometrie des angehaltenen Risses nicht vom Ablauf der Einpressung abhängt. Wenn der Feststoff durchlässig ist, werden die Eigenschaften des gestoppten Risses durch den Flüssig-

Zusammenfassung

keitsabfluss in die Umgebung und die Rissfestigkeit definiert. Die genau Form hängt dabei vom Ablauf der Einpressung ab. Zweitens analysieren wir die Ausbreitung von auftriebsgetriebenen hydraulischen Rissen für ein fortlaufendes Einpressen in ein undurchlässiges Medium. Wir zeigen dabei, dass eine Lösungsfamilie in Abhängigkeit einer einzigen dimensionslosen Zahl existiert. Diese dimensionslose Zahl kombiniert die Eigenschaften des Festkörpers (Dichte, elastische Parameter, Rissfestigkeit), der Flüssigkeit (Dichte und Viskosität), und die Injektionsrate der Einpressung. Wir bestätigen drittens, dass die Entstehung von selbsterhaltenden auftriebskraftgetriebenen hydraulischen Rissen in undurchlässigem Material unabhängig vom Ablauf der Einpressung ist. Dieser dominiert jedoch das Verhalten während der auftriebsgetriebenen Ausbreitung (Teilung zwischen horizontalem und vertikalem Wachstum, Aufstiegsgeschwindigkeit). Wir zeigen weiter, dass Masseverluste der treibenden Flüssigkeit und Spannungsbarrieren die wirksamsten Mechanismen sind, um auftriebsgetriebenen Risse anzuhalten. Zusätzlich legen wir Argumente dar, weshalb ein pulsierendes Wachstum auch bei einer konstanten Injektionsrate auftreten kann.

Stichworte: Hydraulische Risse, auftriebskraftgetriebene hydraulische Risse, selbsterhaltendes Wachstum von auftriebskraftgetriebene hydraulische Rissen, Anhalten von Rissen, Flüssigkeitsabfluss, Flüssigkeitsverfestigung von magmatischen Intrusionen, Spannungsbarrieren, veränderliche Rissfestigkeit, magmatische Intrusionen

Zämäfassig

Hydroulisch Risse wärde dürne innere Flüssigkeitsdruck überem Niveau vor Mindestdruckspannig atrybe u breitesech sänkrächt zu dere Mindestdruckspannig us. Die Art vo Zugrisse het dürt Entwicklig vo viune technische Awändige i dä letste füfzg Jahr geng meh Ufmerksamkeit becho. Ds Ipressse vo Flüssigkeite dürnes Bohrloch zum Erzüge vo hydraulische Risse isch di bekanntschti industrielli Awändig. Settegi Ipressige wärde vor Minerauöuindustriegmacht zum d Durchlässigkeit vo dichte, minerauöltragende Gschteisformation z erhöe. Angeri Awändige ir Industrie si o z mässe vom Spannigszustand im Ungergrund oder z Wyte u lbringe vo Risse zur Förderig vor Wärmeleitig i geothermische Syschtem. Ir Natur gsehtme das Phänomen bispiuswis ir Form vo magmatische Ilagerige oder bim Ufstige vo geothermische Flüssigkeite i Subduktionszonäne.

Ds Spannigsfäud i Sedimentbecki isch i dr Regu so, das d Mindestdruckspannig horizontau isch u grösser wird, je töifer me geit. Hydraulisch Risse biudesech drum ir Vertikale. So entsteht e Uftrybschraft, wüu di trybendi Flüssigkeit e hydrostatische Druck generiert wo andersch isch aus dä vom Schpannigsfäud. D Uftrybschraft zieht dr Riss i dr Richtig vom Gravitationsfäud id Längi. So chasech es säubschterhautends Wachstum ischteue wo kes derzuetue vo meh Flüssigkeit brucht. Faus di trybendi Flüssigkeit liechter isch aus ds Gschtei rundume, wachst dr Riss gäge ufe u chönnt ökologisch sensybli Grundwasservorkomme erreiche. Öb u wie die gravitäre Effekte ds Wachstum vo so drüdimensionale Risse beinflusse, hetme noni quantitativ beschtimmt. Es isch vorauem unklar, wie dasech d Ufteilig vor Energieumwandlig (dür zähflüssig fliessendi Flüssigkeite oder für ds Kreiere vo Oberflächine) ufts Verhäutnis zwüsche horizontalem u vertikalem Wachstum uswürkt.

I dere Dokterarbeit ungersueche mir dr Ifluss vor Schwärchraft ufts Entschtah, Wachse, u Stoppe vo setigne äbenewegs wachsende, drüdimensionale hydroulischä Risse. Für ds Studierä vo dene Ablöif bruchemer d Mechanik vo linear-elastische hydroulische Risse, u luege, wisech fortlaufendi und ändlechi Ipressige vo Flüssigkeite vomne Punkt us verhaute. Zersch vernachlässige mir d Schwärchraft u kläre, wi sech es ändlechs Volume vo ipresster Flüssigkeit verhaute. We ds Gschtei wo dripresst wird undurchlässig isch, chöimer zeige, dass d Form vom gestoppte Riss nüüt mitem Ablouf for Ipressig z tüe het. Angerersits schpiut genau dä Ablouf aber e grossi Roue faus ds Gschtei durchlässig isch. I däm Fau sis d Eigefhafte vom Materialu, vor trybende Flüssigkeit, u ihre Abfluss ids Gschtei wo di aghautnegi Form bestimme. Aus zwöits ungersueche mir Risse wo dürne stetigi Ipressig imne undurchlässige Materialu entstöh u uftrybschrafttrybe si. Daderbi chöimer zeige, dases e ganzi Familie vo Lösige git wo dank ere Zau ohni Einheitä chöi bestimmt wärde. Die Zau setztsech us de Eigefhafte vom

Zämfassig

Gschtei (sini Dychti, elastische Parameter, sini Rissfeschtigkeit), vor trybende Flüssigkeit (sini Dychti und Viskosität), u dr Ipressrate zämä. Imne nächste Schritt chöimer bestätige, dass ds Entschtah vo seubschterhautende hydroulische Risse, tribe vo ihrer egete Uftrybschraft, nid vom Ablouf for Ipressig abhängig isch. Weme aber wot wüsse, wisech di Risse gnau bewege, de het dä Ablouf e grosse Ifluss. Mir zeige wyter, dass dr Abfluss oder ds Gfriere vor tribende Flüssigkeit oder aber Gämp im Spannigsfäud di effizientische Mechanisme si zum so Risse ufhautä. Usserdeäm chöi so uftrybschrafttrybeni Risse pulsierend wachse, sogar we d'Ipressig konstant Flüssigkeit abgit.

Stichwörter: Hydroulische Riss, uftribschrafttrybene hydroulische Riss, Stoppe vo Risse, Flüssigkeitsabfluss i ds Materiau, Gfriere vo magmatische Ilagerige, Gämp im Spannigsfäud, Veränderige vor Rissfeschtigkeit, magmatischi Ilagerige, säubschterhautends Wachstum vo uftribschrafttrybene hydroulische Riss

Contents

| | |
|---|-------------|
| Acknowledgement of support | i |
| Acknowledgements | iii |
| Abstract (English/Français/Deutsch/Bärndütsch) | vii |
| List of Figures | xix |
| List of Tables | xxix |

| | |
|---|-----------|
| I Mechanics of Hydraulic Fractures | 1 |
| 1 Introduction | 3 |
| 1.1 Motivation and background | 4 |
| 1.1.1 Magmatic intrusions / Diking | 4 |
| 1.1.2 Hydraulic fracturing treatments | 5 |
| 1.1.3 Other industrial applications | 6 |
| 1.2 A review of hydraulic fracture growth | 10 |
| 1.2.1 Energy dissipation mechanisms | 10 |
| 1.2.2 Hydraulic fracture tip asymptotics | 11 |
| 1.2.3 Scaling and semi-analytical approaches | 12 |
| 1.2.4 Buoyant hydraulic fractures | 12 |
| 1.2.5 Experimental investigation of hydraulic fractures | 13 |
| 1.3 Research questions addressed | 14 |
| 1.4 Organisation of this manuscript | 15 |
| 2 Mechanics of hydraulic fractures | 17 |
| 2.1 Fundamentals of hydraulic fracture mechanics | 17 |
| 2.1.1 Elasticity | 18 |
| 2.1.2 Boundary element method for planar fractures | 20 |
| 2.2 Fluid flow and leak-off | 25 |
| 2.2.1 Fluid flow | 26 |
| 2.2.2 Leak-off | 28 |
| 2.3 Propagation condition | 32 |

Contents

| | | |
|------------|--|-----------|
| 2.3.1 | Tip-Asymptotes in hydraulic fracturing | 35 |
| 2.4 | Numerical solution of hydraulic fracture problems | 35 |
| 2.4.1 | PyFrac: A python implementation of the implicit level set algorithm (ILSA) | 37 |
| II | Radial Finite Volume Hydraulic Fracture | 43 |
| 3 | Arrest of a radial hydraulic fracture upon shut-in of the injection | 45 |
| 3.1 | Abstract | 46 |
| 3.2 | Introduction | 46 |
| 3.3 | Problem formulation | 48 |
| 3.3.1 | Growth during constant injection ($t < t_s$) | 50 |
| 3.3.2 | Evolution post-shut-in ($t > t_s$) | 51 |
| 3.3.3 | Numerical solver used | 53 |
| 3.4 | Impermeable Medium | 54 |
| 3.4.1 | Arrest radius in the finite toughness case | 54 |
| 3.4.2 | Viscosity-storage pulse solution in the zero toughness limit - case of no arrest | 55 |
| 3.4.3 | Propagation and arrest post-shut-in | 55 |
| 3.5 | Permeable medium | 58 |
| 3.5.1 | Zero toughness case | 58 |
| 3.5.2 | General case | 63 |
| 3.6 | Discussions | 66 |
| 3.6.1 | Orders of magnitude for industrial applications | 66 |
| 3.6.2 | Orders of magnitude for a magmatic pulse release | 69 |
| 3.6.3 | Importance of subcritical crack growth | 71 |
| 3.7 | Conclusions | 73 |
| 3.8 | Appendix of the article | 75 |
| 3.8.1 | Energy budget of a radial hydraulic fracture | 75 |
| 3.8.2 | Viscous pulse solution | 75 |
| III | Buoyant Hydraulic Fractures | 81 |
| 4 | Three-dimensional buoyant hydraulic fractures: constant release from a point source | 83 |
| 4.1 | Abstract | 84 |
| 4.2 | Introduction | 84 |
| 4.3 | Formulation and methods | 86 |
| 4.3.1 | Mathematical formulation | 86 |
| 4.3.2 | Numerical solver | 88 |
| 4.3.3 | Scaling analysis | 89 |
| 4.4 | Onset of the buoyant regime | 91 |
| 4.5 | Toughness-dominated buoyant fractures $\mathcal{M}_{\hat{k}} \ll 1$ | 93 |

| | | |
|----------|--|------------|
| 4.5.1 | Toughness-Dominated Head | 93 |
| 4.5.2 | Viscosity-Dominated Tail | 95 |
| 4.5.3 | Large time buoyant regime | 96 |
| 4.5.4 | Transient toward the late buoyant regime | 99 |
| 4.6 | Viscosity-dominated buoyant fractures $\mathcal{M}_{\hat{k}} \gg 1$ | 100 |
| 4.6.1 | Late-time zero-toughness limit | 102 |
| 4.7 | Intermediate/Finite $\mathcal{M}_{\hat{k}}$ cases | 107 |
| 4.8 | Discussion | 109 |
| 4.8.1 | Orders of magnitude | 109 |
| 4.8.2 | Comparison with experiments | 110 |
| 4.8.3 | Possibility of approximate solutions | 112 |
| 4.9 | Conclusions | 112 |
| 4.10 | Appendix of the article | 114 |
| 4.10.1 | Recapitulating tables of scales | 114 |
| 4.11 | Supplementary material of the article | 114 |
| 4.11.1 | Approximated toughness-dominated solution \hat{K} | 114 |
| 4.11.2 | Viscosity-dominated solution in the source region | 121 |
| 4.11.3 | Post-processing of the numerical results | 122 |
| 4.11.4 | 2D steadily moving semi-infinite buoyant hydraulic Fracture Solver | 126 |
| 4.11.5 | Comparison with experiments | 132 |
| 5 | Three-dimensional buoyant hydraulic fractures: finite volume release | 139 |
| 5.1 | Abstract | 140 |
| 5.2 | Introduction | 140 |
| 5.3 | Preliminaries | 141 |
| 5.3.1 | Arrest of a finite volume radial hydraulic fracture without buoyancy | 143 |
| 5.3.2 | Buoyant hydraulic fracture under a continuous release | 144 |
| 5.3.3 | Hydrostatically loaded radial fracture | 146 |
| 5.4 | Arrest at depth vs. self-sustained propagation of buoyant hydraulic fractures | 147 |
| 5.4.1 | Toughness-dominated at the end of the release | 147 |
| 5.4.2 | Viscosity-dominated at the end of the release $\mathcal{K}_{ms} \ll 1$ | 148 |
| 5.4.3 | Structure of the solution for a finite volume release | 150 |
| 5.5 | Fractures arrested at depth $\mathcal{B}_{ks} < 1$ | 152 |
| 5.6 | Self-sustained finite volume buoyant fractures: $\mathcal{B}_{ks} > 1$ | 152 |
| 5.6.1 | Toughness-dominated, buoyant fractures at the end of the release (region 3): $\mathcal{M}_k \ll 1$ | 152 |
| 5.6.2 | Viscosity-dominated at the end of the release (regions 4 to 6): $\mathcal{M}_k \gg 1$ | 158 |
| 5.6.3 | Late time fracture shapes | 163 |
| 5.7 | Discussion | 166 |
| 5.7.1 | Implications for industrial treatments | 166 |
| 5.7.2 | Comparison with experiments | 167 |
| 5.8 | Conclusions | 169 |

Contents

| | | |
|-----------|---|------------|
| 5.9 | Appendix | 170 |
| 5.9.1 | Recapitulating tables of scales | 170 |
| 5.10 | Supplementary material | 170 |
| 5.10.1 | Approximated toughness-dominated solution $\hat{K}^{[V]}$ | 170 |
| 5.10.2 | Self-Similarity of the Zero-Toughness Solution | 176 |
| 6 | Effects of fluid leak-off or solidification on buoyant hydraulic fractures | 179 |
| 6.1 | Abstract | 180 |
| 6.2 | Introduction | 180 |
| 6.3 | Data and methods | 182 |
| 6.3.1 | Mathematical formulation | 182 |
| 6.3.2 | Model for fluid solidification | 185 |
| 6.3.3 | Leaking/Solidifying buoyant hydraulic fracture | 187 |
| 6.4 | Results | 190 |
| 6.5 | Discussion and conclusion | 192 |
| 6.6 | Appendix | 194 |
| 6.6.1 | Dimensionless leak-off coefficient \hat{K} -regime | 194 |
| 6.6.2 | Transition from \hat{M} to \hat{K} | 195 |
| 7 | Arrest mechanisms of buoyant hydraulic fractures | 199 |
| 7.1 | Abstract | 200 |
| 7.2 | Introduction | 200 |
| 7.3 | Toughness heterogeneities | 203 |
| 7.3.1 | Fracture size dependent toughness | 203 |
| 7.3.2 | Toughness jump | 208 |
| 7.4 | Stress jump | 211 |
| 7.4.1 | Simulations of modest and maximum cases | 213 |
| 7.4.2 | Temporal containment for set 2 | 213 |
| 7.5 | Leak-off | 215 |
| 7.5.1 | Uniform leak-off coefficient | 215 |
| 7.5.2 | Jump in leak-off intensity | 217 |
| 7.6 | Conclusions | 220 |
| IV | Conclusions and Perspectives | 221 |
| 8 | Conclusions and perspectives | 223 |
| 8.1 | Main contributions | 223 |
| 8.2 | Perspectives | 225 |
| | Bibliography | 227 |
| | Curriculum Vitae | 247 |

List of Figures

| | | |
|-----|--|----|
| 1.1 | Example of outcrops of magmatic intrusions: a) Ship Rock in New Mexico (USA) (picture taken by James St. John on 02.09.2007, downloaded on 17.03.2023). b) Fissure eruption on the north flank of Piton de la Fournaise starting on 9th March of 1998 (La Réunion Island, France) (picture taken by Luc Souvet on the 09.03.1998, downloaded on 17.03.2023). c) Makthesh Crater in the Negev Desert (Israel) (picture taken by Andrew Shiva on 24.07.2016, downloaded on 17.03.2023). | 4 |
| 1.2 | Setup of a typical hydraulic fracturing treatment. (picture taken by Evolution Well Services in 08.2019, downloaded on 11.05.2023). | 5 |
| 1.3 | The three most often studied geometries of hydraulic fracture. a) The finite two-dimensional plane strain fracture called KGD-Fracture after Geertsma and De Klerk (1969). b) PKN-fractures using a local two-dimensional plane strain approximation named after Perkins and Kern (1961) and Nordgren (1972). c) The penny-shaped/radial planar three-dimensional fracture, observed for point sources fluid releases in a homogeneous media. | 9 |
| 2.1 | Schematic of a crack boundary value problem in an infinite elastic media under compressive stresses. | 20 |
| 2.2 | Sketch of parallel plates flow with the flow profile and the definition of the leak-off velocity. | 27 |
| 2.3 | Sketched evolution of fracture opening as a function of distance to the fracture tip for a hydraulic fracture without fluid lag. Dashed lines show the respective limiting asymptotes: Red = near-field toughness dominated limit (Rice, 1968a), green = intermediate leak-off dominated asymptote (Lenoach, 1995), and blue = far-field viscosity-dominated limit (Desroches et al., 1994). The black line is a numerical evaluation of the combined asymptote developed by Garagash et al. (2011) using the approximation of Dontsov and Peirce (2015a). | 36 |
| 2.4 | Graphical representation of the main components of the numerical HF Solver PyFrac (Zia and Lecampion, 2020). Top left: Discretization of the fracture plane into a regular rectangular grid with different element types. Top Right: Two-dimensional plane stress asymptotic solutions used at the fracture tip. Bottom: Schematic of finite different five-point stencil used to calculate the fluid flow in the fracture. Adapted figure 2.3 of Peruzzo (2023). | 38 |

List of Figures

| | | |
|-----|--|----|
| 2.5 | Flow Chart of PyFac. Figure reproduced from Zia and Lecampion (2020). | 40 |
| 3.1 | a) Sketch of a radial hydraulic fracture with a zoom on the HF tip viewed as a steadily moving plane-strain case. b) Evolution of the fracture propagation regime for a radial fracture in a linear elastic permeable medium with Carter's leak-off - adapted from Detournay (2016). | 49 |
| 3.2 | Normalized fracture radius as function of the dimensionless shut-in time t/t_s . Numerical (and semi-analytical) predictions of fracture radius scaled by the arrest radius $R_{k,a}$ (3.14a) for various values of shut-in toughness \mathcal{K}_s (3.10) (from 10^{-4} to 10^2). | 56 |
| 3.3 | Characteristical values of post-injection propagation as a function of the dimensionless toughness at shut-in \mathcal{K}_s (impermeable case). a) Ratio between arrest and shut-in radius for a radial fracture in an impermeable medium. b) Time of arrest over shut-in time. Numerical simulations (Black dots) and analytical estimate for small \mathcal{K}_s (dashed purple line). | 59 |
| 3.4 | Numerical evaluation of the arrest radius for different values of \mathcal{C}_s in the zero toughness case. The early shut-in approximation is given in equation (3.21) with its prefactor obtained by regression of these numerical results. The late shut-in solution corresponds to the radius at shut-in given by the viscosity/leak-off propagation solution of Madyarova (2003). | 60 |
| 3.5 | a) Normalised fracture radius as a function of characteristic shut-in time t/t_s . Numerical (and semi-analytical) predictions of fracture radius scaled by the arrest radius $R_a(\mathcal{C}_s)$ for various values of shut-in leak-off coefficient \mathcal{C}_s (from 10^{-6} to 10^2). b) Fracturing efficiency as a function of dimensionless leak-off coefficient $\mathcal{C}_m(t) = \mathcal{C}_s \times (t/t_s)^{7/18}$. Black dashed lines correspond to numerical simulations with different values of shut-in leak-off coefficient \mathcal{C}_s . Blue dots mark the moment of shut-in, and red dots mark the fracture arrest. | 62 |
| 3.6 | Characteristic values of post-injection propagation as a function of the shut-in leak-off coefficient \mathcal{C}_s . a) Overshoot of a radial fracture in the case of zero toughness. b) Square root of time of persistent propagation of a radial fracture in the case of zero toughness. | 64 |
| 3.7 | Normalized arrest radius $R_a/R_{k,a}$ as a function of the dimensionless leak-off coefficient at shut-in \mathcal{C}_s for different values of the trajectory parameter $\phi = \mathcal{C}_s^4/\mathcal{K}_s^{14}$. Black dots are simulation results; red dots correspond to the critical value above which the arrest is immediately upon shut-in. The red dashed line is the zero leak-off arrest radius; the green dashed lines are the "early shut-in" arrest radius approximation, and light blue lines the late shut-in solution. . . . | 65 |

- 3.8 a) Contour plot of propagation after shut-in. Red dots are the numerically evaluated values of immediate arrest at shut-in, the light blue dashed line gives the critical dimensionless leak-off coefficient in the zero-toughness case ($\mathcal{C}_{s,c} \approx 0.53 \pm 0.05$) and the black dashed line is a numerical fit for intermediate values. b) Critical fracturing efficiency as a function of the critical dimensionless toughness at shut-in. 67
- 3.9 Propagation post-shut-in (final arrest radius divided by the radius at shut-in) in the general case as a function of the dimensionless toughness at shut-in \mathcal{K}_s for different values of the trajectory parameter $\phi = \mathcal{C}_s^4 / \mathcal{K}_s^{14}$. The red dashed line corresponds to the impermeable medium case, while the green dashed lines represent the early shut-in leak-off approximation. Red dots indicate the limit of immediate arrest, and black dots are numerical simulations. 68
- 3.10 Dimensionless opening (a) and dimensionless pressure (b). Black dashed lines correspond to the semi-analytical viscosity solution (i.e. $M^{[V]}$ -solution) obtained by the use of Gauss-Chebyshev polynomials ($n = 500$). Black markers show numerical solutions of simulations with PyFrac, and the grey line is the solution of the 1D planar HF Mathematica code described in Lecampion and Desroches (2015). 79
- 4.1 Schematic of a buoyancy-driven hydraulic fracture (head \rightarrow red, tail \rightarrow green, source region \rightarrow grey). The tail length is reduced for illustration, indicated by dashed lines and a shaded area. The fracture propagates in the $x|z$ plane with a gravity vector \mathbf{g} oriented in $-z$. The fracture front $\mathcal{C}(t)$, fracture surface $\mathcal{A}(t)$ (dark gray area), opening $w(x, z, t)$, net pressure $p(x, z, t)$, the local normal velocity of the fracture $v_c(x_c, z_c)$ with $(x_c, z_c) \in \mathcal{C}(t)$ characterize fracture growth under a constant release rate Q_o in a medium with a linear confining stress with depth $\sigma_o(z)$. $\ell^{\text{head}}(t)$ and $b^{\text{head}}(t)$ denote the length and breadth of the head, $\ell(t)$ is the total fracture length, and $b(z, t)$ is the local breadth of the fracture. 86
- 4.2 Toughness-dominated buoyant fracture. Green dashed lines in all figures indicate the 3D $\hat{K}GG$, (2014) solution. a) Opening along the centerline $w(0, z, t) / w_{\hat{K}}^{\text{head}}$ for a simulation with $\mathcal{M}_{\hat{K}} = 1. \times 10^{-2}$. b) Net pressure along the centerline $p(0, z, t) / p_{\hat{K}}^{\text{head}}$ for the same simulation. c) Fracture length $\ell(t) / \ell_b$ for three simulations with large toughness $\mathcal{M}_{\hat{K}} \in [10^{-3}, 10^{-1}]$. Dashed-dotted green lines highlight the late-time linear term of the \hat{K} solution. d) Fracture breadth $b(t) / \ell_b$ (continuous) and head breadth $b^{\text{head}}(t) / \ell_b$ (dashed). Grey lines an error margin of 5 %. e - i) Evolution of the fracture footprint from radial (e) towards the final finger-like shape (h and i) for a fracture with $\mathcal{M}_{\hat{K}} = 1. \times 10^{-3}$. For the fracture shape in i), the vertical extent is cropped between $\ell(t) / \ell_b = 6$ and $\ell(t) / \ell_b = 30$. Thick red dashed lines indicate the head shape according to the 3D $\hat{K}GG$, (2014) solution. Note that the final stage i) has not reached the constant terminal velocity (see inset c). 94

List of Figures

- 4.3 Tip-based scaled opening (a) and pressure (b) of three toughness dominated buoyant simulations with $\mathcal{M}_{\hat{k}} \in [10^{-3}, 10^{-1}]$. Continuous lines correspond to the PyFrac simulations (Zia and Lecampion, 2020) with dots indicating the discretization (the number of elements in the head is > 50), dashed lines to a 2D plane-strain steadily moving solution. The vertical green dashed line indicates the head length, and green continuous lines the 3D \hat{K} solutions. 98
- 4.4 Viscosity-dominated buoyant fracture. a) Opening along the centreline $w(x=0, z, t) / w_{m\hat{m}}$ for a simulation with $\mathcal{M}_{\hat{k}} = \infty$. b) Net pressure along the centreline $p(x=0, z, t) / p_{m\hat{m}}$ for the same simulation. c) Fracture length $\ell(t) / \ell_{m\hat{m}}$ for six simulations with large viscosity $\mathcal{M}_{\hat{k}} \in [5 \times 10^2, \infty[$. d) Fracture breadth $b(t) / \ell_{m\hat{m}}$ for the same simulations. e - i) Evolution of the fracture footprint from radial (e) towards the final elongated inverse cudgel shape (h and i) for the same simulation as in a and b. 101
- 4.5 Scaled evolution of characteristic values of a buoyancy-driven viscosity-dominated fracture. Fracture footprint (a), cross-sectional volume (integral of the opening over the breadth) (b), opening (c), and pressure (d) at various dimensionless times $t / t_{m\hat{m}}$. Blue dashed lines represent the pseudo-three-dimensional near-source solution of Lister (1990a). A shifted coordinate system \tilde{z} is used such that the lowest point of the fracture marks $\tilde{z} = 0$ 103
- 4.6 Footprint and cross-sectional opening profiles of two buoyant, viscosity-dominated fractures. The color code of the fractures represents the scaled opening as described at the top. Black lines correspond to opening-profile evaluations. The horizontal blue dashed line in a) is the limiting height for the viscous solution of Lister (1990a). Blue dashed lines in a) and e) show the Lister (1990a) solution. Red dashed lines mark the maximum breadth and the beginning of the head. Figures b to d show the opening profiles in the cross-section where blue-dashed lines represent the Lister (1990a) solution, dashed-dotted lines correspond to $\mathcal{M}_{\hat{k}} = \infty$ and continuous lines to $\mathcal{M}_{\hat{k}} = 10^5$ 105
- 4.7 Tip-based opening (a) and pressure (b) of a viscosity-dominated buoyant simulation with $\mathcal{M}_{\hat{k}} = \infty$ as a function of the scaled tip coordinate. Continuous lines correspond to the simulations with PyFrac (Zia and Lecampion, 2020) with dots marking the location of discrete evaluations. The dotted-dashed line shows the 2D plane-strain steadily moving solution (see details in the supplementary material). 108
- 4.8 Comparison of maximum breadth for buoyant fractures as a function of the dimensionless viscosity $\mathcal{M}_{\hat{k}} \in [10^{-3}, 5 \times 10^3]$. Black dots are used for fractures with a uniform breadth, and red stars otherwise. The dashed green lines represent the limits of the 3D \hat{K} GG, (2014) solution ($b \sim \pi^{-1/3} \ell_b$) for the breadth limit (horizontal line) and $\mathcal{M}_{\hat{k}} \approx 0.92$ for the stabilization criterion (vertical line)). The grey dashed line emphasizes the scaling relation $\max_{z,t} \{b(z, t)\} \sim \mathcal{M}_{\hat{k}}^{2/5} \ell_b$ 109

| | | |
|------|--|-----|
| 4.9 | Evolution of fracture breadth and length for intermediate fractures without a uniform breadth $\mathcal{M}_{\hat{k}} \in [10^2 - 2 \times 10^3]$ (the simulation with $\mathcal{M}_{\hat{k}} = \infty$ is used as a reference). Dashed lines show fracture breadth, continuous lines fracture height, and horizontal dashed-dotted lines the expected time where lateral growth stops. We indicate the emerging power laws on the figure. | 110 |
| 4.10 | a) Comparison of the experiments of Heimpel and Olson (1994) with our simulations. The experiment takes place within the transient, and the initiation already favors the buoyant propagation. b) Comparison of estimated and observed breadth for various experimental studies. | 111 |
| 4.11 | Propagation diagram for 3D buoyant fractures under a continuous fluid release. Radial growth is initially viscosity-dominated (M-vertex). Transition to buoyancy either occurs before ($\mathcal{M}_{\hat{k}} \gg 1$) or after ($\mathcal{M}_{\hat{k}} \gg 1$) the transition to radial toughness-dominated growth. At late times, a family of buoyancy-driven solutions as a function of $\mathcal{M}_{\hat{k}}$ (4.23) emerges. The large toughness limit (section 4.5) is reached for values of $\mathcal{M}_{\hat{k}} \lesssim 10^{-2}$, whereas the zero-toughness solution (section 4.6) appears at intermediate times $t \in [100t_{m\hat{m}}, t_{\hat{m}\hat{k}}^x]$ for $\mathcal{M}_{\hat{k}} \gtrsim 10^4$ | 113 |
| 4.12 | Flow chart of numerical evaluation. Black circles mark the origin, blue squares are the max head opening, red stars distance to the maximum breadth, green polygons are the location of the head evaluated by the “opening method”, and yellow crosses the update with the pressure check. | 123 |
| 4.13 | 2D semi-infinite opening (a) and pressure (b) in the scaling of equation (4.46). Blue-dashed lines correspond to the solution of Roper and Lister (2007) for $K_{\text{RoLi07}} = 32$ (equations (4.47)). Simulation with $K_{\text{RoLi07}} = 2$ shows the evaluation points as markers. Relative error ((c) opening and (d) pressure) of our numerical evaluation with the solutions (4.47). | 130 |
| 4.14 | Comparison between the zero-toughness solution extracted from Lister (1990b) figure 3 (blue-dashed line) with our zero-toughness Gauss-Chebyshev evaluation (red line). | 131 |
| 5.1 | a) Buoyant self-sustained growth of a hydraulic fracture. b) Arrested hydraulic fracture at depth. Both fractures emerge from a finite fluid volume released from a point source through a block injection and propagate in a homogeneous linear elastic medium ($x z$ plane) with the downwards oriented gravity vector \mathbf{g} (in $-z$) creating a linear confining stress $\sigma_o(z)$. Fracture area is denoted by $\mathcal{A}(t)$ with a closed front $\mathcal{C}(t)$ and a local normal velocity $v_c(x_c, z_c)$ (with $(x_c, z_c) \in \mathcal{C}(t)$). The fracture extent is defined by its local breadth $b(z, t)$ and total length $\ell(t)$. . | 142 |

List of Figures

- 5.2 Structure of the solution for a finite volume release hydraulic fracture as a function of the dimensionless buoyancy \mathcal{B}_{ks} (5.13) and viscosity $\mathcal{M}_{\hat{k}}$ (5.10). Each symbol represents a simulation. Arrested fractures have empty symbols, and filled symbols indicate self-sustained buoyancy-driven pulses. Numbered areas of different colors delimit distinct propagation histories. The color of the symbols represents the value of the horizontal overrun O (5.22). We indicate the simulations presented in figure 5.3 via blue arrows. 150
- 5.3 Final shape and stress intensity factors (SIF) along the front $\mathcal{C}(t)$ of ultimately arrested fractures at depth ($\mathcal{B}_{ks} < 1$) as a function of \mathcal{B}_{ks} and $\mathcal{M}_{\hat{k}}$. Colors indicate the ratio between the local stress intensity factor K_I and the material fracture toughness K_{Ic} from 0 (light grey) to 1 (red). The blue dashed lines in a) to c) correspond to the shape of an expanding head of a propagating toughness-dominated buoyant fracture (Garagash and Germanovich, 2014). 153
- 5.4 Toughness-dominated self-sustained buoyant fractures. Evolution of the dimensionless head breadth $b^{head}(t)/\ell_b$ (a) and fracture length $\ell(t)/\ell(t=t_s)$ (b) as a function of the dimensionless shut-in time t/t_s . The green-dotted line corresponds to the limiting 3D \hat{K} GG (2014) solution ($b^{head}(t \rightarrow \infty) = \pi^{-1/3}\ell_b$ in a), and the orange dashed line is the 3D $\hat{K}^{[V]}$ GG (2014) solution. The inset of figure (b) shows the same quantity on the y-axis with a shifted x-axis (e.g., $(t - t_s)/t_s$). 155
- 5.5 Illustration of the definition of the overrun (5.22). Left: example of a zero overrun (as obtained for toughness-dominated buoyant fractures at the end of the release - region 3). Right: example of an overrun with the maximum breadth larger than the limiting breadth of the 3-D $\hat{K}^{[V]}$ GG (2014) solution (Garagash and Germanovich, 2014, 2022). 156
- 5.6 Evolution of fracture length $\ell(t)/\ell(t=t_s)$ (a) and head breadth $b^{head}(t)/\ell_b$ for viscosity-dominated buoyant non-stabilized fractures at the end of the release as a function of the dimensionless shut-in time t/t_s : $\mathcal{M}_{\hat{k}} \gg 1$, $\mathcal{B}_{ks} \geq 1$, $\mathcal{K}_{\hat{m}x,s} < 1$. Colored dashed-dotted lines in (a) show the corresponding late time, 3D $\hat{K}^{[V]}$ GG (2014) solution, the blue dashed line the continuous release buoyant scaling ($\ell(t)/\ell(t=t_s) \sim t^{5/6}$), the blue dashed-dotted line a numerical zero-toughness fit $\ell(t)/\ell(t=t_s) \approx 1.62(t/t_s)^{0.33}$ (matching the $\hat{M}^{[V]}$ -scaling). The green dashed line in (b) indicates the late-time limit of the 3D \hat{K} GG (2014) solution for the corresponding simulation. The blue-dashed line indicates the scaling dependence in the $\hat{M}^{[V]}$ -scaling, $b^{head}(t) \sim t^{-1/6}$. Note that the two zero-toughness simulations differ by their value of \mathcal{B}_{ms} (100 for the dark red and 25 for the light red simulation). 159

- 5.7 Viscosity-dominated fractures with negligible buoyancy at the end of the release: $\mathcal{B}_{ks} \geq 1$ and $\mathcal{B}_{ms} \ll 1$. a) Opening along the centerline $w(0, z, t) / w_{m\hat{m}}^{[V]}$ for $\mathcal{M}_{\hat{k}} = \infty$, $\mathcal{B}_{ks} = \infty$, and $\mathcal{B}_{ms} = 10^{-3}$ (zero-toughness case). b) Net pressure along the centerline $p(0, z, t) / p_{m\hat{m}}^{[V]}$ for the same case as in a). c) Fracture length $\ell(t) / \ell_{m\hat{m}}^{[V]}$ for large viscosity $\mathcal{M}_{\hat{k}} \in [5.1 \times 10^5, \infty]$ simulations. The blue dashed line is a fit of the zero-toughness simulation $\ell(t) \propto t^{0.33}$. d) Fracture breadth $b(t) / \ell_{m\hat{m}}^{[V]}$ (continuous lines) and head breadth $b^{head}(t) / \ell_{m\hat{m}}^{[V]}$ (dashed lines) for the same simulations. Purple dashed lines indicate the $M^{[V]}$ -solution (see section 3.4.2 of chapter 3), orange dashed lines the 3D $\hat{K}^{[V]}$ GG (2014) solution for the highest value of \mathcal{B}_{ks} . e - i) Evolution of the fracture footprint from radial e) towards the late time shape h) and i)) for the zero-toughness simulation. For the definition of the transition scales $\ell_{m\hat{m}}^{[V]}$ see table 5.4. 164
- 5.8 Phenotypes of possible buoyant hydraulic fractures of finite volume emerging from a point source ($\mathcal{B}_{ks} \geq 1$). a) Toughness-dominated finger-like fracture (region 3 in figure 5.1). b) Intermediate fracture with a stable breadth and negligible overrun. c) Viscosity-dominated buoyant end of the release with stabilized breadth (region 4 in figure 5.1). d) Viscosity-dominated buoyant end of the release without stabilized breadth (region 5 in figure 5.1). e) Zero-toughness case with a buoyant end of the release ($\mathcal{B}_{ms} = 10^2$). a) and b) are scaled by ℓ_b (Lister and Kerr, 1991), c) to e) by $\ell_{m\hat{m}}^{[V]}$ (see table 5.4). 165
- 5.9 Fracture height evolution as a function of dimensionless time for the experiments listed in table 5.2. Data extracted from figure 5a of Davis et al. (2023) based on experiments reported in Smitarello (2019). The black line shows a simulation with similar dimensionless parameters to Exp. 1945 and Exp. 1967. Purple dots mark the moment when the fracture becomes toughness dominated (e.g., $t = t_{mk}$), and dashed lines indicate the limiting solutions derived by Garagash and Germanovich (2014) respectively (green for a continuous release, orange for the release of a finite volume). 168
- 5.10 Height evolution of a toughness-dominated fracture together with the 3D $\hat{K}^{[V]}$ GG (2014) according to equation (5.35). 174
- 5.11 Opening (a) and pressure (b) along the centerline (e.g., $x = 0$) for a toughness-dominated simulation with $\mathcal{M}_{\hat{k}} = 1$ and $\mathcal{B}_{ks} = 2$ at $t / t_{k\hat{k}} = 179$. Black dashed-dotted lines show the tail solutions of equations (5.41) and (5.42). 175
- 5.12 Footprint (a), cross-sectional volume (b), opening (c), and pressure (d) of a zero-toughness, finite volume buoyant hydraulic fracture scaled by the corresponding $\hat{M}^{[V]}$ -scaling (see equation (5.45), or equation (5.24)). The blue dashed line in c) indicates the solution presented by Roper and Lister (2007). 178

List of Figures

- 6.1 Sketch of a buoyant hydraulic fracture propagating within a permeable media.
a) Sketch showing the change in total $\ell(t)$, head $\ell^{\text{head}}(t)$, and tail $\ell^{\text{tail}}(t)$ height in the interval $\Delta t = t_n - t_{n-1}$. The color code shows the fracture opening normalized by the maximum value. b) Zoom on the propagation at the head. The head's positions and the tail's beginning can be related to the coordinates z_n and t_{n-1} . c) Evolution of total fracture height $\ell(t)$ as a function of time for simulations with various leak-off coefficients at the transition from radial to buoyant propagation $\mathcal{C}_{\hat{k}}$. d) Zoom on the evolution of the simulation with $\mathcal{C}_{\hat{k}} = 1$, showing the pulsation of the fracture. 181
- 6.2 a) Sketch of a one-dimensional Stefan problem of a moving solidification boundary. The fracture can either melt the surrounding rock (meltback) such that the opening increases or the fluid solidifies, and the effective fracture opening for fluid flow reduces. b) Section of the considered problem where leak-off and solidification are considered. The fracture opening gets reduced due to the solidification of the fluid, whereas leak-off can still occur across the solidified boundary. 184
- 6.3 Dimensionless maximum opening of the head (equivalent to the maximum overall opening) $\max_{x,z} \left\{ \frac{w(x,z,t)}{w_{k\hat{k}}} \right\}$ with $w_{k\hat{k}} = \frac{K_{Ic}^{4/3}}{E' \Delta \gamma^{1/3}}$ as a function of dimensionless time $t/t_{k\hat{k}}$ (see figure 6.1 for a definition of $t_{k\hat{k}}$) for a simulation with $\mathcal{C}_k(t = t_{k\hat{k}}) = 1$. Black dots mark the reported evaluation points, and green edges indicate the approximate power law. A = Arrested phase, P = Propagation phase. 191
- 6.4 Opening and pressure evolution during propagation (a and b) and arrest (c and d) cycle for $\mathcal{C}_{\hat{k}} = 1$. a) and c) show the tip-based opening evolution. Insets emphasize the reduction (a) and increase (c) during the two stages. b) and d) show the corresponding pressure profiles. At the tip, the linearity disappears, causing the fracture to arrest. Insets show the oscillation of head volume (b)) and the head length (d)). Red dots mark the last moment of arrest before propagation occurs again. 193
- 7.1 Sketch of the numerical simulation setup. We consider a block injection of fluid creating a planar three-dimensional fracture in the (x, z) -plane (point source at $(x, z) = (0, 0)$). The compressibility of the injection line and surface effects are neglected. All considered fluids are positively buoyant, so we study changes in solid properties at a distance $z = d$ from the source point. 202
- 7.2 Evolution of scaled fracture height for simulations with a size-dependent apparent toughness. Green and red lines represent respectively set 1 (crosslink gel into sandstone) and set 2 (slickwater into mudstone), with continuous lines the modest property change and dashed lines the maximum one. Classical scaling laws like the $t^{4/9}$ of radial-viscosity-dominated propagation or the t^1 dependence for toughness-dominated buoyant fractures during the injection are indicated. Black dashed lines indicate the solution for a uniform, constant fracture toughness. 204

| | | |
|------|---|-----|
| 7.3 | Evolution of scaled fracture-size dependent apparent toughness. The color code is equivalent to figure 7.2. Indicated power laws are derived from characteristic length scales of classical HF regimes in equation (7.1). For the becoming buoyant at late time (two lines with smaller slope, set 1 and set 2 with modest values), the toughness seems to become approximately stable with variations of the order of $\pm 15 - 20$ %. | 206 |
| 7.4 | Evolution of fracture height (a) and maximum breadth (b) for simulations with a jump in fracture toughness. Grey lines show an immediate breakthrough (minimal spreading at the interface), turquoise lines a temporal containment (height growth stops temporarily before increasing again), and red lines an indefinite containment (the fracture arrests indefinitely at the interface). | 207 |
| 7.5 | Evolution of the "local" energy release rate at the top front position on the fracture center line (see the inset for a definition) for toughness jump simulations. The color code is as defined in figure 7.4, and dashed horizontal lines indicate the modest (blue) and maximum (red) toughness jumps. | 209 |
| 7.6 | Footprint and opening distribution for the temporarily contained fracture of Set 1 and a toughness Jump of $K_{Ic-2}/K_{Ic-1} = 5$ at $t/t_d = 5.11$. The buoyant HF in the upper layer after the breakthrough is finger-like. A combination of extension and fluid flow into the central buoyant HF generates a complex opening distribution in the low-toughness layer. | 211 |
| 7.7 | Footprint and opening distribution for an indefinitely contained fracture with $\Delta\sigma = 1.00$ (MPa) at $t/t_d = 156$. After a limited penetration into the upper layer, the fluid release ceases. The fracture concentrates in an elongated, nearly elliptical shape just below the interface of the stress jump. | 212 |
| 7.8 | Evolution of fracture height (a) and penetration depth (b) for simulations encountering a stress jump. The color code is equivalent to the one described in figure 7.2. (b) Shows the expected behaviour derived from the analysis of figure 7.9 with no breakthrough if the penetration depth remains below ℓ_{b-1} . | 214 |
| 7.9 | Evolution of the penetration depth for various stress jumps (corresponding to $\mathcal{S} \in (2.20, 13.2)$) applied to the second parameter set. This evaluation shows that breakthrough only occurs once the penetration depths overcome the buoyancy length scale ℓ_{b-1} . | 215 |
| 7.10 | Fracture height evolution for simulations with a uniform leak-off coefficient as a function of $t/t_{m\hat{m}}$ with $\ell_{m\hat{m}} = E'^{5/7} \mu^{4/7} / (Q_o^{3/7} \Delta\gamma^{9/7})$. Color code as in figure 7.2. | 217 |
| 7.11 | Fracture height evolution for simulations with a jump in leak-off coefficient. The dotted lines show the evolution for uniform leak-off simulations with $C = 10^{-10}$ ($\text{m}\cdot\text{s}^{-1/2}$). Color code as in figure 7.2. | 218 |
| 7.12 | Arrested fracture footprint with opening distribution before closure for a uniform (a) and a jump (b) in leak-off coefficient. The figures use parameter Set 2 and a leak-off coefficient $C = \Delta C = 10^{-6}$ ($\text{m}\cdot\text{s}^{-1/2}$). | 219 |

List of Tables

| | | |
|-----|--|----|
| 2.1 | Elastic values of rocks and materials used in laboratory experiments. The references are: ^a (Jaeger et al., 2007), ^b (Reches and Fink, 1988), ^c (Alm et al., 1985), ^d (MacDonald et al., 1988), ^e (Dobson and Houseworth, 2013), ^f (Heimpel and Olson, 1994) (note that gelatines with Air contents between 1.4 % to 4.0 % have values in between the limits), ^g (Taisne and Tait, 2009), ^h (Bunger and Detournay, 2008) (the plain strain modulus $E' = E / (1 - \nu^2)$ only is reported, we estimate E using the generic values of ν provided in this table), ⁱ (Jiang et al., 2018) for the density, ^j (Schwartz et al., 2019) for the density, ^k (Byerly and Knowles, 2017) for the density. | 19 |
| 2.2 | Properties of fluids used in laboratory and field hydraulic fracturing applications. ^a (Guillot and Dunand, 1985), ^b (Dai and Zhao, 2019), ^c (Kefi et al., 2004), ^d (Huppert and Sparks, 1981), ^f (Batchelor, 1967), ^g (Chen et al., 2020; Luo et al., 2014), ^h (Spera et al., 1988), * we only consider the Newtonian plateau observed at low shear rates. | 29 |
| 2.3 | Permeabilities and storage coefficients of various rock formations. ^a (Guéguen and Palciauskas, 1994), ^b (De Marsily, 1986), ^c (Chang and Firoozabadi, 2000), ^d (Hall, 1953), ^e (Jaeger et al., 2007), ^f (Dobson and Houseworth, 2013), ^g (Ripepi et al., 2023), ^h (Ruddy et al., 1989), ⁱ (van Eijs and van der Wal, 2017). | 31 |
| 2.4 | Characteristic values of Mode I fracturing toughness K_{Ic} from different studies and formations. The conditions and methods used in each study are not comparable, such that comparisons between studies are difficult.* the minimum measured parallel to the foliation, whereas the maximum occurs perpendicular to the foliation. | 33 |
| 3.1 | Characteristic scales and evolution parameters in the four propagation regimes for post-shut-in evolution (pulse injection case). | 52 |
| 3.2 | Characteristic values of industrial HF applications for a so-called single entry treatment (propagation of a single hydraulic fracture). | 69 |
| 3.3 | Resulting dimensionless parameters, arrest, and shut-in radius as well as post-injection propagation and elapsed time between shut-in and arrest. | 70 |
| 3.4 | Estimated values for magma injections neglecting buoyant forces. | 71 |
| 3.5 | Resulting fracture dimensions and propagation post-injection for a magmatic release (not accounting for buoyancy forces). | 71 |

List of Tables

| | | |
|-----|--|-----|
| 3.6 | Relative difference between solutions obtained numerically and the results from the self-similar Gauss-Chebyshev collocation scheme. PyFrac simulations (PVP_003 and PVP_005) and a simulation of the code described in Lecampion and Desroches (2015). $\mathcal{E} = \frac{\int_0^1 f_N(\rho)d\rho - \int_0^1 f_{GC}(\rho)d\rho}{\int_0^1 f_{GC}(\rho)d\rho}$ where f_N is an interpolation function of the numerical results and f_{GC} the solution obtained via the Gauss-Chebyshev collocation scheme. The L_2 and L_∞ norms follow their usual definition. | 80 |
| 4.1 | Comparison between characteristic head and tail length, head breadth and head volume for toughness-dominated fractures $\mathcal{M}_{\hat{K}} \in [10^{-3}, 10^{-1}]$ at various dimensionless times $t/t_{k\hat{K}}$. The mismatch is calculated as the relative difference between our numerical results and the approximate 3D \hat{K} GG, (2014) solution (GG in the table). | 96 |
| 4.2 | Comparison between characteristic head length, head volume, and maximum opening in the head $\left(w_{\max}^{\text{head}} = \max_{x,z} \{ w(x, z \in [z_{tip} - \ell^{\text{head}}(t), z_{tip}], t) \} \right)$ for viscosity-dominated fractures $\mathcal{M}_{\hat{K}} \in [1 \times 10^4, \infty[$ at various dimensionless times $t/t_{m\hat{m}}$ | 106 |
| 4.3 | Characteristic scales (and governing dimensionless parameters \mathcal{P}_s) in the different scalings. | 115 |
| 4.4 | Transition scales between regimes. The toughness head scales in table 4.3 corresponds to the transition scales $K \rightarrow \hat{K}$ | 116 |
| 4.5 | Properties of the solids and the fluids used in the experiments of Heimpel and Olson (1994). After the double boundary, the parameters are estimated or derived and not explicitly reported in Heimpel and Olson (1994). | 132 |
| 4.6 | Combinations used for the experiments reported in Heimpel and Olson (1994) and characteristic values derived. | 134 |
| 4.7 | Comparison of finger-like toughness-dominated fracture breadth with the experiments of Heimpel and Olson (1994) shown in their figures 8 and 9. | 135 |
| 4.8 | Breadth comparison for the finite volume release experiments of Taisne and Tait (2009). | 137 |
| 5.1 | The regions of figure 4.11 with their respective propagation history and the estimated limiting values of the dimensionless coefficients. The descriptions of the limiting regimes can be found in Savitski and Detournay (2002) for the M and K regimes, chapter 3 for the $M^{[V]}$ and $K^{[V]}$ regimes, chapter 4 for the \hat{M} and \hat{K} regimes, and in this chapter for the $\hat{M}^{[V]}$ and $\hat{K}^{[V]}$ regimes (see appendix 5.9.1 for a summary of the scalings). | 151 |
| 5.2 | Material parameters and the released volume V_o are taken from table 3 of Davis et al. (2023) (based on the work of Smitarello (2019)). We extract the shut-in time from figure 5a of Davis et al. (2023) and calculate the release rate as $Q_o = V_o/t_s$ | 167 |
| 5.3 | Characteristic scales (and governing dimensionless parameters) in the different scalings. | 171 |

| | | |
|-----|---|-----|
| 5.4 | Transition scales between regimes. The transition scales of the $M^{[V]} \rightarrow K^{[V]}$ transition correspond to the $K^{[V]}$ -scales, and the transition scales of the $\hat{M}^{[V]} \rightarrow \hat{K}^{[V]}$ (head) to the $\hat{K}^{[V]}$ scales of the head, given respectively as the $K^{[V]}$ and $\hat{K}^{[V]}$ (head) in table 5.3. | 172 |
| 6.1 | Characteristic scales (and governing dimensionless parameters \mathcal{P}_s) in the different leak-off/solidification-dominated scalings. | 197 |
| 7.1 | The two sets of parameters used within this study and their main dimensionless parameters. | 201 |
| 7.2 | The two parameters, respectively, changes used throughout the paper. | 203 |

Mechanics of Hydraulic Fractures

Part I

1 Introduction

The propagation of hydraulic fractures through the lithosphere is observed in various anthropogenic activities: geothermal, carbon storage, energy storage, hydrogen production, brine mining, oil and gas production, soil remediation, mining stabilization, and in-situ stress measurements. In most industrial applications, so-called hydraulic fracturing stimulations are performed. During such a stimulation, a pressurized fluid is injected into the targeted rock formation. The injection is either very localized (at a point only) or conducted over a large section of the wellbore. The pressurized fluid creates tensile fractures, propagating into the rock mass. Dependent on the industrial application, the purpose of these fractures differs. In various energy-related applications, the goal is to increase the in-situ permeability of the target formation, achieved through preferential flow paths (fractures) for fluids. The effective increase in permeability of the rock mass then serves as the primary variable to check for the effectiveness of the hydraulic stimulation (Economides and Nolte, 2000). So-called mini-frac tests are performed to measure the in-situ stress. During these tests, a small quantity of fluid is injected, and the pressure when the fracture initiates is reported. The injection is subsequently stopped, and the liquid flows back into the borehole. When fluid flow back is completed, the fracture closes at a given fluid pressure. From these two pressure measurements, the minimum in-situ compressive stress can be estimated (Haimson and Fairhurst, 1969; Haimson and Cornet, 2003).

Hydraulic fractures not only appear due to human activities. Horizontal and vertical magmatic intrusions in the Earth's crust also form through hydraulic fracturing. Such processes are suggested to be the main mechanisms of large-scale mass transport through the lithosphere (Rivalta et al., 2015). Other natural occurrences of hydraulic fractures include base ruptures of glaciers, the calving of ice sheets in arctic regions due to buoyant hydraulic fractures, or hydrocarbon generation creating a significant increase in pore pressure (Tsai and Rice, 2010; Pattyn, 2018; Vernik, 1994).

This thesis focuses on the macro-scale propagation of tensile hydraulic fractures in an initially intact rock mass. Even though the industry has used the technique of hydraulic stimulation for decades, some key aspects, like the finiteness of the volume of fluid released and the effects of



Figure 1.1: Example of outcrops of magmatic intrusions: a) Ship Rock in New Mexico (USA) (picture taken by James St. John on 02.09.2007, downloaded on 17.03.2023). b) Fissure eruption on the north flank of Piton de la Fournaise starting on 9th March of 1998 (La Réunion Island, France) (picture taken by Luc Souvet on the 09.03.1998, downloaded on 17.03.2023). c) Makthesh Crater in the Negev Desert (Israel) (picture taken by Andrew Shiva on 24.07.2016, downloaded on 17.03.2023).

gravitational forces on large fractures, have obtained little attention. Even without considering these effects, three-dimensional planar fractures show complicated behavior depending on in-situ and injection conditions and the host rock and fluid properties. When characterizing these effects and the possible outcomes, we extensively use scaling arguments, which we validate through numerical simulations. Notably, these scalings enable us to cover all possible parameter combinations and hence allow dealing with the inherent uncertainty regarding reservoir properties and in-situ conditions. A particular emphasis is put on validating our simulation results against scaling predictions, approximate and lower dimensional solutions, and analytical solutions.

1.1 Motivation and background

1.1.1 Magmatic intrusions / Diking

The term hydraulic fractures (HF) describes a tensile (Mode I) fracture driven by the flow of a pressurized internal fluid in a solid medium under compressive stresses. This fracture type is genuinely observed in various circumstances in geomaterials (soils and rocks) (Detournay, 2016). The most impressive natural occurrences are geological formations called dikes (Spence et al., 1987; Rivalta et al., 2015). These magmatic intrusions form due to the release of magma at a deep, overpressurized source. The path such intrusions follow may be very complex, occasionally depositing horizontally (so-called sills). Their ascent rate is usually unsteady (Peltier et al., 2007; Sigmundsson et al., 2015) caused by possibly non-constant source conditions or other mechanisms, making it difficult to estimate if the intrusion will become trapped within the subsurface or form a fissure opening at a volcanic flank (Pedersen et al., 2007; Roult et al., 2012). Well-known examples of trapped magmatic intrusions exposed after cooling thanks to erosion include the Shiprock Mountain in New Mexico (Larson and Strangway, 1969; Lister and Kerr, 1991) and formations in the Negev desert in Israel. An example of a fissure

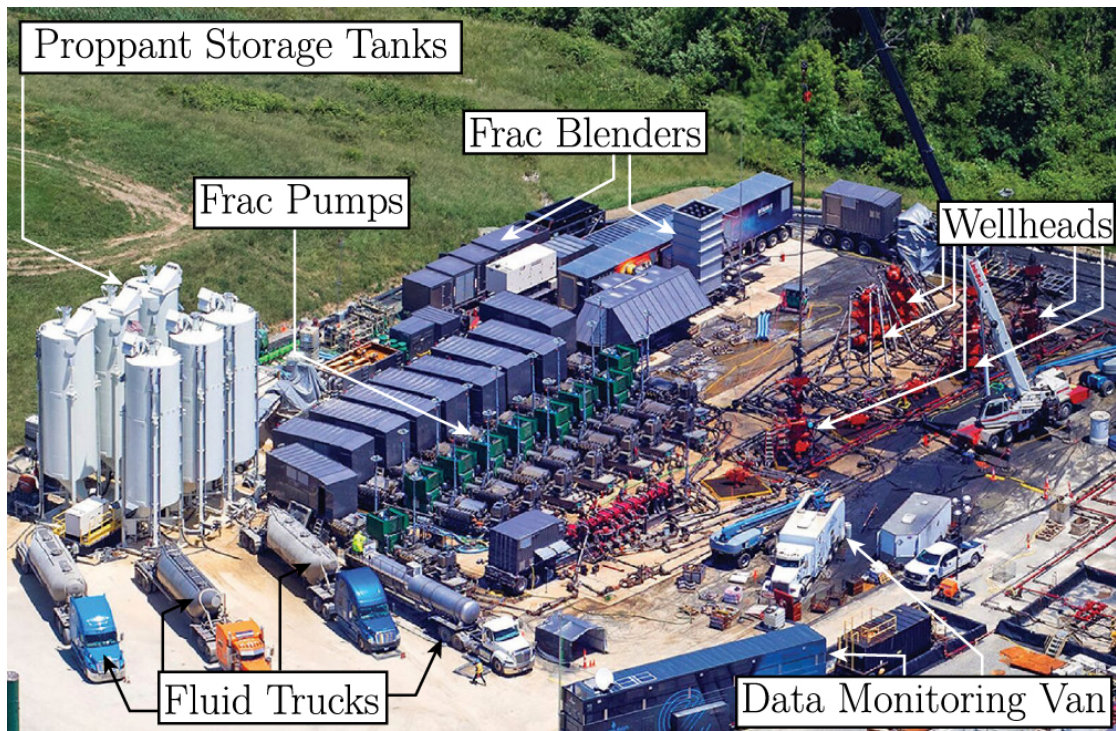


Figure 1.2: Setup of a typical hydraulic fracturing treatment. (picture taken by Evolution Well Services in 08.2019, downloaded on 11.05.2023).

eruption is presented by the 1998 intrusion at Piton de la Fournaise on La Réunion Island (see figure 1.1).

1.1.2 Hydraulic fracturing treatments

The most known appearance of hydraulic fractures is the industrial placement in the oil and gas industry to enhance the permeability of hydrocarbon-bearing formations. Hydrofracturing jobs are performed in low to very-low permeability reservoirs (Smith and Montgomery, 2015) and intend to initiate and propagate one (or multiple) hydraulic fracture(s). This goal is achieved by injecting a fracturing fluid at a controlled pumping rate into the previously drilled wellbore. The fracturing fluid is enriched by a proppant (solid particles, like sand) during the hydrofracturing treatment emplacing the fracture. The filling of the fracture with proppant keeps the fracture open and creates a preferential flow path for fluids due to the increased permeability of the proppant-filled fracture compared to the host rock.

The hydraulic fracturing industry and associated services revenue amounts to about 22.5 Billion USD in the United States alone (see the data of *IBISWorld* last updated on 26.04.2021 and consulted on 18.03.2023). Hydraulic fracturing treatments generally require a significant amount of installations. Notably, achieving the potentially large downhole pressures necessary to fracture the rock need high-pressure pumps installed on so-called pump trucks, capable of generating up to 100 MPa (see figure 1.2). Note that the downhole pressure is not equivalent

Chapter 1. Introduction

to the pressure at the injection pump. The downhole pressure accounts for the hydrostatic pressure of the fluid column in the wellbore and is reduced through the pressure drop caused by the fluid flow inside the wellbore (frictional pressure drop). For typical single fracture treatments, the injection rate of the fracturing fluid into the wellbore falls in the range of $0.5 \text{ m}^3/\text{min}$ to $6.0 \text{ m}^3/\text{min}$ (Wan, 2011). When the treatment aims to initiate multiple fractures, the injection rates of a single fracture can be multiplied by the number of fractures (Lecampion and Desroches, 2015).

Designing hydraulic fracture treatments aims to ensure that the fracture created fulfills a desired geometry and uniform fill by the injected proppant. After fracture initiation, the volume injected is balanced between losses by leak-off to the host rock and the fracture volume. The goal of the design is thus to maximize the fluid volume remaining in the fracture. This goal is supplemented by the aim of uniformly distributing the proppant. Combining the two will increase the permeability and productivity of the well efficiently. A measurement of this design is the "fracturing efficiency", which is the ratio of the fracture volume and the injected fluid volume. This quantity directly relates to the final propped fracture shape (width and surface area). The process is history-dependent such that these final parameters depend on the injection schedule (rate, volume, fluid composition), the fracturing fluid characteristics (rheology, density), the proppant, and the host rock characteristics (stiffness, permeability, toughness). Consequently, designing hydraulic fracturing treatments at a given location with a known geological formation involves not only the correct choice of the fracturing fluid and proppants but also the injection schedule. Finally, one must include considerations of operation safety in the design. A notable concern might be the emergence of a self-sustained buoyant propagation directed to the surface. Such fracture ascent might reach higher laying, potentially ground-water-bearing formations. The fracturing fluid is harmless. Only the natural gas or oil it carries is potentially hazardous. Ensuring a safe operation thus involves additional considerations of buoyancy to exclude such forms of pollution.

1.1.3 Other industrial applications

Many other applications of hydraulic fracturing stimulations exist in various industrial branches like conventional mining (Jeffrey et al., 2013), civil engineering (Lancellotta et al., 2017), in-situ stress measurements (Detournay et al., 1989; Boone and Ingraffea, 1990; Haimson and Cornet, 2003), geothermal energy production, mining of brine, orange hydrogen production, fracture thermal/elastic energy storage, and CO_2 -sequestration programs. An application that aims to connect existing fractures rather than create new ones is enhancing water production from rock aquifers. In this application, low-pressure injections are sufficient because there is no need for newly created fractures. In this thesis, we are mainly interested in the last five industrial applications mentioned because only these fields are prone to generate sufficiently large fractures, such that gravitational effects will become of the first order.

Geothermal energy production

The application of hydraulic fracturing in geothermal energy production is more recent. The geothermal energy sector still comprises only about 0.5 % of the renewable energy production in the world despite its potential (Lebedys et al., 2022; Kiruja et al., 2023; Hutter, 2021). An increase in the installed power by about 50 % since 2013 could not increase the market overall market share. The hydraulic fracturing treatment in the enhanced geothermal system (where the enhanced indicates stimulations to raise the permeability/production of the system) in a project near the Newbury volcano in Oregon in 2013 was the first large-scale implementation of this technique (Adams and Rowe, 2013).

An interesting by-product of geothermal systems is geothermal brines. A geothermal brine is a hot salty fluid. Such brines, with potentially precious dissolved salts/minerals (like lithium), can occur naturally at various places in the subsurface. They can be mined independently of a geothermal site or in combination. A 2020 technical report of the United States Office of Energy Efficiency & Renewable Energy (Stringfellow and Dobson, 2020) indicates that Lithium production from brines will increase significantly in the upcoming years (see figures 2 and 3 of Stringfellow and Dobson (2021)), easily possible to cover the current demands of the United States.

Orange hydrogen

A recent development in the energy industry is the production of so-called "orange hydrogen". The color of hydrogen refers to the way it is produced. In 2021, about 96 % of the world's hydrogen production was "grey" or "black" (Osselin et al., 2022). For those types of hydrogen, the required energy input comes from natural gas (grey) or coal (black). Regarding CO_2 emissions, those two are no options to create a more sustainable energy future and need to be replaced by different types of hydrogen. So far, the commonly used alternative for grey and black hydrogen is "green" hydrogen. The label "green" states that the energy required for electrolysis comes from renewable energy sources. The fact that the electrolysis requires abundant energy and the cost of renewable energy is still large makes green hydrogen expensive. A similar approach to green hydrogen is blue hydrogen. In blue hydrogen production, the reaction to obtain the hydrogen is not electrolysis but either a Steam Methane Reforming (SMR) or Auto Thermal Reforming (ATR). These reactions split natural gas into hydrogen and CO_2 , requiring capturing the produced CO_2 and ensuring that methane losses remain minimal for blue hydrogen to be environmentally friendly (Howarth and Jacobson, 2021). A possible solution to these problems presents "orange" and "white" hydrogen. White hydrogen is naturally produced hydrogen through serpentinization, escaping the Earth's crust mainly on the seafloor but also on land (a long-known example is Mount Chimaera in Yanartaş (Turkey) (Etiope et al., 2011)) (Zgonnik, 2020; Osselin et al., 2022). Skipping the necessary transformations, which require energy and produce unwanted greenhouse gases as a by-product, is an exciting energy source (see an example in Bourakebougou (Mali) (Prinzhofer et al., 2018)). Orange hydrogen is an anthropogenic acceleration of serpentinization. Much like in an Enhanced Geothermal System (EGS),

Chapter 1. Introduction

the idea is to inject water into the many formations on Earth (Kelemen et al., 2011) susceptible to producing hydrogen. The injected water is collected within other wells, and the hydrogen it bears is extracted at the surface. Much like in enhanced Geothermal Systems, respectively, in the oil and gas industry, this process requires engineering the permeability and flow paths within the formation. The goals of the possible hydraulic fracturing treatments in this context are the same as for the production of oil and gas (Osselin et al., 2022).

Carbon capture and sequestration (CCS)

With the production of orange hydrogen goes our last application of hydraulic fracturing treatments, Carbon Capture and Sequestration (CCS). The link between the two is that the same formations are optimal for CCS and producing orange hydrogen (Kelemen et al., 2018). Producing orange hydrogen can thus be an environmentally friendly energy source while capturing additionally already emitted CO_2 . The large-scale CCS projects of Carbfix in Iceland and a pilot project in the Columbia River basalts (Wallula, USA) have demonstrated that the mineralization of the CO_2 works, even after the injection of up to 73 000 t (McGrail et al., 2017; Gíslason et al., 2018; Snæbjörnsdóttir et al., 2020). The design challenges of such large-scale injections remain unchanged from the challenges of increased productivity and safe operation presented for hydraulic fracturing treatments in the oil and gas industry.

Fracture thermal energy storage (FTES)

Finally, hydraulic fracturing techniques can not only be used to generate electricity but also to store energy. For example, fractured thermal energy storage (FTES) aims to store thermal energy through parallel employed hydraulic fractures in crystalline rocks. FTES was first proposed within the HYDROCK project (Larsson and Haag, 1985) in 1985. A test site was established at the turn of the century in Norway (Hellström and Larson, 2001; Ramstad et al., 2007), and the principle gained interest again in the recent energy transition discussion due to its capabilities of seasonal energy storage (Janiszewski et al., 2016). The design of such fractures maximizes their surface to maximize the heat exchange with the surrounding rock. Enhancing the formation's permeability is not wished here, as the fluid flows only in the horizontal fractures, and the exchange with the rock is limited to heat only. Another approach uses a single hydraulic fracture as elastic energy storage. This principle requires a horizontal hydraulic fracture placed in surface proximity. The fractures fluid is pressurized when excess energy is present. After the pressurization of the fluid lens, the borehole is shut-in. When demand for the excess energy arises, the pressurized fluid is released from the borehole and used to operate a turbine at the borehole, converting it back into electricity. The challenges of the design of such a fracture differ slightly. Notably, the plugging at the wellbore must be avoided at all expenses (Bunger et al., 2023; Schmidt et al., 2023).

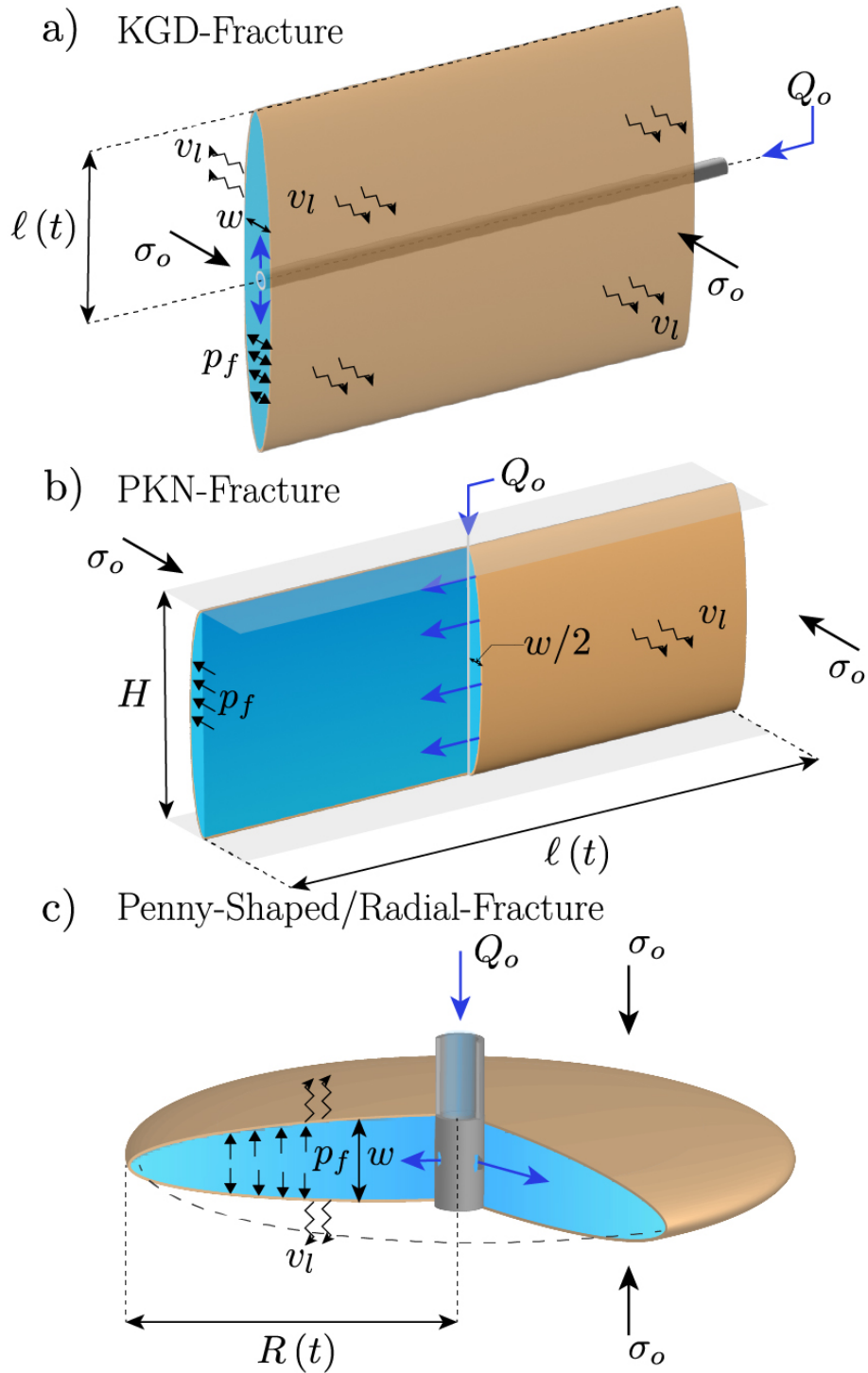


Figure 1.3: The three most often studied geometries of hydraulic fracture. a) The finite two-dimensional plane strain fracture called KGD-Fracture after Geertsma and De Klerk (1969). b) PKN-fractures using a local two-dimensional plane strain approximation named after Perkins and Kern (1961) and Nordgren (1972). c) The penny-shaped/radial planar three-dimensional fracture, observed for point sources fluid releases in a homogeneous media.

1.2 A review of hydraulic fracture growth

The need for understanding the initiation and propagation of hydraulic fractures arose in the 1950s with its development in the oil and gas industry. A first leap in understanding the hydraulic fracturing process recognized the importance of the coupling between the elastic deformation of the surrounding media and the fluid flow within the fracture (Barenblatt, 1962; Khristianovic and Zheltov, 1955). The identified system reveals a complex multi-physical and multi-scale behavior, such that early developments of the 1960/70s were restricted to simplified models. Most models used simplifying assumptions to reduce the fluid flow to one dimension only. One of these simplifying models, still widely used and investigated today, was developed by Perkins and Kern (1961). Their so-called PKN model (named after Perkin, Kerns, and Nordgreen (Nordgren, 1972)) assumes a fracture of a constant height (see figure 1.3b). Along the fracture length in the horizontal direction, each cross-section is supposed to obey a plane-strain deformation law, which results in a one-dimensional flow. Different from the PKN model, the KGD (named after Khristianovic, Geertsma, and De Klerk (Geertsma and De Klerk, 1969)) assumes a two-dimensional plane-strain fracture with a cusp shape (see figure 1.3a). The last of the genuinely considered geometries is axisymmetric. The first axis-symmetric model solved the problem of a fracture placed in an impermeable medium with a high fracturing toughness (Abé et al., 1976) (see figure 1.3c). Based on the original PKN model, Simonson et al. (1978) developed the first pseudo-three-dimensional model for fracture propagation. Their approach divided the fracture laterally into multiple adjacent cells, allowing the fracture height and width to be calculated from the local fluid pressure (Adachi et al. (2010) present a more detailed discussion). At about the same time, the first models considering fracture arrest and closure emerged. Nolte (1979) used the assumption of a PKN-Fracture to derive characteristics of the final fracture from the pressure decline at the wellbore after the end of the injection. One of the main hypotheses of Nolte (1979) was that fracture propagation immediately stops upon the end of the injection. The restriction of immediate arrest was lifted by the work of Settari and Cleary (1984), which developed a pseudo-3D simulator capable of modeling two-phase flow, closure, and production of hydraulic fractures. Efficient numerical simulation of PKN fractures was made accessible by implementing a moving mesh-based explicit finite difference scheme by Detournay et al. (1990). Adachi et al. (2001) then developed a solver for KGD fractures propagating in a zero fracture toughness, elastic media. Other researchers started to investigate axis-symmetric fractures. Desroches and Thiercelin (1993) used a fully coupled numerical tool to this end, including lubrication flow and fluid leak-off, and Gu and Leung (1993) extended the analysis of the closure of a finite fluid volume fracture started by Nolte (1979); Settari and Cleary (1984) to 3D planar hydraulic fractures in heterogeneous stress and leak-off conditions.

1.2.1 Energy dissipation mechanisms

The discussion about the competing mechanisms of energy dissipation by viscous flow and energy dissipation to create new surfaces started in parallel. This debate originated from the

observations of several researchers (Spence and Sharp, 1985; Lister, 1990b) that viscous flow in the fracture may dominate the growth of the hydraulic fractures. The observations revealed that when the fracture resistance of the solid becomes negligible, the fracture behavior close to the propagating edge (the fracture tip) behaves no longer akin to linear elastic fracture mechanics (LEFM). The solution to this limiting, the zero-toughness case, was derived in Desroches et al. (1994) for an impermeable medium and in Lenoach (1995) when accounting for fluid leak-off. These developments and observations formed the basis of an efficient approach to characterize the competition between the two energy dissipation mechanisms. The technique consists of zooming into the near-tip region of a hydraulic fracture, where asymptotic solutions can be derived. From this near-tip behavior, it is possible to deduce the effects of the multi-physical behavior on the macroscale growth of the hydraulic fracture. Unfortunately, the lack of universal near-tip solutions prevented the development of reliable numerical tools for this multi-scale, multi-physical problem for decades (Adachi et al., 2007; Lecampion et al., 2018). Apart from the solutions of Desroches et al. (1994); Lenoach (1995), Garagash and Detournay (2000, 1998) studied the near-tip behavior in an elastic impermeable medium where a fluid lag appears. A fluid lag is a cavity separating the front of the fracturing fluid from the fracture front, where the rock is breaking. In their approach, the fracture toughness can take an arbitrary value, and the cavity is traction free, allowing them to solve for the cavity length as the unknown. The approach can, however, be extended to account for in-flowing fluid from the host rock, allowing studying the circulation of pore fluid between the lag and the surrounding media (Detournay and Garagash, 2003). In this configuration, cavitation of the fluid in the lag is possible, and its limits are discussed. A complete solution accounting for the effects of fluid leak-off, viscosity, and toughness was only developed by Garagash et al. (2011) and approximated with a numerically efficient function by Dontsov and Peirce (2015a); Dontsov (2017).

1.2.2 Hydraulic fracture tip asymptotics

A different line of research, necessary to validate the relationship between the tip behavior and the macroscopic growth of the fracture, studied finite hydraulic fractures. The methods used therein are scaling and dimensional analysis to clarify the interplay between the physical phenomena of viscous flow of the fracturing fluid, creation of new fracture surfaces, leakage of the fracturing fluid to the surrounding medium, and the elastic deformation of the host rock (Detournay, 2016, 2004). These analyses revealed that a finite set of dimensionless numbers is sufficient to quantify the various possible propagation regimes by separating the governing mechanisms. Furthermore, setting one or several of these dimensionless numbers to unity will allow the development of solutions for finite fracture propagation (Madyarova, 2003; Bungert et al., 2005c). During the propagation history of such fractures, the hydraulic fracture often transitions from one limiting regime to another. It is possible to characterize these transitions with well-defined transition lengths and time scales (Garagash, 2009; Madyarova, 2003; Savitski and Detournay, 2002; Lecampion et al., 2017). These limiting solutions serve as a benchmark for numerical solvers and have been validated by laboratory experiments.

1.2.3 Scaling and semi-analytical approaches

With the insights obtained of the behavior at the fracture tip and the expectations of fracture behavior from the finite fracture scaling analysis, sophisticated planar 3D solvers have emerged. Notably, Peirce and Detournay (2008) introduced the implicit level-set algorithm (ILSA) in a scheme for hydraulic fracture propagation in a homogeneous media (Dontsov and Peirce, 2017). The main characteristic of the ILSA scheme is its usage of the near-tip asymptotics at the propagating edges. Thanks to a volume conservation scheme, this local behavior is linked to the coupled hydro-mechanical problem of the system composed of the fracture and the fracturing fluid. The fully implicit scheme proved extraordinarily robust and enabled the solution for finite fractures in plane-strain and axis-symmetric configurations (Garagash, 2000; Savitski and Detournay, 2002; Bungler et al., 2005a; Madyarova, 2003). Their versatility allows them to account for various phenomena like non-Newtonian fluids, buoyant forces, heterogeneities of the host media, and others. A comparison between explicit, implicit, and predictor-corrector schemes was shown to be accurate by Zia and Lecampion (2019) using a Python implementation of the ILSA scheme (Zia and Lecampion, 2020). Several other numerical solvers exist, and we refer the reader to Lecampion et al. (2018) for a review of current trends in the numerical modeling of hydraulic fractures.

1.2.4 Buoyant hydraulic fractures

Simultaneously to these developments, the domain of buoyant hydraulic fractures significantly advanced. The first analogy to buoyant propagation originated from the theory of a two-dimensional (2D), plane strain, hydrostatically loaded fracture developed by Weertman (1971). The so-called Weertman's pulse derives a static equilibrium solution but cannot explain the propagation velocity of the crack. The findings of Weertman (1971) inspired a series of numerical modeling approaches to buoyant hydraulic fractures (Rivalta et al., 2015). These uncoupled models are not suitable to describe vertical crack velocities but underwent considerable extensions accounting for lateral extensions (Heimisson et al., 2015), heterogeneities (Maccaferri et al., 2010), and complex fracture shapes where the fracture propagation direction must be estimated (Dahm, 2000a; Maccaferri et al., 2011; Davis et al., 2020, 2021). A second approach to vertically propagating hydraulic fractures assumed that the resistance to fracture of the rock is negligible and only elastic forces and viscous fluid flow matter (Lister and Kerr, 1991; Spence and Turcotte, 1985; Spence et al., 1987). Modeling buoyant hydraulic fractures assuming a zero-fracture toughness allows for deriving the fracture propagation velocity but fails to include complex propagation paths or heterogeneities. Both modeling approaches and their respective solutions indicate a separation of the propagating fracture in two regions characterized by different energy dissipation mechanisms. A head, where the balance between buoyancy and fracture toughness dominates, and a tail, dominated by viscous fluid flow. Dahm (2000b) tried to combine the two in 2D and inspired a recent extension using an energy approach (Furst et al., 2023). These theories remained within the 2D limits, although Lister (1990a) already proposed a pseudo-3D solution for fractures within

the limit of negligible fracture toughness. Only recently, (Garagash and Germanovich, 2022) were the first to present a full three-dimensional (3D) description. The fundamental features in the 3D planar solution of Garagash and Germanovich (2022) remain the same as for the 2D approximations (toughness-dominated head and viscosity-dominated tail) and assume that the buoyant hydraulic fracture is well established with a vertical height far beyond the lateral extend. Finally, Davis et al. (2021) proposed an extension of the 2D approaches neglecting viscous flow in the fracture to non-planar 3D fracture propagation.

1.2.5 Experimental investigation of hydraulic fractures

Experimental measurements of hydraulic fracture characteristics are a delicate task. Laboratory fractures have tiny openings (on the order of μm), and their planar propagation needs to be monitored in real-time to provide valuable data for propagation models. Nonetheless, laboratory experiments significantly enhanced the understanding of the hydraulic fracturing process. The experimental observation that fractures grow perpendicular to the minimum in-situ stress by Hubbert and Willis (1957) proved that hydraulic fractures grow vertically in the field, where the minimum in-situ stress is usually horizontal. Other examples include the experiments of Daneshy (1978) in layered sand- and limestones, which showed that upon interaction with the bedding plane, the fracture deviates at or breaks through the heterogeneity dependent on the conditions. Comparison of experiments with numerical simulations and theoretical approaches required the development of sophisticated acoustic measurement techniques. Pioneering work in this approach was performed by Medlin and Masse (1984), who used transmitted compressional P-waves to measure fracture length. Their measurements already revealed that two distinct fronts exist, a fluid and a fractured front, confirming the existence of a fluid lag at the fracture tip under given conditions. Observing the fracture front is also possible using diffracted waves from the fracture tip (Savic, 1995). Bunger and Detournay (2008) developed a photometry technique to track hydraulic fracture growth in transparent media, featuring direct observation of the fracture growth dynamics. Thanks to these experimental developments, experiments reproduced the theoretical and numerical predictions of fracture propagation (length scale, radius, net pressure, and tip asymptotics). Most experiments were performed on artificial materials such as PMMA, hydrogels, and cement (Bunger and Detournay, 2008; Wu et al., 2008; Jeffrey et al., 2009; Lai et al., 2015; Lecampion et al., 2017; O’Keeffe et al., 2018; Tanikella and Dressaire, 2022; Tanikella et al., 2023). There exists limited experimental data on geomaterials representative of in-situ conditions (tight mudstone (Lecampion et al., 2015) and sandstone (Lhomme, 2005), gabbro (Liu et al., 2020; Liu and Lecampion, 2022b,a)). The gabbro experiments (Liu et al., 2020; Liu and Lecampion, 2022a) showed that cohesive zone effects, the roughness of the fracture surface, and solid bridges significantly affect hydraulic fracture propagation. They also report that the apparent fracture toughness to explain the propagation velocity and fracture opening seems to increase with the size of the fracture. In addition to these studies of planar fractures in various materials and under various conditions, Bunger et al. (2004, 2005b) studied near-surface effects, Bunger et al. (2011); Kear et al. (2013) stress shadowing mechanisms between multiple

hydraulic fractures, and Bunger et al. (2013, 2008) fracture curving. The influence of a variation in in-situ stress was studied by Wu et al. (2008), aiming to validate the results of a 3D hydraulic fracture solver. The strong influence of the fluid compressibility effect at fracture initiation was demonstrated experimentally and numerically by Lecampion et al. (2017). They observed a transient regime from the compressibility dominated to the steady propagation regime. This transition susceptibly dominates laboratory-scale experiments if not properly designed. It is worth noting that in the experiments of Liu et al. (2020); Liu and Lecampion (2022a), the authors ensured that they are outside of this transition. The scarcity of data in geomaterials led to some experiments on an intermediate (decameter) to large (kilometer) scale. The experiments in the Northparks Mines (Jeffrey et al., 2009) (dry fractured crystalline rock) and overpressurized sedimentary formations (Warpinski et al., 1993) are particular as they differ from typical evaluations thanks to the direct fracture characterization (mine-back or coring) and the supplementary data from geophysical measurements (tiltmeters, active, and micro-seismicity). The field experiment at the intermediate scale of Jeffrey et al. (2009) highlighted that, despite the complexity of fracture initiation at a small scale, the large-scale (late time) behavior follows the planar approximations of a single propagating fracture. In contradiction, the retrieved core from the M-site (Warpinski et al., 1993) shows numerous small micro-cracks around the fracture. These parallel sub-cracks lack the fracturing fluid indicating that the injection process does not create them. They are induced by stress changes caused by fracture propagation. Note that all laboratory experiments support single fracture advancement, showing little to no parallel micro-cracking. In contradiction, recent findings in the west Permian basin (Ciezboka, Jordan. and Courtier, James. and Wicker, Joe., 2018) and numerous observations of sites containing magmatic dikes strengthen the latter assumption of sub-parallel cracking (Weinberger et al., 2000; Delaney et al., 1986). This discrepancy between many laboratory experiments in purely brittle materials and field observation reveals that multiple questions remain to be answered. It is notably unclear how plastic or cohesive zone effects affect apparent fracture toughness and which contributions come from sub-parallel micro-cracks. Concerning sub-parallel micro-cracking, the role of the initial pore pressure remains unclear.

1.3 Research questions addressed

In the absence of heterogeneities and considering a linear elastic isotropic medium, the orientation of a propagating hydraulic fracture is solely governed by the in-situ stress orientation in the rock mass. For such a well-defined case, the fracture will grow perpendicular to the minimum in-situ stress σ_o (see figure 1.3). For fractures at depth, the weight of the overburden usually leads to a stress state with a horizontal minimum in-situ stress. For such a fracture orientation, the confining minimum in-situ stress over the fracture plane generally increases linearly with depth, proportional to the increase in the overburden. If the fracturing fluid and the host rock show a density difference (as is often the case), this configuration gives rise to a uni-directional buoyant force. We investigate the influence of this buoyant uni-directional

force on the propagation of initially radial hydraulic fractures. Notably, we are interested in defining if and when the uni-directional buoyancy force will become dominant, such that the fracture transitions from a radial to an elongated shape due to buoyant forces. We can formulate the first research question we try to answer as

When does the release of a finite volume of fluid from a point source in a linear isotropic elastic medium lead to the emergence of a self-sustained buoyancy-driven hydraulic fracture?

If buoyancy-driven fractures emerge, it is of interest to characterize how these buoyant hydraulic fractures ultimately propagate. We want notably to investigate if previously developed limiting regimes for their late-time propagation apply to real-world cases. For this comparison, a second research question arises.

What characteristic ascent rates, shapes, and opening distributions have buoyant hydraulic fractures?

Finally, once these two things are known, we can address a final question regarding the arrest of buoyant hydraulic fractures.

Which mechanisms can efficiently arrest/stop buoyant hydraulic fractures?

1.4 Organisation of this manuscript

The remainder of this thesis is organized as follows.

Chapter 2 provides the theoretical bases and the numerical tools applied within this thesis and can be skipped by the informed reader.

Chapter 3 investigates the arrest of planar three-dimensional axis-symmetric fractures. The study is the first main contribution of this thesis and a required basis for the following chapters. The chapter investigates the evolution and final extent of hydraulic fractures created by a finite fluid volume block release from a point source. The host rock formation is considered homogeneous, and we assume Newtonian fluid rheology. We simultaneously treat im- and permeable media, using the Carter leak-off model for the latter. The study uses an open-source hydraulic fracture solver for planar three-dimensional fractures. Using such a simulator for an axis-symmetric problem is justified by the need for such a solver for this thesis's research conducted in Part III. Part III of this manuscript consists of chapters 4 to 6 and treats planar three-dimensional buoyant hydraulic fractures. Chapters 4 and 5 treat buoyant hydraulic fractures at depth in a homogeneous, impermeable medium and form a substantial part of the main contribution of this thesis. More particularly, the entire propagation history from a radially propagating hydraulic fracture up to the late-time, fully buoyant behavior is

Chapter 1. Introduction

investigated. The case of a continuous release at a constant rate is described in Chapter 4 and extended to a block release of a finite volume of fluid in Chapter 5. An extension to account for fluid leak-off modeled by Carter's leak-off model is provided in Chapter 6. Buoyant hydraulic fractures from industrial treatments or natural occurrences can theoretically reach the surface or contaminate shallow resources (drinking water reservoirs). Such behavior is rarely observed in the field, so we investigate in Chapter 7 a set of possible arresting mechanisms of buoyant hydraulic fractures.

To conclude, Chapter 8 discusses the performed work and provides perspectives for further research in the field.

2 Mechanics of hydraulic fractures

This chapter summarizes the fundamental mechanics of hydraulic fracture propagation. It further discusses fluid exchange between the fracture and the surrounding media (so-called fluid leak-off). We provide an order of magnitude estimation for the governing material, fluid, and solid properties on various scales for illustrative purposes. The chapter concludes by introducing the numerical tool used in the remainder of this thesis, the planar 3D hydraulic fracture solver PyFrac (Zia and Lecampion, 2020).

2.1 Fundamentals of hydraulic fracture mechanics

The propagation of hydraulic fractures has an inherent complexity caused by the moving boundary problem in combination with degenerative non-linear equations at the propagating edge. A lack of understanding of this complexity in the early attempts of the study and modeling of hydraulic fractures led to the employment of ad-hoc assumptions based on linear elastic fracture mechanics (LEFM) based on the theory of dry cracks (Vandamme and Curran, 1989; Advani et al., 1990). Despite this, under some conditions inaccurate, analogy with dry cracks, these numerical models fostered the understanding of the inherent multiscale behavior. The origin of this intricacy is deeply rooted in the competition between the physical processes controlling fracture propagation. The problem mainly depends on the relative importance of elastic deformation, buoyant forces, fluid leak-off to the surrounding media, creation of a fluid lag at the fracture tip and of new surfaces, and the viscous fluid flow in the fracture. All these parameters interact at the macroscopic scale of the finite fracture and compete in the development of asymptotic solutions at the propagating edge. The resulting two-scale competition relates the asymptotic tip behavior to the global fracture propagation velocity. This connection indicates that distinct solutions dependent on a given near-tip behavior can be obtained for simple geometries. As such, these can represent limiting solutions embedded in a global propagation history of hydraulic fractures (Detournay, 2016).

2.1.1 Elasticity

The relation between stress and strain of linear elasticity in its most general form can be written at any material point as (Ting, 1996)

$$\sigma_{ij} = c_{ijkl} \epsilon_{kl} \quad (2.1)$$

with σ_{ij} and ϵ_{kl} the stress and deformation tensors and c_{ijkl} the symmetric 4th order stiffness tensor. Note that we use the rule of summation of repeated indices. The stresses, as well as the strains, are symmetric, ensuring that the stiffness tensor must satisfy the minor symmetries $c_{ijkl} = c_{jikl} = c_{ijlk}$. It can additionally be shown that an interchange between ij and kl should not change the strain energy density $\psi = \frac{1}{2} \epsilon_{ij} c_{ijkl} \epsilon_{kl}$. A result of this argument is that c_{ijkl} must adhere to the major symmetries $c_{ijkl} = c_{klij}$. When applying these symmetries, the number of independent stresses reduces to six values only. When we additionally consider that the considered media is isotropically linear elastic (its properties are independent of the direction), we can re-write (2.1) as

$$\sigma_{ij} = \frac{E\nu}{(1+\nu)(1-2\nu)} \epsilon_{ij} + \frac{E}{1+\nu} \epsilon_{kk} \delta_{ij} \quad (2.2)$$

with δ_{ik} the Kronecker delta defined as:

$$\delta_{ij} = \begin{cases} 1, & i = j \\ 0, & i \neq j \end{cases} \quad (2.3)$$

In this particular case, the stiffness tensor c_{ijkl} depends on only two elastic parameters: the material's Elastic or Young's modulus E and Poisson's ratio ν . Instead of the Elastic Modulus, the geomechanical community also uses the material's Shear Modulus $G = E / (2(1 + \nu))$ to express (2.2). Note that the inverse relation uses the so-called compliance matrix S_{ijkl} . A collection of values for E and ν of rocks and typical materials of laboratory experiments is given in table 2.1.

Assuming small deformations and removing the rigid body motion, the displacements u_i are related to the strains ϵ_{ij} through the small-strain-tensor

$$\epsilon_{ij} = \frac{1}{2} (u_{i,j} + u_{j,i}). \quad (2.4)$$

The notation $\cdot_{,j}$ represents a partial derivative in direction j (e.g. $\cdot_{,j} = \partial \cdot / \partial j$).

2.1 Fundamentals of hydraulic fracture mechanics

| Material | ρ kg/m ³ | E GPa | ν |
|--|---|---|-----------|
| Charcoal Granite ^a | 2.60×10^3 | 48.3 | 0.27 |
| Long Valley Caldera Granite ^b | 2.6×10^3 | 44.0 | 0.10 |
| Stripa Granite ^c | 2.60×10^3 | 65.0 | 0.21 |
| Westerly Granite ^a | 2.60×10^3 | 37.5 | 0.25 |
| Berea Sandstone ^a | 2.30×10^3 | 14.4 | 0.20 |
| Boise Sandstone ^a | 2.30×10^3 | 9.66 | 0.31 |
| Ohio Sandstone ^a | 2.30×10^3 | 16.0 | 0.28 |
| Pecos Sandstone ^a | 2.30×10^3 | 13.7 | 0.31 |
| Ruhr Sandstone ^a | 2.30×10^3 | 29.1 | 0.12 |
| Weber Sandstone ^a | 2.30×10^3 | 27.6 | 0.29 |
| Tennessee Marble ^{a,k} | 2.60×10^3 – 2.70×10^3 | 60.0 | 0.25 |
| Cleveland Dike ^d | 2.60×10^3 – 3.00×10^3 | 7.50 | 0.25 |
| Eagle Ford Shale ^{e,i} | 2.30×10^3 – 2.60×10^3 | 7.30–15.0 | 0.14 |
| Marcellus Shale ^{e,j} | 2.60×10^3 | 5.70–17.0 | 0.18 |
| Gelatine (1.4 % Air) ^f | 1.00×10^3 | 5.70×10^{-7} | 0.50 |
| Gelatine (4.0 % Air) ^f | 1.00×10^3 | 6.45×10^{-6} | 0.50 |
| Gelatine ^g | 1.00×10^3 | 9.86×10^{-7} – 6.95×10^{-6} | 0.50 |
| PMMA ^h | 1.17×10^3 – 1.20×10^3 | 3.30–3.45 | 0.35–0.40 |
| Glass ^h | 2.40×10^3 | 68.5–72.3 | 0.20–0.30 |

Table 2.1: Elastic values of rocks and materials used in laboratory experiments. The references are: ^a (Jaeger et al., 2007), ^b (Reches and Fink, 1988), ^c (Alm et al., 1985), ^d (MacDonald et al., 1988), ^e (Dobson and Houseworth, 2013), ^f (Heimpel and Olson, 1994) (note that gelatines with Air contents between 1.4 % to 4.0 % have values in between the limits), ^g (Taisne and Tait, 2009), ^h (Bunger and Detournay, 2008) (the plain strain modulus $E' = E/(1 - \nu^2)$ only is reported, we estimate E using the generic values of ν provided in this table), ⁱ (Jiang et al., 2018) for the density, ^j (Schwartz et al., 2019) for the density, ^k (Byerly and Knowles, 2017) for the density.

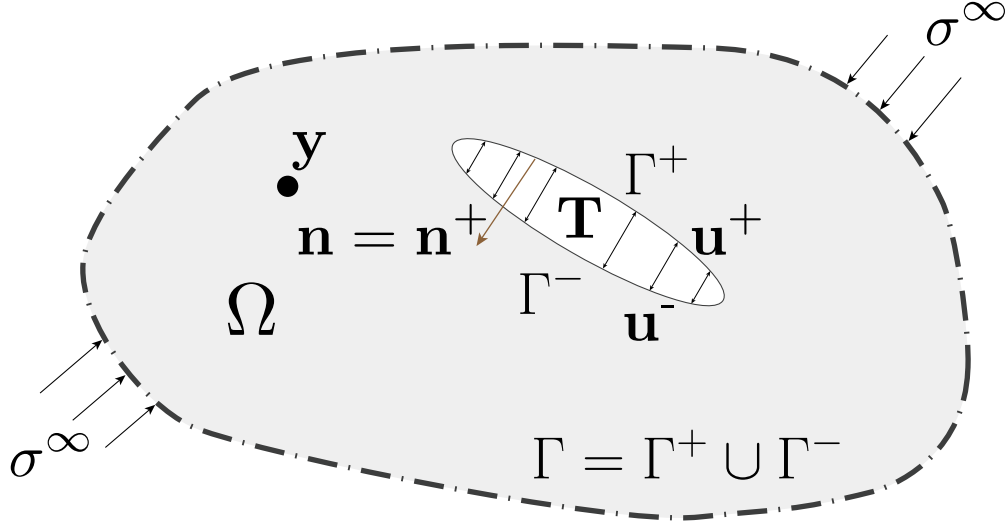


Figure 2.1: Schematic of a crack boundary value problem in an infinite elastic media under compressive stresses.

2.1.2 Boundary element method for planar fractures

The boundary element method (BEM) intends to solve boundary value problems (BVP). For the case of the elastic media, the corresponding BVP expresses the effects on a region Ω by constraints on its boundary $\partial\Omega$. When dealing with crack problems in an infinite media, Ω encloses the crack, which forms an enclosed boundary $\Gamma = \Gamma^+ \cup \Gamma^-$ (see figure 2.1). Boundary element methods are tailored to solve elastostatic and similar problems of dynamic elasticity, linear viscoelasticity, and heat flow. Crouch and Starfield (1983); Massonnet (1965) expressed the elastic field through a combination of surface potentials, representing density functions. For such indirect methods, the physical meaning of the unknown density is generally unclear. When dealing with crack problems, like the one presented in figure 2.1, the unknown is a displacement jump $[[\mathbf{u}]] = \mathbf{u}^+ - \mathbf{u}^-$ (Mogilevskaya, 2014). A second approach to the problem are direct methods described in Cruse (1996); Green (1854), which we shortly outline hereafter. Direct approaches represent the potentials using Green functions based on the reciprocal theorem of Maxwell-Betti and allow us to solve for the boundary stresses or displacements under specified boundary conditions.

Crack boundary value problem

We consider the boundary value problem sketched in figure 2.1 of an infinite three-dimensional medium Ω subjected to a compressive far-field stress σ_{ij}^∞ . In this configuration, the fracture is introduced as a displacement discontinuity $[[\mathbf{u}]] = \mathbf{u}^+ - \mathbf{u}^-$ generating the internal two-dimensional boundary Γ . The equilibrium of the problem enforces that, unlike the displacements, the tractions over Γ remain continuous, such that the elastostatic equilibrium of a loaded crack is reduced to the following field equations

$$\sigma_{ij,j}(\mathbf{y}) = 0, \quad \mathbf{y} \in \Omega \quad (2.5)$$

$$\sigma_{ij}(\mathbf{y}) n_j = T_i, \quad \mathbf{y} \in \Gamma \quad (2.6)$$

$$\sigma_{ij}(|\mathbf{y}| \rightarrow \infty) = \sigma_{ij}^\infty \quad (2.7)$$

In equation (2.5), we have neglected the presence of body forces. n_j in equation (2.6) is the unit normal vector to the boundary surface Γ and \mathbf{T} is the loading vector on the crack. Note that we will hereafter neglect any induced shear force. This assumption is equivalent to considering a pure opening mode (Mode I) tensile fracture (see Wrobel et al. (2017) for a discussion of the effects of tangential forces in hydraulic fracturing).

Reciprocity theorem

When assuming small deformations, quasi-static loading, and linear isotropic elasticity, the principle of elastic superposition is valid. Elastic superposition states that stresses and strains created from a set of concurrently applied tractions or displacements are identical to the sum of stresses and strains obtained when each component is applied individually. The principle of elastic superposition is the first main ingredient of the Maxwell-Betti¹ reciprocity theorem. The second fundamental component consists of the link between equilibrium equations and elastic compatibility through the principle of virtual work. It postulates that for a statically admissible stress field 1 (e.g., a stress field validating equations (2.5) and (2.6)) and a different independent kinematically admissible displacement field 2, the work done by external forces is balanced by its internal counterpart.

$$\underbrace{\int_{\Omega} f_i^1 u_i^2 d\Omega + \int_{\partial\Omega} t_i^1 u_i^2 d\Omega}_{\text{external work}} = \underbrace{\int_{\Omega} \sigma_{ij}^1 \epsilon_{ij}^2 d\Omega}_{\text{internal work}}. \quad (2.8)$$

In equation (2.8), u_i is the deformation at point i . The principle of virtual work is universally valid independent of the actual material constituting the body Ω . Considering now two states of stresses and strains (e.g. $\sigma_{ij}^{(1)}, \epsilon_{ij}^{(1)}$ and $\sigma_{ij}^{(2)}, \epsilon_{ij}^{(2)}$) of the identical elastic body Ω , the reciprocity theorem states that

$$\sigma_{ij}^{(1)} \epsilon_{ij}^{(2)} = \sigma_{ij}^{(2)} \epsilon_{ij}^{(1)}, \quad (2.9)$$

which means that the work of stresses of the first state on the strains of the second state is equal to the work of stresses of the second state done on the strains of the first state. Applying the divergence theorem and the principle of virtual work to equation (2.9), one obtains

¹The Maxwell-Betti theorem was proven by Enrico Bettin in 1872.

$$\int_{\partial\Omega} \sigma_{ij}^{(1)} u_j^{(2)} n_i dS + \int_{\Omega} f_i^{(1)} u_i^{(2)} d\Omega = \int_{\partial\Omega} \sigma_{ij}^{(2)} u_j^{(1)} n_i dS + \int_{\Omega} f_i^{(2)} u_i^{(1)} d\Omega \quad (2.10)$$

Thanks to the validity of the principle of elastic superposition, one and only one solution to an elastic boundary value problem with a specific set of boundary conditions exists. The fact that a solution exists does not imply that it can be obtained analytically, which is the case only for particular configurations. For most boundary value problems in continuum mechanics, only numerical solutions exist. An exception is the so-called Kelvin fundamental solution, describing the induced stresses and strains of a point force.

Kelvin / Point force solution

The Kelvin point force solution is a Green's function defining the influence of a unit point force at the application point \mathbf{x} , in the direction k of a cartesian coordinate system $k = 1, 2, 3$, in a homogeneous isotropic infinite linear elastic medium Ω . This functional derived by Lord Kelvin² is the solution to the well-posed boundary value problem

$$\sigma_{ij,j} + \delta_{ik} \delta(\mathbf{y} - \mathbf{x}) = 0 \quad (2.11)$$

$$\sigma_{ij} = c_{ijkl} \epsilon_{kl} = c_{ijkl} u_{k,l} \quad (2.12)$$

Including (2.4) and (2.2) in (2.11), we obtain the corresponding Navier equations

$$\frac{E}{(1+\nu)(1-2\nu)} U_{l,li}^k + \frac{E}{2(1+\nu)} U_{i,ll}^k + \delta_{ik} \delta(\mathbf{y} - \mathbf{x}) = 0. \quad (2.13)$$

In equation (2.13), we used the notation U_i^k denoting the deformation in direction i at the observation point \mathbf{y} caused by a unitary point force applied in direction k at the source point \mathbf{x} . Equation (2.13) has a solution of the form

$$U_i^k = 2(1-\nu) g_{i,jj}^k - g_{j,ji}^k \quad (2.14)$$

with g_i^k the Galerkin tensor found by the solution of the bi-harmonic equation

$$g_{i,jjll}^k = -\frac{(1+\nu)}{E(1-\nu)} \delta_{ik} \delta(\mathbf{y} - \mathbf{x}) \quad (2.15)$$

subjected to the boundary conditions

²Lord Kelvin, 16 June 1824 - December 1907

2.1 Fundamentals of hydraulic fracture mechanics

$$\lim_{|\mathbf{y}| \rightarrow \infty} \sigma_{ij} = 0, \quad \lim_{|\mathbf{y}| \rightarrow \infty} u_i = 0. \quad (2.16)$$

Solving equation (2.15) for a linear elastic isotropic infinite medium and introducing it into equation (2.14) yields the analytical expression

$$U_i^k(\mathbf{x}, \mathbf{y}) = \frac{1}{8\pi} \frac{1+\nu}{E(1-\nu)} \frac{1}{r} \left[\frac{x_i x_k}{r^2} + (3-4\nu) \delta_{ik} \right] \quad (2.17)$$

with $r = |\mathbf{x} - \mathbf{y}|$ the distance between the observer and force application point. Equation (2.17) is valid for any observation point \mathbf{y} different than \mathbf{x} because of its singularity at the application point. The resulting stresses of the point force solution can be obtained through the constitutive law

$$\begin{aligned} S_{ij}^k(\mathbf{x}, \mathbf{y}) &= c_{ijmn} U_{m,n}^k(\mathbf{x}, \mathbf{y}) \\ &= -\frac{1}{8\pi} \frac{1}{(1-\nu)} \frac{1}{r^2} \left[3 \frac{x_i x_j x_k}{r^3} + (1-2\nu) \left(\delta_{ik} \frac{x_j}{r} + \delta_{jk} \frac{x_i}{r} - \delta_{ij} \frac{x_k}{r} \right) \right]. \end{aligned} \quad (2.18)$$

which can be written as a traction vector

$$T_i^k = S_{ij}^k(\mathbf{x}, \mathbf{y}) n_j(\mathbf{y}) \quad (2.19)$$

The point force solution possesses several interesting properties. Notably, thanks to the validity of the Maxwell-Betti theorem (2.9), the Greens function has the symmetry

$$U_i^k(\mathbf{x}, \mathbf{y}) = U_k^i(\mathbf{y}, \mathbf{x}). \quad (2.20)$$

A direct consequence of the symmetry (2.20) is that the introduction of small perturbations of \mathbf{x} and \mathbf{y} does not change it. If one uses the perturbed symmetry (2.20) and matches the first and second-order terms of the perturbations, it is possible to obtain

$$U_{i,j}^k(\mathbf{x}, \mathbf{y}) = U_{k,\bar{j}}^i(\mathbf{y}, \mathbf{x}) \quad (2.21)$$

$$U_{i,\bar{m}j}^k(\mathbf{x}, \mathbf{y}) = U_{k,m\bar{j}}^i(\mathbf{y}, \mathbf{x}) \quad (2.22)$$

where \bar{j} denotes a derivative with respect to the j -th component of the source \mathbf{x} .

Boundary integral representation

To develop the boundary integral representation, one is looking for Somigliana's identities obtained using the Maxwell-Betti theorem (2.9) to compare an elastic state of a point force solution ((1), see section 2.1.2) and an unknown elastostatic state (2) (Bonnet, 1999)

$$\int_{\Gamma} \left[\sigma_{ij}(\mathbf{y}) U_j^k(\mathbf{x}, \mathbf{y}) - S_{ij}^k(\mathbf{x}, \mathbf{y}) u_j(\mathbf{y}) \right] n_i(\mathbf{y}) dS = \begin{cases} u_k(\mathbf{x}), & \text{if } \mathbf{x} \in \Omega \\ 0, & \text{if } \mathbf{x} \notin \Omega. \end{cases} \quad (2.23)$$

Equation (2.23) describes that the displacement, stresses, and strains at any point inside a deformable elastic Ω can be obtained directly from the distribution of displacements and tractions on the boundary Γ . This boundary integral representation of the displacement u_k inherently generates a compatible deformation field, satisfying the conservation of momentum of the elastostatic state. Because the fundamental point force solution (equations (2.14) and (2.18)) tends to infinity when $\mathbf{x} \in \Gamma$, equation (2.23) becomes undefined and singular on Γ . This unphysical condition can be lifted using regularization techniques (we refer the reader to Bonnet (1999); Mogilevskaya (2014); Mogilevskaya and Nikolskiy (2014) for details).

When restricting the problem to cases where $\mathbf{x} \in \Omega$ and $\mathbf{x} \notin \Gamma$ and introducing a universal traction vector $t_i = \sigma_{ij} n_j$, one obtains after differentiation the strain representation of the boundary integral equation

$$u_{k,l}(\mathbf{x}) = \int_{\Gamma} \left[\sigma_{ij}(\mathbf{y}) U_{j,\bar{l}}^k(\mathbf{x}, \mathbf{y}) - S_{ij,\bar{l}}^k(\mathbf{x}, \mathbf{y}) u_j(\mathbf{y}) \right] n_i(\mathbf{y}) dS \quad (2.24)$$

where we have used the notation $\cdot_{\bar{j}}$ to represent the derivative in direction j at the observation point \mathbf{x} . Finally, one can also obtain the inverse relation for the stress tensor

$$\sigma_{ij}(\mathbf{x}) = \int_{\Gamma} \left[\sigma_{ab}(\mathbf{y}) C_{ijkl} U_{b,\bar{l}}^k(\mathbf{x}, \mathbf{y}) - c_{ijkl} S_{ab,\bar{l}}^k(\mathbf{x}, \mathbf{y}) u_a(\mathbf{y}) \right] n_b(\mathbf{y}) dS \quad (2.25)$$

Planar mode I fracture

Based on the derivations of the BIE representation (2.25), we focus hereafter on the case of a tensile planar fracture. Expanding equation 2.1 by the normal $n_i = n_i^+$ we find the expression of the surface traction as

$$\sigma_{ij}(\mathbf{x}) n_j(\mathbf{x}) = T_i(\mathbf{x}) = -n_j(\mathbf{x}) \int_{\Gamma} c_{ijkl} S_{ab,\bar{l}}^k(\mathbf{x}, \mathbf{y}) (u_a^+(\mathbf{x}) - u_a^-(\mathbf{x})) n_b dS. \quad (2.26)$$

We particularize now equation 2.26 for one or more co-planar fractures in an infinite medium, using the particular case where the fracture propagates in the $(\mathbf{e}_1, \mathbf{e}_3)$ plane

$$\sigma_{ij}^+ n_j^+ + \sigma_{ij}^- n_j^- = 0 \quad (2.27)$$

$$n_n(\mathbf{x}) = n_n(\mathbf{y}) = \mathbf{e}_2 \quad (2.28)$$

$$x_2 = y_2 = 0 \quad (2.29)$$

$$[[\mathbf{u}(\mathbf{x})]]_2 = [[u_2(x_1, x_3)]] \mathbf{e}_2 = u_2^+ - u_2^- = w(\mathbf{y}). \quad (2.30)$$

we obtain (Hills et al., 1996; Crouch and Starfield, 1983)

$$p_f(\mathbf{x}) - \sigma_o(\mathbf{x}) = -\frac{E'}{8\pi} \int_{\Gamma} \frac{w(\mathbf{y}, t)}{\left[(x_1 - y_1)^2 + (x_2 - y_2)^2\right]^{3/2}} dS \quad (2.31)$$

where $E' = E/(1 - \nu^2)$ is the plane strain modulus and $w(\mathbf{y})$ the fracture opening. We further adopted the common praxis of expressing geomechanical problems as the difference from an initial state, given by the initial compressive stress state $\sigma_o(\mathbf{x})$, and performed a sign change such that compressional stresses are positive. Finally, we substitute the surface traction $T_2(\mathbf{x})$ by the negative of the fluid pressure $p_f(\mathbf{x})$ as the contact pressure on the fracture surface is given by the pressure of the fluid.

The distributed dislocation technique exploits the superposition principle, calculating the global solution of the problem from distributed opening (or pressure/point force) solutions along the fracture plane(s). These include the required boundary conditions of an infinite medium. One can express this statement as follows: It is possible to solve for a distribution of displacements (or point forces) along the boundary of an arbitrary elastic body, approximately validating its boundary conditions if the problem is well-posed. One can calculate the fields within the body from the resulting distribution of displacements.

2.2 Fluid flow and leak-off

Once a Mode I planar fracture is created, it consists of an open channel for fluid flow. In the case of hydraulic fractures considered herein, the pressurized fluid inside the fracture is the mechanism enabling the fracture to grow. If the media containing the fracture is permeable, an exchange of fluid between the fracture and the surrounding solid occurs. This fluid loss from the fracture to the solid is commonly called leak-off. Theoretically, it is also possible for formation fluids to flow into the fracture. The specifics of the leak-off type will be discussed later in this section.

2.2.1 Fluid flow

To accurately study the combined problem of hydraulic fracturing, we require a model for fluid flow in the created fracture. In this section, we discuss and derive the lubrication flow model used in the remainder of this thesis.

Governing equations

We assume an incompressible fluid such that the thermodynamics conservation of energy can be neglected, and the system becomes isothermal. The remaining governing equations are limited to the conservation of momentum and mass.

Conservation of mass: This physical principle states that the rate of change of mass in a fixed volume must match up with the rate of mass flux out of this volume. Considering a volume V of fluid constrained into the limits of a surface S on the fracture plane, one obtains

$$\frac{d}{dt} \int_V \rho_f(\mathbf{x}, t) dV = \frac{\partial \rho_f(\mathbf{x}, t)}{\partial t} + \frac{\partial (\rho_f(\mathbf{x}, t) v_i(\mathbf{x}, t))}{\partial x_i} \quad (2.32)$$

with $\rho_f(\mathbf{x}, t)$ kg/m³ the fluid density.

Conservation of momentum: Newton's second law enforces that the same volume V m³ on the same surface S m², moving in the direction of fluid flow must conserve its momentum

$$\rho_f(\mathbf{x}, t) \left(\frac{\partial v_i}{\partial t} + v_j \frac{\partial v_i}{\partial x_j} \right) = \rho_f(\mathbf{x}, t) g_i - \frac{\partial p_f}{\partial x_j} \delta_{ij} + \mu \frac{\partial}{\partial x_j} \left(\frac{\partial v_i}{\partial x_j} + \frac{\partial v_j}{\partial x_i} \right). \quad (2.33)$$

In equation (2.33) g_i represents the components of the gravity vector $\mathbf{g} = (0, 0, -g)$, p_f is the fluid pressure, and μ the dynamic viscosity of the solid (to obtain equation (2.33) the incompressible fluid assumption was used).

Width averaging and lubrication approximation

In the context of hydraulic fractures at depth, the fracture can be seen as a long, thin channel (the extension ℓ of the fracture is much larger than the fracture opening w , e.g., $\ell \ll w$). This configuration is typical of so-called thin-film lubrication flow (see figure 2.2). In this type of flow, inertial terms can be neglected because of low Reynolds numbers (the Reynolds number measures the ratio between inertial and shear forces), such that the conservation of momentum (2.33) (respectively the Navier-Stokes equations describing it) becomes

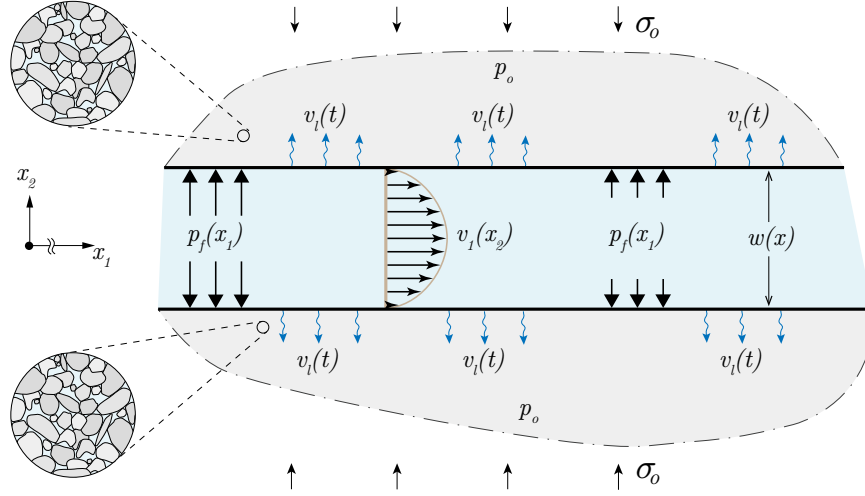


Figure 2.2: Sketch of parallel plates flow with the flow profile and the definition of the leak-off velocity.

$$-\frac{\partial p_f}{\partial x_1} + \mu \frac{\partial}{\partial x_2} \left(\frac{\partial v_1}{\partial x_2} \right) = 0 \quad (2.34)$$

$$\rho_f(\mathbf{x}, t) g - \frac{\partial p_f}{\partial x_3} + \mu \frac{\partial}{\partial x_2} \left(\frac{\partial v_3}{\partial x_2} \right) = 0. \quad (2.35)$$

When integrating equations (2.34) and (2.35) with a no-slip condition between the fluid and the wall (e.g., $v_i \times n_i^w = v_i^w \times n_i^w$), it is possible to obtain the classical parabolic fluid-flow profiles in x_1 and x_3 . We show the example of the formulation in x_1 as

$$v_1(x_2) = -\frac{w^2}{8\mu} \left[1 - 4 \left(\frac{x_2}{w} \right)^2 \right] \frac{\partial p_f}{\partial x_1}, \quad (2.36)$$

noting that for a constant density $\rho_f(\mathbf{x}, t) = \rho_f$ and uniform value of gravity the profile in x_3 contains an additional term related to gravity.

We use the commonly applied approach of averaging the fluid velocity over the fracture opening, assuming plane strain conditions and a thin channel. No restrictions on the time dependence are taken, such that the width averaged velocity in x_1 and x_3 becomes

$$\langle v_i \rangle = \frac{1}{w} \int_{-w/2}^{w/2} v_i(x_2) dx_2 = -\frac{w^2}{12\mu} \frac{\partial p_f}{\partial x_i} = -\frac{w^2}{\mu'} \frac{\partial p_f}{\partial x_i} \quad \text{for: } i = 1, 3 \quad (2.37)$$

where we used the parallel plates' dynamic viscosity $\mu' = 12\mu$. From the opening and the fluid velocity, one can derive the total fluid flux between two parallel plates as

$$q_{x_1} = w \langle v_1 \rangle = -\frac{w^3}{\mu'} \frac{\partial p_f}{\partial x_1}. \quad (2.38)$$

Due to the cubic relation between the opening and the fluid flux, equation (2.38) is often referred to as *the cubic law*. Another widespread definition is *Poiseuille law* because of its experimental derivation by Poiseuille (1838) and Hagen (1839) for pipe flow.

Integrating now the mass conservation equation (2.32) over x_2 in the absence of any source/sink term, we obtain

$$\frac{\partial \rho_f w}{\partial t} + \frac{\partial \rho_f w \langle v_i \rangle}{\partial x_i} + 2\rho_f v_l = 0, \quad (2.39)$$

where we have made use of the no-slip condition at the boundaries and denoted the fluid velocity perpendicular to the boundary as the leak-off rate v_l (e.g., $v_2(x_1, \pm w(x_1, x_3, t), x_3, t) = \pm v_l(x_1, x_3, t)$, see figure 2.2). Considering now a slightly compressible isothermal fluid with a linearized equation of state

$$\rho_f = \rho_f^o \left[1 + c_f (p_f - p_f^o) \right], \quad (2.40)$$

where c_f 1/Pa is the fluid compressibility, equation (2.39) becomes

$$c_f w \frac{\partial p_f}{\partial t} + \frac{\partial w}{\partial t} + \frac{\partial q_{x_i}}{\partial x_i} + 2v_l = 0 \quad \text{for: } i = 1, 3 \quad (2.41)$$

In equation (2.41), we have kept only the linear terms. Note that the presence of a volumetric source/sink in (2.41) would add a term proportional to $Q_s(t) \delta(\mathbf{x} - \mathbf{x}_s)$ on the right-hand side, where Q_s m³/s denotes the volumetric source/sink term and \mathbf{x}_s the source location of Q_s . Note that the substitution of q_{x_i} (see equation (2.38)) gives a cubic dependence on the fracture opening, which is the reason for the highly non-linear behavior.

In table 2.2, we list the characteristic values of some important fracturing fluids, laboratory fluids, and magmas to grasp the order of the wide range of possible applications of hydraulic fracturing procedures.

2.2.2 Leak-off

In equation (2.41), we have modeled leak-off through a leak-off velocity v_L without specifying its magnitude. Considering again the fracture located in the $x_1 x_3$ -plane such that the fracture is on $x_2 = 0$ and assuming the validity of Darcy Flow in the surrounding matrix, we model the leak-off velocity as

2.2 Fluid flow and leak-off

| Fluid | μ Pas | ρ_f kg/m ³ |
|---|---|---|
| Water at 0°–20° ^f | 8.91×10^{-4} – 1.79×10^{-3} | 1.00×10^3 |
| Hydroxypropyl guar at 15°–70° ^{a,*} | 0.10–0.40 | 1.00×10^3 |
| Slickwater ^{g,*} | 5.00×10^{-3} –50.0 | 1.00×10^3 |
| Cross-Link Gel ^b | 1.72×10^{-3} – 3.75×10^{-3} | 1.00×10^3 |
| Viscoelastic Surfactant (VES) at 24° ^{c,*} | 10.0 | - |
| Basaltic Magma ^d | 10.0–100 | 2.70×10^3 |
| Rhyolitic Magma ^h | 2.00×10^4 – 1.58×10^7 | 2.30×10^3 |
| Air at 0°–20° ^f | 1.71×10^{-5} – 1.85×10^{-3} | 1.20×10^{-3} – 1.29×10^{-3} |

Table 2.2: Properties of fluids used in laboratory and field hydraulic fracturing applications. ^a (Guillot and Dunand, 1985), ^b (Dai and Zhao, 2019), ^c (Kefi et al., 2004), ^d (Huppert and Sparks, 1981), ^f (Batchelor, 1967), ^g (Chen et al., 2020; Luo et al., 2014), ^h (Spera et al., 1988), * we only consider the Newtonian plateau observed at low shear rates.

$$v_L = -\frac{k}{\mu} \frac{\partial}{\partial x_2} (p_p - p_o) |_{x_2=0} \quad (2.42)$$

where k m² is the permeability of the solid, p_p the pore pressure in the solid and p_o the initial far-field pore pressure. We adopt again the practice of solving in a difference to an initial state and solve for $\Delta p_p = p_p - p_o$. The evolution of Δp_p assuming Darcy flow is according to the diffusion equation

$$\frac{\partial \Delta p_p(\mathbf{x}, t)}{\partial t} = \frac{k}{S\mu} \nabla^2 \Delta p_p \quad (2.43)$$

where S is storage coefficient of the formation and formation fluid and $\nabla^2 \cdot = \partial^2 \cdot / \partial x_1^2 + \partial^2 \cdot / \partial x_2^2 + \partial^2 \cdot / \partial x_3^2$ denotes the Laplacian operator. The diffusion equation (2.43) forms a BVP subjected to the boundary conditions

$$\Delta p_p(x_1, 0, x_3, t) = p_p(x_1, x_3, t) - p_o, \quad x_1, x_3 \in \mathcal{A}(t) \quad (2.44)$$

$$\lim_{x_2 \rightarrow \infty} \Delta p_p(\mathbf{x}, t) = 0 \quad (2.45)$$

$$\Delta p_p(\mathbf{x}, 0) = 0. \quad (2.46)$$

where we have denoted the fracture plane as $\mathcal{A}(t)$. The system of equations (2.43) - (2.46) is a three-dimensional diffusion equation with time-dependent boundary conditions. An additional computational challenge is that the pressure boundary condition is part of the solution to the coupled hydraulic fracture problem. Historically, the most commonly used simplifications were originally proposed by Carter (Carter, 1957). The so-called Carter's

Chapter 2. Mechanics of hydraulic fractures

leak-off is based on two major simplifications: First, the hydraulic fracture is assumed to propagate much faster than the characteristic diffusion velocity. This assumption often holds for applications in the petroleum industry but was shown to be violated when the permeability of the formation is high (Kovalyshen, 2010). Second, the far-field effective stress $\sigma'_o = \sigma_o - p_o$ is significantly larger than the net pressure of the fracturing fluid $p = p_f - \sigma_o$. The combination of these two assumptions allows for a reduction of the system of equations (2.43) - (2.46) to a one-dimensional diffusion equation (first assumption) uncoupled from the transient net pressure (second assumption, $\Delta p_p = p + \sigma'_o \approx \sigma'_o$). The diffusion equation (2.43) in its reduced form becomes

$$\frac{\partial \Delta p_p(\mathbf{x}, t)}{\partial t} = \frac{k}{S\mu} \frac{\partial^2 \Delta p_p(\mathbf{x}, t)}{\partial x_2^2}, \quad (2.47)$$

and its first boundary condition (2.48) simplifies to

$$\Delta p_p(x_1, 0, x_3, t) = \sigma'_o, \quad x_1, x_3 \in \mathcal{A}(t). \quad (2.48)$$

The partial differential equation built by the system of (2.47) and boundary conditions (2.48), (2.45), and (2.46) is solved analytically to obtain the pressure evolution

$$\Delta p_p(x_2, t) = \sigma'_o \operatorname{Erfc} \left\{ \left(\frac{S\mu}{k} \right)^{1/2} \frac{x_2}{2\sqrt{t}} \right\}. \quad (2.49)$$

Taking the derivative of equation (2.49), evaluating it at $x_2 = 0$ and inserting it into equation (2.42) one obtains

$$v_L = \sqrt{\frac{kS}{\pi\mu}} \frac{\sigma'_o}{\sqrt{t}}. \quad (2.50)$$

The time dependence of this solution is typical for Carter's leak-off model. However, two additional assumptions are required to complete the model. The first assumption is related to the start and end of fluid leak-off. Leak-off can only start once the planar fracture has propagated up to a point \mathbf{x} . One denotes the time t when the condition $\mathbf{x} \in \mathcal{A}(t)$ is validated for the first time as t_o . The so-called exposure time to leak-off becomes $t - t_o(\mathbf{x})$, and the actual time t in equation (2.50) is replaced by the exposure time. A second assumption is related to different mechanisms influencing the rate of fluid loss. The two considered mechanisms are usually the build-up of a filter cake of fracturing fluid at the fracture wall and the difference between fracturing and formation fluid. The latter means that the leaking fracturing fluid must displace the formation fluid. Investigation of both processes reveals that they similarly show a square root dependence of time (Carter, 1957; Entov et al., 2007; Kovalyshen, 2010).

2.2 Fluid flow and leak-off

| Fluid | $k \text{ m}^2$ | $S \text{ Pa}^{-1}$ |
|-----------------------------------|---|---|
| Basalts ^a | 1×10^{-19} – 1×10^{-13} | - |
| Clays, Shales ^{a,b,c} | 1×10^{-23} – 1×10^{-16} | 2.00×10^{-3} – 2.40×10^{-2} |
| Dolomites ^b | 1×10^{-12} – 1×10^{-10} | - |
| Granits, Gneiss ^{a,b} | 1×10^{-20} – 1×10^{-16} | - |
| Limestones ^{a,b,d} | 1×10^{-22} – 1×10^{-12} | 2.76×10^{-4} – 8.14×10^{-3} |
| Sandstones ^{a,b,d} | 1×10^{-17} – 1×10^{-11} | 3.58×10^{-4} – 4.96×10^{-3} |
| Charcoal Granite ^e | 9.87×10^{-20} | 0.02 |
| Westerly Granite ^e | 3.95×10^{-19} | 0.01 |
| Berea Sandstone ^e | 1.88×10^{-13} | 0.19 |
| Boise Sandstone ^e | 7.90×10^{-13} | 0.26 |
| Ohio Sandstone ^e | 5.53×10^{-15} | 0.19 |
| Pecos Sandstone ^e | 7.90×10^{-16} | 0.20 |
| Ruhr Sandstone ^e | 1.97×10^{-16} | 0.02 |
| Weber Sandstone ^e | 9.87×10^{-16} | 0.06 |
| Tennessee Marble ^e | 9.87×10^{-20} | 0.02 |
| Eagle Ford Shale ^{f,g} | 8.0×10^{-22} – 1.7×10^{-21} | 4.87×10^{-4} |
| Marcellus Shale ^{f,g} | 1.5×10^{-21} – 4.5×10^{-21} | 6.96×10^{-4} |
| Valhall Field ^h | - | 0.08–0.27 |
| Slochteren Sandstone ⁱ | - | 0.01–0.95 |

Table 2.3: Permeabilities and storage coefficients of various rock formations. ^a (Guéguen and Palciauskas, 1994), ^b (De Marsily, 1986), ^c (Chang and Firoozabadi, 2000), ^d (Hall, 1953), ^e (Jaeger et al., 2007), ^f (Dobson and Houseworth, 2013), ^g (Ripepi et al., 2023), ^h (Ruddy et al., 1989), ⁱ (van Eijs and van der Wal, 2017).

This observation emphasizes that lumping the contribution of every mechanism into a single leak-off coefficient $C_L \text{ m/s}^{1/2}$ is possible. The value of this coefficient is usually backtracked from model predictions and fracture geometries (Wang and Dempsey, 2011) and obtained with calibration experiments (Nolte, 1979; Castillo, 1987; Barree and Mukherjee, 1996). The final expression of the leak-off velocity when assuming carters leak-off velocity reads

$$v_L(\mathbf{x}, t) = \frac{C_L}{\sqrt{t - t_o(\mathbf{x})}} \quad (2.51)$$

where the simplest expression of C_L without considering any filter cake build-up is given by

$$C_L = \sqrt{\frac{S}{\pi\mu}} \sigma'_o. \quad (2.52)$$

We list in table 2.3 typical values of permeability and storage coefficients. Combined with the knowledge of the effective stress in the formation and the viscosity of the formation fluid, the leak-off coefficient can be calculated with equation (2.52). All these parameters are highly

variable, and the effective stress and the formation fluid viscosity are rarely constrainable. For this reason, the common practice is, as stated before, to perform experiments on the formation using a given fracturing fluid to estimate the value of C_L .

2.3 Propagation condition

In his seminal work, Griffith (1921) investigated a crack of no specific mode with a constant load propagating quasi-statically in increments of da and performed an energy balance of the problem and observed that the work of external forces ∂W_{ext} is split between two components, the work done to create new surfaces Gda and the work necessary to deform the body elastically

$$\partial W_{ext} = dW + Gda. \quad (2.53)$$

Generally, it is common to re-arrange equation (2.53) to obtain the driving force G as a function of the difference between the work done by external forces, and the elastic work performed on the body

$$Gda = \partial W_{ext} - dW. \quad (2.54)$$

It is possible to express equation (2.54) in terms of stresses and strains for temporal variations in loading and crack length during an increment of fracture propagation da . As by the principle of virtual work, the components of the right-hand-side of equation (2.54) related to a non-propagating crack (e.g., changes in time at a constant crack size) cancel out such that the driving force Gda of crack growth in a linear elastic media can be reduced to

$$\begin{aligned} Gda &= \left[\int_{\partial\Omega} \left(\sigma_{ij} n_j \frac{\partial u_i}{\partial a} \right) dS - \frac{\partial}{\partial a} \int_{\Omega} \frac{1}{2} \sigma_{ij} \epsilon_{ij} dV \right] da \\ G &= \frac{1}{2} \int_{\partial\Omega} \left(\sigma_{ij} n_j \frac{\partial u_i}{\partial a} - u_i \frac{\partial \sigma_{ij} n_j}{\partial a} \right) dS, \end{aligned} \quad (2.55)$$

where we have considered an infinite elastic body Ω with a crack boundary $\partial\Omega$ (see figure 2.1). To obtain equation (2.55) we have used the principle of virtual work. Note that G is usually called the energy release rate, even though it does not refer to a variation in time. The energy release rate is the quantity of energy necessary consumed by the propagation of the crack. If the crack would not propagate, the same amount of energy would be stored elastically in the body. It is possible to describe the driving force for cracking as the negative of the *derivative of the elastic potential energy with respect to the crack increment under a constant load*.

2.3 Propagation condition

| Material | Source | K_{Ic} MPam ^{1/2} |
|------------------------------|-----------------------------|---|
| Kumamoto Andesite | Nara et al. (2012) | 1.66–1.91 |
| Basalts | Guha Roy et al. (2017) | 3.14–3.19 |
| Granitic Gneiss | Guha Roy et al. (2017) | 0.88–1.15* |
| Oshima Granite | Nara et al. (2012) | 2.06–2.14 |
| Mudstone | Senseny and Pfeifle (1984) | 0.75–2.25 |
| Sandstone | Senseny and Pfeifle (1984) | 0.60–2.00 |
| Adamsweiler Sandstone | Noël et al. (2021) | 0.33–0.49 |
| Bentheim Sandstone | Noël et al. (2021) | 0.52–0.55 |
| Berea Sandstone | Nara et al. (2012) | 0.30–0.36 |
| Darley Dale Sandstone | Noël et al. (2021) | 0.51–0.79 |
| Dholpur Sandstone | Guha Roy et al. (2017) | 0.36 |
| Fontainbleau Sandstone | Noël et al. (2021) | 1.45–1.60 |
| Jabalpur Sandstone | Guha Roy et al. (2017) | 0.78–1.10 |
| Kushiro Sandstone | Nara et al. (2012) | 0.60–0.89 |
| Rothbach Sandstone | Noël et al. (2021) | 0.65–0.81 |
| Shirahama Sandstone | Nara et al. (2012) | 0.39–0.73 |
| Shale | Senseny and Pfeifle (1984) | 0.25–2.00 |
| Jharia Shale | Guha Roy et al. (2017) | 0.30 |
| Siltstone | Senseny and Pfeifle (1984) | 0.50–2.50 |
| Gelatine (1.4 % - 4.0 % Air) | Heimpel and Olson (1994) | 1.5×10^{-2} – 1.14×10^{-1} |
| Gelatine | Taisne and Tait (2009) | 2.98×10^{-5} – 7.92×10^{-5} |
| PMMA | Bunger and Detournay (2008) | 0.29–0.38 |
| Glass | Bunger and Detournay (2008) | 1.25 |

Table 2.4: Characteristic values of Mode I fracturing toughness K_{Ic} from different studies and formations. The conditions and methods used in each study are not comparable, such that comparisons between studies are difficult. * the minimum measured parallel to the foliation, whereas the maximum occurs perpendicular to the foliation.

Chapter 2. Mechanics of hydraulic fractures

From these energy considerations, it is possible to derive the fracture growth criteria in linear elastic fracture mechanics as

$$\begin{aligned} G < G_c &\rightarrow V = 0 \\ G = G_c &\rightarrow V > 0 \\ (G - G_c) V &= 0. \end{aligned} \tag{2.56}$$

In equation (2.56), we have defined the critical energy release rate G_c as a material property (similar to Poisson's ratio or Young's modulus). It simply states that the fracture is not growing if the energy released is below a critical threshold. The definition of the critical energy release rate has been provided by Irwin (1957) for plane elasticity. To derive the formulation of Irwin (1957), we have to acknowledge that for flat fracture fronts and co-planar fracture growth, it is possible to derive asymptotic expressions for displacements and stresses in the vicinity of the fracture tip. We omit a detailed explanation of the procedure and refer to textbooks such as Kanninen and Popelar (1985); Anderson (2017) for a more detailed description. In the case considered here of a semi-infinite plane-strain fracture, the first-order contributions to the stress field around the propagating edge, in the polar coordinate system centered on the tip (r, θ) , restricted to modes I and II, are

$$\sigma_{rr}(r, \theta) = \frac{K_I}{\sqrt{32\pi r}} \left(5 \cos \frac{\theta}{2} - \cos \frac{3\theta}{2} \right) + \frac{K_{II}}{\sqrt{32\pi r}} \left(-5 \sin \frac{\theta}{2} + 3 \sin \frac{3\theta}{2} \right) + \mathcal{O}(r^{1/2}) \tag{2.57}$$

$$\sigma_{\theta\theta}(r, \theta) = \frac{K_I}{\sqrt{32\pi r}} \left(3 \cos \frac{\theta}{2} + \cos \frac{3\theta}{2} \right) + \frac{K_{II}}{\sqrt{32\pi r}} \left(-3 \sin \frac{\theta}{2} - \sin \frac{3\theta}{2} \right) + \mathcal{O}(r^{1/2}) \tag{2.58}$$

$$\sigma_{r\theta}(r, \theta) = \frac{K_I}{\sqrt{32\pi r}} \left(\sin \frac{\theta}{2} + \sin \frac{3\theta}{2} \right) + \frac{K_{II}}{\sqrt{32\pi r}} \left(-3 \sin \frac{\theta}{2} - \sin \frac{3\theta}{2} \right) + \mathcal{O}(r^{1/2}) \tag{2.59}$$

where the corresponding crack opening displacements are given by

$$[[u_1]] = \sqrt{\frac{32}{\pi}} \frac{K_{II}}{E'} \sqrt{r} + \mathcal{O}(r^{3/2}) \tag{2.60}$$

$$[[u_2]] = \sqrt{\frac{32}{\pi}} \frac{K_I}{E'} \sqrt{r} + \mathcal{O}(r^{3/2}). \tag{2.61}$$

In equations (2.57) to (2.61) K_i are the stress-intensity factors of the respective modes of fracturing. For a 2D plane strain semi-infinite fracture propagating in its plane, Irwin (1957) has proven through a crack-closure analysis that the energy release rate for the co-planar growth of fractures with a flat front can be related to these stress-intensity factors as

2.4 Numerical solution of hydraulic fracture problems

$$G = \frac{K_I^2 + K_{II}^2}{E'} + \frac{K_{III}^2}{E'(1-\nu)}. \quad (2.62)$$

In the case of planar opening mode (mode I) fracturing considered in this thesis, the Irwin relation (2.62) reduces to $G = K_I^2/E'$. It is thus possible to define a so-called fracture toughness K_{Ic} , used equivalently to G_c in the fracture criterion (2.56). We list some characteristic values of fracture toughness in table 2.4.

2.3.1 Tip-Asymptotes in hydraulic fracturing

The propagation condition of equation (2.56) in numerical models is often introduced through the asymptotic behavior of fracture opening at the propagating edge. This so-called tip asymptote is given by equation (2.61) for purely mechanically loaded fractures. It has, however, been demonstrated that in hydraulic fracturing problems, another asymptotic solution dominated by the energy dissipation through viscous flow (Desroches et al., 1994) emerges. This asymptote represents a far-field solution to the hydraulic fracturing problem (Garagash and Detournay, 2000). The transition from the near-field, toughness-dominated classical LEFM asymptotic behavior to the far-field viscosity-dominated asymptote has been validated experimentally by Bungler and Detournay (2008). Until here, we have neglected the effects of fluid leak-off and the possible presence of a so-called fluid lag at the fracture tip (note that (Garagash and Detournay, 2000) discussed the appearance of the fluid lag). The problem of fluid leak-off for a solid with negligible fracturing toughness has been solved by Lenoach (1995), who showed that in the vicinity of the tip, a leak-off dominated asymptote exists for highlight leak-off dominated fractures in a medium with negligible fracturing toughness K_{Ic} . Later Garagash et al. (2011) have combined all three approaches and shown that the leak-off asymptote can appear under specific conditions between the near-tip toughness and far-field viscous asymptotes (see figure 2.3). The combination of all three asymptotes is termed the universal tip asymptote and was numerically approximated by (Dontsov and Peirce, 2015a). An additional asymptotic behavior is observed in the near-field when a fluid lag is considered.

2.4 Numerical solution of hydraulic fracture problems

The problems investigated in this thesis are formed by the fully coupled problem of elastic deformation of the solid (see section 2.1.1), fluid flow in the fracture (see section 2.2.1), leak-off of the fluid into the surrounding media (see section 2.2.2), as well as the fracturing of the rock (see section 2.3). The main focus of this thesis is on planar, three-dimensional fractures, whose numerical simulation remains a challenging task. The difficulty is embedded in the moving boundary problem of the fracture front and the highly non-linear coupling between elastic deformations and fluid flow in the fracture enforced by the non-locality of the former. For the particular case presented in this thesis where the material is linearly elastic and isotropic and fluid flow in the fracture is subjected to the lubrication approximation, the cubic strength

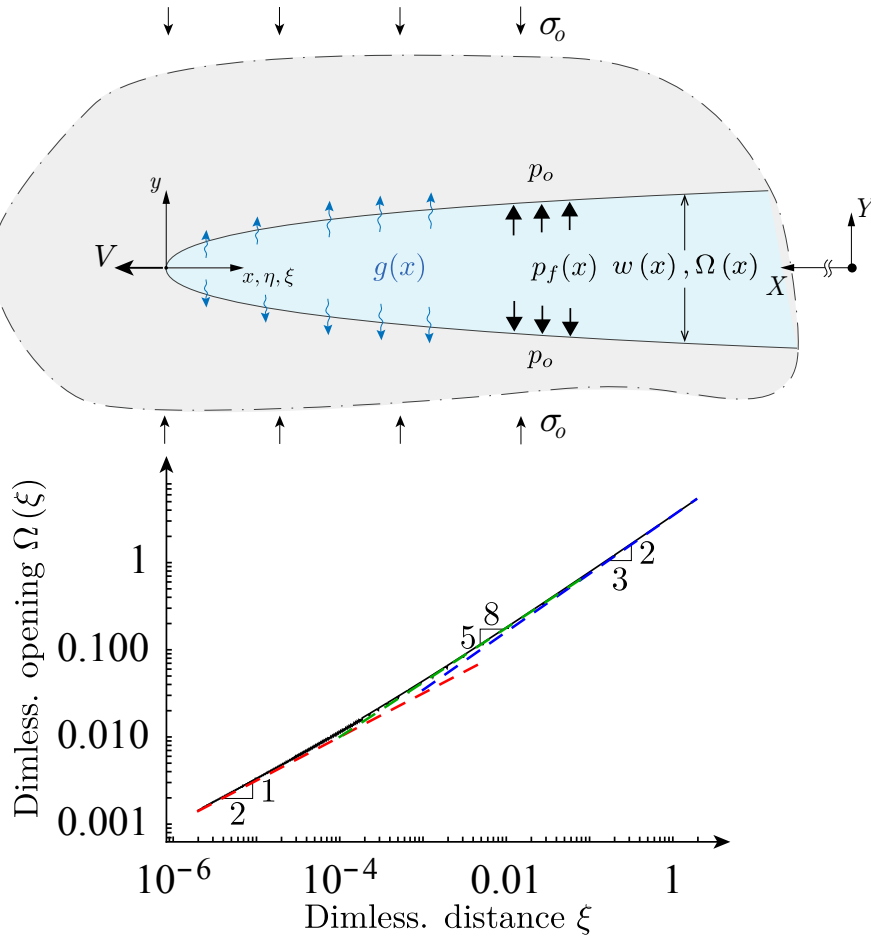


Figure 2.3: Sketched evolution of fracture opening as a function of distance to the fracture tip for a hydraulic fracture without fluid lag. Dashed lines show the respective limiting asymptotes: Red = near-field toughness dominated limit (Rice, 1968a), green = intermediate leak-off dominated asymptote (Lenoach, 1995), and blue = far-field viscosity-dominated limit (Desroches et al., 1994). The black line is a numerical evaluation of the combined asymptote developed by Garagash et al. (2011) using the approximation of Dontsov and Peirce (2015a).

2.4 Numerical solution of hydraulic fracture problems

of the non-linearity of the hydro-mechanical problem comes from the Poiseuille Law (see equation (2.38)). The problem becomes a multiscale problem because of its non-local elastic behavior at the fracture tip coupled to the lubrication equation and the volume conservation over the entire fracture. The complexity of the non-local elastic problem at the fracture tip is particularly increased because the classical square-root singularity of fracture opening observed for Mode I cracks (Rice, 1968b) is only valid over a limited extent (see the derivations in section 2.3.1). No matter the level of complexity of the near-tip behavior chosen, the region of validity of the classical toughness-asymptote (either in the first or second dominant term) evolves during the propagation of the fracture and has the potential to reduce to a thin boundary layer at the propagating edge. For accurate modeling of fracturing problems, the resolution of this zone related to the moving boundary is of utmost importance. Because of its changing size in combination with the moving boundary, accurate tracking of the tip would require a constant adaption of the discretization, which represents a significant challenge for numerical tools.

2.4.1 PyFrac: A python implementation of the implicit level set algorithm (ILSA)

Peirce and Detournay (2008) developed a numerically efficient way of resolving the multiscale nature of the problem using the asymptotic solution of a steadily moving hydraulic fracture (see section 2.3.1) at the propagation edge. The backbone of this approximation consists of reducing the 3D problem locally to a 2D plane strain problem. The previously discussed tip-asymptotes are used to obtain opening and pressure at a given distance from the fracturing front as a function of the local velocity and the material, fluid, and injection properties. The solution strategy of Peirce and Detournay (2008) tracks the position of the fracture front with a level set function on a relatively coarse and constant grid and is capable of deriving the fracture velocity as part of the solution (in an implicit way, hence the name of Implicit Level Set Algorithm (ILSA)).

The numerical hydraulic fracture solver PyFrac (Zia and Lecampion, 2020) developed at the Geo-Energy Laboratory - Gaznat Chair of Geo-Energy at EPFL is an open-source, Python-based implementation of the ILSA scheme to solve for the propagation of three-dimensional planar hydraulic fractures. PyFrac solves the combined set of equations (2.31), (2.41), and (2.56), where the fluid flow follows the lubrication approximation leading to Poiseuille Flow (2.38), and leak-off is approximated by Carter's Leak-Off model (2.51). The unknowns of the problem at any time are the position of the moving boundary of the fracture front, its local velocity, the fracture opening, and the fluid pressure inside the fracture. We approach this problem using a regular, rectangular grid discretizing fracture opening and internal fluid pressure at the cell centers and fracture front velocities perpendicular to front segments in so-called tip-cells (see figure 2.4). Before describing the model in more detail, we highlight several additional assumptions adopted in the code:

- Fracture propagation is planar and perpendicular to the minimum in-situ stress denoted

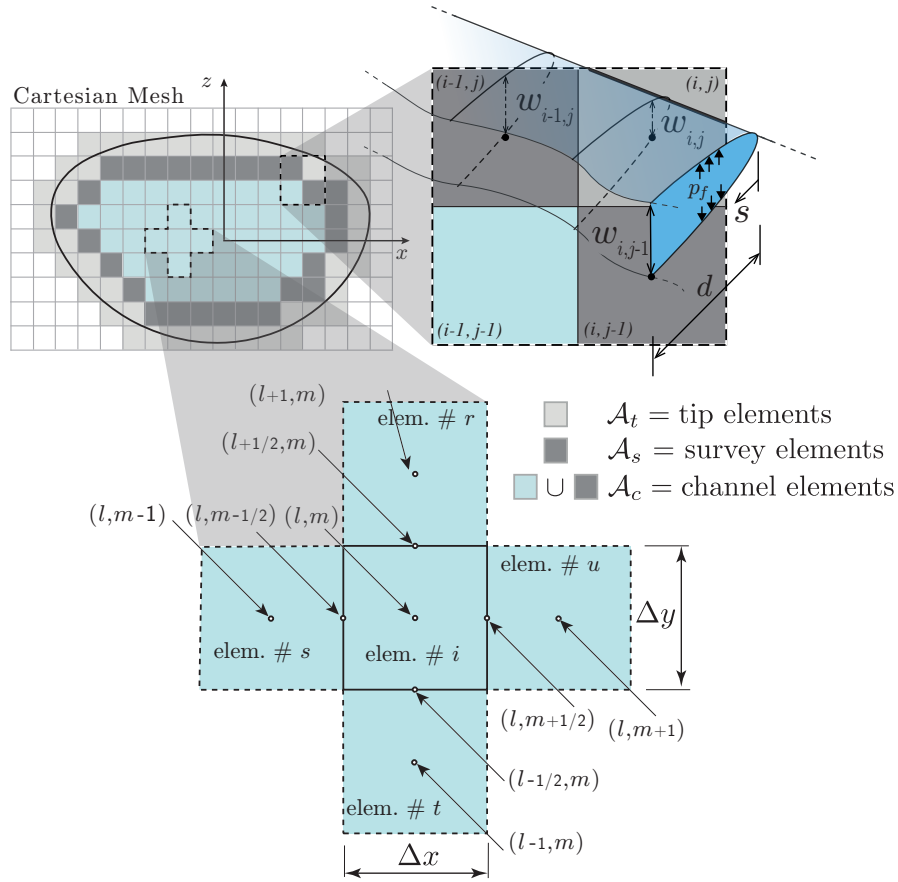


Figure 2.4: Graphical representation of the main components of the numerical HF Solver PyFrac (Zia and Lecampion, 2020). Top left: Discretization of the fracture plane into a regular rectangular grid with different element types. Top Right: Two-dimensional plane stress asymptotic solutions used at the fracture tip. Bottom: Schematic of finite different five-point stencil used to calculate the fluid flow in the fracture. Adapted figure 2.3 of Peruzzo (2023).

2.4 Numerical solution of hydraulic fracture problems

as σ_o . As a result, the shear tractions on the plane are zero, and the fracture propagates in a pure opening mode (Mode I).

- The propagation of hydraulic fractures is a volume-controlled process, leading to a stable propagation with maximum velocities of almost a few meters per second. Inertial effects can thus be safely neglected.
- Only fractures without a fluid lag are considered. This assumption is valid whenever the condition $\mu V E'^2 / \sigma_o^3 \ll 1$ is ensured (Garagash and Detournay, 1998) with, μ the viscosity of the fracturing fluid, E' the plane strain modulus as defined in section 2.3, and σ_o the minimum in-situ stress perpendicular to the fracture plane. Thanks to the cubic dependence on the confining stress, which typically increases with depth, this condition is generally satisfied when studying fractures at depth (see Lecampion and Detournay, 2007, for more details).
- The linear elastic isotropic medium in which the fracture propagates is considered infinite. There are no boundaries nor free surface effects.

In this numerical solver, the elastic deformation of the medium (2.31) is solved for using the displacement discontinuity method relating the surface traction (internal fluid pressure) to the displacements on the regular rectangular grid (see figure 2.4). Combining this method with a five-point stencil finite difference scheme (see figure 2.4) in space to model the fluid flow in the fracture, the so-called elastohydrodynamic lubrication (EHL) system is obtained at a given instance of time. The principle of the numerical scheme then includes a double loop, where we describe here the classical time-implicit solution strategy for the position of the fracture front and refer the reader to the work of Zia and Lecampion (2019) for the two other possible approaches of an explicit and predictor-corrector stepping (see also figure 2.5). Note that the naming of the solution scheme solely refers to the calculation/estimation of the front position, whereas the non-linear EHL is solved implicitly in all approaches.

In the fully implicit scheme, the level set is taken from the previous solution, and the non-linear EHL is solved in terms of incremental fracture opening increment in all the cells. Figure 2.5 describes the details of this step in the orange box to the right. Note that this step mentions a width constraint. In the solver, the fracture is allowed to reduce its opening. However, a complete "healing" of the fracture is not permitted. Instead of this full closure, we impose a residual fracture opening w_a . Because surfaces of fractures are usually rough, a physical interpretation of this residual opening could be that fractures cannot close back completely but instead remain open at a minimum width denoted as w_{min} . We thus define the residual opening as the minimum between the maximum opening the fracture has ever had at each position and the minimum width prescribed

$$w_a(\mathbf{x}) = \min\{\max_t[w(\mathbf{x}, t)], w_{min}\}. \quad (2.63)$$

Chapter 2. Mechanics of hydraulic fractures

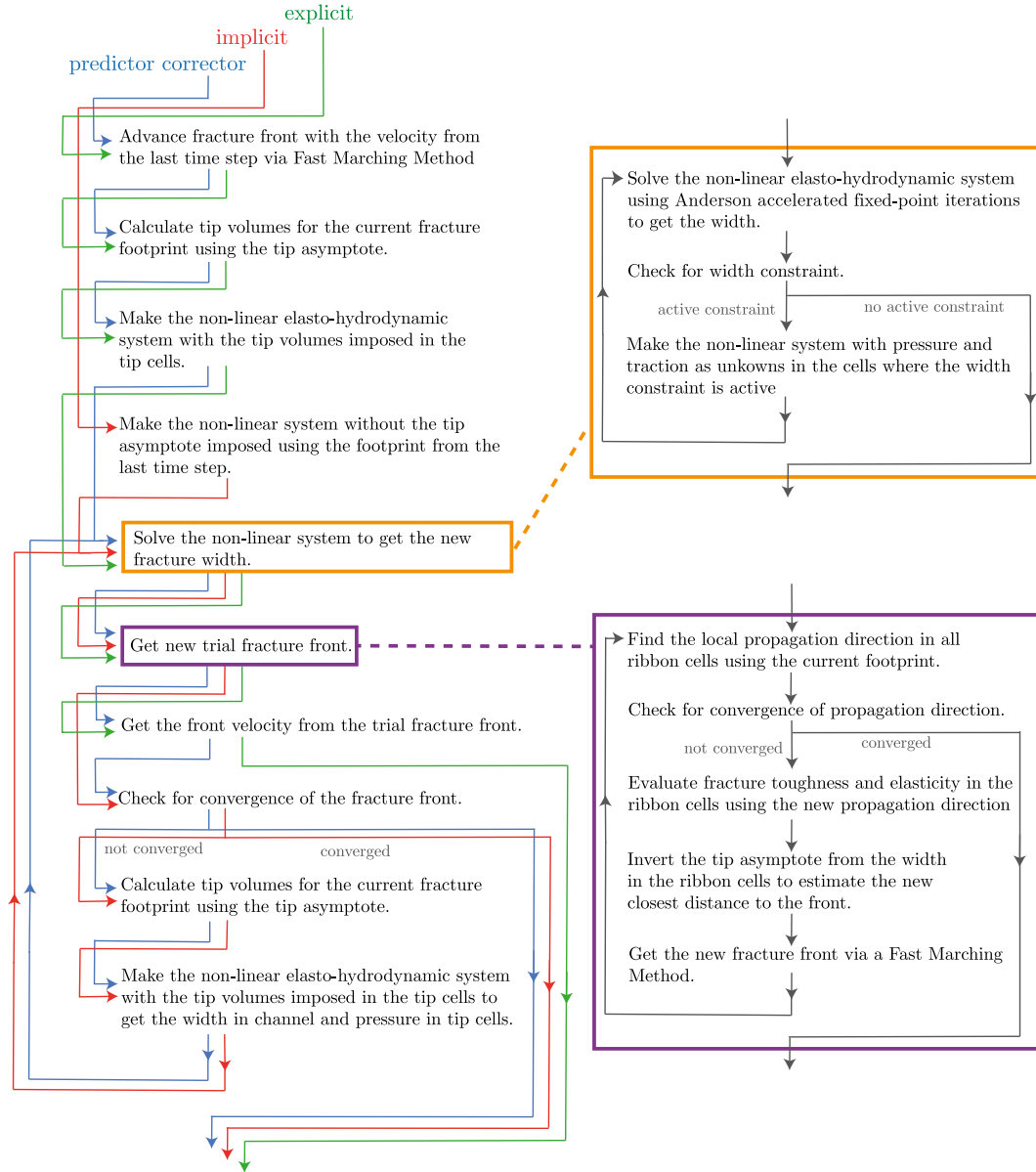


Figure 2.5: Flow Chart of PyFac. Figure reproduced from Zia and Lecampion (2020).

2.4 Numerical solution of hydraulic fracture problems

Numerically, the residual opening of a fracture becomes the minimum between the maximum opening achieved during the history of the fracture and this minimum width. This approach results in a contact condition of the form

$$(w - w_a) \geq 0, \quad (\sigma_{yy} - p_f)(w - w_a) = 0 \quad (2.64)$$

stating notably that the fluid pressure p_f is equal to the normal traction σ_{yy} when the fracture is mechanically open (e.g. $w > w_a$).

Once a solution of the EHL system, including cells with a width constraint, is found, the tip asymptotes are used at the survey (also called ribbon) cells to invert for the position of the new front (see figure 2.4). This inversion gives the value of the level set at the survey cells. Using a Fast Marching Method (Sethian, 1999) to solve the eikonal equation of the distance to the front, the level set is propagated over the domain, and its zero value is used to reconstruct the new position of the front. This new position is constructed from a piece-wise linear approximation within the tip cells and forms the internal loop represented by the purple box in figure 2.5.

The coupling between the front loop and the EHL is ensured by imposing that the tip cell volume corresponds to the asymptotic tip solution. Thanks to the knowledge of the level set at every cell, we obtain the tip cell volumes necessary to re-generate the EHL system for the new footprint. In this adapted EHL, we solve for fracture opening increment in all channel cells while imposing the opening in the tip cells, where we solve for the fluid pressure (see figure 2.4).

The convergence of a time step is ultimately related to the convergence of the fracture front position. In other words, a time step is accepted when the changes of the fracture front fall below a certain threshold. The measuring parameters are the level sets at the survey cells which ensures a local convergence of the fracture front.

More details on the resolution of the various sub-problems and the solver PyFrac can be found in the code release article Zia and Lecampion (2020). The discussion of various extensions, notably a "smooth" fracture front implementation, can be found in Peruzzo (2023). Note that we use the smooth" fracture front according to chapter 2.6 of Peruzzo (2023) in the simulations reported herein.

Radial Finite Volume Hydraulic Fracture

Part II

3 Arrest of a radial hydraulic fracture upon shut-in of the injection

This chapter is a modified version of an article published in the International Journal of Solids and Structures (IJSS).

Möri, A. and Lecampion, B. (2021). Arrest of a radial hydraulic fracture upon shut-in of the injection. *Int. J. Solids Struct.*, 219-220:151–165, DOI: 10.1016/j.ijsolstr.2021.02.022, ©Elsevier.

Contributions

Andreas Möri has conceptualized the problem, performed a formal and scaling analysis, decided on the methodology, adapted the numerical solver, committed validation against known results, generated the visualizations, and wrote the original draft. Brice Lecampion acted as supervisor, supported the conceptualization and methodology, supervised the formal and scaling analysis, acquired the funding, and reviewed and edited the text in iterations with Andreas Möri.

3.1 Abstract

We investigate the propagation and arrest of a radial hydraulic fracture upon the end of the injection. Excess elastic energy may be stored in the surrounding medium depending on the propagation regime at the time of shut-in of the injection. Once the injection has stopped, the hydraulic fracture will arrest when the energy release rate falls under the material fracture energy. Fluid leaking-off to the surrounding medium acts as an energy sink such that the available excess energy for fracture growth decreases faster and, as a result, impacts the arrest (actually controls it in the zero toughness limit). Under the assumption of a homogeneous elastic medium and the Carter's leak-off model, we show that the post-shut-in propagation of the hydraulic fracture depends on the dimensionless toughness \mathcal{K}_s and leak-off \mathcal{C}_s coefficient at the time of shut-in. Our investigation highlights that the arrest radius is independent of the dimensionless toughness at shut-in for an impermeable rock. In the limit of a permeable rock with zero fracture toughness, the arrest radius is independent of the dimensionless leak-off coefficient only for $\mathcal{C}_s < 0.25$. For larger values of \mathcal{C}_s , the radius of arrest reduces with increasing \mathcal{C}_s . We delineate the limit above which the arrest is immediate upon shut-in. This limit is given by a critical leak-off coefficient at shut-in $\mathcal{C}_{s,c} \approx 0.53$ for the large leak-off/small toughness cases and by the relation $\mathcal{C}_{s,c}(\mathcal{K}_{s,c}) \approx 0.78 - 0.313 \cdot \mathcal{K}_{s,c}$ for small leak-off/large toughness (where $\mathcal{K}_{s,c}$ is equivalently the critical dimensionless toughness at shut-in). Immediate arrest in the impermeable limit is observed for $\mathcal{K}_{s,c} \approx 2.5$. If both (\mathcal{K}_s and \mathcal{C}_s) are smaller than their critical value for immediate arrest, post shut-in propagation occurs, and a self-similar pulse viscosity storage solution emerges. Scaling arguments combined with numerical simulations show that the propagation post-shut-in scales as $1.23\mathcal{K}_s^{-2/5}$ in the impermeable and small leak-off cases, and as $0.75\mathcal{C}_s^{-2/13}$ in the zero toughness limit. The growth post-shut-in can be significant in impermeable rocks - with a final radius up to twice larger than the radius at shut-in for realistic material and injection parameters.

Keywords: fracture arrest, shut-in, post-injection propagation, numerical methods

3.2 Introduction

Hydraulic fractures (HF) are tensile fractures created by the injection of a fluid at pressure larger than the minimum in-situ compressive stress (Detournay, 2016). The hydraulic fracturing technique is used in a broad range of engineering applications, from block caving mining (Jeffrey et al., 2013) to soil remediation (Germanovich and Murdoch, 2010), and is a cornerstone of hydrocarbon production from low permeability shales (Smith and Montgomery, 2015). Such tensile fluid-driven fractures also propagate naturally in the form of magmatic intrusion in the upper earth crust, forming volcanic dikes and sills (Rivalta et al., 2015; Spence et al., 1987; Lister and Kerr, 1991). A strong coupling between linear elastic fracture mechanics governs the growth of HFs (LEFM), lubrication flow in the propagating fracture and leak-off of the fluid into the surrounding medium. The competition between these different physical processes is now well understood for a growing fracture under a constant injection rate and results in

various growth regimes (Detournay, 2004, 2016). The propagation of an HF is dependent on the relative importance of two storage and two dissipative mechanisms. The bulk of the injected fluid either remains in the propagating fracture or leaked-off in the surrounding medium (storage vs. leak-off dominated regimes) while the energy is either dissipated in the creation of new fracture surfaces or the viscous flow within the fracture (toughness vs viscosity dominated regimes). For simple geometries (plane-strain and radial), solutions for hydraulic fracture growth have been obtained in these limiting regimes, leveraging the multiscale asymptotic solution of a steadily moving semi-infinite hydraulic fracture (Garagash et al., 2011). These theoretical predictions compare well with experiments performed in impermeable materials, notably for radial fractures (Bunger and Detournay, 2008; Lecampion et al., 2017). The evolution of a radial hydraulic fracture after the end of the injection (often referred to as shut-in in industrial applications) is the topic of this paper. In particular, we aim to quantitatively answer two important questions: under what conditions does the fracture immediately arrest? And if it does not arrest immediately, how far does it propagate before finally arresting?

Interestingly, these questions have seldom been examined in detail despite fracture closure's importance in industrial applications. A large body of work has indeed investigated the closure problem but generally treated the arrest in an ad-hoc manner and/or did not quantitatively investigate the parameters controlling post-shut-in propagation and arrest. Modeling fracture closure aims to interpret better the pressure decline curve measured after shut-in. These measurements are used to estimate relevant parameters (in-situ stress, pore-pressure among others) for the design of well-stimulation treatments by hydraulic fracturing (Economides and Nolte, 2000). One of the first models of fracture closure (Nolte, 1979) assumed a constant area upon the end of the injection (and, as such, an immediate arrest) for a fracture of constant height (Perkins-Kern-Nordgren (PKN) geometry). Settari and Cleary (1984) implemented a pseudo-3D model to address the problem in a more general way and additionally allowed for post-injection propagation. They observed a slight post-shut-in propagation in some of their investigated cases without going into details. Gu and Leung (1993) extended the analysis to three-dimensional planar fractures accounting for non-uniform in-situ stresses and leak-off parameters but did not account for any post-injection growth. Desroches and Thiercelin (1993) model fracture growth and closure for simple geometries (plane-strain and axisymmetric fractures) in a fully coupled manner based on the now classical hypothesis of LEFM, lubrication flow, and Carter's leak-off. They observe a small amount of propagation after shut-in in some of the cases investigated: the complete analysis of this post-shut-in propagation is, however, not treated. Papanastasiou (2000) numerically investigated propagation and closure (accounting also for bulk plasticity). The effect of poroelasticity on fracture closure is mentioned in the work of Boone and Ingraffea (1990) and Detournay et al. (1989) on the modeling of small hydraulic fracturing tests. Recently, the 2D plane-strain problem has been revisited numerically using an extended finite element method (Mohammadnejad and Andrade, 2016). These different modelling works and experimental observations (De Pater et al., 1996; van Dam et al., 2000; Zanganeh et al., 2017) agree with the conclusion that propagation after shut-in can occur in

Chapter 3. Arrest of a radial hydraulic fracture upon shut-in of the injection

some cases. The problem of fracture arrest was quantified in detail only in the large toughness limit for a plane strain hydraulic fracture propagating in an impermeable medium by Garagash (2006a). In that large toughness limit (limit of small dimensionless viscosity \mathcal{M}), the additional propagation post-shut-in (with respect to the length at shut-in) scales as $2.9\mathcal{M}$ for ($\mathcal{M} \ll 1$) (Garagash, 2006a).

We focus here in detail on the case of a radial fracture and quantify the final HF's arrest radius as a function of rock, fluid properties, and injection duration, accounting for both fluid leak-off and fracture toughness. We combine scaling analysis and numerical simulations to do so. One can easily anticipate a series of different behavior as a function of the amount of elastic energy stored in the medium still available upon shut-in (see Appendix 3.8.1 for the complete energy budget). When viscous flow dissipation dominates at shut-in, and thus some excess elastic energy is still available, the fracture will keep growing for a while. On the other hand, it will likely immediately arrest if fracture energy dominates the overall energy dissipation at shut-in. Similarly, a larger leak-off intensity acts as an energy sink reducing the energy available for growth and thus will lead to an earlier arrest after the end of the injection.

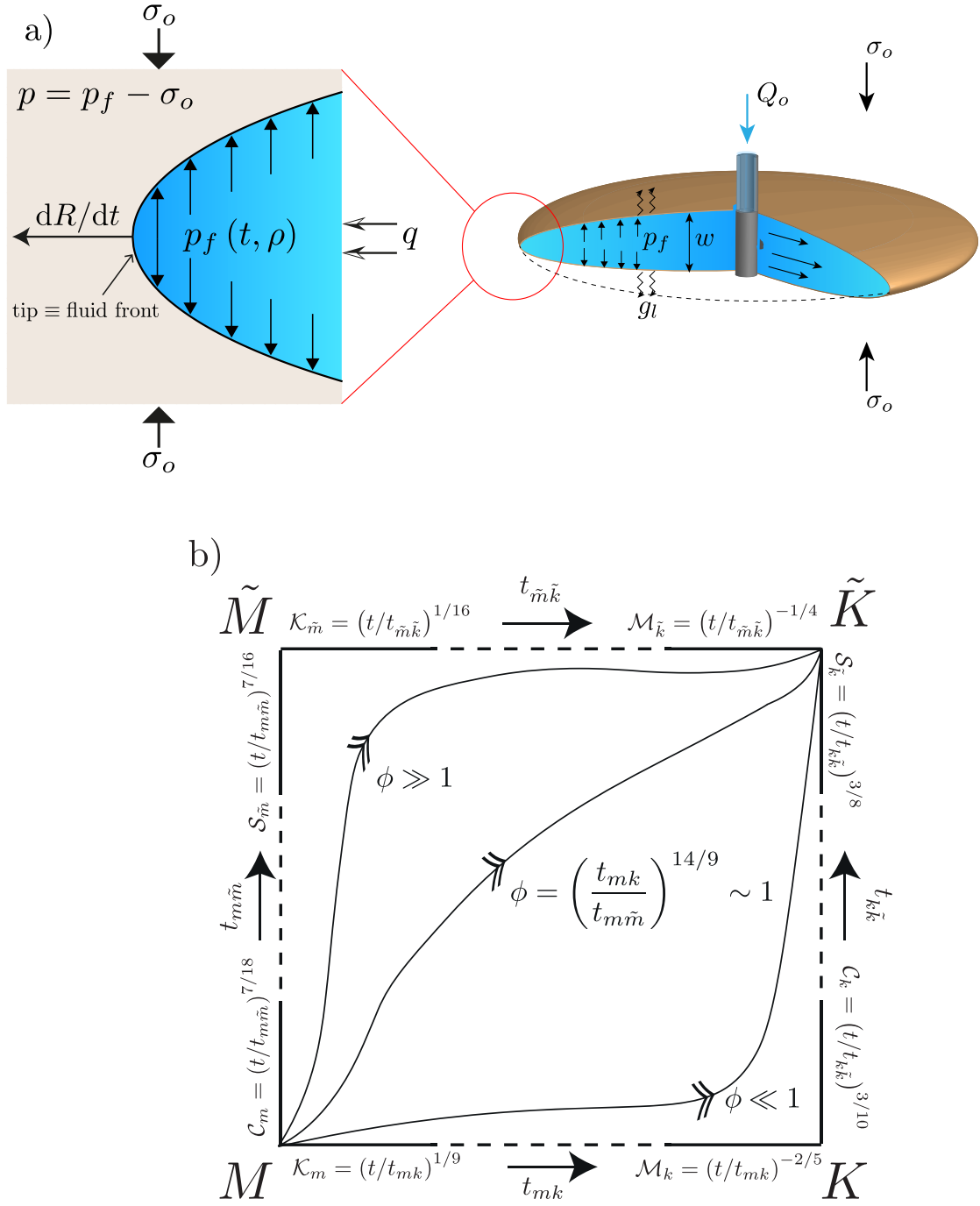
We first present the mathematical formulation of the problem and its scaling and outline the numerical solver used. We then treat first the impermeable case before moving to the case of a permeable medium with zero and finally finite fracture toughness.

3.3 Problem formulation

We focus on a radial hydraulic fracture propagating in a linear isotropic homogeneous elastic medium driven by a Newtonian fluid. Similarly to previous contributions (Savitski and Detournay, 2002; Madyarova, 2003), we neglect the size of the injected wellbore compared to the fracture size and model the injection as a point source. The fluid leak-off in the surrounding medium is modeled using Carter's leak-off model (Carter, 1957), which amounts to an early time 1D approximation of fluid diffusion valid when the net pressure is small compared to the far-field in-situ effective stress (see, for example Lecampion et al. (2018); Kanin et al. (2019) for further discussion). We also neglect the presence of a fluid lag - an assumption which is valid as soon as the shut-in time is larger than the characteristic time-scale $t_{om} = \frac{\mu' E'^2}{\sigma_o^3}$ controlling the coalescence of the fluid and fracture fronts (Garagash, 2006b; Lecampion and Detournay, 2007; Bungier and Detournay, 2007). We briefly recall the governing equations of the coupled moving boundary hydro-mechanical fracture problem. In line with previous contributions, we use the following material constants for clarity

$$E' = \frac{E}{1-\nu^2}, \quad K' = 4\sqrt{\frac{2}{\pi}}K_{Ic}, \quad \mu' = 12\mu, \quad C' = 2C_L \quad (3.1)$$

where C_L is the Carter leak-off coefficient, K_{Ic} the fracture toughness, μ the fluid viscosity, E and ν the material elastic Young's modulus and Poisson's ratio, respectively.



Chapter 3. Arrest of a radial hydraulic fracture upon shut-in of the injection

Quasi-static elasticity relates the fracture width w to the net pressure loading at the fracture faces $p = p_f - \sigma_o$ (the fluid pressure in excess of the in-situ compressive stress). For such a purely tensile axisymmetric fracture, the elastic problem reduces to the following integral representation (Sneddon, 1951)

$$w(\rho) = \frac{8}{\pi} \frac{R(t)}{E'} \int_{\rho}^1 \frac{\xi}{\sqrt{\xi^2 - \rho^2}} \int_0^1 \frac{x p(x\xi R, t)}{\sqrt{1 - x^2}} dx d\xi \quad (3.2)$$

or alternatively its inverse (Gordeliy and Detournay, 2011). Under the assumption of quasi-static linear elastic fracture mechanics, the fracture propagation conditions for fracturing under pure mode I read:

$$(K_I - K_{Ic}) \frac{dR(t)}{dt} = 0 \quad \frac{dR(t)}{dt} \geq 0 \quad (3.3)$$

where the stress intensity factor K_I can be estimated via the Bueckner-Rice integral (Rice, 1972)

$$K_I = \frac{2}{\sqrt{\pi R(t)}} \int_0^{R(t)} \frac{p(t, r)}{\sqrt{R^2 - r^2}} r dr \quad (3.4)$$

Fluid flow in the fracture is modeled under the lubrication approximation (Batchelor, 1967). The fluid continuity equation combined with Poiseuille's law for a Newtonian fluid yields the following Reynolds equation

$$\frac{\partial w(t, r)}{\partial t} - \frac{1}{\mu'} \frac{1}{r} \frac{\partial}{\partial r} \left(r w(t, r)^3 \frac{\partial p(t, r)}{\partial r} \right) + \frac{C'}{\sqrt{t - t_o(r)}} = 0 \quad (3.5)$$

which states that the change of fracture aperture (first term) is balanced by the in/out fluid fluxes (second term) and the rate of fluid leaking out of the fracture into the rock following Carter's law (third term). Integration in space and time gives the global fluid volume balance which relates the injected volume $V(t)$ to the fracture and fluid leak-off volumes:

$$V(t) = 2\pi \int_0^R w(t, r) r dr + 2\pi \int_0^t \int_0^R \frac{2C_L}{\sqrt{\tau - \tau_o(r)}} r dr d\tau \quad (3.6)$$

where the boundary condition of zero fracture width and zero fluid flux at the fracture tip has been used. We assume a simple history for the injection: a constant injection at a rate Q_o up to a time t_s when the pump is "shut-in" such that

$$V(t) = Q_o t, \quad \text{for: } t < t_s \quad V(t) = Q_o t_s = V_o, \quad \text{for: } t \geq t_s \quad (3.7)$$

3.3.1 Growth during constant injection ($t < t_s$)

Hydraulic fracture growth during the injection period ($t < t_s$) is well understood for such a radial geometry (Savitski and Detournay, 2002; Detournay, 2004, 2016) and can be summarised in a rectangular propagation diagram (see Figure 3.1b adapted from Detournay (2016)). No-

tably, the HF growth evolves from a regime initially dominated by viscous dissipation and fluid storage inside the fracture (M -vertex in figure 3.1b) to a regime dominated by fracture toughness and fluid leak-off at large-time (\tilde{K} -vertex in figure 3.1b). The complete evolution of the fracture is governed by a time-dependent dimensionless fracture toughness \mathcal{K}_m (or alternatively dimensionless viscosity \mathcal{M}_k) and a time-dependent dimensionless leak-off coefficient \mathcal{C} (or alternatively dimensionless storage \mathcal{S}). The dimensionless parameters \mathcal{K}_m and \mathcal{C}_m can be expressed as a function of two time-scales t_{mk} and $t_{m\tilde{m}}$ governing the transition from the viscous/storage-dominated regime to, respectively the toughness/storage and viscous/leak-off regimes:

$$\begin{aligned} \mathcal{K}_m &= (t/t_{mk})^{1/9} & \mathcal{C}_m &= (t/t_{m\tilde{m}})^{7/18} \\ t_{mk} &= \frac{E'^{13/2} \mu'^{5/2} Q_o^{3/2}}{K'^9} & t_{m\tilde{m}} &= \frac{\mu'^{4/7} Q_o^{6/7}}{C'^{18/7} E'^{4/7}} \end{aligned} \quad (3.8)$$

The complete evolution of the solution from the viscosity/storage dominated to the toughness/leak-off regime within the propagation diagram of figure 3.1b can be grasped by a trajectory parameter

$$\phi = \left(\frac{t_{mk}}{t_{m\tilde{m}}} \right)^{14/9} = \frac{C'^4 E'^{11} \mu'^3 Q_o}{K'^{14}} = \mathcal{C}_m^4 / \mathcal{K}_m^{14} \quad (3.9)$$

and the dimensionless time t/t_{mk} . The growth solution can be adequately expressed using specific scalings for different propagation regimes, writing the fracture radius, width, and net pressure as

$$R(t) = L(t) \gamma(\mathcal{P}_1, \mathcal{P}_2) \quad w(r, t) = W(t) \Omega(r/R, \mathcal{P}_1, \mathcal{P}_2) \quad p(r, t) = P(t) \Pi(r/R, \mathcal{P}_1, \mathcal{P}_2)$$

where $P(t) = E' W(t) / L(t)$ is the characteristic pressure scale, $L(t)$ and $W(t)$ the characteristics fracture length and width scales while $\mathcal{P}_1, \mathcal{P}_2$ denote the corresponding two dimensionless parameters (e.g., dimensionless toughness and leak-off in the viscosity scaling). We refer to Detournay (2016) for the details of the constant injection case ($t_s \rightarrow \infty$).

3.3.2 Evolution post-shut-in ($t > t_s$)

For the case of a finite injection/pulse injection, after the shut-in time ($t > t_s$), the growth of the hydraulic fracture can be grasped using similar scaling arguments by substituting the finite injected volume $V_o = Q_o t_s$ in place of the rate-dependent volume $Q_o t$. In other words, by replacing Q_o with V_o/t in the constant injection scalings. The scales and evolution parameters for the four different regimes (viscosity/toughness, leak-off/storage) in this case, are presented in table 3.1. Whenever we refer to the constant injection scaling, the superscript will be omitted (for example, L_m denotes the characteristic length scale of the viscosity storage constant injection scaling). On the other hand, the constant volume/pulse injection scaling is indicated by the superscript $[V]$ (for example, $L_m^{[V]}$ denotes the characteristic length scale of the viscosity storage pulse injection scaling).

Chapter 3. Arrest of a radial hydraulic fracture upon shut-in of the injection

| Scaling | $M^{[V]}$ | $K^{[V]}$ | $\tilde{M}^{[V]}$ | $\tilde{K}^{[V]}$ |
|---------------------|---|--|---|--|
| $L^{[V]}$ | $\frac{E^{1/9} t^{1/9} V_o^{1/3}}{\mu^{1/9}}$ | $\frac{E^{2/5} V_o^{2/5}}{K^{2/5}}$ | $\frac{V_o^{1/2}}{C^{1/2} t^{1/4}}$ | $\frac{V_o^{1/2}}{C^{1/2} t^{1/4}}$ |
| $P^{[V]}$ | $\frac{E^{2/3} \mu^{1/3}}{t^{1/3}}$ | $\frac{K^{6/5}}{E^{1/5} V_o^{1/5}}$ | $\frac{\mu^{1/4} C^{3/8} E^{3/4}}{V_o^{1/8} t^{1/16}}$ | $\frac{K' C^{1/4} t^{1/8}}{V_o^{1/4}}$ |
| $W^{[V]}$ | $\frac{V_o^{1/3} \mu^{2/9}}{E^{2/9} t^{2/9}}$ | $\frac{V_o^{1/5} K^{4/5}}{E^{4/5}}$ | $\frac{\mu^{1/4} V_o^{3/8}}{E^{1/4} C^{1/8} t^{5/16}}$ | $\frac{K' V_o^{1/4}}{E' C^{1/4} t^{1/8}}$ |
| $\mathcal{K}^{[V]}$ | $K' \frac{t^{5/18}}{E^{13/18} \mu^{5/18} V_o^{3/18}}$ | 1 | $K' \frac{t^{3/16}}{\mu^{1/4} C^{1/8} E^{3/4} V_o^{1/8}}$ | 1 |
| $\mathcal{M}^{[V]}$ | 1 | $\mu' \frac{E^{13/5} V_o^{3/5}}{K^{18/5} t}$ | 1 | $\mu' \frac{V_o^{1/2} E'^3 C^{1/2}}{K'^4 t^{3/4}}$ |
| $\mathcal{E}^{[V]}$ | $C' \frac{E^{2/9} t^{13/18}}{V_o^{1/3} \mu^{2/9}}$ | $C' \frac{E^{4/5} t^{1/2}}{V_o^{1/5} K^{4/5}}$ | 1 | 1 |
| $\mathcal{S}^{[V]}$ | 1 | 1 | $\frac{E^{1/4} C^{9/8} t^{13/16}}{\mu^{1/4} V_o^{3/8}}$ | $\frac{E' C'^{5/4} t^{5/8}}{K' V_o^{1/4}}$ |

Table 3.1: Characteristic scales and evolution parameters in the four propagation regimes for post-shut-in evolution (pulse injection case).

It is interesting to note that the lengthscales $L^{[V]}$ in both leak-off dominated scalings ($\tilde{M}^{[V]}$ and $\tilde{K}^{[V]}$) listed in table 3.1 are decaying with time. This indicates that for a finite volume injection, if dominated by leak-off, the fracture recesses. Hinting toward an immediate arrest after shut-in in those cases. Similarly, we observe that the fracture length scale is time-independent in the toughness/storage scaling ($K^{[V]}$ in table 3.1). The fracture length scale increases with time only in the viscosity/storage-dominated regime ($M^{[V]}$ in table 3.1). We already get a grasp at the structure of the solution after shut-in from those observations and anticipate that if the shut-in occurs when the fracture is already propagating in the leak-off dominated regime, it will immediately arrest and actually recess. If leak-off is negligible at shut-in, the fracture will continue growing if viscosity dominates. At the same time, it will tend to a constant size if dominated by fracture toughness and, as such, arrest in a finite time.

Our aim in what follows is to investigate the post-shut-in stages thoroughly and delineate when and how further growth after shut-in occurs. To do so, we will combine scaling arguments and semi-analytical solutions in some limiting regimes with full numerical solutions. This evolution post-shut-in will be dependent on the dimensionless toughness and dimensionless leak-off coefficients at shut-in

$$\begin{aligned}
 \mathcal{K}_s = \mathcal{K}_m(t = t_s) &= \mathcal{K}_m^{[V]}(t = t_s) = K' \frac{t_s^{1/9}}{E^{13/18} \mu^{5/18} Q_o^{1/6}} \\
 \mathcal{E}_s = \mathcal{E}_m(t = t_s) &= \mathcal{E}_m^{[V]}(t = t_s) = C' \frac{E^{2/9} t_s^{7/18}}{Q_o^{1/3} \mu^{2/9}}.
 \end{aligned} \tag{3.10}$$

where $V_o = Q_o t_s$ has been used. Alternatively, the evolution can be grasped as a function of one of the two shut-in parameters (\mathcal{K}_s or \mathcal{E}_s) and the trajectory parameter $\phi = (t_{mk}/t_{m\tilde{m}})^{14/9} = \mathcal{E}_m^4 / \mathcal{K}_m^{14} = \mathcal{E}_s^4 / \mathcal{K}_s^{14}$.

3.3.3 Numerical solver used

We will use the open source-planar 3D hydraulic fracture simulator PyFrac (Zia and Lecampion, 2020) extensively. The code is a Python implementation of the implicit level set algorithm (ILSA) (Peirce and Detournay, 2008) for three-dimensional planar HF. The scheme notably combines a finite discretization of the fracture with the use of the near tip HF asymptotic solution (see for example Garagash et al. (2011)), valid close to the moving boundary of the HF (at the tip, see figure 3.1a). We briefly outline the numerical techniques used to solve the governing equations presented in section 3.3 and refer to Zia and Lecampion (2020) for more details.

The fracture propagation plane is discretized using a rectangular Cartesian mesh with constant cell size. The fracture front is defined via a level set evaluated at the center of each cell. The algorithm marches in time such that the solution at time t^{n+1} is obtained from the known solution at t^n . The solution at a given time consists of the level set field (closest distance to the front from a cell center), the fracture front (location of intersections with cell edges), fracture opening, and fluid pressure inside the fracture (defined at the center of the cells). Quasi-static elasticity is discretized using a displacement discontinuity method with piecewise constant rectangular elements, and the Reynolds equation (3.5) is spatially discretized via a finite volume method. The fluid fluxes are notably obtained at the cell edges via a central finite difference scheme. After accounting for the injected volume during $\Delta t^{n+1} = t^{n+1} - t^n$, using a fully implicit time-integration scheme, one obtains a non-linear (elastohydrodynamic) system of equations for a given trial fracture front position. This non-linear system is solved via Anderson acceleration of fixed-point iterations (Anderson, 1965; Walker and Ni, 2011). Once the elastohydrodynamic system is solved, a new fracture front position is found using the ILSA scheme. This scheme updates the values of the level set function according to the widths in the ribbon elements close to the tip obtained from the elastohydrodynamic system. An iteration procedure between the front location and the resolution of the elastohydrodynamic system (for a given fracture front position) is performed until the fracture front converges between subsequent iterations. We use the approximation of the universal tip asymptote provided by Dontsov and Peirce (2017). For computational efficiency and robustness, we use a predictor-corrector scheme for the fracture front advancing scheme where the starting point of the iteration on the fracture front is obtained with an explicit time step using the velocity obtained in the previous time step (see (Zia and Lecampion, 2019) for more details). The scheme has been extensively tested against known solutions and proved robust and accurate (Peirce, 2015, 2016; Zia et al., 2018; Zia and Lecampion, 2020; Moukhtari et al., 2020). In what follows, all the reported simulations use a grid size of 61x61 elements, and a re-meshing (coarsening of the element size by a factor 2) is performed when the fracture reaches the end of the grid, such that at most, the fracture contains approximately 61x61 elements and at minimum 30x30 elements (for details on numerical accuracy see Appendix 3.8.2).

3.4 Impermeable Medium

In the case of an impermeable medium, the fracture will arrest when the excess elastic energy present at shut-in falls below the energy required for subsequent fracture growth.

3.4.1 Arrest radius in the finite toughness case

If the fracture toughness is finite, the arrest will occur when the stored elastic energy present at shut-in has been entirely consumed by viscous flow. When the fluid velocity vanishes, the fluid pressure is uniform inside the fracture (as per Poiseuille law's $v = -w^2/\mu'\partial p/\partial z = 0 \rightarrow \partial p/\partial z = 0$). The radius of arrest is simply obtained as the solution of the quasi-static equilibrium of a crack under uniform net loading p with a prescribed volume V_o for which the stress intensity factor is strictly equal to K_{Ic} . For a uniform net pressure p , the elasticity (3.2) reduces to (Sneddon, 1946)

$$w(r) = \frac{8}{\pi} \frac{p}{E'} \sqrt{R^2 - r^2} \quad (3.11)$$

and the fracture volume V_f and mode I stress intensity factor are given as

$$V_f = \frac{16}{3} \frac{pR^3}{E'} \quad (3.12)$$

$$K_I = \frac{2}{\sqrt{\pi}} pR^{1/2} \quad (3.13)$$

In the absence of leak-off (impermeable case), imposing a fracture volume equal to the injected volume V_o and a stress intensity factor K_I equal to the fracture toughness, one can easily solve for the corresponding radius, net pressure, and width:

$$R_{k,a} = \left(\frac{3}{\pi\sqrt{2}} \right)^{2/5} \left(\frac{E'V_o}{K'} \right)^{2/5}, \quad (3.14a)$$

$$p_{k,a} = \left(\frac{\pi^6}{3 \times 2^{17}} \right)^{1/5} \left(\frac{K'^6}{E'V_o} \right)^{1/5}, \quad (3.14b)$$

$$w_{k,a}(r) = \left(\frac{3}{8\pi} \right)^{1/5} \sqrt{1 - \left(\frac{r}{R_{k,a}} \right)^2} \left(\frac{V_o K'^4}{E'^4} \right)^{1/5}. \quad (3.14c)$$

We shall denote this solution as the toughness arrest solution (with subscript k, a). It only depends on the rock properties (elasticity and toughness) and the total volume injected. This solution (equations (3.14a)-(3.14c)) corresponds to the $K^{[V]}$ -Vertex characteristic scales multiplied by prefactors of order one. It is also worth noting that the solution for a toughness-dominated growth under a constant injection rate (see Abé et al. (1976); Savitski and Detournay (2002)) is merely obtained by replacing V_o by $Q_o t$ in this solution.

3.4.2 Viscosity-storage pulse solution in the zero toughness limit - case of no arrest

In the limit of zero toughness (for example, when re-opening a pre-existing fracture), we see from (3.14a) that the arrest radius becomes infinite. In other words, in that limit, the hydraulic fracture will continue to grow ad vitam æternam. Given the scaling of table 3.1 in this regime of zero toughness and zero leak-off, the growth of an HF with a finite volume V_o does not depend on any dimensionless parameter ($\mathcal{K}_m^{[V]} = \mathcal{C}_m^{[V]} = 0$). As a result, the growth is self-similar, and a solution can be derived using the viscosity/storage $M^{[V]}$ scaling. Equations (3.2) to (3.6) in the $M^{[V]}$ scaling can be re-written as:

$$\bar{\Omega}_{m0}^{[V]}(\rho) = \frac{8}{\pi} \int_{\rho}^1 \frac{\xi}{\xi^2 - \rho^2} \int_0^1 \frac{x \Pi_{m0}^{[V]}(\rho)}{\sqrt{1 - x^2}} dx d\xi \quad (3.15a)$$

$$\frac{1}{9} \rho + \left(\bar{\Omega}_{m0}^{[V]}(\rho) \right)^2 \frac{d\Pi_{m0}^{[V]}(\rho)}{d\rho} = 0 \quad (3.15b)$$

$$\int_0^1 \frac{\Pi_{m0}^{[V]}(\rho)}{\sqrt{1 - \rho^2}} \rho d\rho = 0 \quad (3.15c)$$

$$\gamma_{m0}^{[V]} = \left(2\pi \int_0^1 \bar{\Omega}_{m0}^{[V]}(\rho) \rho d\rho \right)^{-1/3} \quad (3.15d)$$

subjected to the boundary conditions of zero dimensionless opening and fluid flux at the tip. The dimensionless solution $\mathcal{F}_{m0}^{[V]}$ (where the subscript $m0$ refer to the zero toughness / leak-off limit) consists of the dimensionless fracture radius $\gamma_{m0}^{[V]}$, net pressure $\Pi_{m0}^{[V]}$, and reduced opening $\bar{\Omega}_{m0}^{[V]}(\rho) = \Omega_{m0}^{[V]}(\rho) / \gamma_{m0}^{[V]}$.

This set of equations can be solved numerically using Gauss-Chebyshev quadrature and barycentric Lagrange differentiation and interpolation. Such a numerical method follows previous work (Viesca and Garagash, 2018; Liu et al., 2019) and is described in Appendix 3.8.2. The dimensionless opening and pressure profiles are shown in figure 3.10 of Appendix 3.8.2. The dimensionless fracture length obtained numerically is $\gamma_{m0}^{[V]} \approx 0.8360$. We also note that the numerical results obtained using PyFrac matches very well the one obtained via this Gauss-Chebyshev-based scheme (see table 3.6 in Appendix 3.8.2).

3.4.3 Propagation and arrest post-shut-in

We now turn to investigate the propagation after shut-in in the impermeable case and the subsequent arrest due to a finite toughness numerically.

In the case of growth after shut-in (pulse injection) for a finite toughness in an impermeable medium, the final radius of arrest is given by equation (3.14a), and the growth solution toward

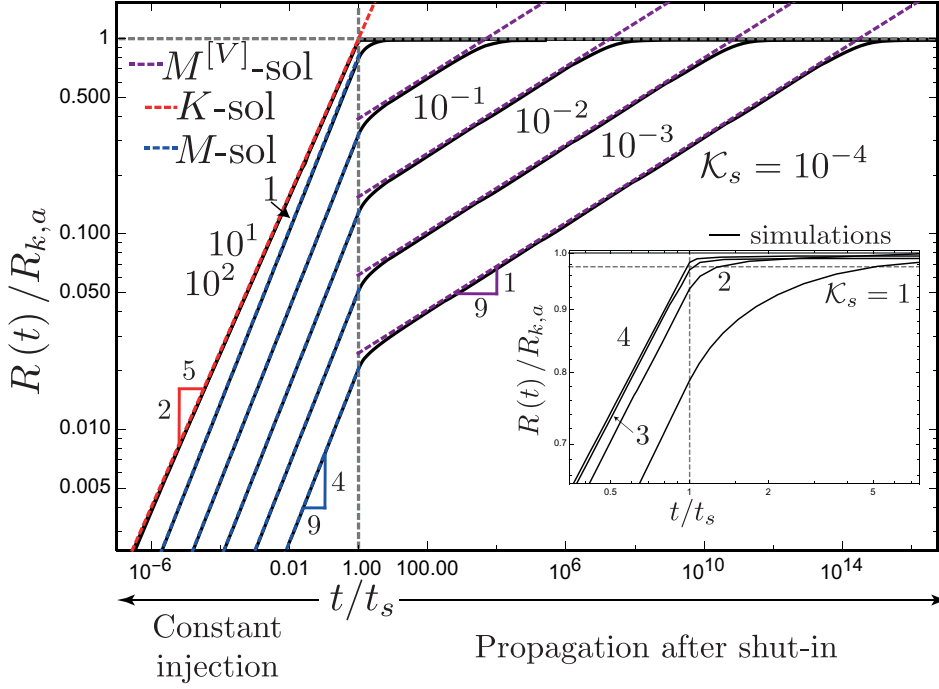


Figure 3.2: Normalized fracture radius as function of the dimensionless shut-in time t/t_s . Numerical (and semi-analytical) predictions of fracture radius scaled by the arrest radius $R_{k,a}$ (3.14a) for various values of shut-in toughness \mathcal{K}_s (3.10) (from 10^{-4} to 10^2).

this arrest only depends on a dimensionless toughness $\mathcal{K}_m^{[V]}(t)$ (see table 3.1) which can be expressed as a function of the dimensionless toughness at shut-in $\mathcal{K}_s = \mathcal{K}_m(t_s)$:

$$\mathcal{K}_m^{[V]}(t) = \left(\frac{t}{t_s}\right)^{5/18} \mathcal{K}_s. \quad (3.16)$$

The evolution of the fracture radius as a function of t/t_s for a series of simulations with different values of \mathcal{K}_s (equivalent to different shut-in time) is displayed in figure 3.2. The radius is scaled by the final arrest radius $R_{k,a}$ (3.14a). We note that during the injection phase ($t/t_s < 1$), we retrieve the semi-analytical solutions for growth under a constant injection rate derived in Savitski and Detournay (2002) (red (toughness dominated) and blue (viscosity dominated) dashed lines in figure 3.2). Upon shut-in, the behaviour of the fracture changes depending on the dimensionless toughness at shut-in \mathcal{K}_s . However, the arrest radius is uniquely defined (it does not depend on \mathcal{K}_s) and equals, up to numerical precision (between 1 to 3.5% relative error), to the theoretical value given by equation (3.14a). For small values of \mathcal{K}_s (where the shut-in happens when the HF is in the viscosity-dominated regime), one observes the transition from the constant injection rate viscosity solution (Savitski and Detournay, 2002) to the pulse viscosity-dominated solution discussed in section 3.4.2 (dashed magenta line on figure 3.2). This self-similar propagation appears at intermediate times before the fracture finally arrests at a radius equal to $R_{k,a}$ (3.14a). Larger values of $\mathcal{K}_s \gtrsim 3$ result in an

immediate arrest as the stored elastic energy is already balanced by fracture energy at shut-in: the radius at shut-in is equal to the arrest radius.

We post-process these results to estimate the limiting value of $\mathcal{K}_{s,c}$ (c for critical) above which immediate arrest occurs after shut-in. We define immediate arrest at shut-in when the radius at shut-in $R_s = R(t = t_s)$ is equal or larger to 97.5% of the final arrest radius ($R_s/R_{k,a} \geq 0.975$). In other words, when the radius at shut-in is within 2.5% of the toughness/arrest dominated solution (3.14a). We obtain $\mathcal{K}_{s,c} \approx 2.75 \pm 0.2$ from our series of numerical simulations. Such an estimate is in line with the one that can be derived from the first-order propagation solution for large toughness (dimensionless radius $\gamma_m \approx 0.8546\mathcal{K}^{-2/5} - 0.7349\mathcal{K}^{-4}$ expressed in the viscosity scaling - see Savitski and Detournay (2002)). Savitski and Detournay (2002) estimate $\mathcal{K} \approx 3.5$ for a fully toughness dominated growth assuming a 1% relative difference between the zero $0.8546\mathcal{K}^{-2/5}$ and first-order $(0.8546\mathcal{K}^{-2/5} - 0.7349\mathcal{K}^{-4})$ solutions. One obtains $\mathcal{K} \approx 2.67$, respectively $\mathcal{K} \approx 2.5$ when taking 2.5% respectively 3% relative difference. These values are consistent with the estimate directly derived from our numerical simulations. We take $\mathcal{K}_{s,c} \approx 2.5$ for simplicity in the following - in line with the upper bound of the relative error of our numerical solution (between 1 to 3.5% relative accuracy with respect to self-similar growth solutions for the mesh resolution used here, see Appendix 3.8.2).

For the case of dimensionless shut-in toughness lower than $\mathcal{K}_{s,c}$, the fracture continues to grow after shut-in up to the arrest radius $R_{k,a}$. When the fracture propagates in the viscosity dominated regime at shut-in ($\mathcal{K}_s \ll 1$ cases), the distance propagated after shut-in can be estimated by simply comparing the final arrest radius $R_{k,a}$ (see equation (3.14a)) with the radius of the fracture at shut-in ($t = t_s$) from the constant injection viscosity dominated solution (Savitski and Detournay, 2002):

$$R_m(t = t_s) = R_s = 0.6978 \frac{E'^{1/9} Q_o^{1/3} t_s^{4/9}}{\mu'^{1/9}} \quad (3.17)$$

We thus obtain the following relation between the arrest and shut-in radius and the dimensionless toughness at shut-in:

$$\frac{R_{k,a}}{R_s} = \frac{\left(\frac{3}{\pi\sqrt{2}}\right)^{2/5} \left(\frac{E'V_o}{K'}\right)^{2/5}}{0.6978 \left(\frac{E'^{1/9} Q_o^{1/3} t_s^{4/9}}{\mu'^{1/9}}\right)} \approx 1.23 \mathcal{K}_s^{-2/5} \quad (3.18)$$

Figure 3.3 shows that this semi-analytical approximation falls exactly on our numerical results for values of \mathcal{K}_s below 1. It slightly underestimates the ratio R_a/R_s for values of the dimensionless shut-in toughness between 1 and the value for immediate arrest $\mathcal{K}_{s,c} \approx 2.5$. This is simply because, for values of \mathcal{K}_s larger than one, the estimate of the radius at shut-in provided by the constant injection viscosity dominated (zero toughness) solution is no longer a valid approximation as the fracture toughness impacts the solution.

From equation (3.16), we can similarly estimate the following relation between the shut-in time ($t = t_s$) and the time of arrest ($t = t_a$):

$$\frac{t_a}{t_s} \propto \mathcal{K}_s^{-18/5}. \quad (3.19)$$

We use our numerical simulations to capture the corresponding prefactor leading to the relation $t_a/t_s \approx 5.0\mathcal{K}_s^{-18/5}$, again valid for \mathcal{K}_s smaller than 1. Figure 3.3 illustrates that the time of arrest can be significantly larger than the shut-in time for values of \mathcal{K}_s smaller than the critical value for immediate arrest $\mathcal{K}_{s,c} \approx 2.5$.

3.5 Permeable medium

We now switch to the case of a permeable medium. The loss of fluid in the surrounding rock is an additional arresting mechanism after shut-in as it acts as an energy sink for the excess elastic energy available for subsequent growth. We, therefore, anticipate that the arrest radius may significantly differ from the impermeable estimate given by equation (3.14a).

3.5.1 Zero toughness case

In the zero toughness case, the arrest is solely governed by the loss of fluid, and no analytical or semi-analytical expressions are currently available for the post-shut-in phase. As mentioned previously, the scaling for a pulse HF indicates an immediate recession in the viscosity/leak-off regime ($\tilde{M}^{[V]}$). We can thus anticipate an immediate arrest if the shut-in occurs when the HF already propagates in the so-called viscosity/leak-off dominated regime (\tilde{M}). In the constant injection case (prior to shut-in), the transition from the viscosity/storage (M) to the viscosity/leak-off (\tilde{M}) regime is governed by a dimensionless leak-off coefficient $\mathcal{C}_m(t) = (t/t_{m\tilde{m}})^{7/18}$ (see equation (3.8)). The leak-off /viscosity-dominated solution is fully reached within 1% for $\mathcal{C}_m \approx 13$, and within 3% for $\mathcal{C}_m \approx 4$ (Madyarova, 2003; Dontsov, 2016).

In the zero toughness case, the growth after shut-in is governed solely by the dimensionless leak-off coefficient

$$\mathcal{C}_m^{[V]}(t) = \left(\frac{t}{t_s}\right)^{13/18} \mathcal{C}_s.$$

Similar to the impermeable case, the dimensionless leak-off coefficient at shut-in \mathcal{C}_s (3.10) will govern the arrest of the fracture. We can hypothesize that fracture arrest will occur when the HF enters the viscosity/leak-off regime ($\tilde{M}^{[V]}$). This is equivalent to stating that $\mathcal{C}_m^{[V]} \sim 1$ such that we can estimate the time of arrest as

$$t_{\tilde{m},a} \sim t_s \mathcal{C}_s^{-18/13}. \quad (3.20)$$

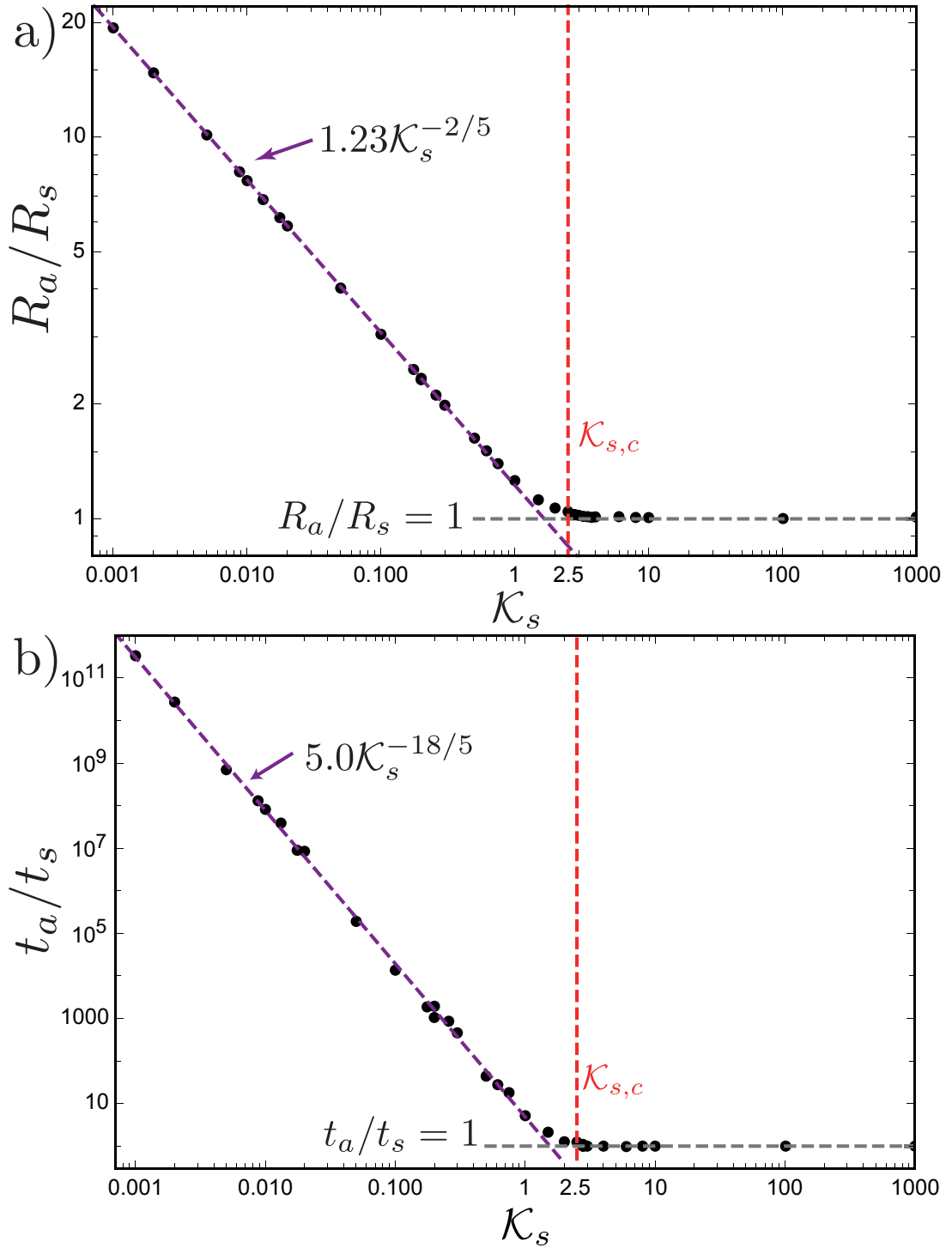


Figure 3.3: Characteristical values of post-injection propagation as a function of the dimensionless toughness at shut-in \mathcal{K}_s (impermeable case). a) Ratio between arrest and shut-in radius for a radial fracture in an impermeable medium. b) Time of arrest over shut-in time. Numerical simulations (Black dots) and analytical estimate for small \mathcal{K}_s (dashed purple line).

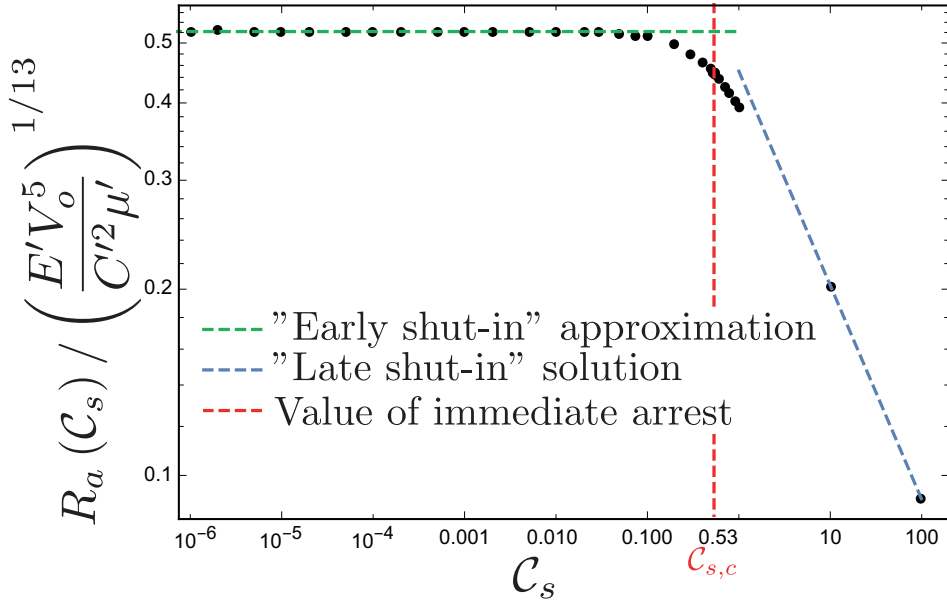


Figure 3.4: Numerical evaluation of the arrest radius for different values of \mathcal{C}_s in the zero toughness case. The early shut-in approximation is given in equation (3.21) with its prefactor obtained by regression of these numerical results. The late shut-in solution corresponds to the radius at shut-in given by the viscosity/leak-off propagation solution of Madyarova (2003).

The estimation of the arrest radius then emerges from the scaling (table 3.1) as

$$R_{\tilde{m},a} = \gamma_{\tilde{m},a} L_m^{[V]}(t = t_{\tilde{m},a}) = \gamma_{\tilde{m},a} \times \frac{E'^{1/13} V_o^{5/13}}{C'^{2/13} \mu'^{1/13}} \quad (3.21)$$

where $\gamma_{\tilde{m},a}$ is an unknown constant of order 1.

We perform a series of simulations for different values of \mathcal{C}_s ranging from 10^{-15} to 10^2 . The arrest radius as a function of \mathcal{C}_s is displayed in figure 3.4. We confirm that indeed the arrest radius scales with $L_m^{[V]}(t = t_{\tilde{m},a})$. In addition, two regimes can be observed. For $\mathcal{C}_s \lesssim 0.25$, the arrest radius scaled by $L_m^{[V]}(t = t_{\tilde{m},a})$ is indeed strictly constant, while for large values of \mathcal{C}_s the arrest is immediate such that the arrest radius corresponds to the radius at shut-in given by the large leak-off propagation solution (\tilde{M} -solution).

More precisely, for $\mathcal{C}_s \lesssim 0.25$, we can estimate the pre-factor of the exact arrest radius which scales with $L_m^{[V]}(t = t_{\tilde{m},a})$. We obtain $\gamma_{\tilde{m},a} \approx 0.5218$ from a linear regression of our numerical results, such that the arrest radius can be approximated as

$$R_{\tilde{m},a} \approx 0.5218 \frac{E'^{1/13} V_o^{5/13}}{C'^{2/13} \mu'^{1/13}} \text{ for } \mathcal{C}_s \lesssim 0.25. \quad (3.22)$$

We will refer to this estimate of the arrest radius as the “early shut-in” approximation (where early refers to small \mathcal{C}_s). On the other hand, for values of \mathcal{C}_s larger than 2.5, the arrest radius

is the radius at shut-in, which follows the viscosity/leak-off regime (\tilde{M}) constant injection solution (Madyarova, 2003; Detournay, 2016; Dontsov, 2016), as can be seen in figure 3.4. We refer to this limit as the “late shut-in” (large \mathcal{C}_s) solution hereafter. We can infer that the fracture will immediately stop its propagation somewhat for \mathcal{C}_s between 0.25 and 2.5. We estimate the critical dimensionless leak-off coefficient at shut-in $\mathcal{C}_{s,c}$ for immediate arrest from our simulations as $\mathcal{C}_{s,c} \approx 0.53 \pm 0.05$ by again using the criterion $R_s/R_a(\mathcal{C}_s) \geq 0.975$ for immediate arrest (red dashed line in figure 3.4). It is important to note that contrary to the impermeable case, the arrest radius is not uniquely defined for all \mathcal{C}_s . For small \mathcal{C}_s (below 0.25), the arrest radius is constant but not for larger values. Immediate arrest occurs for $\mathcal{C}_{s,c} \approx 0.53$ and the arrest radius for \mathcal{C}_s larger than $\mathcal{C}_{s,c}$ coincides with the shut-in radius, which can be well approximated by the viscosity/leak-off dominated injection solution (within a few percent for $\mathcal{C}_s > 4$).

We now turn to quantify the amount of propagation after the end of the injection. As expected, the propagation in the zero toughness case follows the known solutions during injection (Savitski and Detournay, 2002; Madyarova, 2003; Dontsov, 2016) ($t/t_s < 1$ in figure 3.5 left, blue (storage), and light blue (leak-off) dashed lines). One can observe from figure 3.5a that the propagation after shut-in ($t/t_s > 1$) for the “early shut-in” cases ($\mathcal{C}_s \lesssim 0.25$) follows the viscosity/storage pulse solution (developed in section 3.4.2) at intermediate times before the final arrest. We can thus estimate the amount of propagation after shut-in for values of $\mathcal{C}_s \lesssim 0.25$ by comparing the radius at shut-in (evaluated from the viscosity storage injection solution (Madyarova, 2003; Dontsov, 2016)) with the “early shut-in” arrest radius (3.22):

$$\frac{R_{\tilde{m},a}}{R_s} \approx \frac{0.5218 \left(\frac{E^{1/13} V_o^{5/13}}{C^{2/13} \mu^{1/13}} \right)}{0.6978 \left(\frac{E^{1/9} Q_o^{1/3} t_s^{4/9}}{\mu^{1/9}} \right)} \approx 0.75 \mathcal{C}_s^{-2/13}. \quad (3.23)$$

We recall that the prefactor of 0.5218 is obtained by fitting our numerical results such that equation (3.23) is also an approximation. Such an approximation compares very well with our numerical results up to $\mathcal{C}_s \lesssim 0.25$ as can be seen in Figure 3.6a. The power-law dependence of the ratio between the time of arrest and the shut-in time can be similarly derived from (3.20) as $t_a/t_s \propto \mathcal{C}_s^{-18/13}$. Such a dependence captures well our numerical results as displayed in Figure 3.6b where a linear regression was performed to obtain a prefactor of 0.044 (Figure 3.6b). The time of arrest can thus be estimated for small \mathcal{C}_s as:

$$\frac{t_a}{t_s} \approx 0.044 \mathcal{C}_s^{-18/13} \quad \text{for } \mathcal{C}_s \lesssim 0.25.$$

The effect of leak-off on arrest can also be grasped by looking at the evolution of fracturing efficiency η , defined as the ratio between the fracture volume V_f and the injected volume V_{inj} :

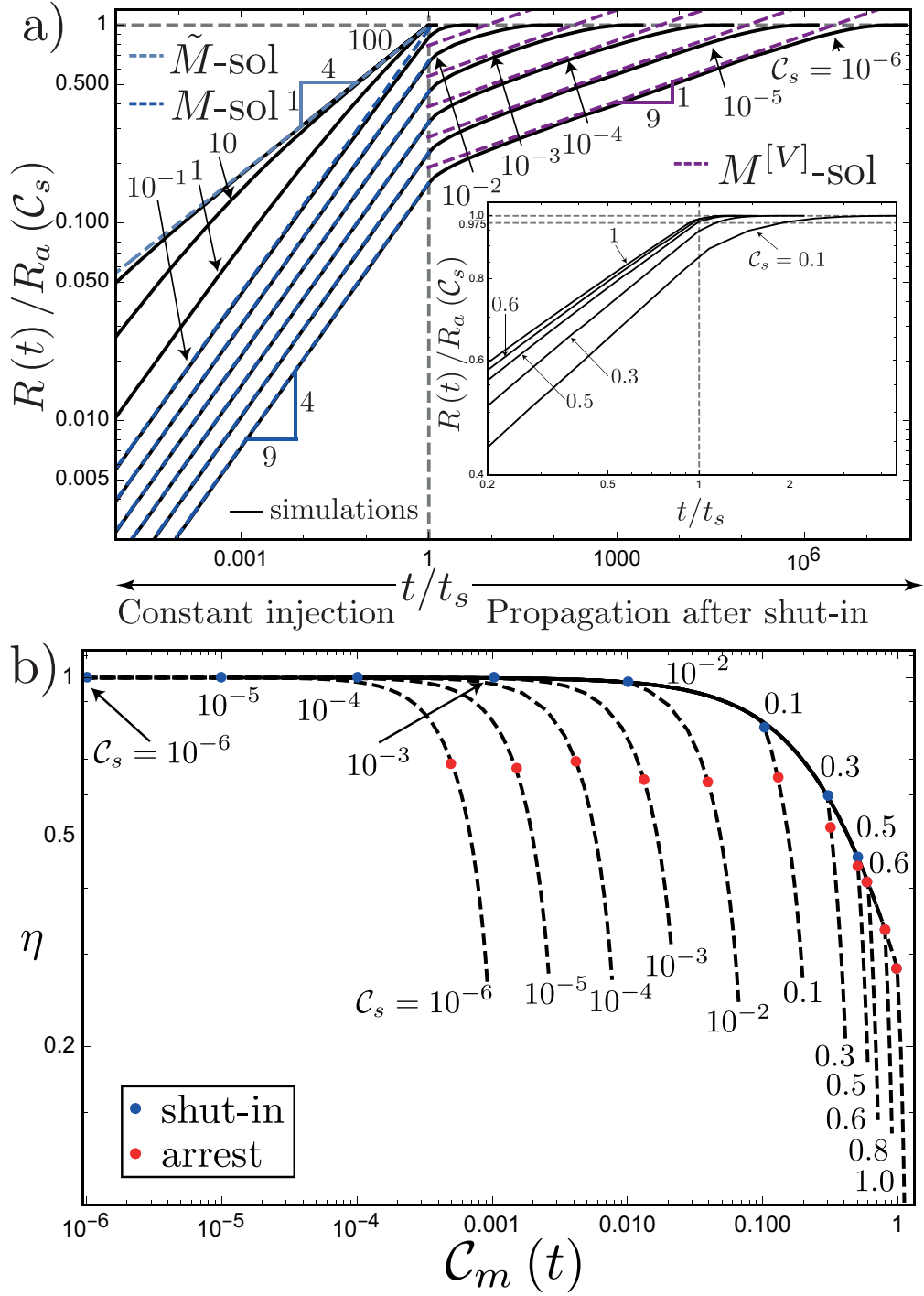


Figure 3.5: a) Normalised fracture radius as a function of characteristic shut-in time t/t_s . Numerical (and semi-analytical) predictions of fracture radius scaled by the arrest radius $R_a(C_s)$ for various values of shut-in leak-off coefficient C_s (from 10^{-6} to 10^2). b) Fracturing efficiency as a function of dimensionless leak-off coefficient $C_m(t) = C_s \times (t/t_s)^{7/18}$. Black dashed lines correspond to numerical simulations with different values of shut-in leak-off coefficient C_s . Blue dots mark the moment of shut-in, and red dots mark the fracture arrest.

$$\eta = \frac{V_f}{V_{inj}}, \quad \text{with: } V_{inj} = \begin{cases} Q_o t & \text{for } t < t_s \\ V_o & \text{for } t \geq t_s \end{cases} \quad (3.24)$$

For example, an efficiency of $\eta = 0.5$ indicates that half of the fluid injected remains inside the fracture, while the rest has leaked to the surrounding rock. The dimensionless leak-off coefficient is linked in a non-linear way to fracturing efficiency, and both help to characterize the propagation and arrest of the fracture after shut-in. From Figure 3.5b, we can relate the critical value of dimensionless leak-off coefficient at shut-in $\mathcal{C}_{s,c} \approx 0.53$, to a unique critical value of fracturing efficiency of $\eta_c = \eta(\mathcal{C}_m(t_s) = \mathcal{C}_{s,c}) \approx 0.44$. This allows us to estimate the loss of fluid necessary to stop instantaneously the fracture from propagating at shut-in. In other words, from the moment on that a bit more than half of the total amount of fluid injected is lost due to leak-off, the fracture will stop immediately upon shut-in. Finally, we can assess the possibility of post-injection propagation via the fracturing efficiency η , by observing Figure 3.5b. One can see that for \mathcal{C}_s smaller than 0.25 (for which the “early shut-in” approximation is valid), the arrest seems to occur when the fracturing efficiency falls to a common value of 0.68 irrespective of \mathcal{C}_s . From this, we infer that the fracturing efficiency at shut-in $\eta_s = \eta(\mathcal{C}_s)$ indicates the potential of post-injection propagation, as follows:

$$\begin{aligned} \eta_s > \eta_a = 0.68 & \quad \text{post-shut-in propagation,} \\ \eta_c \leq \eta_s < \eta_a & \quad \text{negligible post-shut-in propagation,} \\ \eta_s < \eta_c = 0.44 & \quad \text{immediate arrest.} \end{aligned} \quad (3.25)$$

3.5.2 General case

When accounting for both finite toughness and leak-off, the solution now depends on the corresponding dimensionless parameters at shut-in (\mathcal{K}_s and \mathcal{C}_s). The two are directly related by the trajectory parameter $\phi = \mathcal{C}_s^4 / \mathcal{K}_s^{14}$. We alternatively use \mathcal{K}_s (or \mathcal{C}_s) and ϕ to characterize the arrest radius and post-shut-in propagation.

We numerically evaluate the radius of arrest by performing a large number of simulations (≈ 450 simulations) for various values of the trajectory parameter $\phi = \mathcal{C}_s^4 / \mathcal{K}_s^{14}$ ranging from 10^{-12} to 10^{20} . The results are displayed in figure 3.7 together with limiting solutions in the impermeable and zero toughness cases. First of all, we observe that for $\mathcal{C}_s > 2.5$, the arrest radius is immediate independent of the value of \mathcal{K}_s (i.e., independent of ϕ): one retrieves the “late shut-in” arrest radius (viscosity / leak-off regime injection solution (Madyarova, 2003; Dontsov, 2016)). For $\phi > 1$, the arrest radius follows the early shut-in approximation (equation (3.22)) for intermediate values of \mathcal{C}_s . For a given value of ϕ , the arrest radius tends to the impermeable arrest radius $R_{k,a}$ (equation (3.14a)) when \mathcal{C}_s vanishes. Finally, the impermeable arrest radius $R_{k,a}$ (equation (3.14a)) is already a good estimate for values of $\mathcal{C}_s \leq 10^{-2}$ when $\mathcal{K}_s \lesssim 0.8$ (i.e when $\phi \leq 10^{-6}$).

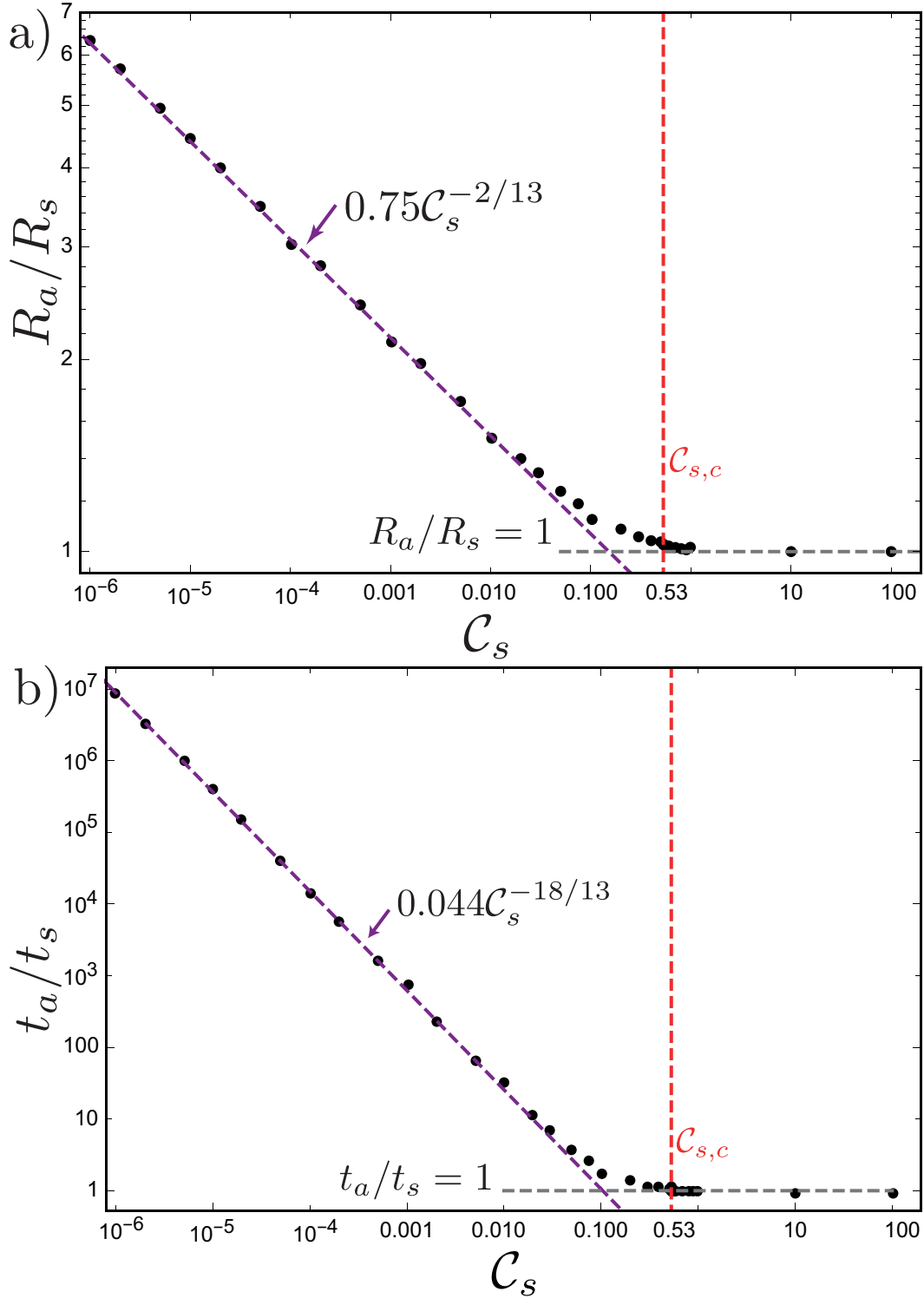


Figure 3.6: Characteristic values of post-injection propagation as a function of the shut-in leak-off coefficient \mathcal{C}_s . a) Overshoot of a radial fracture in the case of zero toughness. b) Square root of time of persistent propagation of a radial fracture in the case of zero toughness.

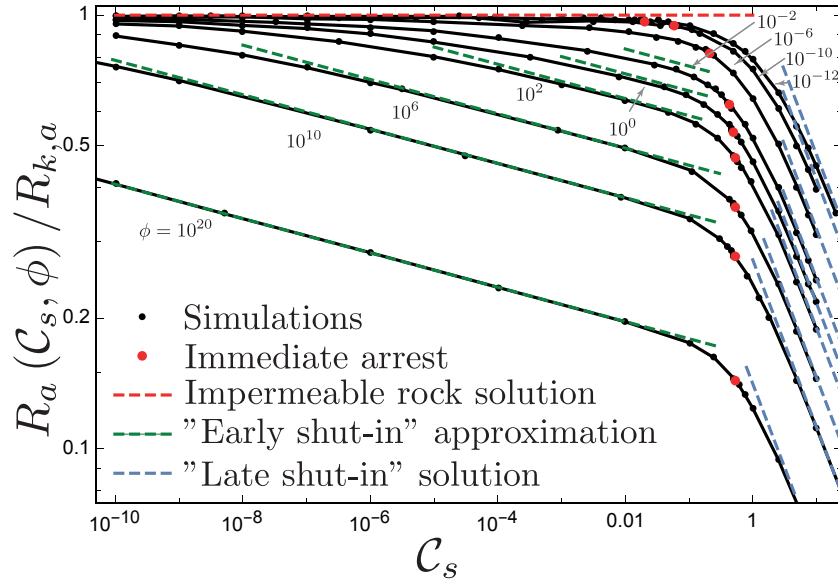


Figure 3.7: Normalized arrest radius $R_a/R_{k,a}$ as a function of the dimensionless leak-off coefficient at shut-in \mathcal{C}_s for different values of the trajectory parameter $\phi = \mathcal{C}_s^4 / \mathcal{K}_s^{14}$. Black dots are simulation results; red dots correspond to the critical value above which the arrest is immediately upon shut-in. The red dashed line is the zero leak-off arrest radius; the green dashed lines are the “early shut-in” arrest radius approximation, and light blue lines the late shut-in solution.

From this series of simulations as well as the limits for arrest obtained in the impermeable ($\mathcal{K}_{s,c} \approx 2.5$) and zero-toughness case ($\mathcal{C}_{s,c} \approx 0.53$), we can delineate in the $(\mathcal{K}_s, \mathcal{C}_s)$ phase space, the regions where post-shut-in growth does or does not occur. Figure 3.8a displays the ratio between the final arrest radius and the shut-in radius, and red dots correspond to the boundary for immediate arrest (estimated numerically following the same threshold of 2.5% then in the limiting zero-toughness and impermeable cases). From these results, we can further provide the following approximation for this boundary for immediate arrest:

$$\begin{aligned} \mathcal{C}_{s,c} &\approx 0.53 & \mathcal{K}_{s,c} &< 0.8 \\ \mathcal{C}_{s,c}(\mathcal{K}_{s,c}) &\approx 0.78 - 0.313 \cdot \mathcal{K}_{s,c} & \text{for } \mathcal{K}_{s,c} &\in [0.8, 2.5]. \end{aligned} \quad (3.26)$$

where the limit of $\mathcal{K}_{s,c} = 2.5$ is retrieved for $\mathcal{C}_s = 0$. Such a boundary is approximate with a resolution of about 3 to 5 percent, accounting for our numerical errors and our sampling of the $(\mathcal{K}_s, \mathcal{C}_s)$ phase space.

Using figure 3.5b the value of $\mathcal{K}_{s,c}$ can be used to get an equivalent value of the fracturing efficiency $\eta_c = \eta_s(\mathcal{K}_{s,c})$. As expected, the critical efficiency tends towards the zero toughness limit of $\eta_c = 0.44$ when $\mathcal{K}_{s,c}$ gets below 0.8. A critical fracturing efficiency of 1 is reached for $\mathcal{K}_{s,c} = 2.5$ which corresponds to the critical shut-in toughness in the impermeable case. The evolution of the critical fracturing efficiency (upon which arrest is immediate at shut-in) as a

Chapter 3. Arrest of a radial hydraulic fracture upon shut-in of the injection

function of $\mathcal{K}_{s,c}$ can be approximated in a piece-wise linear manner as follow:

$$\begin{aligned} \eta_c &\approx 0.44 & \mathcal{K}_{s,c} < 0.8 \\ \eta_c &\approx 0.190 + 0.317 \cdot \mathcal{K}_{s,c} & \text{for } \mathcal{K}_{s,c} \in [0.8, 2.5) \\ \eta_c &= 1.00 & \mathcal{K}_{s,c} = 2.5. \end{aligned} \quad (3.27)$$

Similarly, for the limiting impermeable and zero-toughness cases, we quantify the post-shut-in propagation in terms of propagated distance and time of arrest. Figures 3.9 (a) and (b) display respectively the ratio of the final arrest radius over the shut-in radius and the time of final arrest over the shut-in time. We observe that as the trajectory parameter ϕ / leak-off increases (\mathcal{C}_s increases at constant \mathcal{K}_s), the arrest time and corresponding radius decrease. They depart from the impermeable solution (3.14a) and switch to the early shut-in approximation (3.22) for intermediate values of \mathcal{K}_s . The limit of immediate arrest is clearly visible in those plots: it corresponds to the lowest value of \mathcal{K}_s for which $R_a/R_s = t_a/t_s = 1$ and is highlighted by a red dot for a given ϕ . From figures 3.9 (a) and (b), we can see that the impermeable solution provides a good estimate of the post-injection propagation and time of arrest for values of $\phi \leq 10^{-6}$ for all \mathcal{K}_s . For values of $\phi > 10^{-6}$, the impermeable solution is valid up to a given value of \mathcal{K}_s , which decreases as ϕ increases. For a given ϕ , the zero-toughness estimate is valid in the intermediate range of \mathcal{K}_s , nearly up to $\mathcal{K}_{s,c}(\mathcal{C}_{s,c})$. These plots provide a simple and efficient way to estimate quickly the amount of propagation post-shut-in as a function of \mathcal{K}_s and \mathcal{C}_s ($\phi = \mathcal{C}_s^4 / \mathcal{K}_s^{14}$).

3.6 Discussions

3.6.1 Orders of magnitude for industrial applications

The results of the previous sections are notably applicable to industrial applications related to well stimulation (Economides and Nolte, 2000; Detournay, 2016). Hydraulic fracturing treatments usually consist of a series of injections under a constant rate propagating fluid-driven fractures in a rock formation. These fractures are then filled by a proppant-bearing fluid (keeping the fracture open / propped) to enhance the permeability of such sand- and mudstone reservoirs. We focus on the case of a single-entry treatment where a single hydraulic fracture is propagated. A broad range of fluids have been designed for these treatments, linear or cross-linked gels, as well as slickwater, are commonly used (Barbati et al., 2016; Lecampion and Zia, 2019). To assess the order of magnitude of post-injection propagation, we illustrate our findings with the two examples listed in table 3.2.

We assume two values for the leak-off parameter, $C' = 10^{-6} [\text{m} \cdot \text{s}^{-1/2}]$ and $C' = 10^{-10} [\text{m} \cdot \text{s}^{-1/2}]$ (see discussion in Lecampion et al. (2018) for an estimation of the range of leak-off properties). The large leak-off coefficient is likely to occur in porous sandstones, whereas the small value is more likely for tight mudstones (although the coefficient also depends on the fracturing fluid type). However, we will apply both coefficients to cases (1) and (2) to assess the entire range of

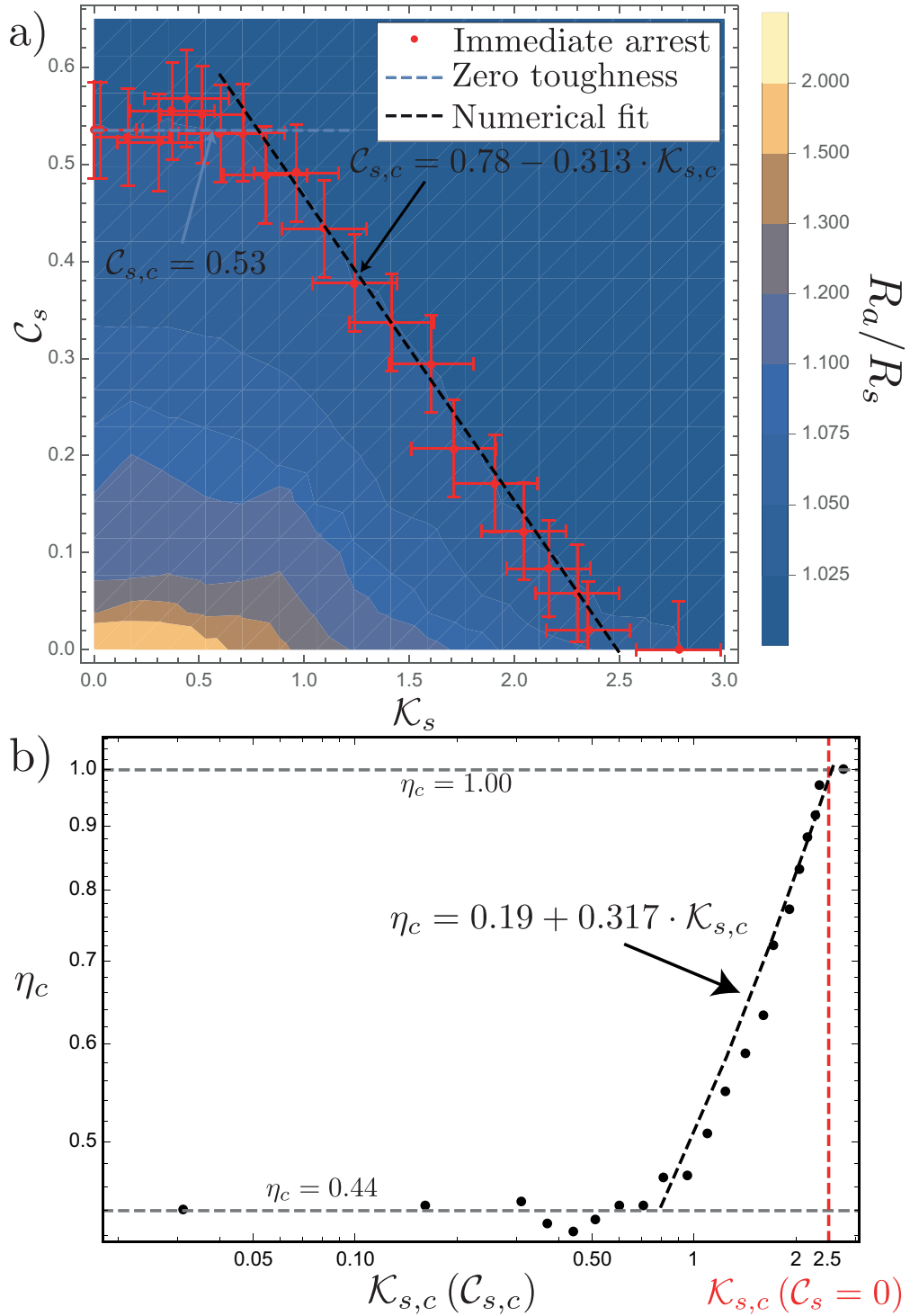


Figure 3.8: a) Contour plot of propagation after shut-in. Red dots are the numerically evaluated values of immediate arrest at shut-in, the light blue dashed line gives the critical dimensionless leak-off coefficient in the zero-toughness case ($\mathcal{C}_{s,c} \approx 0.53 \pm 0.05$) and the black dashed line is a numerical fit for intermediate values. b) Critical fracturing efficiency as a function of the critical dimensionless toughness at shut-in.

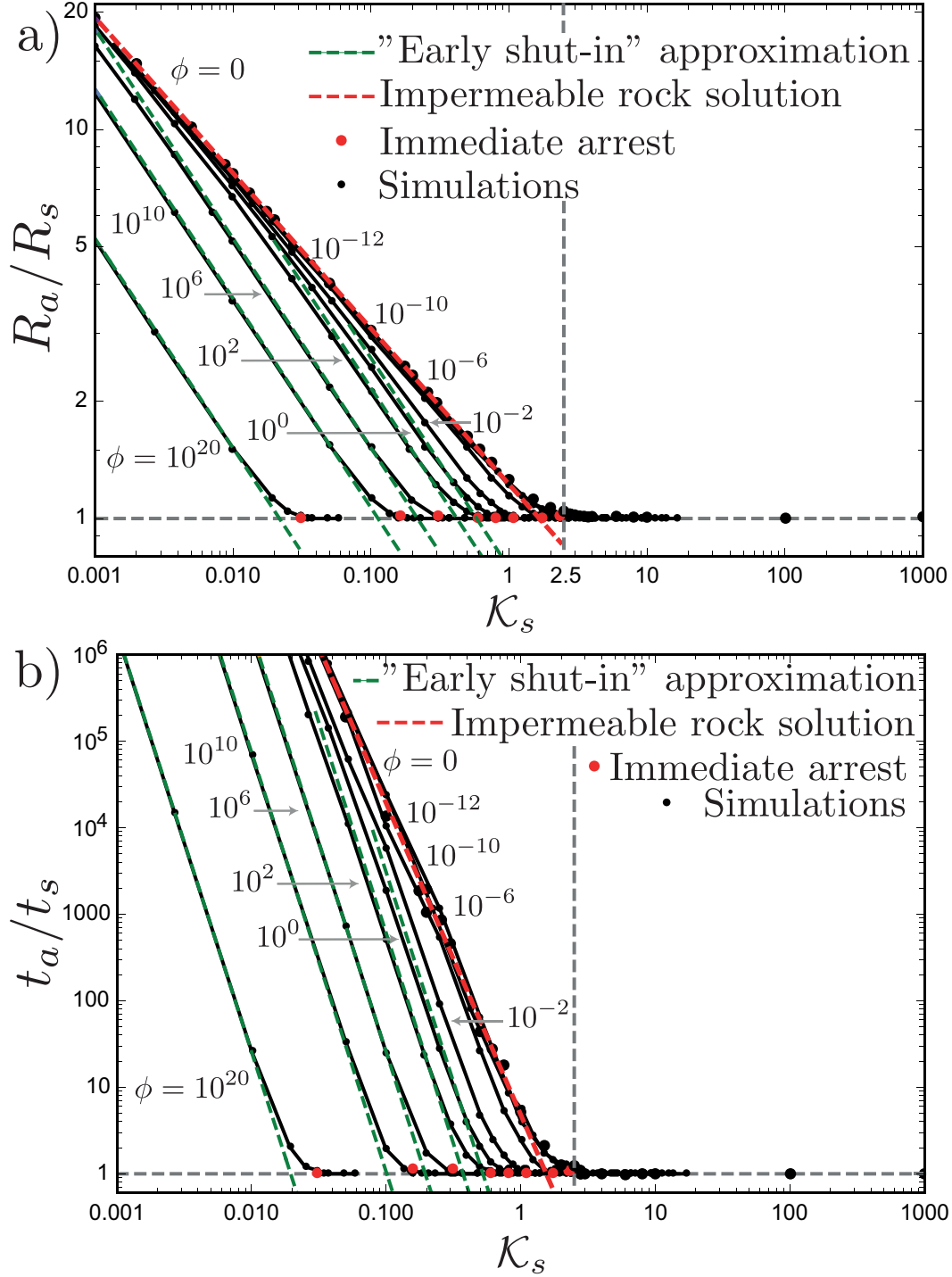


Figure 3.9: Propagation post-shut-in (final arrest radius divided by the radius at shut-in) in the general case as a function of the dimensionless toughness at shut-in \mathcal{K}_s for different values of the trajectory parameter $\phi = \mathcal{C}_s^4 / \mathcal{K}_s^{14}$. The red dashed line corresponds to the impermeable medium case, while the green dashed lines represent the early shut-in leak-off approximation. Red dots indicate the limit of immediate arrest, and black dots are numerical simulations.

| Cases | $\mu[\text{Pa} \cdot \text{s}]$ | $Q_o[\text{m}^3/\text{s}]$ | $t_s[\text{s}]$ | $V_o[\text{m}^3]$ | $E[\text{GPa}]$ | $\nu[-]$ | $K_{Ic}[\text{MPa} \cdot \sqrt{\text{m}}]$ |
|--|---------------------------------|----------------------------|-----------------|-------------------|-----------------|----------|--|
| (1) Gel injection into a sandstone | 5×10^{-3} | 0.05 | 2700 | 135 | 20 | 0.25 | 1.50 |
| (2) Slickwater injection into a mudstone | 1.00 | 0.01 | 2700 | 27 | 30 | 0.25 | 1.0 |

Table 3.2: Characteristic values of industrial HF applications for a so-called single entry treatment (propagation of a single hydraulic fracture).

possible propagation after shut-in.

The four possible combinations (cases (1) and (2) of table 3.2 with the two values of C') result in a large range of trajectory parameters $\phi \in [10^{-25}, 5 \cdot 10^1]$. The value of the dimensionless shut-in toughness in these cases varies within one order of magnitude ($\mathcal{K}_s^{(1)} = 1.44$ and $\mathcal{K}_s^{(2)} = 0.21$) and the dimensionless shut-in leak-off coefficient from $\mathcal{C}_s = 10^{-6}$ to $\mathcal{C}_s = 0.022$. We discuss case (1) combined with the higher leak-off parameter (minimum propagation after shut-in) and case (2) with the low leak-off coefficient (maximum propagation after shut-in). The results of all four combinations are listed in table 3.3.

The slickwater injection into sandstone with a large leak-off coefficient ($C' = 10^{-6}[\text{m} \cdot \text{s}^{-1/2}]$) results in a dimensionless shut-in toughness of $\mathcal{K}_s = 1.44$, a shut-in leak-off parameter of $\mathcal{C}_s = 0.022$ and a trajectory parameter $\phi = 1.5 \cdot 10^{-9}$. Following figure 3.7, we estimate the radius of arrest as approximately $0.95 \cdot R_{k,a} \approx 166[\text{m}]$ (where $R_{k,a}$ is given by equation (3.14a)). We derive the ratio between arrest and shut-in radius from Figure 3.9a as $R_a/R_s \approx 1.10$ corresponding to a propagation after shut-in of about 10%. From figure 3.7, we estimate that $t_a/t_s \approx 2.5$ leading to an elapsed time between shut-in and arrest of about $t_a - t_s \approx 1.5 t_s \approx 4050[\text{s}]$.

For the second case with a small leak-off coefficient ($C' = 10^{-10}[\text{m} \cdot \text{s}^{-1/2}]$), the dimensionless parameters at shut-in are now $\mathcal{K}_s = 0.21$, $\mathcal{C}_s = 1.2 \cdot 10^{-6}$, corresponding to $\phi = 5.5 \cdot 10^{-15}$. This allows us to estimate the arrest radius using equation (3.14a) yielding a value of $R_a = 127[\text{m}]$. It is further possible to estimate the radius at shut-in with the viscous propagation solution of Savitski and Detournay (2002) $R_s = 56[\text{m}]$ giving us a precise estimation of the propagation after shut-in of $R_a/R_s \approx 2.27$. The arrest radius is thus more than twice the radius at shut-in, and growth after shut-in accounts for another 127 % of the growth during the injection ($R_a - R_s \approx 1.27 R_s$). The ratio between the arrest and the shut-in time is substantial and estimated as $t_a/t_s \approx 5.0 \mathcal{K}_s^{-18/5} \approx 1272$, leading to an arrest time of $t_a \approx 3.43 \cdot 10^6[\text{s}] \approx 40[\text{d}]$.

3.6.2 Orders of magnitude for a magmatic pulse release

Natural hydraulic fractures can occur via magmatic intrusion through the lithosphere. We illustrate the impact of the post-injection propagation of a dike assuming a strictly impermeable medium. We neglect buoyant forces for simplicity and assume Newtonian rheology

Chapter 3. Arrest of a radial hydraulic fracture upon shut-in of the injection

| Cases | $\phi[-]$ | $\mathcal{C}_s[-]$ | $\mathcal{K}_s[-]$ | $R_a[\text{m}]$ | $R_s[\text{m}]$ | R_a/R_s | t_a/t_s |
|---|-------------------------|------------------------|--------------------|-----------------|-----------------|----------------|----------------|
| (1) Gel injection into a sandstone with $C' = 10^{-6}[\text{m}\cdot\text{s}^{-1/2}]$ | $\mathcal{O}(10^{-9})$ | 0.022 | 1.44 | ≈ 166 | ≈ 151 | ≈ 1.10 | ≈ 2.5 |
| (1) Gel injection into a sandstone with $C' = 10^{-10}[\text{m}\cdot\text{s}^{-1/2}]$ | $\mathcal{O}(10^{-25})$ | $\mathcal{O}(10^{-6})$ | 1.44 | 175 | ≈ 159 | ≈ 1.10 | ≈ 2.5 |
| (2) Slickwater injection into a mudstone with $C' = 10^{-6}[\text{m}\cdot\text{s}^{-1/2}]$ | 54.7 | 0.012 | 0.21 | ≈ 82 | 56 | ≈ 1.47 | ≈ 50 |
| (2) Slickwater injection into a mudstone with $C' = 10^{-10}[\text{m}\cdot\text{s}^{-1/2}]$ | $\mathcal{O}(10^{-15})$ | $\mathcal{O}(10^{-6})$ | 0.21 | 127 | 56 | 2.27 | ≈ 1272 |

Table 3.3: Resulting dimensionless parameters, arrest, and shut-in radius as well as post-injection propagation and elapsed time between shut-in and arrest.

for the magma. We use the material parameters specified in table 3.4, where we estimate the volume V_0 as a mean volume for dike intrusions at the Piton de la Fournaise volcano on La Réunion between 1998 and 2016 (Froger et al., 2004; Fukushima et al., 2010; Smittarello et al., 2019). Estimation of the injection time is difficult, but measurements of mean magma flow rates and injection durations allow to define a range from 0.1 to 10[m³s⁻¹] (Fukushima et al., 2005, 2010), which allows us to approximate the injection duration. The viscosity of the basaltic magma at Piton de la Fournaise is evaluated by Villeneuve et al. (2008) and expected to range between 300[Pa·s] and 100[Pa·s] at around 1100–1150[°] Celsius (temperature observed by Fukushima et al. (2010)). We use an average value of 200[Pa·s] here. This leads to values of the shut-in toughness of $\mathcal{K}_s^{(3)} \approx 0.044$, and $\mathcal{K}_s^{(4)} \approx 0.16$ allowing to estimate the shut-in radius via the storage/viscosity dominated M -solution (Savitski and Detournay, 2002) and the arrest radius from equation (3.14a). The results are summarised in table 3.5 and indicate a significant propagation after shut-in ranging from 156% to 327% of the shut-in radius. We observe that the propagation time post-shut-in is very long such that cooling of the magma will likely reduce the post-release propagation significantly. Such an effect of cooling could be, at first order, modeled in a similar manner than fluid-leak-off as it is dominated by thermal conduction between the dike and the surrounding rock. Another crucial point is that buoyant forces can not be neglected in this case, such that the fracture will likely deviate from the radial shape and elongate to form a three-dimensional buoyancy-driven dike (Rivalta et al., 2015). The characteristic length scale for buoyancy-driven propagation is given as $L_b = (K'/\Delta\rho g)^{2/3}$ (Lister and Kerr, 1991). Taking an average rock density of $\rho_s = 2900[\text{kg}/\text{m}^3]$ and the density of the basaltic magma at Piton de la Fournaise from (Villeneuve et al., 2008) as $\rho_f \approx 2800[\text{kg}/\text{m}^3]$, the characteristic length scale for buoyant propagation is $L_b \approx 288[\text{m}]$, which is significantly smaller than the arrest radius $R_{k,a} = 4.64[\text{km}]$. This clearly indicates that buoyancy forces are of first-order in that particular case such that, most likely, they take over and elongate the fracture before it reaches the radial arrest radius. The further investigation of

| Cases | $\mu[\text{Pa} \cdot \text{s}]$ | $V_o[\text{m}^3]$ | $Q[\text{m}^3/\text{s}]$ | t_s | $E[\text{GPa}]$ | $\nu[-]$ | $K_{Ic}[\text{MPa} \cdot \sqrt{\text{m}}]$ |
|------------------------------------|---------------------------------|-------------------|--------------------------|------------------------|-----------------|----------|--|
| (3) Short injection with high rate | 200 | $5 \cdot 10^5$ | 10 | $\approx 14[\text{h}]$ | 20 | 0.2 | 1.5 |
| (4) Long injection with low rate | 200 | $5 \cdot 10^5$ | 0.1 | 60[d] | 20 | 0.2 | 1.5 |

Table 3.4: Estimated values for magma injections neglecting buoyant forces.

| Cases | $R_{k,a}[\text{km}]$ | $R_s[\text{km}]$ | R_a/R_s | t_a/t_s |
|------------------------------------|----------------------|------------------|----------------|--------------------------|
| (3) Short injection with high rate | 4.64 | 1.09 | ≈ 4.27 | $\approx 3.8 \cdot 10^6$ |
| (4) Longer injection with low rate | 4.64 | 1.81 | ≈ 2.56 | $\approx 3.8 \cdot 10^3$ |

Table 3.5: Resulting fracture dimensions and propagation post-injection for a magmatic release (not accounting for buoyancy forces).

the conditions for the transition from a radial to a buoyant dike after a given volume release is out of the scope of this contribution, one can nevertheless anticipate that such a transition will be grasped by the ratio between the arrest radius and the buoyancy lengthscale.

3.6.3 Importance of subcritical crack growth

Stable crack propagation can occur even when $K_{I,min} < K_I < K_{Ic}$ (where $K_{I,min}$ is a material-dependent limit below which no growth is observed), albeit at small velocities (Atkinson, 1984, 1987). An empirical relation between fracture velocity dR/dt and the ratio K_I/K_{Ic} is known to reproduce well experimental observations in this sub-critical regime (Charles, 1958a,b)

$$\frac{dR}{dt} = A \left(\frac{K_I}{K_{Ic}} \right)^n \quad (3.28)$$

where A and n are experimentally determined parameters. Subcritical crack growth has been observed in laboratory HF experiments (Lu et al., 2017; Winner et al., 2018) when a constant fluid pressure below the critical value required for toughness-dominated crack growth is applied. We briefly discuss the implications of additional sub-critical growth even after the arrest radius estimated from linear elastic fracture mechanics has been reached. We restrict ourselves to the impermeable case for simplicity. The effect will be maximal for that case as toughness is the sole arresting mechanism.

For a toughness-dominated case, the fluid pressure is spatially uniform in the fracture, fracture width is given by (3.12), the mode I stress intensity factor K_I remains given by (3.13) while the fracture volume is equal to V_o . Replacing the classical LEFM propagation condition $K_I = K_{Ic}$ by the sub-critical crack law (3.28) in this set of equations, one obtains the following differential

Chapter 3. Arrest of a radial hydraulic fracture upon shut-in of the injection

equation for the radius evolution

$$\frac{dR}{dt} = A' \left(\frac{E' V_o}{K_{Ic}} \right)^n R^{-5n/2} \quad (3.29)$$

with $A' = A(3/8\sqrt{\pi})^n$. We are interested in gauging sub-critical crack growth beyond the arrest provided by linear elastic fracture mechanics. We thus use the LEFM radius of arrest given by equation 3.14a as the initial condition to solve (3.29). We obtain the following crack radius evolution

$$R(t - t_{k,a}) = \left(AR_{k,a}^{5n/2} \times \left(1 + \frac{5n}{2} \right) \times (t - t_{k,a}) \right)^{\frac{2}{2+5n}} \quad (3.30)$$

Equation (3.30) is valid when $t - t_{k,a} > 2R_{k,a}/(2A + 5An)$. Assuming common orders of magnitudes for $R_{k,a} = \mathcal{O}(10^1 - 10^3)$ [m], $A = \mathcal{O}(10^3)$ [m/s], and $n = \mathcal{O}(10^1 - 10^2)$ (Lu et al., 2017), this temporal limit is of the order $t - t_{k,a} \geq \mathcal{O}(10^{-4} - 10^{-1})$ [s].

The criterion for complete fracture arrest is reached when K_I drops below the minimum value $K_{I,min}$ which is in the order of $K_{I,min} = K_{Ic}/10$ (Lu et al., 2017). This lower limit allows us to estimate the time when the stress intensity factor drops below $K_{I,min}$ and sub-critical propagation comes to a halt:

$$t_{sc,a} - t_{k,a} = \frac{2R_{k,a} \left(10^{\frac{2}{5}+n} - 1 \right)}{A(2 + 5n)} \quad (3.31)$$

where $t_{sc,a}$ is the arrest time of sub-critical propagation. The radius (3.30) at that time corresponds to the final arresting radius, including sub-critical growth:

$$R_{sc,a} = \left(10^{\frac{2}{5}+n} - 1 \right)^{\frac{2}{2+5n}} R_{k,a} \approx 10^{2/5} R_{k,a} \approx 2.51 R_{k,a} \quad (3.32)$$

For the range of n typical for rocks ($n \in [10, 200]$, Lu et al. (2017)), this subcritical arrest radius is interestingly reduced to a constant amount of the arrest radius $R_{k,a}$. We thus see that sub-critical crack growth adds a significant amount of propagation, about 2.5 times the LEFM arrest radius. Subcritical fracture propagation is thus likely an important mechanism in the impermeable case. It needs to be pointed out that the time during which the fracture grows subcritical is considerable (the minimum arrest time is $\min(t_{sc,a} - t_{k,a}) = \mathcal{O}(10^7)$ [s] for common values of $R_{k,a}$, n and A). The influence of leak-off will decrease the impact of sub-critical crack growth as arrest will likely occur first due to leak-off. The case of an impermeable medium corresponds thus to the maximum upper bound for the post shut-in sub-critical growth. We leave the quantitative details of the competition between a small amount of leak-off and sub-critical crack growth to additional studies.

3.7 Conclusions

We have numerically quantified the propagation of a hydraulic fracture after the end of the injection in an isotropic, homogeneous, elastic medium, driven by a Newtonian fluid under the assumption of Carter leak-off.

For an impermeable medium, the arrest radius R_a corresponds to the solution of a quasi-static crack at equilibrium ($K_I = K_{Ic}$) under a uniform net loading with a volume equal to the injected one. The arrest radius does not depend on any dimensionless number and is independent of the injection history in that case. For a permeable medium, the arrest radius is independent of the injection history only for small values of the dimensionless leak-off coefficient at shut-in $\mathcal{C}_s \lesssim 0.25$ and reduces for increasing values of \mathcal{C}_s . Based on scaling arguments and numerical simulations, we obtain an approximation (3.22) of the arrest radius in the zero-toughness case valid for $\mathcal{C}_s \lesssim 0.25$. The arrest radius for $\mathcal{C}_s > 2.5$ and $\mathcal{K}_s = 0$ (“late shut-in” solution) corresponds to the viscosity/leak-off dominated solution for a constant injection rate (Madyarova, 2003). In the general case of finite toughness and leak-off, the solution of the arrest radius for an impermeable rock is a good estimate for small $\phi = \mathcal{C}_s^4 / \mathcal{K}_s^{14}$ / leak-off, while the “early shut-in” approximation is valid for large ϕ / leak-off. In any case, for $\mathcal{C}_s > 2.5$, the arrest radius follows the “late shut-in” solution.

The arrest is immediate upon shut-in if the dimensionless toughness \mathcal{K}_s at shut-in is larger than a critical value $\mathcal{K}_{s,c} = 2.5$ in the impermeable case. Leak-off reduces the value of this critical dimensionless toughness for immediate arrest. In the zero-toughness case, the arrest is immediate for $\mathcal{C}_s \geq \mathcal{C}_{s,c} \approx 0.53$, where $\mathcal{C}_{s,c}$ is the critical value of a dimensionless coefficient at shut-in. The immediate arrest for finite toughness and leak-off can be approximated as $\mathcal{C}_{s,c} \approx 0.53$ for $\mathcal{K}_{s,c} < 0.8$ and $\mathcal{C}_{s,c}(\mathcal{K}_{s,c}) \approx 0.78 - 0.313 \cdot \mathcal{K}_{s,c}$ for $\mathcal{K}_{s,c} > 0.8$.

When $\mathcal{K}_s < \mathcal{K}_{s,c}$ and $\mathcal{C}_s < \mathcal{C}_{s,c}(\mathcal{K}_{s,c})$, post-injection propagation does occur. For $\phi < 10^{-2}$ and $\mathcal{K}_s < 1$, the ratio between the arrest and shut-in radius is given by $R_a/R_s \approx 1.23 \mathcal{K}_s^{-2/5}$ (equation (3.18)) which corresponds to the impermeable limit. For $\phi > 1$, we still observe $R_a/R_s \approx 1.23 \mathcal{K}_s^{-2/5}$ for small values of \mathcal{K}_s while the early shut-in approximation $R_a/R_s \approx 0.75 \mathcal{K}_s^{-7/13} \phi^{-1/26}$ is valid for intermediate values of \mathcal{K}_s smaller than the critical value given by $\mathcal{K}_{s,c}(\mathcal{C}_{s,c})$. For small values of dimensionless toughness and leak-off coefficient at shut-in ($\mathcal{K}_s \leq 0.1$ and $\mathcal{C}_s < 10^{-2}$), the post-shut-in growth is well captured by an intermediate self-similar viscosity-storage pulse solution. This self-similar solution can be accurately obtained numerically using a collocation method based on Gauss-Chebyshev quadrature and barycentric differentiation and interpolation (see Appendix 3.8.2 for details). The fracture radius evolves as $R(t) \approx \frac{0.836 E^{1/9} V_o^{1/3} t^{1/9}}{\mu^{1/9}}$ in that viscosity-storage pulse regime where the fracture velocity decreases much faster ($\frac{dR}{dt} \propto t^{-8/9}$) than during continuous injection ($\frac{dR}{dt} \propto t^{-5/9}$).

For realistic parameters, fracture propagation after shut-in may be of the same order as the propagation during the injection. Sub-critical crack growth can further extend this post-injection propagation (we provide an upper limit for this mechanism). The time of arrest

Chapter 3. Arrest of a radial hydraulic fracture upon shut-in of the injection

can be orders of magnitude larger than the shut-in time. As shown, post-shut-in growth is very sensitive to the amount of leak-off. It is clear that the estimate obtained here under the assumption of Carter leak-off has to be taken with caution. Indeed, Carter's leak-off is, by essence, pressure independent: it assumes a constant over-pressure in the fracture, resulting in the $1/\sqrt{t}$ behavior. This assumption is clearly questionable at large time after the end of the injection. Accounting for pressure-dependent leak-off (Kanin et al., 2019) would certainly modify the estimation of arrest in large leak-off cases. Similarly, poroelastic effects will promote an earlier arrest due to the back stress associated with the increased pore pressure around the fracture (Detournay and Cheng, 1991). Another factor possibly reducing the fracture extent in industrial applications is the presence of proppant. The fracture may close on the proppant, thus modifying the arrest. We thus see that the estimates we have derived here provide an upper bound for the post-injection growth of hydraulic fractures. The impact of the previously mentioned effects (pressure-dependent leak-off, poroelasticity, proppant) favoring an earlier fracture arrest after the end of the injection remains to be quantified in detail.

3.8 Appendix of the article

3.8.1 Energy budget of a radial hydraulic fracture

We briefly recall the energy budget of a radial hydraulic fracture to highlight the energy split after shut-in. The energy balance for the elastic material under the assumption of linear elastic fracture mechanics and a propagating radial fracture read (Rice, 1968a):

$$2\pi R G_c \frac{dR}{dt} = \int_0^R \frac{1}{2} \left(p(r, t) \frac{\partial w(r, t)}{\partial t} - w(r, t) \frac{\partial p(r, t)}{\partial t} \right) 2\pi r dr \quad (3.33)$$

while the energy budget of the lubrication flow in a radial hydraulic fracture is given by (Lecampion and Detournay, 2007):

$$\int_0^R p(r, t) \frac{\partial w(r, t)}{\partial t} 2\pi r dr + \int_0^R \frac{\mu'}{w(r, t)} V_f^2(r, t) 2\pi r dr + \int_0^R v_L(r, t) p(r, t) 2\pi r dr = Q_o(t) p(0, t). \quad (3.34)$$

where $V_f = q/w$ is the width-average fluid velocity inside the fracture and v_L is the leak off rate $v_L = C'/\sqrt{t-t_o(r)}$. Summing up the two previous equations and integrating in time from the shut-in time t_s to the current time $t \geq t_s$, one obtains the following global energy balance after shut-in (where $Q_o = 0$ and such is the input energy):

$$\underbrace{G_c \pi (R^2(t) - R^2(t_s))}_{\text{creation of new surfaces}} + \underbrace{\int_{t_s}^t \int_0^R \frac{1}{2} \left(p(r, t) \frac{\partial w(r, t)}{\partial t} + w(r, t) \frac{\partial p(r, t)}{\partial t} \right) 2\pi r dr}_{\text{stored elastic energy}} + \underbrace{\int_{t_s}^t \int_0^R \frac{\mu'}{w(r, t)} V_f^2(r, t) 2\pi r dr}_{\text{viscous flow}} + \underbrace{\int_{t_s}^t \int_0^R v_L(r, t) p(r, t) 2\pi r dr}_{\text{leak-off}} = 0. \quad (3.35)$$

We clearly see that the terms associated with viscous flow inside the fracture and leak-off (under the assumption of Carter's leak-off) are always positive. Similarly, the energy spent in the creation of new fracture surfaces is always positive as $R(t) \geq R(t_s)$. On the contrary, after shut-in, the width and pressure decreases: $\partial w(r, t)/\partial t < 0$ and $\partial p(r, t)/\partial t < 0$. The available elastic stored energy term decreases with time, thus ultimately leading to arrest. The fracture arrests when an equilibrium is reached between fracture energy, leak-off, and viscous flow when the available stored energy goes to zero as $\partial w(r, t)/\partial t = \partial p(r, t)/\partial t = 0$.

3.8.2 Viscous pulse solution

The self-similar solution of a viscosity-dominated radial hydraulic fracture after shut-in (after a pulse injection) is solved numerically. Following the techniques described in Liu et al. (2019) and Viesca and Garagash (2018), we combined Gauss-Chebyshev quadrature with Barycentric Lagrange interpolation and differentiation. The problem is thus reduced to a system of non-linear equations that can be solved by root finding. We recall here the most important points

Chapter 3. Arrest of a radial hydraulic fracture upon shut-in of the injection

and refer to Viesca and Garagash (2018) for a detailed description of this spatial discretization method and to Liu et al. (2019) for its application to finite hydraulic fractures under constant injection.

Gauss-Chebyshev quadrature

Gauss-Chebyshev quadrature is a well-known technique for solving elastic boundary integral equations arising in fracture problems (Erdogan et al., 1973). The quadrature uses two sets of nodes, a primary one $\mathbf{s} = \{s_j\}$ with $j = 1, \dots, n$ and a complementary set $\mathbf{z} = \{z_i\}$ with $i = 1, \dots, m$. These nodes discretize the normalized fracture within the interval $(-1, 1)$. The Chebyshev polynomials ($\phi(s)$ and $\psi(z)$) have their roots at these same points. It is due to the density dislocation singularity appearing at the tips, that the choice of the Chebyshev polynomials has been made. It is easy to include the singularity known from linear elastic fracture mechanics (LEFM) within these polynomials by the weight functions. Expressing the singularity with the weight function $\omega(s)$ gives

$$d_s w = \omega(s) F(s), \quad \omega(s) = \frac{1}{\sqrt{1-s^2}} \quad (3.36)$$

where $F(s)$ is an unknown, non-singular function. For such a square-root singularity, as observed in equation (3.36), the corresponding polynomials are the first $\phi_n(s) = T_n(s)$ and second $\psi_m(z) = U_m(z)$ kind of Chebyshev polynomials (with $m = n - 1$). For optimal distribution of nodes, their set is given by (following Viesca and Garagash (2018))

$$s_j = \cos\left(\frac{\pi(j-1/2)}{n}\right), j = 1, \dots, n; \quad z_i = \cos\left(\frac{\pi i}{n}\right), i = 1, \dots, n-1 \quad (3.37)$$

Elasticity for an axisymmetric fracture

The elastic boundary integral equation (3.2) can be inverted to work with the following integral equation relating net pressure and the dislocation density

$$p(x) = \int_0^R G(x, \xi) \frac{\partial w}{\partial \xi} d\xi$$

where the kernel G is obtained from the ring dislocation solution (Hills et al., 1996):

$$G(\xi, \xi') = \begin{cases} \text{sign}(\xi \xi') \left[\frac{1}{\xi - \xi'} \mathbf{E}(k) - \frac{1}{\xi} \mathbf{K}(k) \right], & |\xi'| < |\xi| \\ \frac{1}{\xi - \xi'} \mathbf{E}(1/k), & |\xi'| > |\xi| \end{cases}$$

For an axisymmetric fracture, the kernel is in the leading order of the Cauchy type like for

plane-strain fracture, but it also contains a weaker logarithm singularity. Similarly to Liu et al. (2019), we write it as:

$$G(z, s) = \frac{1}{z-s} + \frac{\ln|z-s|}{2z} + \Delta G(z, s) \quad (3.38)$$

where $\Delta G(z, s)$ corresponds to the non-singular part of $G(z, s)$. To maintain the accuracy of the quadrature in this case, we represent the logarithm term as an integral of the Cauchy-like term, $\ln|z-s| = \int_0^z \frac{dz}{z-s} + \ln s$, where the latter term is inconsequential (it gives zero contribution to the elasticity integral). Using integration on the \mathbf{z} -grid for the logarithm term, the final elasticity matrix for axisymmetric fracture can be written as:

$$\mathbb{G} = \mathbb{H} + \frac{1}{2\mathbf{z}} \mathbb{T} \cdot \mathbb{H} + \Delta \mathbb{G} \quad (3.39)$$

where $\mathbb{T} = \{T_{ij}\}$ is the \mathbf{z} -grid integration matrix and $\Delta \mathbb{G} = \{\frac{1}{n} \Delta G(z_i, s_j)\}$, and \mathbb{H} is the discretized form of the Hilbert transform

$$H_{ij} = \frac{1}{n} \frac{1}{z_i - s_j} \quad (3.40)$$

Discretised form of the set of equations

The dimensionless form of the system of equations for this zero-toughness solution given by equations (3.15b)-(3.15d) can be discretized using a collocation method on the z -points of the chosen Gauss-Chebyshev quadrature. The primary unknowns are the value of F at the n s -points and the dimensionless fracture length $\gamma_{m0}^{[V]}$.

- Using the discretized Hilbert transformation on equation (3.15b), one obtains after integration from z_i to the tip, the following system of $n-1$ equations

$$\frac{1}{9} \mathbf{z} + \frac{1}{4} (\mathbb{S} \cdot \mathbf{F})^2 \mathbb{D} \cdot \mathbb{G} \cdot \mathbf{F} = 0 \quad (3.41)$$

where $\mathbf{z} = (z_1, \dots, z_i, \dots, z_{n-1})$ is the vector of the coordinates of the z -points, and $\mathbf{F} = (F_1, \dots, F_i, \dots, F_n)$ the vector of unknowns value of F at the s -points. \mathbb{D} represents the Barycentric differentiation matrix on the z -grid and \mathbb{S} the integration matrix from z to the fracture tip (see Viesca and Garagash (2018) for details).

- The propagation criterion (zero stress intensity factor) reduces to the following scalar equation

$$\mathbf{Q} \cdot \mathbf{F} = 0 \quad (3.42)$$

where \mathbf{Q} is the Barycentric interpolation vector allowing to obtain the value of F at the fracture tip (and thus the stress intensity factor).

Chapter 3. Arrest of a radial hydraulic fracture upon shut-in of the injection

- The global volume balance (3.15d) becomes after discretization:

$$\mathbb{S}_H \cdot (\mathbf{s}^2 \mathbf{F}) + \frac{1}{\pi (\gamma_{m0}^{[V]})^3} = 0 \quad (3.43)$$

where \mathbb{S}_H is the integration matrix (from 0 to 1).

These $n + 1$ discretized non-linear equations allow solving for the n unknown values of F on the s -grid and the dimensionless fracture length $\gamma_{m0}^{[V]}$.

Results

We use the built-in Newton scheme of Mathematica (version 12) to solve the non-linear system (3.41)-(3.43) using $n = 500$ points. We notably obtain the following value for the dimensionless fracture length: $\gamma_{m0}^{[V]} \approx 0.8360$.

The obtained solution has been verified against the numerical 3D planar HF simulator PyFrac Zia and Lecampion (2019) and the 1D HF simulator developed in Lecampion and Desroches (2015). Figure 3.10 shows the opening (a) and pressure profiles (b) from the numerical simulations compared to the semi-analytical Gauss-Chebyshev solution obtained in 3.8.2. We evaluate the relative difference between the numerical solutions with the Gauss-Chebyshev collocation scheme for the dimensionless radius, dimensionless inlet opening, and net pressure. All these relative differences are reported in table 3.6, for two PyFrac simulations with two different grids (61x61, respectively 121x121, elements for PVP_003, respectively PVP_005) and a simulation (using a grid with 80 elements) with the 1D code of Lecampion and Desroches (2015).

The relative difference of the PyFrac simulation reduces with finer mesh. For the coarse mesh used, the relative difference in fracture radius is at most 3.5 %. We use such a mesh resolution for all the ~ 450 simulations reported in the main text. We use thresholds of 2.5% throughout the paper and then adapt the obtained values to account for the slightly larger uncertainty induced by the numerical error. The 1D numerical results (using a grid with 80 elements) are closer to the one obtained with the Gauss-Chebyshev quadrature, consistent with the fact that the axisymmetric geometry is built-in. The geometrical error on the fracture circular shape is null, like for the Gauss-Chebyshev quadrature, contrary to a planar 3D scheme.

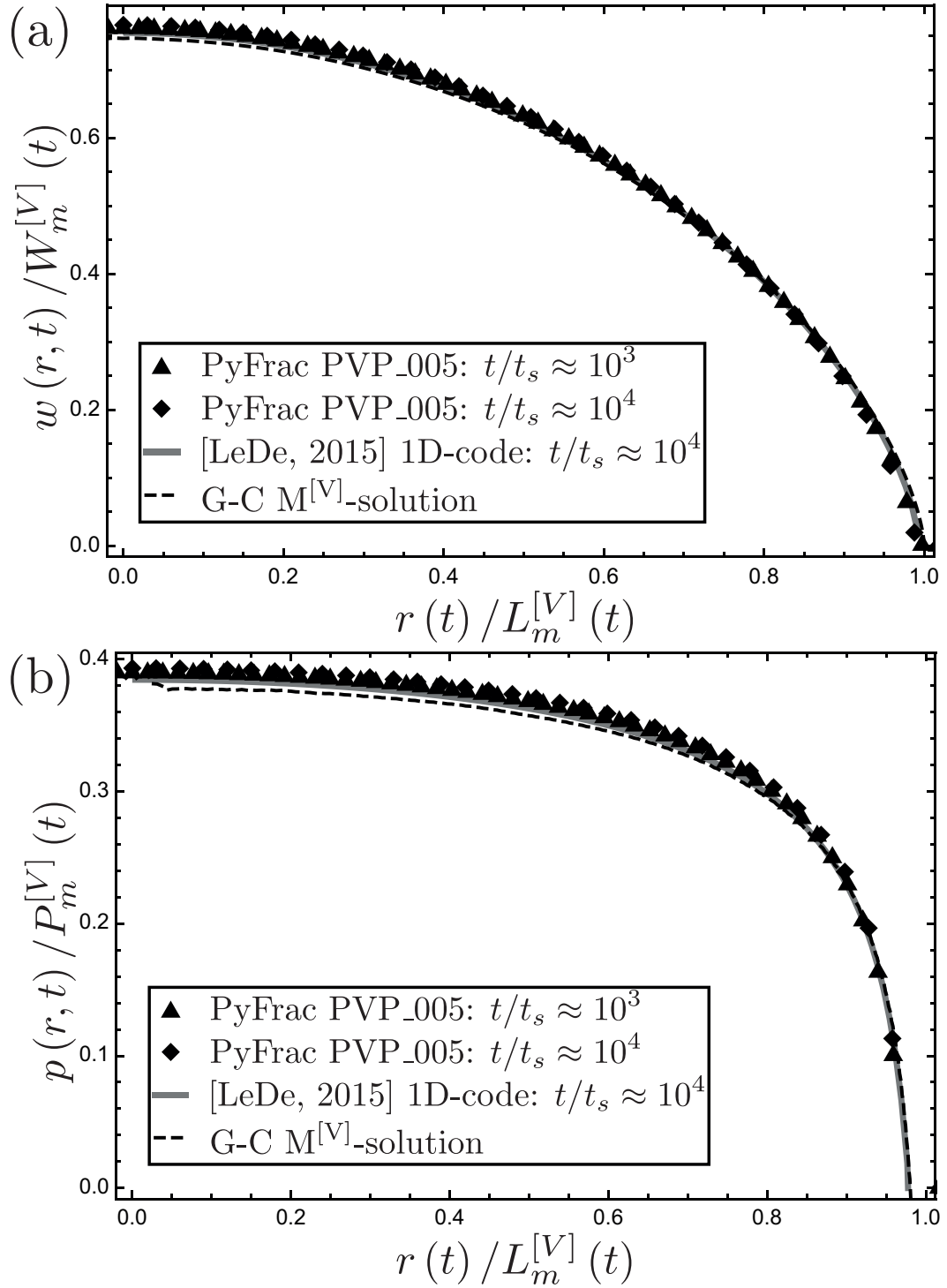


Figure 3.10: Dimensionless opening (a) and dimensionless pressure (b). Black dashed lines correspond to the semi-analytical viscosity solution (i.e. $M^{[V]}$ -solution) obtained by the use of Gauss-Chebyshev polynomials ($n = 500$). Black markers show numerical solutions of simulations with PyFrac, and the grey line is the solution of the 1D planar HF Mathematica code described in Lecampion and Desroches (2015).

| Simulation | t/t_s | \mathcal{E}_p [%] | $L_{2,p}$ [-] | \mathcal{E}_w [%] | $L_{2,w}$ [-] | $L_\infty(p(0, t))$ [%] | $L_\infty(w(0, t))$ [%] | $L_2(R(t)) = L_\infty(R(t))$ [%] |
|--------------|---------|---------------------|---------------|---------------------|---------------|-------------------------|-------------------------|----------------------------------|
| PVP_003 | 10^3 | 5.13 | 2.22 | 2.67 | 2.98 | 3.90 | 4.85 | 2.75 |
| | 10^4 | 6.59 | 2.88 | 3.42 | 11.32 | 5.76 | 6.20 | 3.46 |
| | 10^3 | 2.29 | 1.15 | 1.12 | 1.76 | 3.24 | 2.00 | 1.16 |
| | 10^4 | 3.53 | 1.05 | 1.47 | 1.78 | 0.01 | 2.64 | 1.57 |
| PVP_005 | 10^3 | 1.27 | 1.50 | 0.69 | 2.47 | 1.13 | 1.27 | 0.66 |
| | 10^4 | 1.13 | 1.55 | 0.60 | 2.34 | 1.36 | 1.09 | 0.59 |
| [LeDe, 2015] | | | | | | | | |

Table 3.6: Relative difference between solutions obtained numerically and the results from the self-similar Gauss-Chebyshev collocation scheme. PyFrac simulations (PVP_003 and PVP_005) and a simulation of the code described in Lecampion and Destroches (2015). $\mathcal{E} = \frac{\int_0^1 f_N(\rho) d\rho - \int_0^1 f_{GC}(\rho) d\rho}{\int_0^1 f_{GC}(\rho) d\rho}$ where f_N is an interpolation function of the numerical results and f_{GC} the solution obtained via the Gauss-Chebyshev collocation scheme. The L_2 and L_∞ norms follow their usual definition.

Buoyant Hydraulic Fractures

Part III

4 Three-dimensional buoyant hydraulic fractures: constant release from a point source

This chapter is a modified version of an article published in the Journal of Fluid Mechanics (JFM).

Möri, A. and Lecampion, B. (2022). Three-dimensional buoyant hydraulic fractures: constant release from a point source. *J. Fluid Mech.*, 950, A12, DOI: 10.1017/jfm.2022.800.

Contributions

Andreas Möri has conceptualized the problem, performed a formal and scaling analysis, decided on the methodology, adapted the numerical solver, committed validation against known results, generated the visualizations, and wrote the original draft. Brice Lecampion acted as supervisor, supported the conceptualization and methodology, supervised the formal and scaling analysis, acquired the funding, and reviewed and edited the text in iterations with Andreas Möri.

4.1 Abstract

Hydraulic fractures propagating at depth are subjected to buoyant forces caused by the density contrast between fluid and solid. This paper is concerned with the analysis of the transition from an initially radial towards an elongated buoyant growth – a critical topic for understanding the extent of vertical hydraulic fractures in the upper Earth crust. Using fully coupled numerical simulations and scaling arguments, we show that a single dimensionless number governs buoyant hydraulic fracture growth: the dimensionless viscosity of a radial hydraulic fracture at the time when buoyancy becomes of order one. It quantifies if the transition to buoyancy occurs when the growth of the radial hydraulic fracture is either still in the regime dominated by viscous flow dissipation or is already in the regime where fracture energy dissipation dominates. A family of fracture shapes emerges at late time from finger-like (toughness regime) to inverted elongated cudgel-like (viscous regime). 3D toughness dominated buoyant fractures exhibit a finger-like shape with a constant volume toughness dominated head and a viscous tail having a constant uniform horizontal breadth: There is no further horizontal growth past the onset of buoyancy. However, if the transition to buoyancy occurs while in the viscosity-dominated regime, both vertical and horizontal growths continue to match scaling arguments. As soon as the fracture toughness is not strictly zero, horizontal growth stops when the dimensionless horizontal toughness becomes of order one. The horizontal breadth follows the predicted scaling.

4.2 Introduction

We investigate the propagation of three-dimensional hydraulic fractures emerging from a point source accounting for buoyancy forces. Hydraulic fractures (HF) are tensile fluid-filled fractures propagating under internal fluid pressure which exceeds the minimum compressive in-situ stress of the surrounding media (Detournay, 2016). HFs are encountered in various engineering applications (Smith and Montgomery, 2015; Jeffrey et al., 2013; Germanovich and Murdoch, 2010) but also occur in nature due to fluid over-pressure at depth, for example during the formation of magmatic intrusions (Rivalta et al., 2015; Spence et al., 1987; Lister and Kerr, 1991). The minimum physical ingredients to model HF growth are lubrication flow within the elastically deformable fracture coupled to quasi-static fracture propagation under the assumption of linear elastic fracture mechanics (LEFM) (Detournay, 2016). In the absence of buoyancy, theoretical predictions reproduce well experiments in brittle and impermeable materials (Bunger and Detournay, 2008; Lecampion et al., 2017; Xing et al., 2017).

HFs propagate radially from a point source and remain so in the absence of buoyancy. For such a geometry, the growth is initially dominated by energy dissipation in viscous flow and transitions to a regime dominated by fracture energy dissipation at late time (in association with the increase of the fracture perimeter). Growth solutions in both regimes are well known (Abé et al., 1976; Spence and Sharp, 1985; Savitski and Detournay, 2002). The presence of buoyant forces necessarily elongates the fracture. A large body of work investigated the impact

of buoyant forces on two-dimensional plane strain fractures (Weertman, 1971; Spence and Turcotte, 1990; Spence et al., 1987; Lister, 1990b; Roper and Lister, 2007; Spence and Turcotte, 1985). The early work of Weertman (1971) focused on a toughness-dominated fracture with a linear pressure gradient and did not consider any fluid flow. These considerations lead to a fluid-filled pocket with a stress intensity factor equal to the material resistance at the upper tip, respectively zero at the lower tip of such a bubble crack. A two-dimensional pulse is hence created. Owing to the lack of coupling with lubrication flow, a description of the dynamics of its ascent is missing. A first attempt to include viscous effects was made by Spence et al. (1987) and Spence and Turcotte (1990). Lister (1990b) has obtained solutions as a function of a dimensionless fracture toughness focusing on small fracture toughness / large viscosity cases. These 2D buoyant HF's exhibit a distinct head region close to the propagating edge, where a hydrostatic gradient develops, and a tail region where viscous flow occurs within a conduit of constant width. The solution in the so-called toughness-dominated regime was obtained by Roper and Lister (2007) complementing earlier work (Lister, 1990b; Lister and Kerr, 1991).

A pseudo-three-dimensional solution for viscosity-dominated buoyant fractures was developed by Lister (1990a) in conjunction with a scaling analysis. Assuming a large aspect ratio for the fracture allows for a partial uncoupling of elasticity and lubrication flow. The boundary conditions of his model are such that the fracture has an unprescribed open upper end, such that this approximate solution is deemed to be valid in the near-source region. It predicts an ever-increasing horizontal extent of the fracture, which must be limited in the case of a finite, non-zero fracture toughness. A planar three-dimensional solution has been derived by Garagash and Germanovich (2022) (see also Garagash and Germanovich, 2014; Germanovich et al., 2014) in the limit of large material toughness. This approximate solution is constructed by matching a constant breadth (blade-like) viscosity-dominated tail with a 3D toughness-dominated head under a hydrostatic gradient. This approximate toughness solution shows a propagating head akin to a constant 3D Weertmann pulse (Weertman, 1971), propagating upward due to the linear extension of a fixed breadth in a viscosity-dominated tail. Recently the problem of a finite volume release has been investigated in the limit of zero fluid viscosity numerically by Davis et al. (2020), focusing on the minimal volume required for the start of buoyant propagation. Similar simulations are reported in Salimzadeh et al. (2020), where lubrication flow is included, but only small volume releases are investigated without an extensive study of the late-time growth of buoyant 3D HF.

In this contribution, we investigate the transition of initially radial expansion HF's to the late-time fully three-dimensional buoyant regimes accounting for the complete coupling between elastohydrodynamic lubrication flow and linear elastic fracture mechanics. We notably aim to clarify the domain of validity of previous contributions in the viscosity and toughness dominated limits and to fully understand the solution space of three-dimensional buoyant fractures under constant volume release.

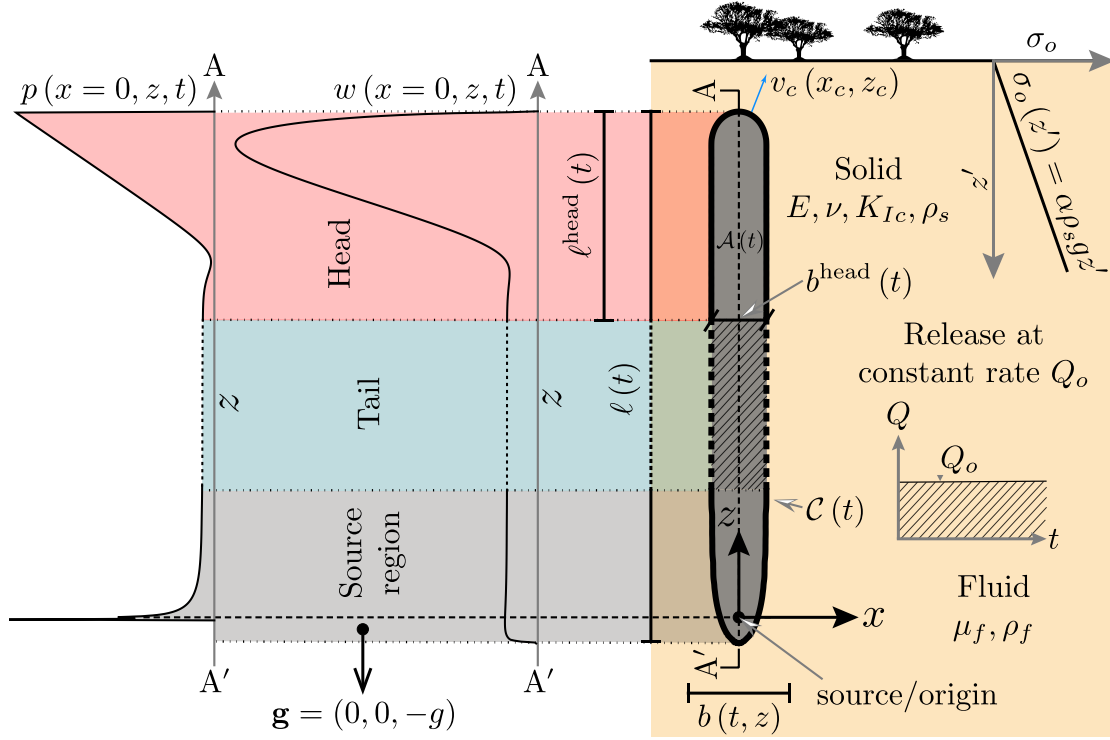


Figure 4.1: Schematic of a buoyancy-driven hydraulic fracture (head → red, tail → green, source region → grey). The tail length is reduced for illustration, indicated by dashed lines and a shaded area. The fracture propagates in the $x|z$ plane with a gravity vector \mathbf{g} oriented in $-z$. The fracture front $\mathcal{C}(t)$, fracture surface $\mathcal{A}(t)$ (dark gray area), opening $w(x, z, t)$, net pressure $p(x, z, t)$, the local normal velocity of the fracture $v_c(x_c, z_c)$ with $(x_c, z_c) \in \mathcal{C}(t)$ characterize fracture growth under a constant release rate Q_o in a medium with a linear confining stress with depth $\sigma_o(z)$. $\ell^{\text{head}}(t)$ and $b^{\text{head}}(t)$ denote the length and breadth of the head, $\ell(t)$ is the total fracture length, and $b(z, t)$ is the local breadth of the fracture.

4.3 Formulation and methods

4.3.1 Mathematical formulation

We consider a pure opening mode (mode I) hydraulic fracture propagating from a point source located at depth in the $x|z$ plane as sketched in figure 4.1. This $x|z$ plane is perpendicular to the minimum in-situ stress $\sigma_o(z)$ (taken positive in compression). We assume that the minimum in-situ stress acts in the y -direction and is thus perpendicular to the gravity vector $\mathbf{g} = (0, 0, -g)$ (with g the earth's gravitational acceleration). Owing to the possibly large fracture dimensions, we account for a linear vertical gradient of the in-situ stress (resulting from the initial solid equilibrium). Assuming a linear elastic medium with uniform properties, the quasi-static balance of momentum for a planar tensile hydraulic fracture reduces to a hyper-singular boundary integral equation over the fracture surface $\mathcal{A}(t)$. This integral equation relates the fracture width $w(x, z, t)$ to the net loading, which is equivalent to the difference

between the fluid pressure inside the fracture $p_f(x, z, t)$ and the minimum compressive in-situ stress $\sigma_o(x, z)$ (Crouch and Starfield, 1983; Hills et al., 1996)

$$p(x, z, t) = p_f(x, z, t) - \sigma_o(x, z) = -\frac{E'}{8\pi} \int_{\mathcal{A}(t)} \frac{w(x', z', t)}{[(x' - x)^2 + (z' - z)^2]^{3/2}} dx' dz' \quad (4.1)$$

where $E' = E/(1 - \nu^2)$ is the plane-strain modulus with E the material Young's modulus and ν its Poisson's ratio. As typically observed in the Earth's crust (Heidbach et al., 2018; Cornet, 2015; Jaeger et al., 2007), the minimum confining stress $\sigma_o(z)$ increases linearly with depth proportional to the solid weight $\gamma_s = \rho_s g$ multiplied by a dimensionless lateral earth pressure coefficient α . Accounting for the downward orientation of the gravitational vector in the chosen coordinate system (see figure 4.1), the vertical gradient for $\sigma_o(z)$ is linear over the entire medium

$$d\sigma_o(z)/dz = -\alpha\rho_s g \rightarrow \nabla\sigma_o = \alpha\rho_s \mathbf{g}. \quad (4.2)$$

Fluid flow within the thin deforming fracture is governed by lubrication theory (Batchelor, 1967). Neglecting any fluid exchange between the rock and the fracture (a reasonable assumption for tight formations and high-viscosity fluids), the width-averaged continuity equation for an incompressible fluid reduces to

$$\frac{\partial w(x, z, t)}{\partial t} + \nabla \cdot (w(x, z, t) \mathbf{v}_f(x, z, t)) = \delta(x)\delta(z)Q_o(t) \quad (4.3)$$

where $\mathbf{v}_f(x, z)$ is the width averaged fluid velocity, and Q_o is the volumetric flow rate at the point source located at the origin $(x, z) = (0, 0)$. Additionally, the assumption of no fluid exchange with the surrounding medium dictates that the total volume of the fracture is equal to the total volume released. Assuming a constant release rate Q_o , the global volume conservation is chiefly:

$$\mathcal{V}(t) = \int_{\mathcal{A}(t)} w(x, z) dx dz = Q_o t. \quad (4.4)$$

Assuming laminar flow and Newtonian rheology, the fluid flux $\mathbf{q}(x, z, t) = w(x, z, t) \mathbf{v}_f(x, z, t)$ reduces to Poiseuille's law accounting for buoyancy forces:

$$\mathbf{q}(x, z, t) = w(x, z, t) \mathbf{v}_f(x, z, t) = -\frac{w(x, z, t)^3}{\mu'} (\nabla p_f(x, z, t) - \rho_f \mathbf{g}) \quad (4.5)$$

where $\mu' = 12\mu_f$ is the equivalent parallel plates fluid viscosity, μ_f is the fluid viscosity, and ρ_f is the fluid density. Introducing the net pressure $p(x, z, t) = p_f(x, z, t) - \sigma_o(z)$ and using equation (4.2), (4.5) is rewritten as

$$\mathbf{q}(x, z, t) = -\frac{w(x, z, t)^3}{\mu'} \left(\nabla p(x, z, t) + \Delta\gamma \frac{\mathbf{g}}{|\mathbf{g}|} \right) \quad (4.6)$$

where $\Delta\gamma = \Delta\rho g = (\alpha\rho_s - \rho_f)g$ is the effective buoyancy contrast of the system. For a value of $\alpha = 1$, it equals the buoyancy contrast between the solid and the fluid. Values of the lateral earth pressure coefficient α different than one have no other influence than affecting the value

Chapter 4. Three-dimensional buoyant hydraulic fractures: constant release from a point source

of the effective buoyancy contrast $\Delta\gamma$ of the system. We consider hydraulic fractures at depth such that the confining stress is assumed to be sufficiently large for the presence of a fluid lag to be negligible (see discussion in Garagash and Detournay (2000); Lecampion and Detournay (2007); Detournay (2016)). In this limit, the boundary conditions at the fracture front reduce to a zero fluid flux normal to the front ($\mathbf{q}(x_c, z_c) = 0$) and zero fracture width ($w(x_c, z_c) = 0$) (see Detournay and Peirce (2014) for a detailed discussion).

Finally, the fracture is assumed to propagate in a quasi-static equilibrium under the assumption of linear elastic fracture mechanics (LEFM). For a pure opening mode fracture, the propagation criterion reduces to

$$(K_I(x_c, z_c) - K_{Ic}) \nu_c(x_c, z_c) = 0 \quad \nu_c(x_c, z_c) \geq 0 \quad K_I(x_c, z_c) \leq K_{Ic} \quad (4.7)$$

for all $(x_c, z_c) \in \mathcal{C}(t)$. In this equation, K_I is the stress intensity factor, K_{Ic} the material fracture toughness, and $\nu_c(x_c, z_c)$ the local fracture velocity normal to the front (see figure 4.1). When the fracture is propagating at a point (x_c, z_c) , the velocity is positive, and the stress intensity factor equals the material toughness ($\nu_c(x_c, z_c) > 0$, $K_I(x_c, z_c) = K_{Ic}$).

4.3.2 Numerical solver

For the numerical solution of the moving boundary problem presented in section 4.3.1, we use the open-source 3D-planar hydraulic fracture solver PyFrac (Zia and Lecampion, 2020). This solver is based on the implicit level set algorithm (ILSA) originally developed by Peirce and Detournay (2008) for three-dimensional planar hydraulic fractures (see also Dontsov and Peirce (2017) for more details). The numerical scheme combines the discretization of a finite domain with the steadily moving plane-strain hydraulic fracture asymptotic solution (Garagash et al., 2011) near the fracture front. Even with a coarse discretization of the finite domain, the coupling between these two scales allows for an accurate estimation of the fracture front velocity $\nu_c(x_c, z_c)$. We use the improvement of Peruzzo et al. (2021), which imposes strict continuity of the fracture front during its reconstruction from the level set values at the cell center. The discretization of the elasticity equation (4.1) is performed using piece-wise constant rectangular displacement discontinuity elements, while an implicit finite volume scheme is used for elastohydrodynamic lubrication flow. In various implementations, this numerical scheme has proved to be both accurate and robust when tested against known hydraulic fracture growth solutions (Peirce, 2015, 2016; Zia et al., 2018; Zia and Lecampion, 2020; Moukhtari et al., 2020).

We use a minimal initial discretization of 61x61 elements and add elements as the fracture elongates for all simulations presented herein. Our simulations must run over several orders of magnitude in time and space to capture the transition and the late-time buoyant propagation stage. We thus adopt two different re-meshing techniques to ensure that the smaller spatial dimension (horizontal in our case) always satisfies a minimum discretization of 61 elements. A second condition of the discretization is that the original element-aspect-ratio is ensured

during the entire simulation, even when the aspect ratio of the mesh domain is changing. This discretization constrains the maximum relative error on the fracture radius to 2 %–3 % for radial fractures, as demonstrated in section 3.8.2 and Zia and Lecampion (2020). The fracture is initialized as a radial hydraulic fracture in the viscosity-dominated regime (Savitski and Detournay, 2002), which corresponds to the early time solution of this type of fracture. We use this technique to ensure that we consistently capture the entire propagation in all the different regimes.

4.3.3 Scaling analysis

In the configuration studied herein, the hydraulic fracture initially propagates radially outwards from a point source. It remains radial as long as the fracture is sufficiently small that buoyancy forces remain negligible. At late time, the fracture elongates in the direction of the buoyant force. A head and tail structure similar to the plane-strain (2D) case is expected to develop. This head-tail structure has either a horizontal breadth stabilizing in space at late times or an ever-growing one (Lister, 1990a; Garagash and Germanovich, 2014). We capture the evolution of the fracture shape by introducing $\ell(t)$ as the vertical extent (to which we will alternatively refer to as the fracture length) and $b(z, t)$ as the horizontal breadth (see figure 4.1). We recognize that the horizontal breadth may not be uniform in space and will thus refer to $b(t)$ as the maximum horizontal breadth of the fracture. We scale these fracture dimensions as

$$\ell(t) = \ell_*(t)\gamma(\mathcal{P}_i), \quad b(t) = b_*(t)\beta(\mathcal{P}_i) \quad (4.8)$$

where $\ell_*(t)$ and $b_*(t)$ are a characteristic fracture length and (maximum) breadth, respectively, and γ , and β the corresponding dimensionless extent. Following the notation of previous contributions (Detournay, 2004), we scale the fracture width and net pressure as

$$w(x, z, t) = w_*(t)\Omega(x/b_*, z/\ell_*, \mathcal{P}_i) \quad p(x, z, t) = p_*(t)\Pi(x/b_*, z/\ell_*, \mathcal{P}_i) \quad (4.9)$$

with $w_*(t)$ and $p_*(t)$ the characteristic width and net pressure scales, Ω and Π are the dimensionless width and pressure. In the previous expressions, we recognized that the characteristic scales may depend on time and that the dimensionless solution is a function of a finite set of dimensionless numbers \mathcal{P}_i .

Introducing such a scaling into the governing equations provides a set of dimensionless groups denoted by \mathcal{G} . In particular, the scaling of the elasticity equation (4.1) provides, besides the characteristic aspect ratio of the fracture

$$\mathcal{G}_s = b_*/\ell_*,$$

Chapter 4. Three-dimensional buoyant hydraulic fractures: constant release from a point source

a dimensionless group defined as the ratio between the characteristic elastic pressure $w_* E' / b^*$ and the characteristic net pressure p_*

$$\mathcal{G}_e = \frac{w_* E'}{p_* b_*}. \quad (4.10)$$

Elasticity is always of first order for a fracture problem (i.e., $\mathcal{G}_e = 1$), such that this equation yields a direct relation between the characteristic net pressure, fracture opening, and a fracture dimension. Scaling wise, the global volume conservation (4.4) provides a ratio between the released volume $Q_o t$ and the characteristic fracture volume $w_* b_* \ell_*$

$$\mathcal{G}_v = \frac{Q_o t}{w_* b_* \ell_*}. \quad (4.11)$$

A dimensionless fracture toughness \mathcal{G}_k emerges from the linear fracture propagation criteria $K_I = K_{Ic}$ as a ratio between the characteristic linear elastic fracture mechanics pressure for the material $K_{Ic} / \sqrt{b_*}$ and the characteristic net pressure p_*

$$\mathcal{G}_k = \frac{K_{Ic}}{p_* \sqrt{b_*}}. \quad (4.12)$$

Poiseuille's viscous drop (4.6) inside the fracture provides a dimensionless group akin to a dimensionless viscosity defined as the ratio between the characteristic viscous pressure $\mu' Q_o / w_*^3$ and the characteristic pressure p_*

$$\mathcal{G}_m = \frac{\mu' Q_o}{w_*^3 p_*}. \quad (4.13)$$

Finally, a last dimensionless group relates the characteristic buoyancy pressure $\Delta \gamma \ell_*$ to the characteristic pressure p_*

$$\mathcal{G}_b = \frac{\Delta \gamma \ell_*}{p_*}. \quad (4.14)$$

Using these dimensionless groups to emphasize the relative importance of the underlying physical mechanism, one obtains different scalings associated with varying regimes of propagation.

4.4 Onset of the buoyant regime

The contribution of buoyant forces is negligible for a small enough fracture: from (4.14), $\mathcal{G}_b \ll 1$. In the absence of buoyancy, the HF propagates with a radial penny-shaped geometry. In an impermeable medium, Savitski and Detournay (2002) have shown that the HF transitions from a viscosity-dominated regime at early time towards a toughness-dominated regime at late time. The increase in fracture energy dissipation is directly related to the increase in the fracture perimeter. Self-similar solutions have been obtained in both the M/viscous scaling and the K/toughness scaling. Following Savitski and Detournay (2002), the characteristic scales are denoted with a subscript m for the M/viscous scaling, and k for the K/toughness scaling (see table 4.3 in appendix 4.10.1). The transition from the early time viscosity-dominated to the toughness-dominated regime is entirely captured by a dimensionless toughness \mathcal{K}_m increasing with time as (Savitski and Detournay, 2002)

$$\mathcal{K}_m = K_{Ic} \frac{t^{1/9}}{E'^{13/18} Q_o^{1/6} \mu'^{5/18}}. \quad (4.15)$$

This dimensionless toughness (defined in the M-scaling) is directly related to a dimensionless viscosity defined in the K-scaling

$$\mathcal{M}_k = \mathcal{K}_m^{-18/5} = (t_{mk}/t)^{2/5}. \quad (4.16)$$

In the absence of buoyancy, the toughness-dominated regime is reached when $\mathcal{K}_m \sim \mathcal{M}_k \sim 1$ (Savitski and Detournay, 2002) (note our use of the fracture toughness K_{Ic} instead of the reduced fracture toughness used in some previous work $K' = \sqrt{32/\pi} K_{Ic}$), or alternatively for times greater than a characteristic time t_{mk} defined as the time when $\mathcal{K}_m = \mathcal{M}_k = 1$

$$t_{mk} = \frac{E'^{13/2} \mu'^{5/2} Q_o^{3/2}}{K_{Ic}^9}. \quad (4.17)$$

The corresponding characteristic fracture radius at this time of transition between viscous and toughness growth is, according to Savitski and Detournay (2002)

$$\ell_{mk} = \frac{E'^3 Q_o \mu'}{K_{Ic}^4}. \quad (4.18)$$

To estimate when the buoyancy forces will start to play a role, still assuming that $b_* \sim \ell_*$, a hypothesis valid at the onset of the buoyant regime, it is worth computing the dimensionless buoyancy \mathcal{G}_b (4.14):

Chapter 4. Three-dimensional buoyant hydraulic fractures: constant release from a point source

$$\mathcal{B}_m = \Delta\gamma \frac{Q_o^{1/3} t^{7/9}}{E'^{5/9} \mu'^{4/9}}, \quad \mathcal{B}_k = \Delta\gamma \frac{E'^{3/5} Q_o^{3/5} t^{3/5}}{K_{Ic}^{8/5}} \quad (4.19)$$

in the viscous (subscript m) and toughness (subscript k) scaling respectively. As expected, the effect of buoyancy increases with time as the fracture grows. For each limiting regime, we deduce a transition time scale where buoyancy becomes dominant as the time when \mathcal{B}_m (respectively \mathcal{B}_k) equals one:

$$t_{m\hat{m}} = \frac{E'^{5/7} \mu'^{4/7}}{\Delta\gamma^{9/7} Q_o^{3/7}}, \quad t_{k\hat{k}} = \frac{K_{Ic}^{8/3}}{E' Q_o \Delta\gamma^{5/3}}. \quad (4.20)$$

In the following, we use a $\hat{\cdot}$ to highlight scalings where buoyancy plays a dominant role. Similar to the previous viscosity to toughness transition, it is practical to obtain the corresponding transition length scales (see table 4.4 in appendix 4.10.1 for details)

$$\ell_{m\hat{m}} = \frac{E'^{3/7} Q_o^{1/7} \mu'^{1/7}}{\Delta\gamma^{4/7}}, \quad \ell_{k\hat{k}} = \frac{K_{Ic}^{2/3}}{\Delta\gamma^{2/3}} \equiv \ell_b. \quad (4.21)$$

It is worth noting that the toughness-buoyancy length scale $\ell_{k\hat{k}}$ - that we will alternatively refer to as ℓ_b - can be directly obtained by assuming $b_* \sim \ell_*$ and balancing the toughness pressure $K_{Ic}/\sqrt{\ell_*}$ with the buoyancy pressure $\Delta\gamma\ell_*$. Such a buoyancy length scale ℓ_b is strictly equal to the one obtained in the 2D plane-strain case (Weertman, 1971; Lister, 1990b; Lister and Kerr, 1991; Roper and Lister, 2007; Heimpel and Olson, 1994) as well as for a finger-like three-dimensional geometry (Garagash and Germanovich, 2014).

The buoyancy effect becomes of order one either when the initially radial hydraulic fracture is still propagating in the viscous (which implies $\mathcal{K}_m(t = t_{m\hat{m}}) < 1$ (4.15)) or when it is already in the toughness-dominated regime (for which $\mathcal{K}_k(t = t_{k\hat{k}}) < 1$ (4.16)). The interplay between the radial transition from viscosity- to toughness-dominated and the one from radial to buoyant can thus be captured by either

$$\mathcal{K}_{\hat{m}} = \mathcal{K}_m(t = t_{m\hat{m}}) = \frac{K_{Ic}}{E'^{9/14} Q_o^{3/14} \Delta\gamma^{1/7} \mu'^{3/14}} = \left(\frac{\ell_{m\hat{m}}}{\ell_{mk}} \right)^{1/4} = \left(\frac{t_{m\hat{m}}}{t_{mk}} \right)^{1/9} \quad (4.22)$$

or

$$\mathcal{K}_{\hat{k}} = \mathcal{K}_k(t = t_{k\hat{k}}) = \mu' \frac{Q_o E'^3 \Delta\gamma^{2/3}}{K_{Ic}^{14/3}} = \frac{\ell_{mk}}{\ell_{k\hat{k}}} = \left(\frac{t_{mk}}{t_{k\hat{k}}} \right)^{2/5}. \quad (4.23)$$

These two dimensionless numbers are related as $\mathcal{K}_{\hat{k}}^{-3/14} = \mathcal{K}_{\hat{m}}$. In fact, the different transition time-scales (4.20), and (4.17) are related as $t_{m\hat{m}}/t_{mk} = (t_{k\hat{k}}/t_{mk})^{27/35}$. The transition to

buoyancy can therefore be grasped by any ratio of these transition time scales, such that only one of the two parameters of equations (4.22) and (4.23) is required to define the transition.

In the following, we choose $\mathcal{M}_{\hat{k}}$ to quantify the transition from a radial to a buoyant hydraulic fracture. Physically, $\mathcal{M}_{\hat{k}}$ quantifies if the fracture is viscosity- ($\mathcal{M}_{\hat{k}} > 1$) or toughness-dominated ($\mathcal{M}_{\hat{k}} < 1$) at the onset of the buoyant regimes. Interestingly, $\mathcal{M}_{\hat{k}}$ is directly the ratio of the characteristic viscous-toughness transition length scale ℓ_{mk} (without buoyancy) with the buoyant toughness transition scale $\ell_b = \ell_{k\hat{k}}$. This confirms that $\mathcal{M}_{\hat{k}}$ (4.23) properly captures the competition between the transition from viscous to toughness growth and the transition to the buoyant regime.

4.5 Toughness-dominated buoyant fractures $\mathcal{M}_{\hat{k}} \ll 1$

We first focus on toughness-dominated buoyant fractures ($\mathcal{M}_{\hat{k}} \ll 1$), for which the transition to the buoyant regime occurs when the initially radial fracture is already propagating in the toughness dominated regime ($t_{k\hat{k}} \gg t_{mk}$). Figures 4.2e-i show the complete fracture evolution for a value of $\mathcal{M}_{\hat{k}} \approx 1.0 \times 10^{-3}$. The fracture is initially radial (figure 4.2e), elongates as buoyancy commences to act (figures 4.2f and g), and ends-up being akin to a finger-like fracture (figures 4.2h and i). It is worth noting that for $t > t_{k\hat{k}}$, the breadth is uniform such that the creation of new fracture surfaces only occurs in the head region. This buoyant fracture exhibits a head-tail structure qualitatively similar to the plane-strain 2D case (Lister, 1990b; Roper and Lister, 2007). The breadth is constant in the tail, and no new fracture surfaces are created in the horizontal direction. This can be clearly observed from figure 4.2 (footprints i-h and the evolution of the breadth). In other words, the head is toughness-dominated, while only a viscous vertical flow dissipates energy in the tail.

4.5.1 Toughness-Dominated Head

The characteristic scales of the toughness-dominated head are such that $b_{\hat{k}}^{\text{head}} \sim \ell_{\hat{k}}^{\text{head}}$ and can be obtained assuming that toughness, buoyancy, and elasticity are all of first-order in the head. One obtains the following head scales:

$$\begin{aligned} b_{\hat{k}}^{\text{head}} = \ell_{\hat{k}}^{\text{head}} = \ell_b &= \frac{K_{Ic}^{2/3}}{\Delta\gamma^{2/3}}, \quad w_{\hat{k}}^{\text{head}} = \frac{K_{Ic}^{4/3}}{E'\Delta\gamma^{1/3}}, \\ p_{\hat{k}}^{\text{head}} &= K_{Ic}^{2/3}\Delta\gamma^{1/3}, \quad V_{\hat{k}}^{\text{head}} = Q_o t_{k\hat{k}} = \frac{K_{Ic}^{8/3}}{E'\Delta\gamma^{5/3}}. \end{aligned} \quad (4.24)$$

which correspond precisely to the characteristic scales for a radial hydraulic fracture at the transition to buoyancy $t = t_{k\hat{k}}$. This scaling is similar (up to numerical factors) to those previously obtained for 3D and 2D buoyant fractures (Lister, 1990b; Roper and Lister, 2007;

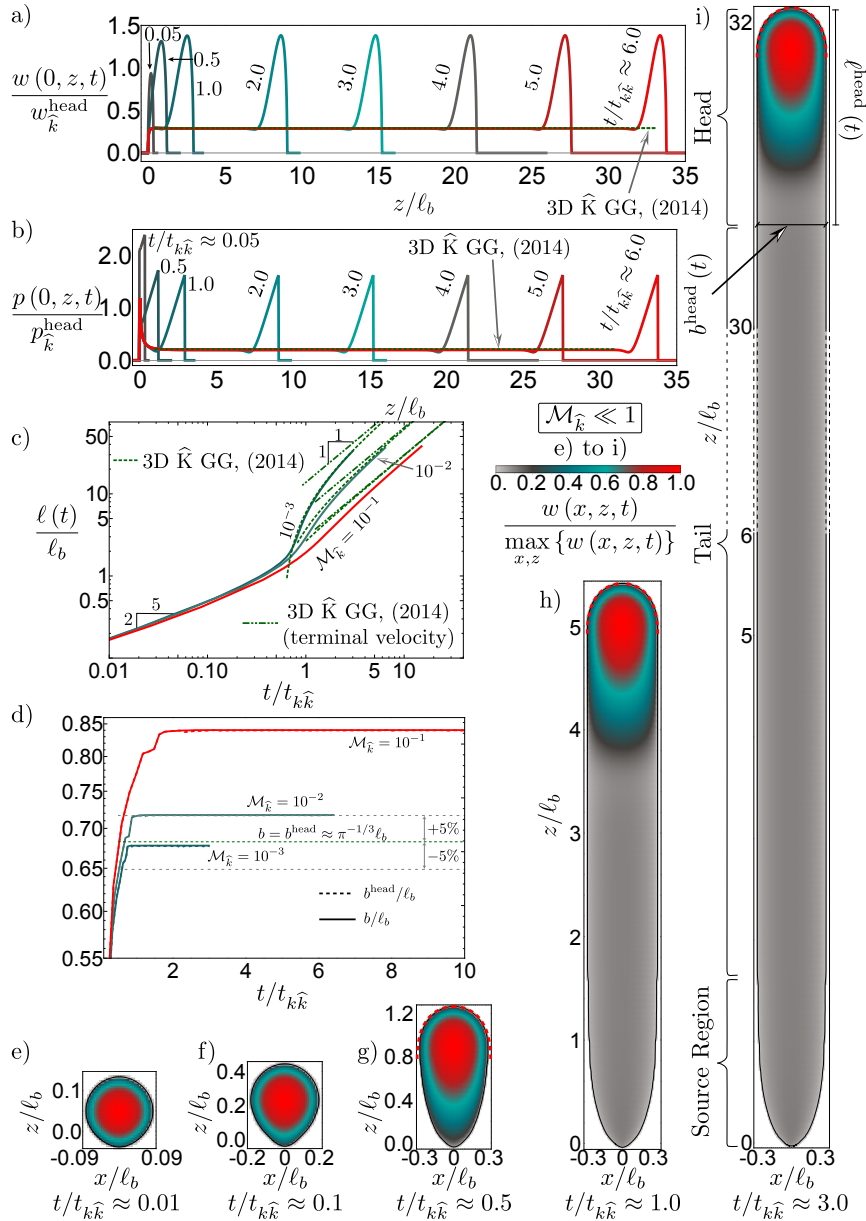


Figure 4.2: Toughness-dominated buoyant fracture. Green dashed lines in all figures indicate the 3D \hat{K} GG, (2014) solution. a) Opening along the centerline $w(0, z, t) / w_k^{\text{head}}$ for a simulation with $\mathcal{M}_{\hat{k}} = 1. \times 10^{-2}$. b) Net pressure along the centerline $p(0, z, t) / p_k^{\text{head}}$ for the same simulation. c) Fracture length $\ell(t) / \ell_b$ for three simulations with large toughness $\mathcal{M}_{\hat{k}} \in [10^{-3}, 10^{-1}]$. Dashed-dotted green lines highlight the late-time linear term of the \hat{K} solution. d) Fracture breadth $b(t) / \ell_b$ (continuous) and head breadth $b^{\text{head}}(t) / \ell_b$ (dashed). Grey lines an error margin of 5%. e - i) Evolution of the fracture footprint from radial (e) towards the final finger-like shape (h and i) for a fracture with $\mathcal{M}_{\hat{k}} = 1. \times 10^{-3}$. For the fracture shape in i), the vertical extent is cropped between $\ell(t) / \ell_b = 6$ and $\ell(t) / \ell_b = 30$. Thick red dashed lines indicate the head shape according to the 3D \hat{K} GG, (2014) solution. Note that the final stage i) has not reached the constant terminal velocity (see inset c).

Garagash and Germanovich, 2022).

4.5.2 Viscosity-Dominated Tail

The tail has a constant breadth equal to the characteristic breadth scale of the head. In the tail, the viscous flow dissipation in the vertical direction is quantified by the ratio of viscous pressure $\mu' v_{z*} \ell_* / w_*^2$ to the characteristic buoyancy pressure $\Delta\gamma \ell_*$ (with $\partial p / \partial z \ll \Delta\gamma$ in the tail):

$$\mathcal{G}_{mz} = \frac{\mu' v_{z*}}{w_*^2 \Delta\gamma}, \quad (4.25)$$

and is clearly dominant over any horizontal viscous dissipation. $\mathcal{G}_{mz} = 1$ sets the characteristic vertical velocity as a function of the characteristic tail opening. The elongated form of this buoyant fracture is such that its aspect ratio is directly related to the ratio of characteristic horizontal v_{x*} to vertical v_{z*} fluid velocities,

$$\frac{b_*}{\ell_*} \sim \frac{v_{x*}}{v_{z*}}. \quad (4.26)$$

and the characteristic vertical fracture velocity is of the same order of magnitude as the vertical fluid velocity:

$$\frac{\partial \ell}{\partial t} \sim \frac{\ell_*}{t} = v_{z*}. \quad (4.27)$$

Assuming a viscosity-dominated tail of constant breadth $b_* = \ell_b$ set by buoyancy ($\mathcal{G}_{mz} = 1$), global volume conservation, elasticity ($\mathcal{G}_v = \mathcal{G}_e = 1$), and equations (4.26)-(4.27) provide the following characteristic tail scales:

$$\begin{aligned} \ell_{\hat{k}} &= \frac{Q_o^{2/3} \Delta\gamma^{7/9} t}{K_{Ic}^{4/9} \mu'^{1/3}} & b_{\hat{k}} &= \ell_b \\ w_{\hat{k}} &= \frac{Q_o^{1/3} \mu'^{1/3}}{K_{Ic}^{2/9} \Delta\gamma^{1/9}} = \mathcal{M}_{\hat{k}}^{1/3} w_{\hat{k}}^{\text{head}} & p_{\hat{k}} &= E' \frac{\Delta\gamma^{5/9} Q_o^{1/3} \mu'^{1/3}}{K_{Ic}^{8/9}} = \mathcal{M}_{\hat{k}}^{1/3} p_{\hat{k}}^{\text{head}} \end{aligned}$$

The corresponding horizontal characteristic fluid velocity decreases in inverse proportion to time as $v_{x*} = \ell_b / t$.

Chapter 4. Three-dimensional buoyant hydraulic fractures: constant release from a point source

| $\mathcal{M}_{\hat{k}}$ | 10^{-3} | | | | 10^{-2} | | | | 10^{-1} | | | |
|--|-----------|------|------|------|-----------|------|------|------|-----------|------|------|------|
| $t/t_{k\hat{k}}$ | 1.0 | 2.0 | 2.5 | 3.0 | 1.0 | 2.5 | 5.0 | 6.0 | 1.0 | 2.5 | 5.0 | 10.0 |
| $\ell^{\text{head}}(t)/\ell_b$ | 1.85 | 1.84 | 1.85 | 1.84 | 2.07 | 1.92 | 1.92 | 1.92 | 1.66 | 2.06 | 2.07 | 2.07 |
| mismatch with GG (%) | 4.52 | 4.30 | 4.44 | 3.79 | 17.3 | 8.59 | 8.76 | 8.52 | 6.24 | 16.7 | 17.2 | 17.3 |
| $b^{\text{head}}(t)/\ell_b$ | 0.68 | 0.68 | 0.68 | 0.68 | 0.72 | 0.72 | 0.72 | 0.72 | 0.78 | 0.84 | 0.84 | 0.84 |
| mismatch with GG (%) | 0.52 | 0.60 | 0.56 | 0.54 | 5.19 | 5.32 | 5.29 | 5.36 | 13.9 | 23.1 | 23.3 | 23.3 |
| $V^{\text{head}}(t)/V_{\hat{k}}^{\text{head}}$ | 0.76 | 0.76 | 0.76 | 0.76 | 0.91 | 0.90 | 0.90 | 0.90 | 0.96 | 1.35 | 1.35 | 1.35 |
| mismatch with GG (%) | 8.36 | 8.21 | 8.25 | 8.15 | 29.3 | 28.7 | 28.7 | 28.6 | 37.0 | 92.3 | 93.1 | 93.2 |
| $\ell^{\text{tail}}(t)/\ell_b$ | 3.60 | 17.5 | 24.4 | 31.3 | 0.89 | 10.2 | 25.7 | 31.9 | 0.271 | 3.43 | 9.86 | 22.8 |
| mismatch with GG (%) | 12.3 | 2.40 | 1.57 | 1.10 | 54.4 | 11.2 | 6.58 | 5.93 | 69.5 | 36.0 | 22.7 | 17.4 |

Table 4.1: Comparison between characteristic head and tail length, head breadth and head volume for toughness-dominated fractures $\mathcal{M}_{\hat{k}} \in [10^{-3}, 10^{-1}]$ at various dimensionless times $t/t_{k\hat{k}}$. The mismatch is calculated as the relative difference between our numerical results and the approximate 3D \hat{K} GG, (2014) solution (GG in the table).

4.5.3 Large time buoyant regime

The head and tail structure of such a fracture with uniform breadth can be further leveraged to obtain an approximate solution at late time ($t \gg t_{k\hat{k}}$) when assuming a state of plane strain for each horizontal cross-section. Such an approximate 3D solution was obtained by Garagash and Germanovich (2022), imposing a toughness-dominated head and a viscosity-dominated tail (in which $\partial p/\partial z \ll \Delta\gamma$). In that solution, which we will refer to as the 3D \hat{K} GG, (2014) solution, the head is constant, and the extension of the viscous tail governs the upward growth. We compare numerical simulations with this late-time solution (this approximate solution in the scaling used here is recalled in the supplementary material). We perform a series of simulations for $\mathcal{M}_{\hat{k}} = 10^{-3}, 10^{-2}$ and 10^{-1} . A typical evolution of the fracture opening and net pressure along the centreline ($x = 0$) of a buoyant toughness fracture ($\mathcal{M}_{\hat{k}} = 10^{-2}$) is reported in figures 4.2a and b respectively. The time evolution of length and breadth are illustrated in figure 4.2c and d. We can observe that both the fracture length and breadth compare well with the 3D \hat{K} GG, (2014) solution at late time, especially for $\mathcal{M}_{\hat{k}} = 10^{-3}, 10^{-2}$.

We further compare various characteristic quantities from our simulations with the 3D \hat{K} GG, (2014) late time solution of Garagash and Germanovich (2022) in table 4.1. Our numerical evolution of the head length $\ell^{\text{head}}(t)/\ell_b$ shows a marked variability but converges for the cases $\mathcal{M}_{\hat{k}} = 1. \times 10^{-3}$ and $\mathcal{M}_{\hat{k}} = 1. \times 10^{-2}$ to their solution $\ell^{\text{head}}(t)/\ell_b \sim 1.77$ at late time. The explanation for the variability lies within our automatic evaluation of the head length from our numerical results. Before an inflection point forms in the opening along the centreline, we estimate the head length as the maximum distance between the source point and the front. Once an inflection point forms (see figure 4.3a), we use either this inflection point or a local pressure minimum between the opening inflection and the maximum pressure in the head (see figure 4.3b). These changes in criteria are more visible for the less toughness-dominated

simulation $\mathcal{M}_{\hat{k}} = 1. \times 10^{-1}$. Nonetheless, they do not affect the estimation of $\ell^{\text{head}}(t)$ for lower values of $\mathcal{M}_{\hat{k}}$. Overall, the length of the head stabilizes once it is evaluated via the pressure minima. The reason is because Garagash and Germanovich (2022) similarly define the length of the head as the point where the minimum pressure is reached (see figure 4.3). The relative difference of $\sim 4\%$ for the simulation with $\mathcal{M}_{\hat{k}} = 1. \times 10^{-3}$ is within the precision of our post-processing method. The increased mismatch of $\sim 8.5\%$ for $\mathcal{M}_{\hat{k}} = 1. \times 10^{-2}$ is caused by a deviation from the strictly zero viscosity case and the uncertainties of our evaluation method. Finally, the simulation with $\mathcal{M}_{\hat{k}} = 1. \times 10^{-1}$ has a relative difference $\sim 17\%$, which clearly reflects a significant deviation from the approximate 3D $\hat{\text{K}}\text{GG}$, (2014) solution.

Defining the head breadth $b^{\text{head}} = b(z = z^{\text{head}} = z_{\text{Tip}} - \ell^{\text{head}})$ with $z_{\text{Tip}} = \max\{z_c\}$ (see figures 4.1 and 4.2i), figure 4.2d shows that the maximum breadth $b(t)$ (continuous lines) is equivalent to the head breadth b^{head} (dashed lines) for $\mathcal{M}_{\hat{k}} \leq 1. \times 10^{-2}$. Combining these observations with figures 4.2h and i, we conclude that this breadth corresponds to the stabilized breadth of the finger-like fracture. From figure 4.2d, we observe that the breadth in simulations $\mathcal{M}_{\hat{k}} = 1. \times 10^{-3}$ and $\mathcal{M}_{\hat{k}} = 1. \times 10^{-2}$ is fully established for $t/t_{k\hat{k}} \gtrsim 1$, corresponding to the moment when the head is entirely formed. This is supported by the values displayed in table 4.1 that are stable for the corresponding simulations. We validate the semi-analytical 3D $\hat{\text{K}}\text{GG}$, (2014) solution $b \approx \pi^{-1/3} \ell_b$ (green dotted line in figure 4.2d) within our numerical precision. The mismatch lies below $< 1\%$ for $\mathcal{M}_{\hat{k}} = 1. \times 10^{-3}$, and is around $\sim 5\%$ for $\mathcal{M}_{\hat{k}} = 1. \times 10^{-2}$. For the simulation with $\mathcal{M}_{\hat{k}} = 1. \times 10^{-1}$, the breadth remains stable but shows a relative mismatch of about $\sim 25\%$, indicating the limit of validity of the 3D $\hat{\text{K}}\text{GG}$, (2014) solution.

To ensure that the head is effectively constant in time, we additionally estimate its volume. Generally, our estimated head volumes are larger than the semi-analytical solution: $V^{\text{head}} \approx 0.701 V_{\hat{k}}^{\text{head}}$. This phenomenon is not surprising as we overestimate the head length with the post-processing of our numerical results. We can confirm the emergence of a constant head volume and verify the order of magnitude derived by Garagash and Germanovich (2022) for small values of $\mathcal{M}_{\hat{k}}$ (4.23). In conclusion, our numerical evaluation indicates that the head of a buoyancy-driven hydraulic fracture is constant and that the semi-analytical 3D $\hat{\text{K}}\text{GG}$, (2014) solution of Garagash and Germanovich (2022) is valid as long as $\mathcal{M}_{\hat{k}} \leq 1. \times 10^{-2}$.

It is interesting to compare the fully 3D results reported here with the 2D plane-strain solutions previously reported in the literature (Lister and Kerr, 1991; Lister, 1990b; Roper and Lister, 2007). At late time, assuming that we are far enough from the source region and neglecting any 3D curvature, one can approximate the fracture as semi-infinite propagating at a constant velocity. Such a two-dimensional solution has notably been presented by Roper and Lister (2007) for large toughnesses. Their scaling can be retrieved from ours (4.24) by replacing the two-dimensional injection rate with $Q_{2D} \sim \partial \ell_{\hat{k}} / \partial t w_{\hat{k}}$. We construct a two-dimensional numerical solver for a semi-infinite hydraulic fracture combining a Gauss-Chebyshev quadrature for elasticity and finite difference for lubrication flow similar to the one used in Moukhtari and Lecampion (2018). This 2D solver verifies exactly the large fracture toughness limit of Roper and Lister (2007), and we use it to compare with this contribution hereafter (we report details

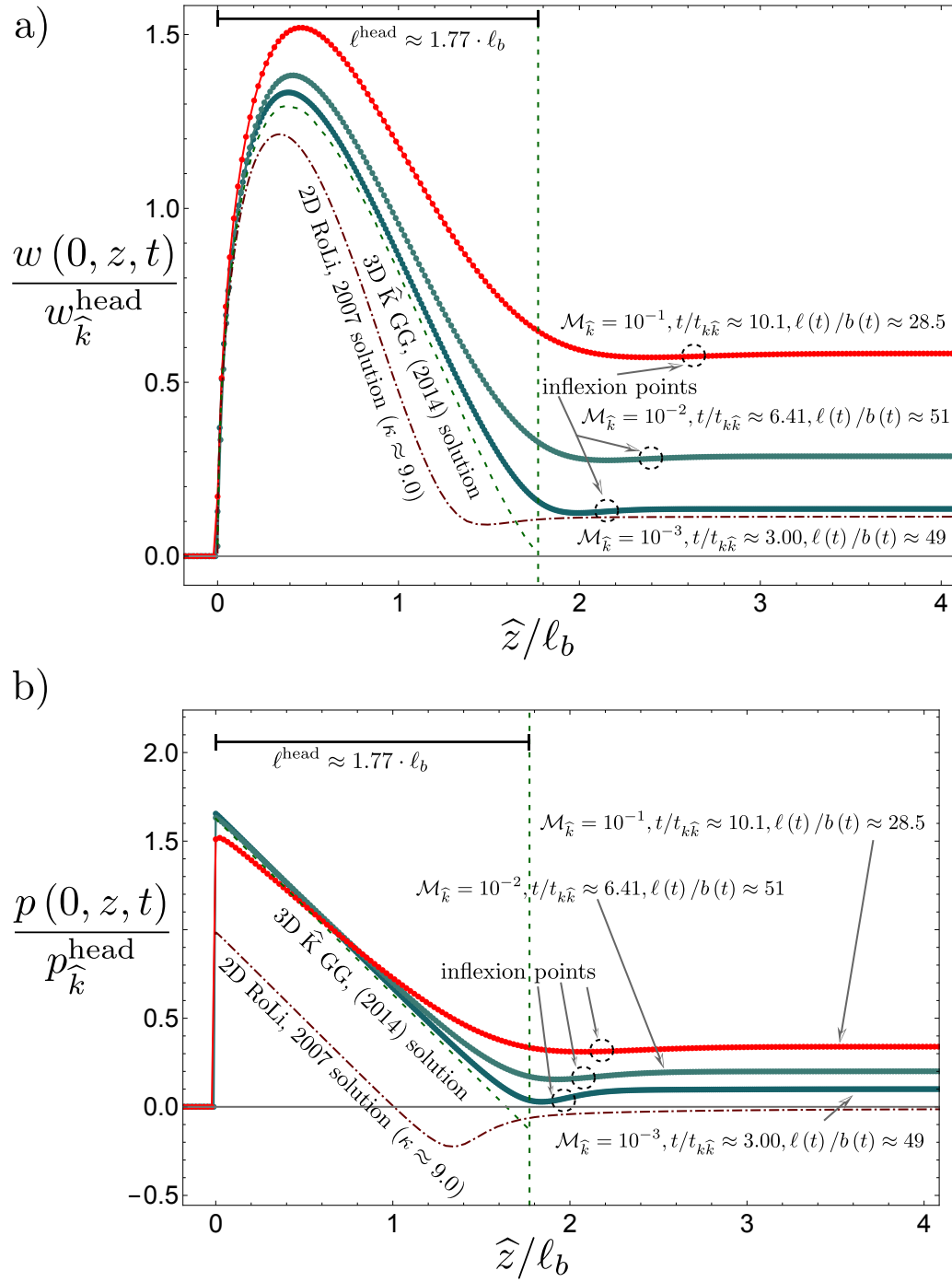


Figure 4.3: Tip-based scaled opening (a) and pressure (b) of three toughness dominated buoyant simulations with $\mathcal{M}_{\hat{k}} \in [10^{-3}, 10^{-1}]$. Continuous lines correspond to the PyFrac simulations (Zia and Lecampion, 2020) with dots indicating the discretization (the number of elements in the head is > 50), dashed lines to a 2D plane-strain steadily moving solution. The vertical green dashed line indicates the head length, and green continuous lines the 3D \hat{K} solutions.

of this 2D solver in the supplementary material).

In figure 4.3, we plot the opening and pressure along the centreline ($x = 0$) as a function of the tip based coordinate $\hat{z}(t) = z_{Tip}(t) - z$, such that $\hat{z}(t) \in [0, \ell(t)]$ marks the interior of the fracture. Even for very small dimensionless viscosities ($\mathcal{M}_{\hat{k}} \ll 1$), the pressure gradient in the head from the 3D numerical simulations is not entirely linear and presents a gentler slope than the limiting 3D \hat{K} GG, (2014) solution (green dashed line (Garagash and Germanovich, 2022)). Only for the simulation with $\mathcal{M}_{\hat{k}} = 1. \times 10^{-3}$ is the viscous flow small enough to allow for a truly linear pressure gradient in the head. The shape of the opening is qualitatively similar between 2D and 3D (see $\mathcal{M}_{\hat{k}} = 1. \times 10^{-3}$), but the 2D ones shrink in the direction of the buoyant force. The difference with the 2D solution is directly related to three-dimensional effects associated with the curvature of the head.

The 3D Garagash and Germanovich (2022) and 2D Roper and Lister (2007) solutions predict a negative net pressure at the end of the head. Our 3D simulations do not show such a feature and exhibit a smaller “neck” than the one described by Roper and Lister (2007) in 2D. The “neck” defines the region at the end of the head, where fracture opening is reduced compared to its stable value in the tail. This location is a pinch point leading to fluid influx from the tail into the head. Nevertheless, figure 4.3 shows that the minimum pressure in the neck decreases with a decreasing $\mathcal{M}_{\hat{k}}$. We expect that a negative net pressure should appear for smaller values of $\mathcal{M}_{\hat{k}}$. These observations directly influence the opening distribution (figure 4.3a). We observe only a limited reduction of the opening between the tail and the head in the fully 3D simulations. Nonetheless, such a neck is present, and an inflection point can be identified (black circles in figure 4.3a). In the limit of zero fluid viscosity, the opening in the tail would become 0. This would be when the neck fully pinches and a finite volume pulse forms.

4.5.4 Transient toward the late buoyant regime

In figure 4.2c, an acceleration phase associated with the transition to buoyancy can be observed. Such an acceleration is directly related to the fact that, when radial, the fracture velocity decreases with time as $\ell_k \propto t^{2/5}$ and ultimately, once in the fully buoyant regime, reaches a constant velocity. The intensity of such acceleration can be directly related to the dimensionless number $\mathcal{M}_{\hat{k}}$ by comparing this terminal velocity with the radial velocity at the onset of buoyancy $t = t_{k\hat{k}}$ (4.20):

$$v_{\hat{k}}/v_k(t_{k\hat{k}}) = \mathcal{M}_{\hat{k}}^{-1/3}. \quad (4.28)$$

The fracture needs to “catch up” from a length $\ell_k(t_{k\hat{k}}) \sim \ell_b$ to the buoyant late time solution ($\ell_{\hat{k}}(t_{k\hat{k}}) \sim \mathcal{M}_{\hat{k}}^{-1/3} \ell_b$) and thus accelerates. According to figure 4.2c, the acceleration starts approximately when $t/t_{k\hat{k}} \approx 0.5$. Correlating this with the observations of figure 4.2a, it corresponds approximately to the time when the bulk of the head starts to leave the source region. The acceleration is thus driven by the pressure difference between the head and tail visible in figure 4.2b. Figure 4.2c further shows that around $t/t_{k\hat{k}} \approx 3$, the fracture starts to decelerate and

Chapter 4. Three-dimensional buoyant hydraulic fractures: constant release from a point source

approaches the complete 3D \hat{K} solution (green dashed lines). The simulation then presents a good match until the end of the simulation (around $t/t_{k\hat{k}} \approx 6.5$). Approximation to the linear, dominant term (green dashed-dotted lines) is only observed once a simulation reaches about $t/t_{k\hat{k}} \approx 10$ (see the simulation with $\mathcal{M}_{\hat{k}} = 1. \times 10^{-1}$ in figure 4.2c). This is consistent with the approximate 3D \hat{K} GG, (2014) solution, which predicts that the linear velocity is reached within 5 % in relative terms when $t/t_{k\hat{k}} \approx 14$ (see supplementary material for details).

In the limiting case of zero fluid viscosity ($\mu' = 0 \rightarrow \mathcal{M}_{\hat{k}} = 0$), the acceleration is infinite, and we can not hope to capture such a sharp transition numerically. The strictly $\mathcal{M}_{\hat{k}} = 0$ limit corresponds to a three-dimensional Weertmans pulse (Weertman, 1971) associated with a zero-width tail. For minimal but non-zero values of $\mu'|\mathcal{M}_{\hat{k}}$, overcoming the transition phase is numerically challenging but possible. Defining the end of the transient via the 5 % deviation level from the 3D approximate solution ($t/t_{k\hat{k}} \approx 14$), we obtain a corresponding fracture length of $\ell(t) \sim 19\mathcal{M}_{\hat{k}}^{-1/3}\ell_b$. Expressing this limit as the aspect ratio $\ell(t)/b(t)$, assuming that the breadth follows the Garagash and Germanovich (2022) solution ($b(t) \approx \pi^{-1/3}\ell_b$), the required aspect ratio is $\ell(t)/b(t) \approx 28\mathcal{M}_{\hat{k}}^{-1/3}$. The numerical example with $\mathcal{M}_{\hat{k}} = 1. \times 10^{-2}$ (largest value of $\mathcal{M}_{\hat{k}}$ validating the 3D \hat{K} solution) leads to a aspect ratio of $\ell(t)/b(t) \sim 132$ with a corresponding fracture length of $\ell(t) \sim 90\ell_b$. Such fracture lengths require a significant number of discretization cells. Numerically, the discretization is mainly bounded by two parameters: the distance of the source point to the fracture front and the number of elements discretizing the head where a strong gradient of opening and pressure takes place. In the toughness-dominated case, the first is more restrictive and requires discretizations of about 44 elements per ℓ_b . The total number of degrees of freedom thus quickly exceeds the current computational capacities of PyFrac (Zia and Lecampion, 2020) and ultimately explains why we do not report simulations for values of $\mathcal{M}_{\hat{k}}$ lower than 1×10^{-3} .

4.6 Viscosity-dominated buoyant fractures $\mathcal{M}_{\hat{k}} \gg 1$

We now turn to the viscosity-dominated limit for which the transition to buoyancy occurs before the transition to the radial toughness-dominated regime: $t_{m\hat{m}} \ll t_{mk}$, i.e., $\mathcal{M}_{\hat{k}} \gg 1$. We focus on the limiting case of a strictly zero-fracture toughness ($\mathcal{M}_{\hat{k}} = \infty$), that we will also refer to as the \hat{M} limit (at late time). The evolution of such a fracture can be grasped from the numerical results reported in figures 4.4e-i. Similar to the toughness case (figure 4.2), the fracture is initially radial (figure 4.4e) and elongates (figures 4.4f-i) as soon as buoyancy plays a role ($t \sim t_{m\hat{m}}$). The overall footprint is strikingly different from the toughness limit. Notably, the fracture breadth is not uniform along the vertical direction and continuously grows horizontally due to the lack of any resistance to fracture. The shape of the fracture at late time is akin to an inverted cudgel with distinct source and head regions.

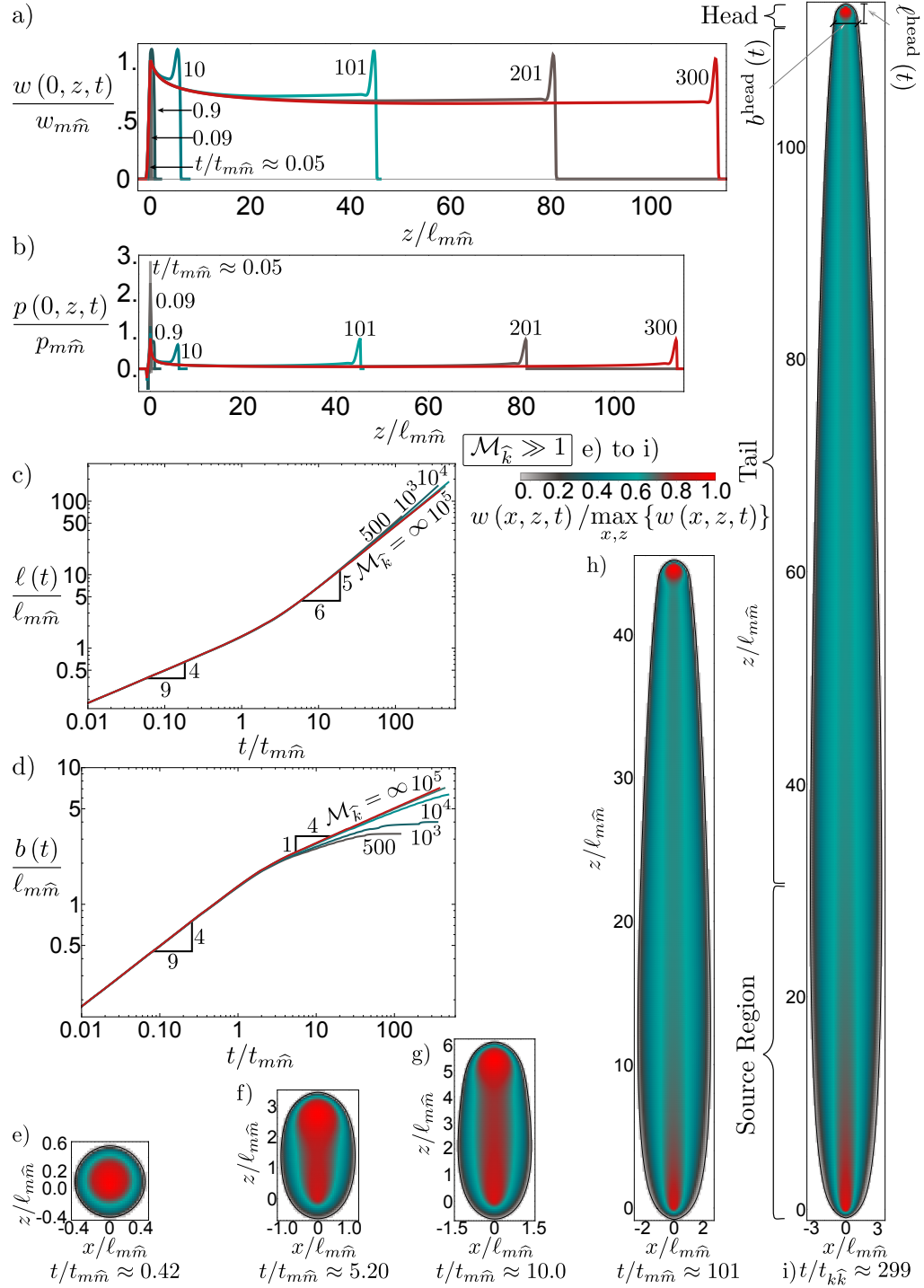


Figure 4.4: Viscosity-dominated buoyant fracture. a) Opening along the centreline $w(x=0, z, t) / w_{m\hat{m}}$ for a simulation with $\mathcal{M}_k = \infty$. b) Net pressure along the centreline $p(x=0, z, t) / p_{m\hat{m}}$ for the same simulation. c) Fracture length $\ell(t) / \ell_{m\hat{m}}$ for six simulations with large viscosity $\mathcal{M}_k \in [5 \times 10^2, \infty]$. d) Fracture breadth $b(t) / \ell_{m\hat{m}}$ for the same simulations. e - i) Evolution of the fracture footprint from radial (e) towards the final elongated inverse cudgel shape (h and i) for the same simulation as in a and b.

4.6.1 Late-time zero-toughness limit

It is enlightening to compare this simulation for $\mathcal{M}_{\hat{k}} = \infty$ with the scaling originally derived by Lister (1990a) for this problem (and his near-source solution). We first recall briefly the argument of such scaling. Contrary to the toughness limit, the breadth is not constant, but the aspect ratio of the fracture remains related to the ratio of the characteristic horizontal v_{x*} to vertical v_{z*} fluid velocities

$$\frac{b_*}{\ell_*} \sim \frac{v_{x*}}{v_{z*}}. \quad (4.29)$$

The horizontal and vertical extent are linked to their corresponding velocities as $b_* = v_{x*} t$, $\ell_* = v_{z*} t$. Viscous fluid dissipation for viscous fractures occurs as much in the vertical as it does in the horizontal direction. Vertically, the net pressure gradient $\partial p / \partial z$ is negligible compared to $\Delta\gamma$ such that, similarly to the viscosity-dominated tail in the \hat{K} limit, the dimensionless ratio

$$\mathcal{G}_{mz} = \frac{\mu' v_{z*}}{w_*^2 \Delta\gamma}, \quad (4.30)$$

is of order one. Horizontally, in the absence of gravitational forces, the magnitude of viscous flow is quantified by the ratio of the horizontal viscous pressure $\mu' v_{x*} b_* / w_*^2$ to the characteristic net pressure p_*

$$\mathcal{G}_{mx} = \frac{\mu' v_{x*} b_*}{w_*^2 p_*} \quad (4.31)$$

which is also of order one. Combined with elasticity ($\mathcal{G}_e = 1$) and global volume balance ($\mathcal{G}_v = 1$), solving for the lengths, width, and pressure scales, we recover the scaling of Lister (1990a):

$$\begin{aligned} \ell_{\hat{m}} &= \frac{\Delta\gamma^{1/2} Q_o^{1/2}}{E^{1/6} \mu^{1/3}} t^{5/6}, & b_{\hat{m}} &= \frac{E^{1/4} Q_o^{1/4}}{\Delta\gamma^{1/4}} t^{1/4}, \\ w_{\hat{m}} &= \frac{Q_o^{1/4} \mu^{1/3}}{\Delta\gamma^{1/4} E^{1/12}} t^{-1/12}, & p_{\hat{m}} &= \frac{E^{2/3} \mu^{1/3}}{t^{1/3}}. \end{aligned} \quad (4.32)$$

Interestingly, in that scaling, the dimensionless toughness ($\mathcal{G}_k \equiv \mathcal{K}_{\hat{m}}$) associated with horizontal growth (defined with b_* as the characteristic fracture length) increases with time. From equation (4.12), we obtain the “horizontal” (subscript x) dimensionless toughness

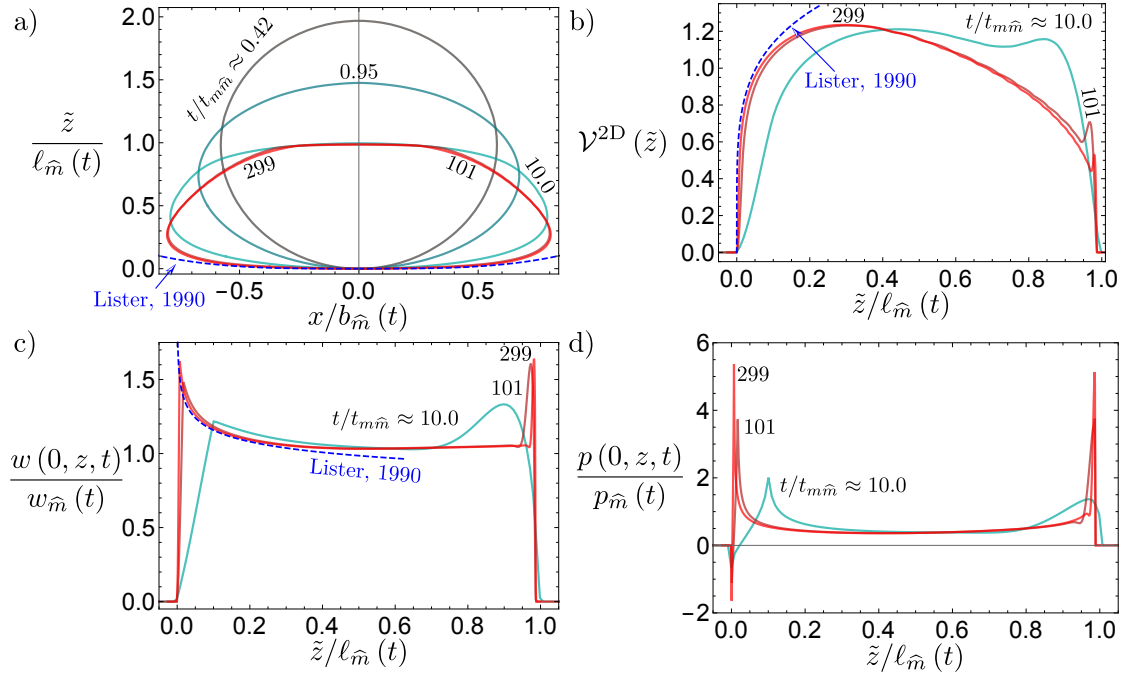


Figure 4.5: Scaled evolution of characteristic values of a buoyancy-driven viscosity-dominated fracture. Fracture footprint (a), cross-sectional volume (integral of the opening over the breadth) (b), opening (c), and pressure (d) at various dimensionless times $t/t_{m\hat{m}}$. Blue dashed lines represent the pseudo-three-dimensional near-source solution of Lister (1990a). A shifted coordinate system \tilde{z} is used such that the lowest point of the fracture marks $\tilde{z} = 0$.

$$\mathcal{K}_{\hat{m},x}(t) = K_{Ic} \frac{\Delta\gamma^{1/8} t^{5/24}}{E^{19/24} Q_0^{1/8} \mu^{1/3}} = \mathcal{M}_{\hat{k}}^{-3/14} \left(\frac{t}{t_{m\hat{m}}} \right)^{5/24}. \quad (4.33)$$

As a result, in the case of finite fracture toughness, one expects the horizontal growth to stop (and thus the breadth to stabilize) when $\mathcal{K}_{\hat{m},x}(t)$ reaches order one.

The time evolution of fracture length and breadth obtained numerically (figures 4.4c and d) exhibit a transition from the radial viscosity regime to this late buoyant viscous scaling. The power-law evolution with time of length and breadth matches equation (4.32) precisely at late time for the $\mathcal{M}_{\hat{k}} = \infty$ simulation. Contrary to the toughness case, where the horizontal growth stops abruptly, we observe a smoother horizontal deceleration accompanied by vertical acceleration, which is less abrupt than in the toughness case.

In this zero toughness limit, at late time, the growth of the fracture is self-similar and will not stop (neither horizontally nor vertically) as long as the volume release continues. To confirm the overall self-similarity of such a viscous, buoyant late-time regime, we rescaled our numerical results at different times and plot scaled footprints, centreline width, and net pressure, as well as the volume of each horizontal cross-section in figure 4.5. The z -axis is shifted such that the lowest point of the fracture coincides with $\tilde{z} = 0$. A nice collapse of the

Chapter 4. Three-dimensional buoyant hydraulic fractures: constant release from a point source

scaled footprint is observed for $t/t_{m\hat{m}} \gtrsim 100$. A similar collapse appears for centreline sections of width, pressure, and cross-section volume. We recognize that the head region shrinks with time and eventually reduces to a boundary layer. Before discussing the head region, we observe that the source region solution derived in Lister (1990a) matches our numerical results, albeit in a relatively narrow zone close to the injection point only. The Lister (1990a) solution is based on a pseudo-three-dimensional approximation assuming only horizontal growth with an unspecified upper “head” part. In this approximate solution, the breadth increases monotonically with the scaled coordinate $z/\ell_{\hat{m}}(t)$ without any possibility of reduction at large $z/\ell_{\hat{m}}(t)$ to model the fracture “head”. For the Lister (1990a) solution, the distance within which this source solution is applicable depends on the material, fluid, and release properties. This distance is equivalent to the transition length scale of a fracture without buoyancy ℓ_{mk} , which for the zero toughness case becomes infinite. This solution, however, appears as the correct inner solution in the near-source region (but not up to $z \sim \ell_{mk}$). Further comparison of the width profiles at different cross-sections between our numerical solution and this approximation is reported in figure 4.6.

Head region

From both the footprints with width contours displayed in figure 4.4 and the scaled profiles in figure 4.5, we observe that, contrary to the toughness case, the head region shrinks with time. Self-similarity of the overall fracture growth becomes evident when the head and the source region volumes are negligible compared to the volume in the tail, i.e., for times greater than $\sim 100 t_{m\hat{m}}$. The following scaling argument can explore the depletion of the head. In a viscous head ($b_*^{\text{head}} \sim \ell_*^{\text{head}}$), the horizontal and vertical fluid velocities are of the same order, elasticity ($\mathcal{G}_e = 1$), buoyancy ($\mathcal{G}_b = 1$), and viscous dissipation dominates ($\mathcal{G}_{mz} = 1$), but its volume is *a priori* unknown. In addition, we assume that the characteristic fluid velocity in the head is given by the vertical characteristic velocity $v_{z\hat{m}} \sim \ell_{\hat{m}}/t$ from equation (4.32). In other words, the volumetric flow rate between the head and the tail is $Q_* = w_*^{\text{head}} b_*^{\text{head}} v_{z\hat{m}}$. Under those assumptions, the corresponding characteristic viscous head scales are:

$$\begin{aligned} \ell_{\hat{m}}^{\text{head}} = b_{\hat{m}}^{\text{head}} &= \frac{E'^{11/24} Q_o^{1/8} \mu'^{1/6}}{\Delta\gamma^{5/8} t^{1/24}}, & w_{\hat{m}}^{\text{head}} &= \frac{Q_o^{1/4} \mu'^{1/3}}{E'^{1/12} \Delta\gamma^{1/4} t^{1/12}}, \\ p_{\hat{m}}^{\text{head}} &= \frac{E'^{11/24} Q_o^{1/8} \mu'^{1/6} \Delta\gamma^{3/8}}{t^{1/24}}, & V_{\hat{m}}^{\text{head}} &= \frac{E'^{5/6} Q_o^{1/2} \mu'^{2/3}}{\Delta\gamma^{3/2} t^{1/6}}. \end{aligned} \quad (4.34)$$

These characteristic scales are consistent with the shrinking/depleting viscous head observed numerically. The numerical validation is presented in table 4.2, where we observe the evolution of the head length, head volume, and the maximum opening in the head. Even though we do not have an analytical or semi-analytical solution to compare to, stabilization, when normalized with the depleting scales 4.34, is observed in table 4.2 within the precision of our automatic evaluation of the head length. It is interesting to note that at the onset of

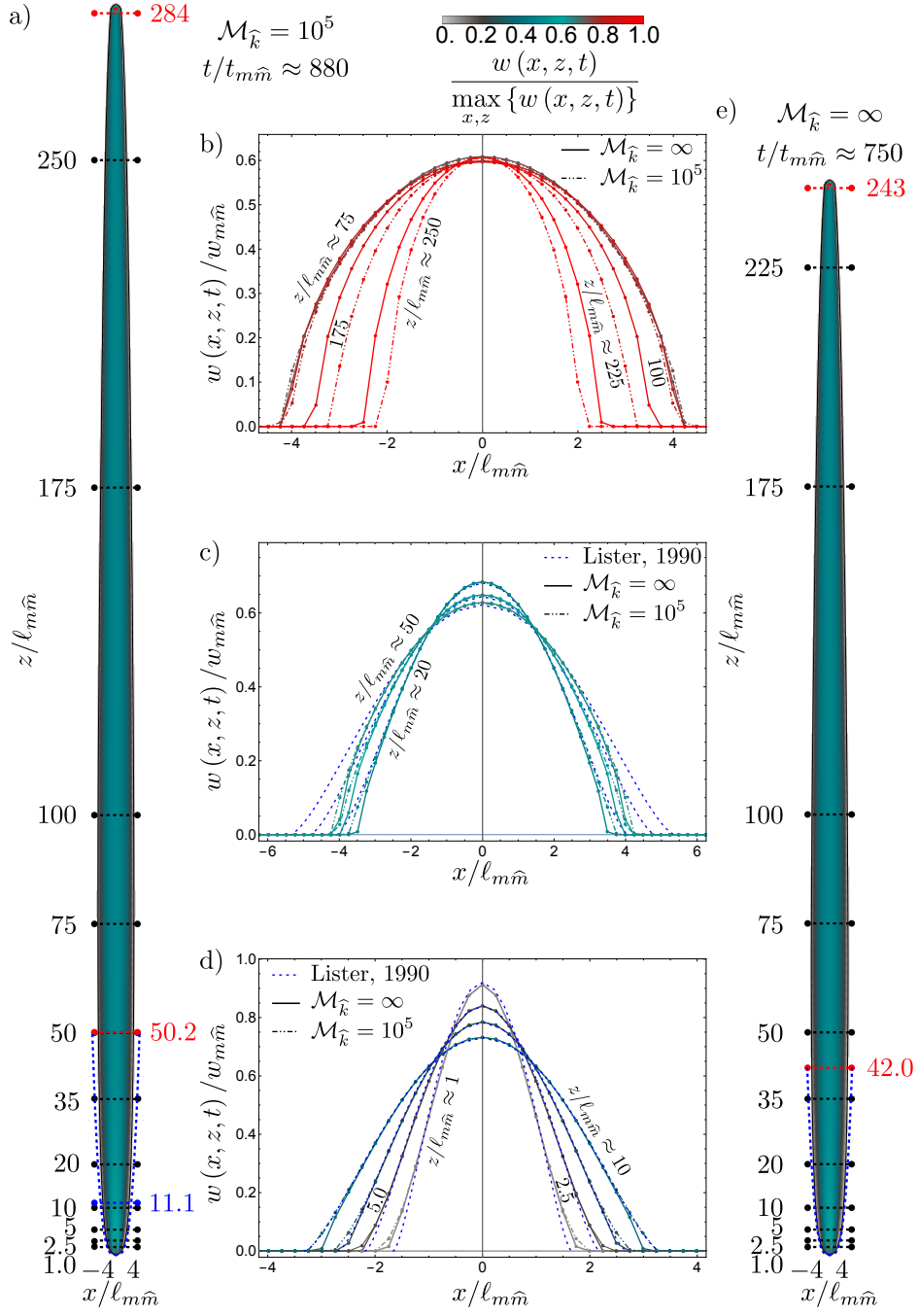


Figure 4.6: Footprint and cross-sectional opening profiles of two buoyant, viscosity-dominated fractures. The color code of the fractures represents the scaled opening as described at the top. Black lines correspond to opening-profile evaluations. The horizontal blue dashed line in a) is the limiting height for the viscous solution of Lister (1990a). Blue dashed lines in a) and e) show the Lister (1990a) solution. Red dashed lines mark the maximum breadth and the beginning of the head. Figures b) to d) show the opening profiles in the cross-section where blue-dashed lines represent the Lister (1990a) solution, dashed-dotted lines correspond to $\mathcal{M}_{\hat{k}} = \infty$ and continuous lines to $\mathcal{M}_{\hat{k}} = 10^5$.

Chapter 4. Three-dimensional buoyant hydraulic fractures: constant release from a point source

| $\mathcal{M}_{\hat{k}}$ | 10^4 | | | | 10^5 | | | | ∞ | | | |
|--|--------|------|------|------|--------|------|------|------|----------|------|------|------|
| $t/t_{m\hat{m}}$ | 10 | 100 | 200 | 350 | 10 | 100 | 200 | 350 | 10 | 50 | 100 | 125 |
| $\ell^{\text{head}}(t)/\ell_{\hat{m}}^{\text{head}}(t)$ | 2.39 | 2.33 | 2.29 | 2.33 | 2.39 | 2.37 | 2.31 | 2.21 | 2.63 | 2.86 | 2.79 | 2.77 |
| $V^{\text{head}}(t)/V_{\hat{m}}^{\text{head}}(t)$ | 4.66 | 5.34 | 5.38 | 5.58 | 4.66 | 5.34 | 5.29 | 5.08 | 5.07 | 5.78 | 5.63 | 5.56 |
| $w_{\text{max}}^{\text{head}}(t)/w_{\hat{m}}^{\text{head}}(t)$ | 1.35 | 1.70 | 1.71 | 1.73 | 1.34 | 1.62 | 1.65 | 1.65 | 1.27 | 1.30 | 1.30 | 1.30 |

Table 4.2: Comparison between characteristic head length, head volume, and maximum opening in the head $\left(w_{\text{max}}^{\text{head}} = \max_{x,z} \{w(x, z \in [z_{\text{tip}} - \ell^{\text{head}}(t), z_{\text{tip}}], t)\}\right)$ for viscosity-dominated fractures $\mathcal{M}_{\hat{k}} \in [1 \times 10^4, \infty[$ at various dimensionless times $t/t_{m\hat{m}}$.

buoyancy, for $t \approx t_{m\hat{m}}$ (defined in equation (4.20)), these scales are strictly equal to the radial viscosity-dominated scales (e.g. $\ell_{\hat{m}}^{\text{head}}(t_{m\hat{m}}) = \ell_m(t_{m\hat{m}})$, $V_{\hat{m}}^{\text{head}}(t_{m\hat{m}}) = Q_o t_{m\hat{m}}$). This confirms the mechanism of a viscous head that detaches from the source region and slowly depletes as it moves upward.

Comparison with the Semi-Infinite Plane-Strain Solution

Such a 3D viscous head can be compared to the existing 2D plane-strain solution for a viscosity-dominated steadily moving buoyant fracture (Lister, 1990b). The 2D scales of Lister (1990b) are based on a constant fracture velocity. For the three-dimensional case, the characteristic fracture velocity $v_{z\hat{m}}$ decreases as

$$v_{z\hat{m}} = \frac{\ell_{\hat{m}}}{t} = \frac{\Delta\gamma^{1/2} Q_o^{1/2}}{E'^{1/6} \mu'^{1/3} t^{1/6}}$$

which can be translated into a two-dimensional release rate reducing in time by multiplication with the characteristic tail opening

$$Q_{2D} \sim v_{z\hat{m}} w_{\hat{m}} \sim \frac{Q_o^{3/4} \Delta\gamma^{1/4}}{E'^{1/4} t^{1/4}}. \quad (4.35)$$

Replacing this injection rate into the scales of Lister (1990b), we retrieve exactly the scaling of equation (4.34). Rescaled 3D numerical results are shown along with the zero-toughness solution of Lister (1990b) using a tip based coordinate system ($\hat{z}(t) = z_{\text{tip}}(t) - z$) in figure 4.7. The 3D and 2D solutions practically coincide (relative error of $\sim 5\%$) for times $t \gtrsim 50 t_{m\hat{m}}$. In the viscosity-dominated case, the shrinking of the head indeed reduces the effect of the 3D curvature at large time (see also the scaled footprint in figure 4.5) and thus renders the elastic state of plane-strain more valid.

In conclusion, the buoyant viscosity-dominated fracture exhibits a viscous source region following the Lister (1990a) solution, combined with a depleting head according to the scaling (4.34) at the propagating edge for late times ($t \gg t_{m\hat{m}}$). The depleting head follows the solution of a 2D semi-infinite plane-strain fracture along the centreline. It may be possible

to construct a complete pseudo-3D approximation matching these asymptotes in the source and head region, a task we leave open for further studies.

4.7 Intermediate/Finite $\mathcal{M}_{\hat{k}}$ cases

In the toughness-dominated case, we have seen that the \hat{K} limit is captured by the Garagash and Germanovich (2022) finger-like solution for $\mathcal{M}_{\hat{k}} \lesssim 1 \times 10^{-2}$. On the other end, for zero-toughness ($\mathcal{M}_{\hat{k}} = \infty$), horizontal growth continues as $\sim t^{1/4}$ at late times ($t \gtrsim 100 t_{m\hat{m}}$). Numerical results for *large* but finite values of $\mathcal{M}_{\hat{k}}$ (see insets c and d in figure 4.4) show that, as anticipated (Lister, 1990a; Garagash and Germanovich, 2022), horizontal growth arrests after some time. The vertical velocity thus increases to a constant terminal velocity due to volume balance. This is confirmed by the $\mathcal{M}_{\hat{k}} = 500, 10^3$ simulations displayed in figures 4.4c and d (and to a lesser extent for $\mathcal{M}_{\hat{k}} = 10^4$ where the horizontal arrest was not completely reached). The characteristic time-scale for such a horizontal arrest can be estimated as the time at which the horizontal dimensionless toughness $\mathcal{K}_{\hat{m},x}$ (4.33) in the viscous tail scaling reaches order one. We obtain

$$\mathcal{K}_{\hat{m},x}(t_{\hat{m}\hat{k}}^x) = 1 \rightarrow t_{\hat{m}\hat{k}}^x = \frac{E'^{19/5} Q_o^{3/5} \mu'^{8/5}}{K_{lc}^{24/5} \Delta\gamma^{3/5}} = \mathcal{M}_{\hat{k}}^{36/35} t_{m\hat{m}} \quad (4.36)$$

and the corresponding maximum breadth and length scales are

$$b_{\hat{m}}(t_{\hat{m}\hat{k}}^x) = \mathcal{M}_{\hat{k}}^{2/5} \ell_b, \quad \ell_{\hat{m}}(t_{\hat{m}\hat{k}}^x) = \ell_{mk}. \quad (4.37)$$

From our previous discussion, the zero-toughness ($\mathcal{M}_{\hat{k}} = \infty$) self-similar growth is established for $t \gtrsim 100 t_{m\hat{m}}$. For large values of $\mathcal{M}_{\hat{k}}$, such a zero toughness solution is thus expected to be realized at intermediate times after the transition to buoyancy but before the characteristic time of horizontal arrest: for $t \in [100 t_{m\hat{m}}, t_{\hat{m}\hat{k}}^x]$. Using (4.36), we thus expect to see a period of lateral growth for dimensionless viscosities at least larger than $\mathcal{M}_{\hat{k}}^{36/35} \sim \mathcal{M}_{\hat{k}} = 100$.

We performed a series of simulations spanning a wide range of values of $\mathcal{M}_{\hat{k}}$ from 10^{-3} to 10^3 for which the simulations were run long enough to observe a cessation of horizontal growth. We report in figure 4.8 the evolution of the maximum breadth of the buoyant fracture with $\mathcal{M}_{\hat{k}}$. As expected, in the toughness-dominated limit $\mathcal{M}_{\hat{k}} < 1$, the fracture breadth remains close to the \hat{K} limit. The maximum breadth then increases with $\mathcal{M}_{\hat{k}}$ from the Garagash and Germanovich (2022) $b \sim \pi^{-1/3} \ell_b$ solution for $\mathcal{M}_{\hat{k}} < 10^{-2}$ up to $b \sim 5 \ell_b$ for $\mathcal{M}_{\hat{k}} = 100$. For values up to $\mathcal{M}_{\hat{k}} \sim 100$, we always observe a uniform breadth along the fracture footprint, and no horizontal growth is observed after the transition to buoyancy. These fractures have a clear finger-like shape. It is worth noting that from their approximate 3D toughness solution Garagash and Germanovich (2022) obtain a lower value $\mathcal{M}_{\hat{k}} \approx 0.92$ as a criterion for no further horizontal growth. Accounting for fully 3D effects, the domain of “finger-like” fracture shapes

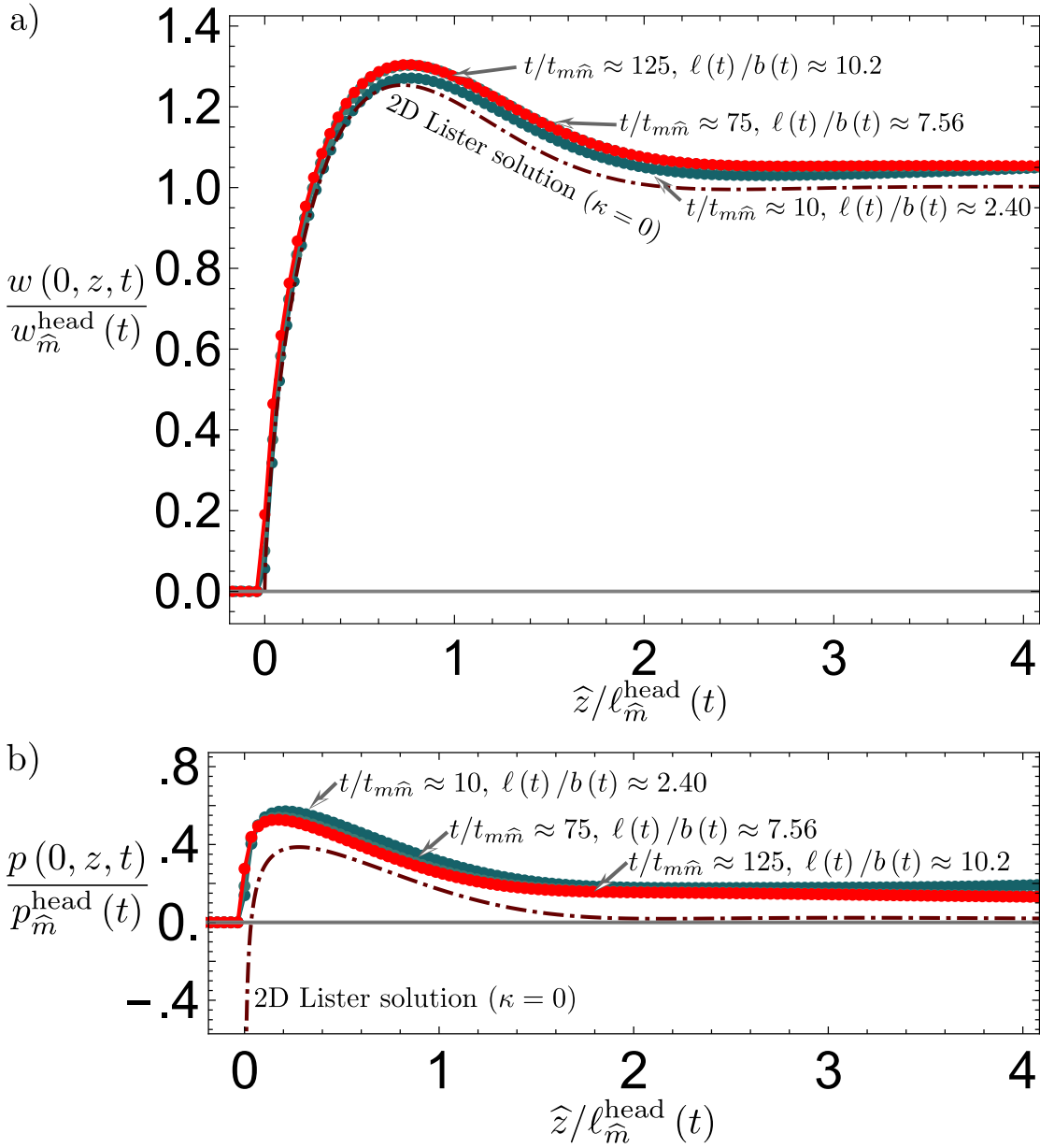


Figure 4.7: Tip-based opening (a) and pressure (b) of a viscosity-dominated buoyant simulation with $\mathcal{M}_{\hat{\kappa}} = \infty$ as a function of the scaled tip coordinate. Continuous lines correspond to the simulations with PyFrac (Zia and Lecampion, 2020) with dots marking the location of discrete evaluations. The dotted-dashed line shows the 2D plane-strain steadily moving solution (see details in the supplementary material).

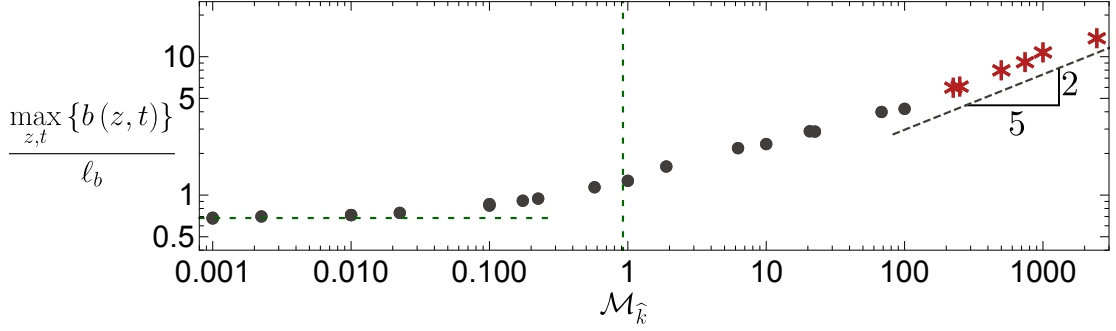


Figure 4.8: Comparison of maximum breadth for buoyant fractures as a function of the dimensionless viscosity $\mathcal{M}_{\hat{k}} \in [10^{-3}, 5 \times 10^3]$. Black dots are used for fractures with a uniform breadth, and red stars otherwise. The dashed green lines represent the limits of the 3D \hat{K} GG, (2014) solution ($b \sim \pi^{-1/3} \ell_b$) for the breadth limit (horizontal line) and $\mathcal{M}_{\hat{k}} \approx 0.92$ for the stabilization criterion (vertical line)). The grey dashed line emphasizes the scaling relation $\max_{z,t} \{b(z,t)\} \sim \mathcal{M}_{\hat{k}}^{2/5} \ell_b$.

is seen to extend up to $\mathcal{M}_{\hat{k}} = 100$.

For values of $\mathcal{M}_{\hat{k}} > 100$, the fractures have a distinctly different late-time shape akin to an inverted cudgel (non-uniform horizontal breadth) with an ultimately fixed maximum horizontal breadth. We recover the predicted evolution of the maximum breadth (4.37) as $\mathcal{M}_{\hat{k}}^{2/5} \ell_b$ (red stars in figure 4.8). A fit of our numerical results actually provides $\max_{z,t} \{b(z,t)\} \approx 0.6858 \mathcal{M}_{\hat{k}}^{2/5} \ell_b$ for $\mathcal{M}_{\hat{k}} \in [10^2 - 2 \times 10^3]$. Using this fitted pre-factor on the breadth evolution, assuming $b \sim b_{\hat{m}}(t)$ before stabilization, we estimate the time for breadth stabilization to be $\sim 0.22 t_{\hat{m}\hat{k}}^x$. We graphically show in figure 4.9 that this estimation agrees fairly well with the numerical results. For the reported simulations, the fracture length ultimately evolves linearly in time (indicated by a 1 to 1 slope in figure 4.9) as $\ell(t) / \ell_{m\hat{m}} \sim \mathcal{M}_{\hat{k}}^{-6/35} (t / t_{m\hat{m}})$.

We also performed simulations for $\mathcal{M}_{\hat{k}} > 10^3$, which did not reach the arrest of horizontal growth within a reasonable computational time limit. It is worth pointing out that from these numerical results, the self-similar viscous ($\mathcal{M}_{\hat{k}} = \infty$) evolution is actually visible at intermediate times only for dimensionless viscosities larger than 10^4 (see figures 4.4c and d).

4.8 Discussion

4.8.1 Orders of magnitude

In nature, buoyant hydraulic fractures are suggested to be a major contributor to magma transport through the lithosphere (Rivalta et al., 2015). For such cases, data collection is difficult and often restricted to the investigation of outcrops from dikes. A broad range of rarely well-constrained parameters are possible. We thus only briefly illustrate the emergence of dikes using the following parameters: $E' \sim 10 \text{ GPa}$, $K_{Ic} \sim 1.5 \text{ MPa} \cdot \text{m}^{1/2}$, $\mu_f = 100 \text{ Pa} \cdot \text{s}$,

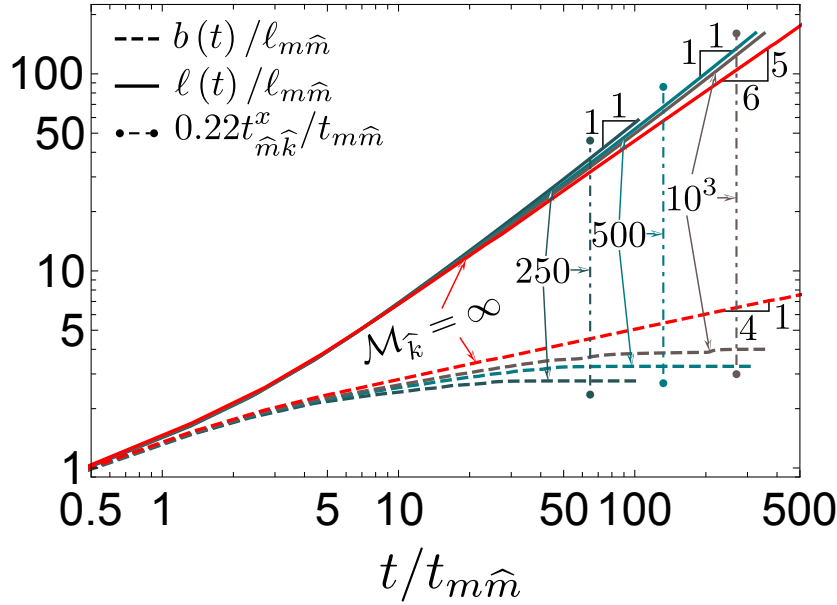


Figure 4.9: Evolution of fracture breadth and length for intermediate fractures without a uniform breadth $\mathcal{M}_{\hat{k}} \in [10^2 - 2 \times 10^3]$ (the simulation with $\mathcal{M}_{\hat{k}} = \infty$ is used as a reference). Dashed lines show fracture breadth, continuous lines fracture height, and horizontal dashed-dotted lines the expected time where lateral growth stops. We indicate the emerging power laws on the figure.

$\Delta\rho \sim 250 \text{ kg} \cdot \text{m}^{-3}$, and a low value of the release rate $Q_o \sim 1 \text{ m}^3 \cdot \text{s}^{-1}$. For this set of parameters, the dike intrusion is strongly viscosity dominated with $\mathcal{M}_{\hat{k}} \approx 3.29 \times 10^6$ and has a maximum lateral extent of tens of kilometers. The use of a higher release rate would linearly increase the value of $\mathcal{M}_{\hat{k}}$ and thus only render the growth more viscosity dominated. The corresponding fracture height easily exceeds the thickness of the lithosphere, as already pointed out by Lister (1990a). As a result, such large extents will necessarily clash with the length scales of stress and material heterogeneities. It also indicates the very strong effect of buoyancy on upward growth.

4.8.2 Comparison with experiments

Various experiments on buoyant fractures have been performed in the laboratory (Heimpel and Olson, 1994; Taisne and Tait, 2009; Rivalta et al., 2005; Taisne et al., 2011; Ito and Martel, 2002). Most of these experiments consist of a finite (not continuous) release and aim at investigating various mechanisms (arrest due to material heterogeneities, among others). In figure 4.10a, we evaluate the evolution of the fracture velocity with time for the experiments performed by Heimpel and Olson (1994). The data in their figure 2 is transformed to correspond to our scaled velocity and time. All experimental parameters except the release rate Q_o are taken from Heimpel and Olson (1994). The good match of figure 4.10a was obtained using an estimate of the release rate of $Q_o \sim 10^{-8} \text{ m}^3 \cdot \text{s}^{-1}$. The corresponding dimensionless

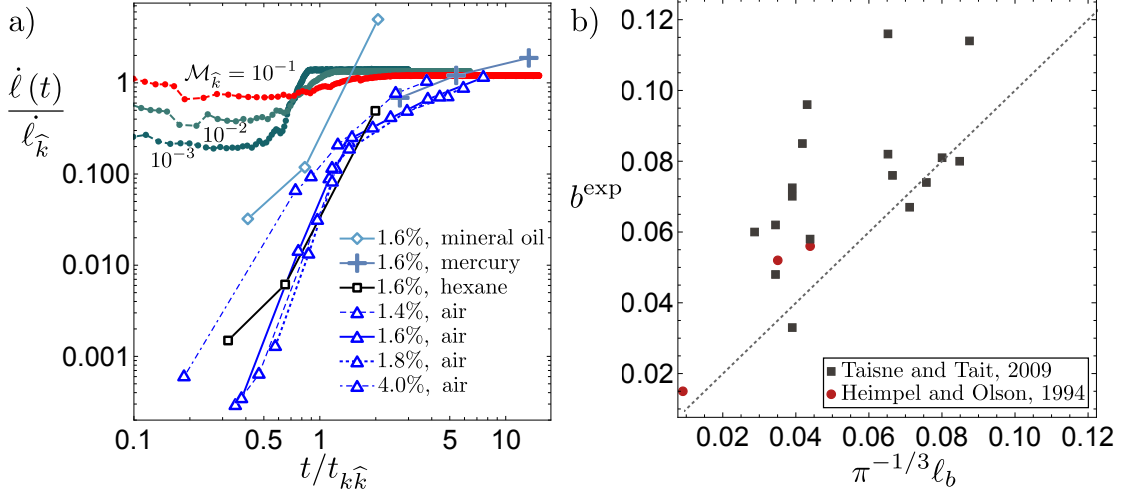


Figure 4.10: a) Comparison of the experiments of Heimpel and Olson (1994) with our simulations. The experiment takes place within the transient, and the initiation already favors the buoyant propagation. b) Comparison of estimated and observed breadth for various experimental studies.

viscosities range between $\mathcal{M}_{\hat{k}} \in [8.8 \times 10^{-8}, 2.3 \times 10^{-3}]$ (see details in supplementary material). When superimposing their velocity evolution with our numerical results for $\mathcal{M}_{\hat{k}} \in [10^{-3}, 10^{-1}]$, we observe that their experiments start in the transition between the radial and buoyant regimes. In other words, their experiments are situated within the accelerating phase, and their velocities tend to stabilize only towards the very end of the experiment. Some experiments show a deceleration but do not quite reach a constant velocity as the time to overcome the transient ($t/t_{k\hat{k}} \approx 14$) is reached in none of the experiments. This is a direct consequence of the limited sample size, which is insufficient in all experiments to reach the end of the transient regime (see details in supplementary material). We thus conclude that these experiments are strongly influenced by their initial conditions (a too-large initial notch) and the finiteness of the specimens, which prevents them from reaching the constant terminal velocity.

As described in section 4.5.4, we can compare the fracture breadth in the transient phase in that range of such low dimensionless viscosities. We could extract information on the fracture breadth from two contributions, albeit with uncertainties on some reported parameters. We assume that for such toughness-dominated buoyant fractures, the \hat{K} solution of Garagash and Germanovich (2022) is also valid in the case of a finite volume release, which allows us to use the data from Taisne and Tait (2009). We report in figure 4.10b the measured breadth b^{exp} and compare it to the limiting 3D \hat{K} GG, (2014) solution of $\pi^{-1/3}\ell_b$. The breadth is generally underestimated for both contributions. In most cases, the extension of the fracture in these experiments clashes with the finite size of the sample, and the initial notch size might be inadequate. These boundary and initiation effects may also modify the linear gradient of the background stress and thus render the evaluation of $\Delta\gamma$ erroneous.

4.8.3 Possibility of approximate solutions

The computational cost of the reported simulations is considerable and tests the limits of the numerical solver used herein (see section 4.3.2 for details). For example, the simulations presented in figures 4.2 and 4.4 took between two to two and a half weeks on a multithreaded Linux desktop system with twelve Intel®Core i7-8700 CPUs and used at most 30 GB of RAM. Such requirements are typical for the simulations presented in this contribution.

Interestingly, our results point to the possible development of reduced-order pseudo-3D models (Adachi and Peirce, 2008; Adachi et al., 2010) that would inevitably be much more computationally efficient. For example, the 3D \hat{K} GG, (2014) solution of Garagash and Germanovich (2022) is based on a finger-like fracture approximation for the tail while keeping a complete description of the elasticity in the head region. We could demonstrate the validity of this assumption as discussed in section 4.5. Employing the knowledge gained from our results, the development of accurate and computationally efficient models similar to the ones presented in Dontsov and Peirce (2015b) may be possible. The solution derived in Lister (1990a) is based on a similar approach for the zero-toughness case. We could show that this approach works fairly well within the source region but fails to capture the transition to the head region, which has not been prescribed in the work of Lister (1990a). The insights gained from our simulations (see section 4.6.1) could be used further to develop an enhanced pseudo-3D model for the viscous case. Such a model could bridge the source-region solution of Lister (1990a) with a viscous head.

4.9 Conclusions

For a homogeneous linear elastic solid subjected to a linear background confining stress and Newtonian fluid, using numerical simulations and scaling analysis, we have shown that under a constant release rate the growth of 3D buoyant fractures is governed by a single dimensionless number $\mathcal{M}_{\hat{k}}$ (4.23). It is worth emphasizing the very large computational cost of the simulations reported here, which span more than ten, respectively, twenty orders of magnitude in space and time. They reach the computational limit of our current implicit level set algorithm implementation. Nonetheless, from this series of simulations, we have shown that a family of buoyant HF emerges at late times as a function of $\mathcal{M}_{\hat{k}}$ (HF = Hydraulic Fractures – see def at the beginning of the paper). The solution phase space can be summarized in the diagram displayed in figure 4.11. At early time, all fractures start with a radial shape and are initially dominated by viscous dissipation (M-vertex), and remain radial for times lower than the buoyancy transition time scales 4.20. Depending on the ratio between the radial viscosity to toughness transition time-scale t_{mk} (without buoyancy) and the viscous buoyancy transition time-scale $t_{m\hat{m}}$ (or $t_{k\hat{k}}$), encapsulated in the definition of the dimensionless viscosity $\mathcal{M}_{\hat{k}}$ (4.23), a family of solutions exists at late time when buoyancy dominates. If the transition to buoyancy occurs when the hydraulic fracture is already in the toughness-dominated regime ($\mathcal{M}_{\hat{k}} \lesssim 10^{-2}$), the late time growth is well captured by the \hat{K} approximate solution of Gara-

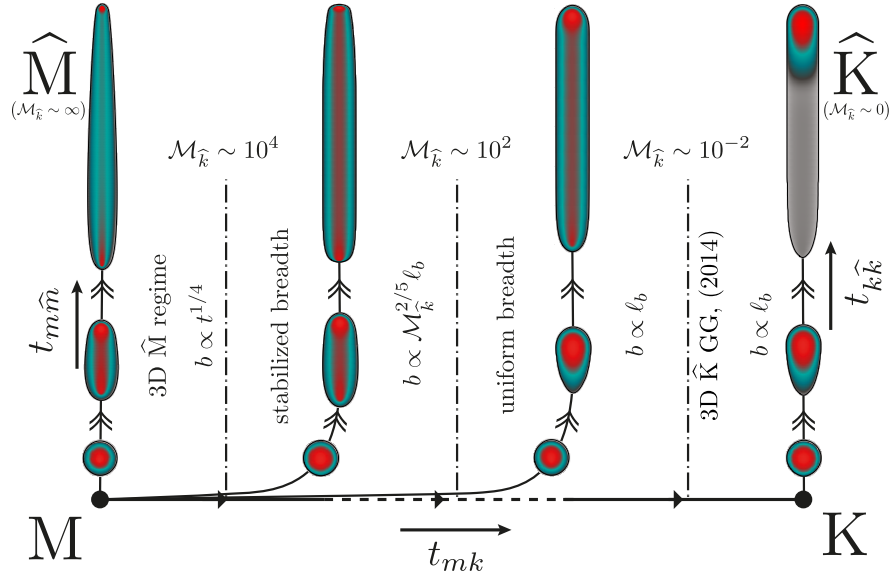


Figure 4.11: Propagation diagram for 3D buoyant fractures under a continuous fluid release. Radial growth is initially viscosity-dominated (M-vertex). Transition to buoyancy either occurs before ($\mathcal{M}_{\hat{k}} \gg 1$) or after ($\mathcal{M}_{\hat{k}} \ll 1$) the transition to radial toughness-dominated growth. At late times, a family of buoyancy-driven solutions as a function of $\mathcal{M}_{\hat{k}}$ (4.23) emerges. The large toughness limit (section 4.5) is reached for values of $\mathcal{M}_{\hat{k}} \lesssim 10^{-2}$, whereas the zero-toughness solution (section 4.6) appears at intermediate times $t \in [100t_{m\hat{m}}, t_{\hat{m}\hat{k}}^x]$ for $\mathcal{M}_{\hat{k}} \gtrsim 10^4$.

gash and Germanovich (2022). In this limit of large toughness, the buoyant HF has a distinct toughness-dominated head with a constant volume and shape, and a viscosity-dominated tail that governs its upward growth. For an intermediate range of $\mathcal{M}_{\hat{k}} \in [10^{-2}, 10^2]$, the fracture remains finger-like with a uniform breadth for each cross-section albeit with an increasing breadth with $\mathcal{M}_{\hat{k}}$. Above $\mathcal{M}_{\hat{k}} > 100$, the hydraulic fractures exhibit an inverted cudgel shape at late time (the breadth is no longer spatially uniform in the tail) and the maximum horizontal breadth increases as $\mathcal{M}_{\hat{k}}^{2/5} \ell_b$ as horizontal growth occurs until a given time $t_{\hat{m}\hat{k}}^x$ (4.36). For values of $\mathcal{M}_{\hat{k}} \gtrsim 10^4$, a zero-toughness self-similar \hat{M} limit (section 4.6) can be observed at intermediate times. This self-similar \hat{M} viscosity-dominated limit exhibits an ever-increasing breadth in association with the zero toughness assumption. The scaling of the \hat{M} , regime originally presented in Lister (1990a), is confirmed by our numerical results. In that limit, the viscous head is slowly depleting with time with a centerline evolution akin to the known 2D plane-strain near-tip asymptotic solution at late time. It might be possible to develop an approximate solution for that viscous limit along similar lines as in the toughness-dominated case when combining the source solution and the near-tip viscous head. A finite toughness always ensures an ultimate arrest of horizontal growth at a characteristic time $t_{\hat{m}\hat{k}}^x = \mathcal{M}_{\hat{k}}^{36/35} t_{m\hat{m}}$ for which the horizontal dimensionless toughness becomes of order one. Besides their final shapes, the transition to the buoyant regime is another important difference between buoyant toughness-dominated HF and viscous ones. For toughness-dominated fractures, a significant

Chapter 4. Three-dimensional buoyant hydraulic fractures: constant release from a point source

vertical acceleration ($\propto \mathcal{M}_k^{-1/3}$) is observed, whereas viscosity-dominated fractures have a smoother vertical acceleration thanks to horizontal growth.

Natural magmatic buoyant fractures are likely always viscosity-dominated, while on the other hand, all laboratory experiments have been performed under toughness-dominated conditions. It appears that even in the toughness regime, precise experiments are still lacking for quantitative comparison with the theoretical predictions reported here for buoyant fractures. Orders of magnitude for magmatic dikes also indicate that their horizontal and vertical extent will necessarily clash with length scales of stress and material heterogeneities at late times. These heterogeneities and the possibility of fluid exchange with the surrounding rock and thermal effects may play a critical role in the growth and potential arrest of buoyant hydraulic fractures on their way toward the surface. The interplay of these effects on linear hydraulic fracture mechanics growth remains to be investigated. Finally, most fluid releases are of a finite volume rather than having an ever-ongoing release at a constant injection rate. This particular problem is part of ongoing research and is essentially based on the findings presented in this contribution.

Data availability statement. The version of the open-source solver PyFrac, corresponding scripts, and results of the simulations of this study are openly available at [10.5281/zenodo.6511166](https://doi.org/10.5281/zenodo.6511166).

4.10 Appendix of the article

4.10.1 Recapitulating tables of scales

We list all the scales used within this contribution in the following tables for completeness. A Wolfram Mathematica notebook containing their derivation and the different scalings is further provided in the supplementary material.

4.11 Supplementary material of the article

4.11.1 Approximated toughness-dominated solution \hat{K}

The solution of Germanovich et al. (2014) recognizes that in the toughness limit, the 3D buoyant fracture has a finger-like geometry consisting of a toughness-dominated head and a viscosity-dominated tail. The head has a constant volume and shape and strictly hydrostatic net pressure, as viscous dissipation is neglected. The viscous tail has a constant breadth, the net force is uniform at every horizontal cross-section, and the vertical net pressure gradient is negligible compared to buoyancy.

| | <i>radial</i> | | | <i>elongated</i> | | |
|-----------------|--|---|---|---|---|---|
| | M | K | \hat{M} (tail) | \hat{M} (head) | \hat{K} (tail) | \hat{K} (head) |
| ℓ_* | $\frac{E^{1/9} Q_0^{1/3} t^{4/9}}{\mu^{1/9}}$ | $\frac{E^{2/5} Q_0^{2/5} t^{2/5}}{K_{Ic}^{2/5}}$ | $\frac{Q_0^{1/2} \Delta \gamma^{1/2} t^{5/6}}{E^{1/6} \mu^{1/3}}$ | $\frac{E^{11/24} Q_0^{1/8} \mu^{1/6}}{\Delta \gamma^{5/8} t^{1/24}}$ | $\frac{Q_0^{2/3} \Delta \gamma^{7/9} t}{K_{Ic}^{4/6} \mu^{1/3}}$ | ℓ_b |
| b_* | ℓ_* | ℓ_* | $\frac{E^{1/4} Q_0^{1/4} t^{1/4}}{\Delta \gamma^{1/4}}$ | ℓ_* | $\ell_b = \frac{K_{Ic}^{2/3}}{\Delta \gamma^{2/3}}$ | ℓ_* |
| w_* | $\frac{Q_0^{1/3} \mu^{2/9} t^{1/9}}{E^{2/9}}$ | $\frac{K_{Ic}^{4/5} Q_0^{1/5} t^{1/5}}{E^{4/5}}$ | $\frac{Q_0^{1/4} \mu^{1/3}}{E^{1/12} \Delta \gamma^{1/4} t^{1/12}}$ | w_*^{tail} | $\frac{Q_0^{1/3} \mu^{1/3}}{K_{Ic}^{2/9} \Delta \gamma^{1/9}}$ | $w k \hat{k}$ |
| V_* | $Q_0 t$ | $Q_0 t$ | $Q_0 t - V_*^{\text{head}}$ | $\frac{E^{5/6} Q_0^{1/2} \mu^{2/3}}{\Delta \gamma^{3/2} t^{1/6}}$ | $Q_0 t - V_*^{\text{head}}$ | $K_{Ic}^{8/3}$ |
| p_* | $\frac{E^{2/3} \mu^{1/3}}{t^{1/3}}$ | $\frac{K_{Ic}^{6/5}}{E^{1/5} Q_0^{1/5} t^{1/5}}$ | $\frac{E^{2/3} \mu^{1/3}}{t^{1/3}}$ | $\frac{E^{11/24} Q_0^{1/8} \Delta \gamma^{3/8} \mu^{1/6}}{t^{1/24}}$ | $\frac{E' \Delta \gamma^{5/9} Q_0^{1/3} \mu^{1/3}}{K_{Ic}^{8/9}}$ | $\frac{E' \Delta \gamma^{5/3}}{E' \Delta \gamma^{5/3}}$ |
| \mathcal{P}_s | $\mathcal{K}_m = (t/t_{mk})^{1/9}$ $\mathcal{B}_m = (t/t_{m\hat{m}})^{7/9}$ | $\mathcal{M}_k = (t/t_{mk})^{-2/5}$ $\mathcal{B}_k = (t/t_{k\hat{k}})^{3/5}$ | $\mathcal{K}_{\hat{m},x} = \mathcal{M}_{\hat{k}}^{-3/14} (t/t_{m\hat{m}})^{5/24}$ | $\mathcal{M}_{\hat{k}} = \mu' \frac{Q_0 E' \Delta \gamma^{2/3}}{K_{Ic}^{14/3}}$ | | |

 Table 4.3: Characteristic scales (and governing dimensionless parameters \mathcal{P}_s) in the different scalings.

Chapter 4. Three-dimensional buoyant hydraulic fractures: constant release from a point source

| | t | $\ell_* = b_*$ | w_* | p_* |
|-------------------------|--|---|--|--|
| $M \rightarrow K$ | $t_{mk} = \frac{E^{13/2} Q_o^{3/2} \mu^{5/2}}{K_{Ic}^9}$ | $\ell_{mk} = \frac{E^{13} Q_o \mu'}{K_{Ic}^4}$ | $w_{mk} = \frac{E^{1/2} Q_o^{1/2} \mu'^{1/2}}{K_{Ic}}$ | $p_{mk} = \frac{K_{Ic}^3}{E^{3/2} Q_o^{1/2} \mu'^{1/2}}$ |
| $M \rightarrow \hat{M}$ | $t_{m\hat{m}} = \frac{E^{5/7} \mu'^{4/7}}{Q_o^{3/7} \Delta\gamma^{9/7}}$ | $\ell_{m\hat{m}} = \frac{E^{3/7} Q_o^{1/7} \mu'^{1/7}}{\Delta\gamma^{4/7}}$ | $w_{m\hat{m}} = \frac{Q_o^{2/7} \mu'^{2/7}}{E^{1/7} \Delta\gamma^{1/7}}$ | $p_{m\hat{m}} = E^{3/7} Q_o^{1/7} \mu'^{1/7} \Delta\gamma^{3/7}$ |
| $K \rightarrow \hat{K}$ | $t_{k\hat{k}} = \frac{K_{Ic}^{8/3}}{E' Q_o \Delta\gamma^{5/3}}$ | $\ell_{k\hat{k}} = \ell_b = \frac{K_{Ic}^{2/3}}{\Delta\gamma^{2/3}}$ | $w_{k\hat{k}} = \frac{K_{Ic}^{4/3}}{E' \Delta\gamma^{1/3}}$ | $p_{k\hat{k}} = K_{Ic}^{2/3} \Delta\gamma^{1/3}$ |

Table 4.4: Transition scales between regimes. The toughness head scales in table 4.3 corresponds to the transition scales $K \rightarrow \hat{K}$.

Toughness-dominated head

The shape of the head is solved numerically by Germanovich et al. (2014) such that $K_I = K_{Ic}$ all along the propagating part of the head front. A linear hydrostatic pressure is set in the head, which leads to a constant and uniform breadth in its lower part. The toughness head scaling applies. In other words, the characteristic scales are:

$$b_{\hat{k}}^{\text{head}} = \ell_{\hat{k}}^{\text{head}} = \ell_b = \frac{K_{Ic}^{2/3}}{\Delta\gamma^{2/3}}, \quad w_{\hat{k}}^{\text{head}} = \frac{K_{Ic}^{4/3}}{E' \Delta\gamma^{1/3}},$$

$$p_{\hat{k}}^{\text{head}} = K_{Ic}^{2/3} \Delta\gamma^{1/3}, \quad V_{\hat{k}}^{\text{head}} = Q_o t_{k\hat{k}} = \frac{K_{Ic}^{8/3}}{E' \Delta\gamma^{5/3}} = \ell_b^2 w_{\hat{k}}^{\text{head}}.$$

These scales are also given in equation (4.24).

In the head, fluid flow is negligible such that according to Poiseuille's law,

$$\frac{\partial p}{\partial z} = \Delta\gamma$$

The head is divided into a rounded part where lateral expansion occurs and a bottom, laterally stationary part. Using a local coordinate system whose origin is centered at the boundary between the expanding and stationary part: $\tilde{z} = z - \ell_{\hat{k}}^{\text{head}}(\gamma^{\text{head}} - \lambda)$, in dimensionless form, the dimensionless pressure becomes

$$\Pi(\zeta, \xi) = \zeta - (\gamma^{\text{head}} - \lambda)$$

where γ^{head} the dimensionless head length scaled by ℓ_b and $\zeta = z/\ell_b$. The condition

$$K_I = K_{Ic}$$

is imposed for $\zeta \in [0, \lambda]$, while the breadth is constant for $\zeta < 0$ and given by $\beta\ell_b$, i.e.:

$$b(\zeta < 0)/\ell_b = \beta$$

where β is the unknown dimensionless breadth in the laterally stationary part and $db/d\zeta = 0$ at $\zeta = 0$. Solving numerically the elasticity equation using a piece-wise constant displacement discontinuity method in combination with the previous constraints, Germanovich et al. (2014) arrives at the following solution for the total breadth of the fracture

$$b(\zeta > 0)/\ell_b = \beta \sqrt{1 - a(\zeta/\lambda)^2 - (1 - a)(\zeta/\lambda)^4} \quad a \approx 0.6967 \quad (4.38)$$

in the laterally spreading part of the head with the following dimensionless extent of the laterally extending region

$$\lambda \approx 1.3935 \times \left(0.249\sqrt{2/\pi}\right)^{2/3} \approx 0.4745$$

the dimensionless head size

$$\gamma^{\text{head}} \approx 5.19 \times \left(0.249\sqrt{2/\pi}\right)^{2/3} \approx 1.7671$$

and dimensionless breadth:

$$\beta \approx 2 \times (0.249\sqrt{2/\pi})^{2/3} \approx 0.6809 \approx \pi^{-1/3}.$$

We show that the evolution of the breadth in the head (over λ , equation (4.38)) matches our simulations in figures 4.2g - i of section 4.5.3 by red dashed lines. In fine, the dimensional head breadth, length, net pressure, and volume are, respectively

$$\begin{aligned} b &\approx 0.6809\ell_b \approx \pi^{-1/3}\ell_b \\ \ell^{\text{head}} &\approx 1.7671\ell_b \\ p &\approx p_{\hat{k}}^{\text{head}} \times \left(z/\ell_b - (\gamma^{\text{head}} - \lambda)\right) \\ V^{\text{head}} &\approx 0.7008\ell_b^2 w_{\hat{k}}^{\text{head}} \end{aligned}$$

Viscous tail

The tail is modeled as a long finger-like hydraulic fracture for which the usual PKN hydraulic fracture model assumptions apply. Notably, the elastic relation can be written at the cross-

Chapter 4. Three-dimensional buoyant hydraulic fractures: constant release from a point source

section z

$$w(z, x) = 2 \frac{bp(z)}{E'} \sqrt{1 - 4x^2/b^2} \quad x \in [-b/2, b/2]$$

with p the net pressure. The average width of the cross-section is related to the net pressure simply as:

$$\bar{w}(z) = \pi \frac{bp(z)}{2E'}$$

The fluid flow in the tail is 1D,

$$\frac{\partial \bar{w}}{\partial t} + \frac{\partial q_z}{\partial z} = \delta(z) Q_o / b$$

and with a cross-sectional average of Poiseuille's law is:

$$q_z = -\frac{\bar{w}^3}{\pi^2 \mu} \left(\frac{\partial p}{\partial z} - \Delta \gamma \right)$$

In the viscous tail $\frac{\partial p}{\partial z} \ll \Delta \gamma$, such that

$$q_z \approx \frac{\bar{w}^3 \Delta \gamma}{\pi^2 \mu}.$$

and the global volume balance in the tail is

$$b \int_0^{\ell^{\text{tail}}} \bar{w} dz = Q_o t - V^{\text{head}}$$

accounting for the constant volume of the head. Looking for a self-similar solution for which the average width \bar{w} is uniform and constant in the tail, and the velocity in the tail is constant such that

$$v_z = \frac{d\ell^{\text{tail}}}{dt} = q_z / \bar{w} = \frac{\bar{w}^2 \Delta \gamma}{\pi^2 \mu}.$$

The volume balance of the tail becomes

$$b\ell^{\text{tail}} \bar{w} = Q_o t - V_{\text{head}}$$

which provides the expression for the velocity in the tail:

$$\frac{d\ell^{\text{tail}}}{dt} = \frac{Q_o}{b\bar{w}} = \frac{\bar{w}^2 \Delta\gamma}{\pi^2 \mu}$$

such that we obtain

$$\bar{w} = \left(\pi^2 \frac{Q_o \mu}{b \Delta\gamma} \right)^{1/3} \quad p = \frac{2E'}{\pi b} \left(\pi^2 \frac{Q_o \mu}{b \Delta\gamma} \right)^{1/3}$$

and

$$\ell^{\text{tail}} = \frac{Q_o t}{b\bar{w}} - \frac{V_{\text{head}}}{b\bar{w}}. \quad (4.39)$$

It is possible to rewrite equation (4.39) using the characteristic tail length $\ell_{\hat{k}}$ as

$$\ell^{\text{tail}} = \frac{12^{1/3}}{\pi^{2/3} \beta^{2/3}} \ell_{\hat{k}} - \frac{V_{\text{head}}}{b\bar{w}}$$

where we now replace V^{head} (with its numerical prefactor) and \bar{w} as defined previously and used by the scales in (4.24) using $\ell^{\text{tail}} = \gamma^{\text{tail}} \ell_b$ to obtain

$$\gamma^{\text{tail}} \approx \frac{12^{1/3}}{\pi^{2/3} \beta^{2/3}} \left(\frac{\Delta\gamma^{13/9} Q_o^{2/3} t}{K_{Ic}^{10/9} \mu'^{1/3}} - 0.7008 \frac{K_{Ic}^{14/9}}{\mu'^{1/3} Q_o^{1/3} \Delta\gamma^{2/9} E'} \right).$$

We now replace the time as $\tau = t/t_{k\hat{k}}$ and note that

$$\mathcal{M}_{\hat{k}}^{-1/3} = \frac{K_{Ic}^{14/9}}{\mu'^{1/3} Q_o^{1/3} \Delta\gamma^{2/9} E'}$$

such that we get

$$\gamma^{\text{tail}} \approx \frac{12^{1/3}}{\pi^{2/3} \beta^{2/3}} \mathcal{M}_{\hat{k}}^{-1/3} (\tau - 0.7008) \approx 1.3789 \mathcal{M}_{\hat{k}}^{-1/3} (\tau - 0.7008). \quad (4.40)$$

A comparison of our numerical simulations with this value is presented in table 4.1 of section 4.5.3.

We estimate from this equation the dimensionless time τ for which the dominant linear term will be valid within a given percentage. We pose the equation as

Chapter 4. Three-dimensional buoyant hydraulic fractures: constant release from a point source

$$\varepsilon \frac{12^{1/3}}{\pi^{2/3} \beta^{2/3}} \mathcal{M}_{\hat{k}}^{-1/3} \tau = \gamma^{\text{tail}} \rightarrow \tau_{\varepsilon} = \frac{0.7008}{1 - \varepsilon}$$

where ε is the “error” between the linear term and the complete solution. We estimate the error to be within our maximum numerical error of 5 % (e.g. $\varepsilon = 0.95$) such that we get a dimensionless time of

$$\tau_{0.95} = (t/t_{k\hat{k}})_{0.95} \approx 14.0$$

this limit for convergence is used within section 4.5.4 to describe the transient.

It is now possible to derive the total fracture length by the addition of the head length to the tail length (4.40) as

$$\gamma^{\text{total}} = \gamma^{\text{tail}} + \gamma^{\text{head}} \approx 1.3789 \mathcal{M}_{\hat{k}}^{-1/3} (\tau - 0.7008) + 1.7671$$

This expression for γ^{total} is plotted with green dashed lines in figure 4.2c of the main text. We additionally present the dominant term $1.3789 \mathcal{M}_{\hat{k}}^{-1/3} \tau$ with green dashed-dotted lines.

We finally derive the scales of the opening and the pressure in the tail. According to Germanovich et al. (2014), they are given in their scaling as

$$p/p_* = \bar{w}/w_* = \left(\frac{Q_o/Q_*}{2\alpha} \right)^{1/3}$$

where \bar{w} is the average opening in the tail. Transformed in our scaling, these two quantities read

$$\begin{aligned} \frac{p}{1.3674 p_{\hat{k}}^{\text{head}}} &= 0.7281 \mathcal{M}_{\hat{k}}^{1/3} \rightarrow p/p_{\hat{k}}^{\text{head}} = 0.9956 \mathcal{M}_{\hat{k}}^{1/3} \\ \frac{\bar{w}}{1.46264 w_{\hat{k}}^{\text{head}}} &= 0.7281 \mathcal{M}_{\hat{k}}^{1/3} \rightarrow \bar{w}/w_{\hat{k}}^{\text{head}} = 1.0650 \mathcal{M}_{\hat{k}}^{1/3}. \end{aligned}$$

From this, we can now derive the maximum opening (at the centreline $x = 0$) as

$$w(0, z) = \frac{4}{\pi} \bar{w}(z) \rightarrow w(0, z)/w_{\hat{k}}^{\text{head}} = 1.3559 \mathcal{M}_{\hat{k}}^{1/3}.$$

Limit of applicability of their theory

Germanovich et al. (2014) argue that their solution is only valid as long as the breadth in the tail is stationary. To validate this condition, the pressure in the tail cannot exceed the value required for lateral fracturing (i.e., $p \leq K_{Ic} / \sqrt{\pi \beta \ell_b}$). This condition results in a dimensionless release rate in their contribution

$$Q/Q_* < 0.1761.$$

We can translate their dimensionless release rate into our scaling as

$$Q/Q_* = 0.1922 \mathcal{M}_{\hat{k}}$$

such that the above inequality leads to the following limit

$$0.1922 \mathcal{M}_{\hat{k}} < 0.1761 \rightarrow \mathcal{M}_{\hat{k}} < 0.9159$$

which is reported as the limit of $\mathcal{M}_{\hat{k}} \approx 0.92$ in section 4.7.

4.11.2 Viscosity-dominated solution in the source region

The scales presented by Lister (1990a) in his equations (2.14) correspond qualitatively (upon numerical prefactors and by replacing t by solving $\ell(t) = z$ for t) to the scaling listed in equation (4.32) of the main text. We re-derive their scaling using our parameters to plot the corresponding solutions in figures 4.5 and 4.6 of section 4.6.1. First, we can retrieve his scales using our characteristic fracture length

$$\ell_{\hat{m}}(t) = z = \frac{\Delta\gamma^{1/2} Q_o^{1/2}}{E^{1/6} \mu^{1/3}} t^{5/6} \rightarrow t_z = \frac{E^{1/5} \mu^{2/5}}{\Delta\gamma^{3/5} Q_o^{3/5}} z^{6/5}$$

such that we obtain them as

$$\begin{aligned} b^{\text{Lister, 1990}}(z) &= 0.6335 \times b_{\hat{m}}(t = t_z) = 0.6335 \frac{Q_o^{1/10} \mu^{1/10} E^{3/10}}{\Delta\gamma^{4/10}} z^{3/10} \\ w^{\text{Lister, 1990}}(z) &= 0.5086 \times w_{\hat{m}}(t = t_z) = 0.5086 \frac{Q_o^{3/10} \mu^{3/10}}{E^{3/10} \Delta\gamma^{6/10}} z^{-1/10} \\ h^{\text{Lister, 1990}}(t) &= 2.5698 \times \ell_{\hat{m}}(t) = 2.5698 \times \frac{\Delta\gamma^{1/2} Q_o^{1/2}}{E^{1/6} \mu^{1/3}} t^{5/6} \end{aligned}$$

Chapter 4. Three-dimensional buoyant hydraulic fractures: constant release from a point source

It is now possible to get the breadth plotted in figure 4.5a by replacing $z = \zeta \ell_{\hat{m}}(t)$, using the prefactors to his solution and then dividing by our breadth scale

$$\frac{b^{\text{pseudo 3D}}(\zeta)}{b_{\hat{m}}(t)} = 1.6629 \times \zeta^{3/10}$$

similarly, we can get the opening at the centreline, the opening profile (with $\xi = x/b_{\hat{m}}$), and the cross-sectional volume as

$$\begin{aligned} \frac{w^{\text{pseudo 3D}}(\xi = 0, \zeta)}{w_{\hat{m}}(t)} &= 0.9197 \times \zeta^{-1/10} \\ \frac{w^{\text{pseudo 3D}}(\xi, \zeta)}{w_{\hat{m}}(t)} &= 0.9197 \times \left(1 - 0.3616 \frac{\xi^2}{\zeta^{3/5}}\right) \zeta^{-1/10} \\ \frac{\int_{-1}^1 w^{\text{pseudo 3D}}(\xi, \zeta) d\xi}{w_{\hat{m}}(t) b_{\hat{m}}(t)} &= 1.8017 \zeta^{1/5} \end{aligned}$$

The central opening and the 2D cross-sectional volume are used in figures 4.5b and c of the main text. We give further their transition scale from viscosity- to toughness-dominated for buoyant fractures as

$$\ell_{mk}^{\text{Lister, 1990}} = 5.76 \times 10^{-4} \ell_{mk}.$$

The opening distribution used in figures 4.6c and d is scaled by the time-independent transition scales $\ell_{m\hat{m}}$ and $w_{m\hat{m}}$. The opening distribution in such scaling is interestingly exactly equivalent to the one presented previously.

4.11.3 Post-processing of the numerical results

Automatic evaluation of characteristic quantities

All of the following is performed by the two PyFrac functions:

- `get_fracture_geometric_parameters()`
- `get_fracture_head_volume()`

Global quantities

The numerical data of PyFrac (Zia and Lecampion, 2020) includes the intersections of the

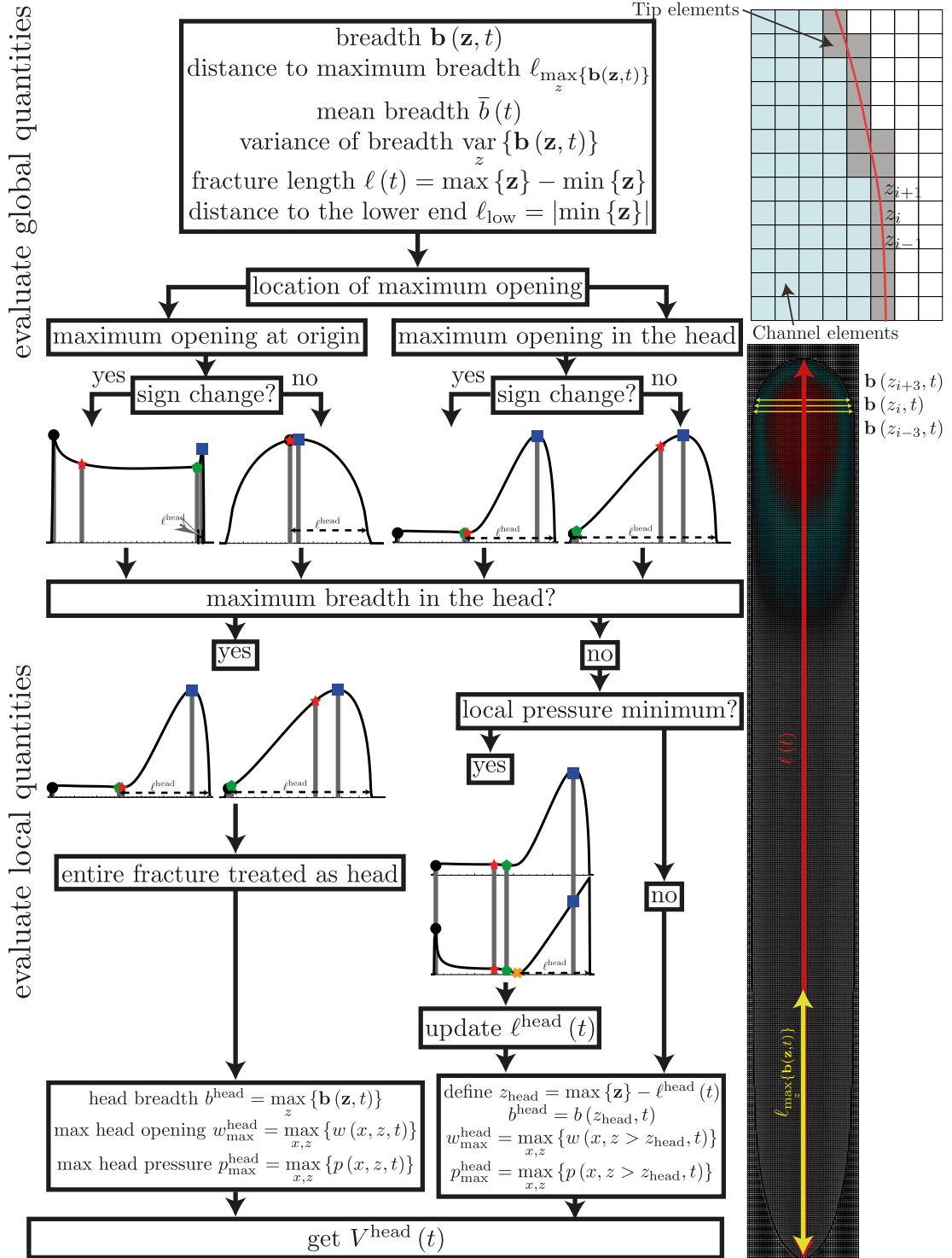


Figure 4.12: Flow chart of numerical evaluation. Black circles mark the origin, blue squares are the max head opening, red stars distance to the maximum breadth, green polygons are the location of the head evaluated by the “opening method”, and yellow crosses the update with the pressure check.

Chapter 4. Three-dimensional buoyant hydraulic fractures: constant release from a point source

fracture front $\mathcal{C}(t)$ with the cell edges (c.f. figure 4.12). We extract from these points the fracture breadth vector at the locations z_i as $\mathbf{b}(\mathbf{z}, t)$ from the subtraction between the intersections on the positive (i.e. where $x_i > 0$) and the negative side (i.e. where $x_i < 0$). In the vector notation, we have \mathbf{z} as the vector of all the intersections of the front with a discrete cell edge on the z -axis. There is no ambiguity in this evaluation as the release point is chosen as $(x, z) = (0, 0)$ and needs to be at a cell center, and the z -axis is an axis of symmetry of the problem.

From the breadth, we obtain the maximum breadth by simply taking the maximum of $\mathbf{b}(\mathbf{z}, t)$. Note that between two edge intersections, the connection is a straight line, ensuring that the maximum breadth evaluated as such is actually the maximum breadth in the simulation. We then also estimate the distance to the maximum breadth as

$$\ell_{\max\{\mathbf{b}(\mathbf{z}, t)\}} = \min_z \left\{ z_i \in \mathbf{b}(\mathbf{z}, t) \geq 0.975 \cdot \max_z \{\mathbf{b}(\mathbf{z}, t)\} \right\}.$$

We acknowledge a variation of 2.5 % along the breadth as numerical noise. To stabilize the scheme, notably for toughness-dominated cases, we thus decide to take the distance to the maximum breadth as the smallest value of an intersection z_i where the breadth exceeds 97.5 % of its maximum observed. This further allows us to get an average breadth $\bar{b}(t)$ and a variance of the breadth $\text{var}_z \{\mathbf{b}(\mathbf{z}, t)\}$.

The fracture height is evaluated as the distance between the maximum vertical extent and the minimum vertical extent,

$$\ell(t) = \max\{\mathbf{z}\} - \min\{\mathbf{z}\}.$$

The last quantity we measure is the distance to the lower end of the fracture from the release point (i.e., the downward growth of the fracture) as $\ell_{\text{low}} = |\min\{\mathbf{z}\}|$.

Some of the quantities are displayed in figure 4.12. See also the sketch of figure 4.1 of chapter 4.

Local quantities

We are mainly interested in the quantities within the head of the fracture. We must first decide if a head exists and its extent to achieve those. To do so, we get the pressure and opening profiles along the centreline of the fracture (e.g., $w(x=0, z, t)$) evaluated at the cell center. We then search for the release point (i.e. $z=0$) and get the location of the overall maximum opening $\max_z \{w(x=0, z, t)\}$. We check if the maximum opening is at the origin (with a security margin of 4 cells around the origin) or elsewhere.

1. **Maximum opening at the origin:** If the maximum opening is at the origin, we check

for a sign change in the derivative of the opening between the origin and the top of the fracture. If we do not have such a case, the opening monotonically decreases from the injection point to the fracture tip, and we do not have a head. In this case, we evaluate the head length $\ell^{\text{head}}(t)$ as

$$\ell^{\text{head}}(t) = \max\{\mathbf{z}\} \quad \text{if no head exists.}$$

If the decrease between the release point and the fracture tip exists, we check for the location where the opening starts to increase again towards the fracture tip. This allows us to define the location of the maximum opening in the head, which is further away than the previously mentioned slope change but still inside the fracture. Between this maximum opening and the location where fracture breadth starts to increase again must necessarily be at least two inflection points. We take the first inflection point from the sign change in the opening as the location of the head length (the second is where the opening slope starts to decrease towards the head).

2. **Maximum opening in the head:** If the maximum opening is not at the origin, it must be in the head. If such is the case, we search for a sign change between the origin and the maximum opening and proceed as previously described. There might not be any sign change (flat tail above the release point). In the configuration without sign change, we directly search for all inflection points and take the one second closest to the maximum opening in the head (the closest one would be where the slope of the opening starts to decrease towards the head).

The just described evaluation method is called the “opening method” from here on.

We perform a “check” using the pressure distribution on all opening method evaluations. The primordial usage of the opening is favored because our scheme provides a better estimate of opening than pressure. For the pressure “check”, we first evaluate if the maximum breadth occurs in the head using the head length defined via the “opening method”. If such is the case, we chose the head breadth $b^{\text{head}}(t) = b(z_{tip}(t) - \ell^{\text{head}}(t), t)$ as the maximum breadth to reduce numerical noise in our results. If a head exists, we check if a local pressure minimum exists inside the previously evaluated head. If so, we redefine the beginning of the head from this local minimum to the tip. Otherwise, we leave the evaluation unchanged.

The maximum head opening and pressure are then defined according to our evaluation of the head dimensions and the breadth is calculated as

$$b^{\text{head}}(t) = b(z_{tip}(t) - \ell^{\text{head}}(t), t).$$

It remains for us to obtain the volume of the head. We obtain this by simply summing the elements in the head. We define the channel e_{ci}^{head} channel means fully inside the fracture, c.f. figure 4.12) and the tip e_{ti}^{head} (elements where the front passes, c.f. figure 4.12) elements in the

Chapter 4. Three-dimensional buoyant hydraulic fractures: constant release from a point source

head using the previously obtained dimensions of the head. The volume in the head is then given by

$$V^{\text{head}}(t) = A_e \left\{ \sum_{i=1}^{n_c} w(x(e_{ci}), z(e_{ci}), t) + \sum_{j=1}^{n_t} f(e_{tj}) w(x(e_{tj}), z(e_{tj}), t) \right\}$$

where A_e is the (uniform) element area, and f the filling fraction of the tip element. The filling fraction is the percentage of the area occupied by the fracture.

Definition of uniform breadth

The distinction between uniform and non-uniform breadth is based on a post-processing evaluation within Mathematica©(Wolfram Research, 2020). The evaluation is performed on the last time step of the simulation. From the post-processing within PyFrac (Zia and Lecampion, 2020), we know where the head starts and where the maximum breadth is located. On the footprint, we thus extract the breadth in between as the breadth of the tail

$$b^{\text{tail}}(z^{\text{tail}}, t) \quad \text{for } \ell_{\max|\mathbf{b}(z,t)} \leq z^{\text{tail}} \leq z_{\text{tip}} - \ell^{\text{head}}(t).$$

This is the domain for which the breadth must be uniform for the fracture to be classified as finger-like. We recall that we defined the distance to the maximum breadth with a 2.5 % margin. We need to account for this uncertainty in our decision regarding a uniform breadth. We define our decision upon the breadth being uniform using the maximum difference in breadth in the tail

$$\frac{\max_z \{b^{\text{tail}}(z^{\text{tail}}, t)\} - \min_z \{b^{\text{tail}}(z^{\text{tail}}, t)\}}{\max_z \{b^{\text{tail}}(z^{\text{tail}}, t)\}} \leq 0.04$$

which corresponds to a 4 % relative difference. If we subtract the 2.5 % error already included due to the evaluation of the distance. This leaves us with a maximum variation of 1.5 % that we accept. This evaluation is used to obtain figure 8 of the main text and defines the discussion of uniform (finger-like) vs non-uniform (inverted cudgel) breadth.

4.11.4 2D steadily moving semi-infinite buoyant hydraulic Fracture Solver

We derive from the two-dimensional formulation the following scales

$$\ell_b^{2D} = \frac{E'^{1/2} Q_{2D}^{1/6} \mu^{1/6}}{(\Delta \rho g)^{2/3}}, \quad w_b^{2D} = \frac{Q_{2D}^{1/3} \mu^{1/3}}{(\Delta \rho g)^{1/3}}, \quad p_b^{2D} = E'^{1/2} Q_{2D}^{1/6} \mu^{1/6} (\Delta \rho g)^{1/3} \quad (4.41)$$

and a dimensionless toughness

$$\kappa = \frac{K_{Ic}}{E'^{3/4} \mu'^{1/4} Q_o^{1/4}}$$

where the 2D release rate is obtained using $Q_{2D} = \nu_{z*} w_*$. This leads us to the following set of scaled equations for the 2D semi-infinite fracture

$$\begin{aligned} \Pi^{2D}(\hat{\xi}^{2D}) &= \frac{1}{4\pi} \int_0^\infty \frac{\partial \Omega}{\partial \hat{\eta}^{2D}} \frac{d\hat{\eta}^{2D}}{\hat{\xi}^{2D} - \hat{\eta}^{2D}} \quad \text{elasticity} \\ 1 &= \Omega^2 \left(\frac{\partial \Pi}{\partial \hat{\xi}^{2D}} + 1 \right) \quad \text{lubrication} \\ \Omega &= \sqrt{\frac{32}{\pi}} \kappa (\hat{\xi}^{2D})^{1/2} \quad \hat{\xi}^{2D} \ll 1 \quad \text{LEFM} \end{aligned}$$

where $\hat{\xi}^{2D} = \hat{x}/\ell_b^{2D}$ is the scaled distance to the tip with $\hat{x} = \nu_{z*} t - z$ the tip-based coordinate.

The two-dimensional semi-infinite buoyant hydraulic fracture is now solved via a numerical scheme based on a Gauss-Chebyshev quadrature. Using this approach for elastic boundary integral equations is well established (Erdogan et al., 1973) and has been used for similar problems before (Viesca and Garagash, 2018; Moukhtari and Lecampion, 2018). We follow mainly the developments presented in Moukhtari and Lecampion (2018), albeit including the buoyant stress gradient. The same discretization method is chosen such that one has

$$\frac{\partial \Omega}{\partial \hat{\xi}^{2D}} = \sqrt{\frac{32}{\pi}} \frac{\kappa}{\hat{\xi}^{2D}} + \sqrt{\hat{\xi}^{2D}} \phi(\hat{\xi}^{2D}) \quad (4.42)$$

with $\phi(\hat{\xi}^{2D})$ the unknown, non-singular dislocation density represented as a Chebyshev polynomial. This approach allows us to embed the LEFM condition naturally in the discretization, which will thus automatically be verified. We solve for the values of the Chebyshev polynomials using third kind Gauss-Chebyshev polynomials, which use two sets of nodes $\mathbf{v} = \{v_j\}$ with $j = 1, \dots, n$ and $\mathbf{u} = \{u_i\}$ with $i = 1, \dots, n$. The use of third-kind polynomials directly declines from equation (4.42), as naturally the corresponding weight function $\omega(s)$ appears after the following variable transformation (Ioakimidis and Theocaris, 1980; Viesca and Garagash, 2018)

$$\hat{\xi}^{2D} = \frac{1+v}{1-v}, \quad \omega(s) = \sqrt{\frac{1+v}{1-v}}.$$

The related set of points corresponding to the roots of the third and fourth Chebyshev polynomials, respectively, are given as

Chapter 4. Three-dimensional buoyant hydraulic fractures: constant release from a point source

$$v_j = \cos\left(\frac{\pi j}{n+1/2}\right), j = 1, \dots, n; \quad u_i = \cos\left(\frac{\pi i}{n+1/2}\right), i = 1, \dots, n.$$

This allows us to discretize the elasticity equation as

$$\frac{\Pi^{2D}(\hat{\xi}_j^{2D})}{1-v_j} = \frac{1}{4\pi} \sum_i^n \frac{A_i}{1-u_i} \frac{\phi(\hat{\xi}_j^{2D})}{v_j-u_j}$$

where $\hat{\xi}_j^{2D} = \hat{\xi}^{2D}(v_j)$ and $A_i = \pi(1+u_i)/(n+1/2)$ are the quadrature weights. From this equation, we create the following elasticity matrix

$$\mathbb{K}_{ij} = \frac{1}{4\pi} \sum_i^n \frac{A_i}{1-u_i} \frac{1-v_j}{v_j-u_j}.$$

The lubrication equation is discretized via a finite difference scheme at the mid-points $\hat{\xi}_{j+1/2}^{2D}$

$$\Omega(\hat{\xi}_{j+1/2}^{2D})^2 \left\{ \frac{\Pi^{2D}(\hat{\xi}_{j+1}^{2D}) - \Pi^{2D}(\hat{\xi}_j^{2D})}{\hat{\xi}_{j+1}^{2D} - \hat{\xi}_j^{2D}} + 1 \right\} = 1 \quad (4.43)$$

where we recall that due to equation (4.42), the opening is given by

$$\Omega(\hat{\xi}_{j+1/2}^{2D}) = \sqrt{\frac{32}{\pi} \kappa \hat{\xi}_{j+1/2}^{2D}} + \phi(\hat{\xi}_{j+1/2}^{2D}). \quad (4.44)$$

Note that we obtain $\phi(\hat{\xi}_{j+1/2}^{2D})$ by linear interpolation of $\phi(\hat{\xi}^{2D})$. We need now to set a single last condition to close the system, which we choose as a zero pressure condition at infinity $\Pi^{2D}(\hat{\xi}_n^{2D}) = 0$. The problem is then solved via the built-in Mathematica©(Wolfram Research, 2020) find root function using a quasi-Newton method with a finite difference approximation of the jacobian. The sequence to solve the problem is then as follows:

1. Create the discretization with the elasticity matrix \mathbb{K} and the interpolation function of $\phi(\hat{\xi}_{j+1/2}^{2D})$
2. Give an initial estimate of the pressure. The estimate of the initial pressure is performed stepwise:
 - (a) We use the so-called viscosity asymptote (Desroches et al., 1994) as an initial guess for a value of $\kappa \approx 0.16$, which we know to have a good convergence. We then stepwise reduce its value to $\kappa \approx 0.02$, using the previously obtained pressure distribution as an initial guess.

- (b) Depending on the value of κ in our problem, we choose the closest corresponding pressure distribution. The value of $\kappa \approx 0.02$ is sufficient to get a good convergence for the solver even when $\kappa = 0$ in the zero toughness case.
3. Solve iteratively until the residual convergence (Accuracy Goal of Mathematica set to 8):
- (a) We use the built-in linear solve function of Mathematica©(Wolfram Research, 2020) to solve the equation

$$\Pi^{2D} = \mathbb{K} \cdot \phi$$

at the discrete points for $\phi(\hat{\xi}_j^{2D})$.

- (b) Evaluate the opening at the mid-points by equation (4.44).
- (c) Use equation (4.43) to build a residual.
- (d) Estimate the new pressure distribution from the residual and restart at (a)

Note: The K_* used in the code is directly equal to

$$K_* = \sqrt{\frac{32}{\pi}} \kappa.$$

Validation with Limiting Solutions

Large-Toughness Limit

The article Roper and Lister (2007) solves the large toughness limit. However, to compare, we need to make our scales equivalent, which requires some additional steps. We have the following equivalencies between their and our scales

$$\hat{x} = \frac{1}{2} \ell_b^{2D}, \quad \hat{h} = \frac{1}{2} w_b^{2D}, \quad \hat{p} = \frac{1}{2}, \quad K_{\text{RoLi07}} = \frac{1}{2} \sqrt{\frac{32}{\pi}} \kappa = \frac{1}{2} K_* \quad (4.45)$$

where K_{RoLi07} is their dimensionless toughness as in their equation (2.10). We need to emphasize that their opening h equals our $w/2$. Roper and Lister (2007) then rescale those parameters again to obtain

$$X = \frac{x/\hat{x}}{K_{\text{RoLi07}}^{2/3}} = \frac{2 \cdot 2^{2/3} x/\ell_b^{2D}}{K_*^{2/3}}, \quad H = \frac{h/\hat{h}}{K_{\text{RoLi07}}^{4/3}} = \frac{2^{4/3} w/w_b^{2D}}{K_*^{4/3}}, \quad P = \frac{p/\hat{p}}{K_{\text{RoLi07}}^{2/3}} = \frac{2 \cdot 2^{2/3} p/p_b^{2D}}{K_*^{2/3}} \quad (4.46)$$

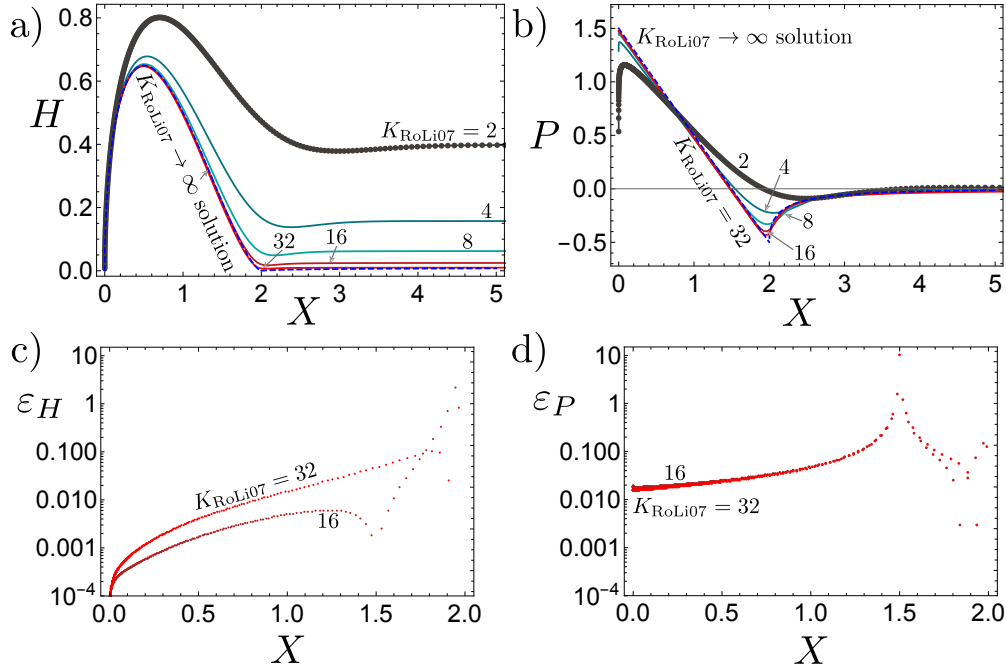


Figure 4.13: 2D semi-infinite opening (a) and pressure (b) in the scaling of equation (4.46). Blue-dashed lines correspond to the solution of Roper and Lister (2007) for $K_{\text{RoLi07}} = 32$ (equations (4.47)). Simulation with $K_{\text{RoLi07}} = 2$ shows the evaluation points as markers. Relative error ((c) opening and (d) pressure) of our numerical evaluation with the solutions (4.47).

They now derive an approximated solution for the opening and pressure in this scaling. The output of our numerical solver is the scaled coordinates x/ℓ_b^{2D} , opening w/w_b^{2D} , and pressure p/p_b^{2D} .

We use as a comparison and validation of our code the opening with the first-order tail correction and the zero-order pressure

$$H = \frac{1}{2} X^{1/2} (2 - X)^{3/2} + \mathcal{H}(x - 2) K_{\text{RoLi07}}^{-4/3} \sqrt{2} \frac{X^{1/4} (x - 2)^{3/4}}{(2x^2 - 2x - 1)^{1/2}}$$

$$P = \frac{3}{2} - X + \mathcal{H}(x - 2) \frac{(2X - 1)(X - 2)^{1/2}}{2X^{1/2}} \quad (4.47)$$

where \mathcal{H} is the Heaviside theta function. We compare the solutions graphically in figures 4.13a and b and present the errors in the head obtained for an evaluation with $n = 400$ and $\kappa \approx 10, 20$ ($K_{\text{RoLi07}} = 16, 32$) in figures 4.13c and d. Note that we present the relative error, which explains the increase when approaching the zero in pressure at $X \approx 1.5$. The absolute error in this range is small if we compare it using figure 4.13b. Generally, the relative error remains within a few percent except towards the end of the head. This can be explained by the enforced continuity of our model as opposed to the Heaviside functions present in the analytical

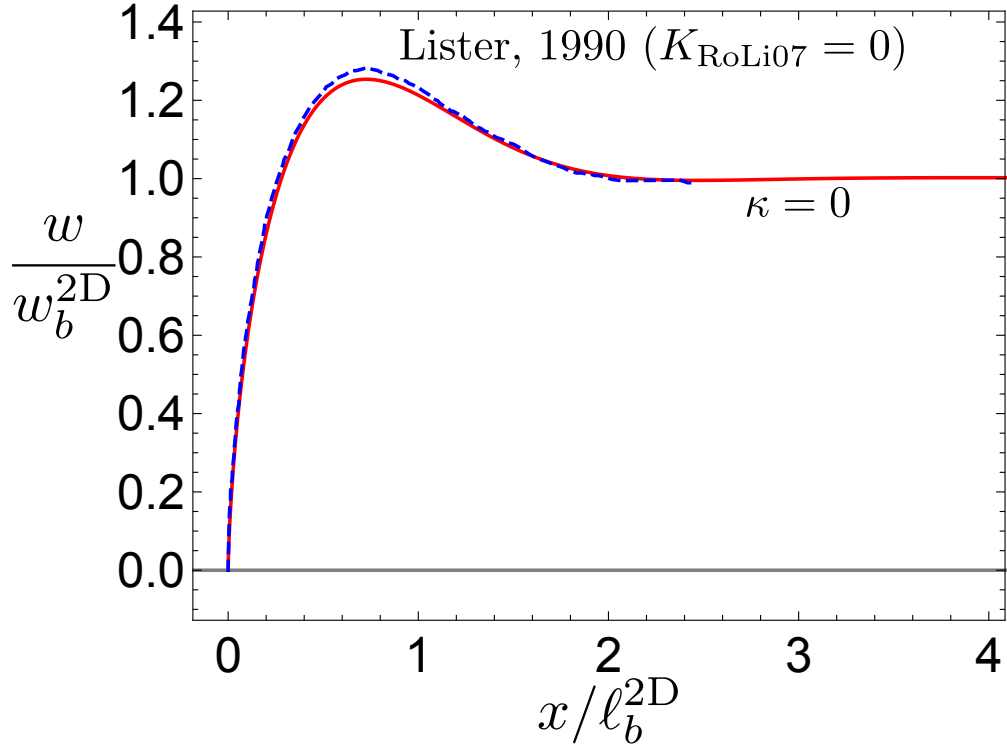


Figure 4.14: Comparison between the zero-toughness solution extracted from Lister (1990b) figure 3 (blue-dashed line) with our zero-toughness Gauss-Chebyshev evaluation (red line).

solutions (4.47). Additionally, one observes that the error on the opening increases towards the transition from the head to the tail. The reason is that the corrected head solution tends to 0 at $X = 2$, whereas our solution is continuous. The match between the solutions in the tail is then again well visible when comparing the opening at values of $X \gg 2$.

Zero-Toughness Limit

To ensure that the code also works in the other limit of zero-toughness we compare the results to the numerical results with $K_* = 0$ presented in figure 3 of Lister (1990b). This data is picked numerically and then rescaled from the scales provided in the figure. Figure 4.14 is comparing our opening profile graphically for a simulation with $K_* = K_{RoLi07} = \kappa = 0$ in “our” scales (4.41). Generally, the match is nearly perfect except around the maximum opening. Around the maximum opening, picking the data from the figure was very difficult as the resolution there made it very hard to determine the exact location of the graph. Nonetheless, the very good match elsewhere, as well as the correspondence for the toughness-dominated case, allow us to conclusively state that our numerical 2D Gauss-Chebyshev solver of the semi-infinite fracture is valid for the entire range of κ possible.

Chapter 4. Three-dimensional buoyant hydraulic fractures: constant release from a point source

| Gelatines | | | | | |
|---------------------|---------------------|------------------------------------|------------------------|--|-----------|
| Concentration | G [Pa] | K_{Ic} [Pa · $\sqrt{\text{m}}$] | ν [-] | ρ_s [kg · m ⁻³] | E' [Pa] |
| 1.4 % | 190 | 15 | 0.5 | 1000 | 760 |
| 1.6 % | 276 | 19 | | | 1104 |
| 1.8 % | 355 | 23 | | | 1420 |
| 4.0 % | 2150 | 114 | | | 8600 |
| Fluids | | | | | |
| Fluid type | μ [Pa · s] | g' [m · s ⁻²] | μ' [Pa · s] | $\Delta\gamma$ [Pa · m ⁻¹] | |
| Air | 10 ⁻⁵ | 9.8 | 1.2 × 10 ⁻⁴ | 9.8 × 10 ³ | |
| Hexane | 10 ⁻⁴ | 3.4 | 1.2 × 10 ⁻³ | 3.4 × 10 ³ | |
| 1 Cst silicon Oil | 10 ⁻³ | 1.8 | 1.2 × 10 ⁻² | 1.8 × 10 ³ | |
| Mineral Oil | 10 ⁻¹ | 1.5 | 1.2 | 1.5 × 10 ³ | |
| Corn syrup solution | 5 × 10 ⁰ | -4.1 | 6 × 10 ¹ | -4.1 × 10 ³ | |
| Corn syrup/cadmium | 5 × 10 ⁰ | 1.41 | 6 × 10 ¹ | -1.41 × 10 ³ | |
| Mercury | 10 ⁻³ | -126 | 1.2 × 10 ⁻² | -1.26 × 10 ⁵ | |

Table 4.5: Properties of the solids and the fluids used in the experiments of Heimpel and Olson (1994). After the double boundary, the parameters are estimated or derived and not explicitly reported in Heimpel and Olson (1994).

4.11.5 Comparison with experiments

Heimpel and Olson (1994)

We try to compare the experimental investigations performed by Heimpel and Olson (1994) with our numerical results. Their experiments' equivalent solid and fluid properties are reported in table 4.5. The plain strain modulus E' is derived from their shear modulus G with the assumption of a Poisson's coefficient of $\nu \approx 0.5$ (also estimated by them) as

$$E' = \frac{2G(1 + \nu)}{1 - \nu^2}.$$

The toughnesses reported are the ones they obtain using a critical volume. It is interesting to note that this critical volume corresponds to our toughness-dominated head volume $V_{\hat{k}}^{\text{head}}$ (see equation (4.24) of section 4.5). We infer this correspondence because our simulations present a similar kink in the velocity (see figure 4.10a of section 4.8.2) as observed in their experiments. Using this resemblance, we can estimate the fracturing toughness from the critical volume as

$$V^c = \frac{K_{Ic}^{8/3}}{E' \Delta\gamma^{5/3}} \rightarrow K_{Ic}^c = (V^c)^{3/8} E'^{3/8} \Delta\gamma^{5/8}$$

where we use the superscript \cdot^c to indicate the critical volume. We report the result in table 4.6

and observe an acceptable match between the two approaches.

A buoyancy g' is reported for the fluids. From their reported values, we obtain our $\Delta\gamma$ with the assumption of a gelatine density akin to the density of water $\rho_s \approx 1000 [\text{kg} \cdot \text{m}^{-3}]$

$$g' = \frac{\Delta\gamma}{\rho_s} \rightarrow \Delta\gamma = \rho_s g'.$$

Velocity comparison

For a series of experiments, Heimpel and Olson (1994) report the injected volume and fracture velocity (their figure 2). We extract the values of this visualization and scale the results with our \hat{K} head scales (see equation (4.24) of section 4.5) as follows

$$\frac{V}{V_{\hat{k}}^{\text{head}}} = \frac{Q_o E' \Delta\gamma^{5/3} t}{K_{Ic}^{8/3}} = \frac{t}{t_{k\hat{k}}}$$

$$\frac{U}{\partial \ell_{\hat{k}}(t) / \partial t} = \frac{\dot{\ell}(t)}{\dot{\ell}_{\hat{k}}} = \dot{\ell}(t) \frac{Q_o^{2/3} \Delta\gamma^{7/9}}{K_{Ic}^{4/9} \mu^{1/3}}$$

where we estimate the unknown Q_o for laboratory experiments as $Q_o = 1. \times 10^{-8} [\text{m}^3 \cdot \text{s}^{-1}]$. We can thus obtain our numerical velocity using the time steps and increments of height (i.e., $\dot{\ell}(t_i) \approx (\ell_i - \ell_{i-a}) / (t_i - t_{i-1})$) and compare it to their values of U reported in figure two. Similarly, the volume of the abscissa of their figure 2 can be transformed into a dimensionless time using their parameters for the experiments. The so obtained figure is figure 4.10a of section 4.8.2) overlayed with three numerical simulations.

We report for the experiments the obtained value of the dimensionless viscosity $\mathcal{M}_{\hat{k}}$ (equation (4.23) of section 4.4) to derive the length necessary to overcome the transient phase

$$\ell_t \approx 19. \mathcal{M}_{\hat{k}}^{-1/3} \ell_b.$$

In table 4.6, this value is compared with the sample height H_s . We observe that the distance to overcome the transient is generally much larger than the sample size. This indicates that boundary effects due to the finiteness of the sample and the poorly known initiation conditions significantly influence the results.

Breadth comparison

In figure 4.10b of section 4.8.2, we compare three values of fracture breadth from this contribution to the limiting breadth of the \hat{K} -solution of Germanovich et al. (2014). The breadth values

| Experiments of Heimpel and Olson (1994) | | | | | | | | |
|---|--------------------|-------------------------|----------------------|---------------------------------|--------------------------------------|------------------|-------------------------|----------------------------|
| Solid | Fluid | V^c [m ³] | K_{fc}^c [Pa · √m] | \overline{K}_{fc}^c [Pa · √m] | $1 - K_{fc}/\overline{K}_{fc}^c$ [%] | ℓ_t/H_s [-] | Q_o [m ³] | $\mathcal{M}_{\hat{K}}[-]$ |
| 1.4% | Air | $4. \times 10^{-7}$ | 15 | 15 | 0.11 | 55.6 | | 7.8×10^{-7} |
| 1.6% | Air | $6. \times 10^{-7}$ | 20 | | | 64.8 | | $8. \times 10^{-7}$ |
| 1.6% | Hexane | $6. \times 10^{-6}$ | 25 | | | 77.0 | | 3.9×10^{-6} |
| 1.6% | Mineral Oil | 1.5×10^{-5} | 21 | 24.4 | 22.1 | 15.9 | 10^{-8} | 2.3×10^{-3} |
| 1.6% | Mercury | $3. \times 10^{-8}$ | 32 | | | 1.44 | | 4.4×10^{-4} |
| 1.8% | Air | $1. \times 10^{-6}$ | 27 | 27 | 13.9 | 77.0 | | $7. \times 10^{-7}$ |
| 1.8% | Corn syrup/cadmium | | continuous release | | | 5.43 | | 9.5×10^{-2} |
| 4.0% | Air | $1. \times 10^{-5}$ | 124 | 124 | 8.39 | 446 | | $8.8. \times 10^{-8}$ |

Table 4.6: Combinations used for the experiments reported in Heimpel and Olson (1994) and characteristic values derived.

| Breadth evaluation | | | | |
|--------------------|--------------------|--|-------------------------------------|--|
| Solid | Fluid | Measured breadth b^{obs} [cm] | Predicted breadth b^{pred} | $ 1 - b^{\text{obs}}/b^{\text{pred}} $ [%] |
| 1.4 % | Air | 1.5 | 0.9 | 65.4 |
| 1.8 % | Corn syrup/cadmium | 5.6 | 4.4 | 27.5 |
| 4.0 % | Air | 5.2 | 3.5 | 48.3 |

Table 4.7: Comparison of finger-like toughness-dominated fracture breadth with the experiments of Heimpel and Olson (1994) shown in their figures 8 and 9.

Chapter 4. Three-dimensional buoyant hydraulic fractures: constant release from a point source

are extracted from figures 8 and 9 of Heimpel and Olson (1994). We list the values in table 4.7 along with their relative error.

Taisne and Tait (2009)

We use the table of breadths reported in Taisne and Tait (2009) to compare their breadth to the predicted breadth from the \hat{K} -solution of Germanovich et al. (2014). We use their values of Young's modulus reported in their table 1 and again estimate the Poisson's coefficient of the gelatine as $\nu \approx 0.5$. As they directly report $\Delta\rho$, we obtain the buoyancy $\Delta\gamma$ by simple multiplication with the earth acceleration $g = 9.81 \text{ [m} \cdot \text{s}^{-2}]$. We document our values in table 4.8, where the experiment N° corresponds to the value reported in table 1 of Taisne and Tait (2009). The definitions of b^{obs} and b^{pred} are as in table 4.7.

| Experiments of Taisne and Tait (2009) | | | | | | | | | | |
|---------------------------------------|----------|--|-----------------------|-----------|-----------|--|--|------------------------|--|--|
| experiment N° | E [Pa] | $\Delta\rho$ [$\text{kg}\cdot\text{m}^{-3}$] | b^{obs} [cm] | ν [-] | E' [Pa] | K_{Ic} [$\text{Pa}\cdot\sqrt{\text{m}}$] | $\Delta\gamma$ [$\text{Pa}\cdot\text{m}^{-1}$] | b^{pred} [cm] | $ 1 - b^{\text{obs}}/b^{\text{pred}} $ [%] | |
| 7 | 5352 | 240 | 11.6 | | 7136.00 | 69.50 | 2354.4 | 6.52 | 77.87 | |
| 8 | 5352 | 240 | 8.2 | | 7136.00 | 69.50 | 2354.4 | 6.52 | 25.7 | |
| 9 | 1544 | 103 | 7.4 | | 2058.67 | 37.32 | 1010.4 | 7.57 | 2.29 | |
| 10 | 1544 | 240 | 9.6 | | 2058.67 | 37.32 | 2354.4 | 4.31 | 122 | |
| 11 | 6950 | 240 | 6.7 | | 9266.67 | 79.20 | 2354.4 | 7.11 | 5.83 | |
| 12 | 2338 | 102 | 1.14 | | 3117.33 | 45.94 | 1000.6 | 8.75 | 30.2 | |
| 14 | 1787 | 102 | 8.1 | | 2382.67 | 40.16 | 1000.6 | 8.00 | 1.20 | |
| 15 | 2129 | 102 | 8.0 | | 2838.67 | 43.83 | 1000.6 | 8.48 | 5.71 | |
| 16 | 1903 | 373 | 6.2 | 0.5 | 2537.33 | 41.44 | 3659.1 | 3.44 | 80.1 | |
| 17 | 1903 | 373 | 4.8 | | 2537.33 | 41.44 | 3659.1 | 3.44 | 39.4 | |
| 20 | 1843 | 255 | 5.8 | | 2457.33 | 40.78 | 2501.6 | 4.39 | 32.1 | |
| 22 | 2770 | 373 | 7.01 | | 3693.33 | 50.00 | 3659.1 | 3.90 | 79.6 | |
| 23 | 2770 | 373 | 7.25 | | 3693.33 | 50.00 | 3659.1 | 3.90 | 85.8 | |
| 24 | 2770 | 373 | 3.3 | | 3693.33 | 50.00 | 3659.1 | 3.90 | 15.4 | |
| 25 | 1102 | 373 | 6.0 | | 1469.33 | 31.54 | 3659.1 | 2.87 | 109 | |
| 26 | 3402 | 373 | 8.5 | | 4536.00 | 55.41 | 3659.1 | 4.18 | 103 | |
| 28 | 3402 | 186 | 7.6 | | 4536.00 | 55.41 | 1824.7 | 6.65 | 14 | |

Table 4.8: Breadth comparison for the finite volume release experiments of Taisne and Tait (2009).

5 Three-dimensional buoyant hydraulic fractures: finite volume release

This chapter is a modified version of an article submitted to the Journal of Fluid Mechanics (JFM).

Möri, A. and Lecampion, B. (2023). Three-dimensional buoyant hydraulic fractures: Finite volume release. *Submitted to: J. Fluid Mech.*, ArXiv: 2304.00907v1.

Contributions

Andreas Möri has conceptualized the problem, performed a formal and scaling analysis, decided on the methodology, adapted the numerical solver, committed validation against known results, generated the visualizations, wrote the original draft, and edited the manuscript iteratively. Brice Lecampion acted as supervisor, supported the conceptualization and methodology, supervised the formal and scaling analysis, acquired the funding, and reviewed and edited the text in iterations with Andreas Möri.

5.1 Abstract

In impermeable media, a hydraulic fracture can continue expanding even without additional fluid injection if its volume exceeds the limiting volume of a hydrostatically loaded radial fracture. This limit depends on the mechanical properties of the surrounding solid and the density contrast between the fluid and the solid. We show that two dimensionless numbers characterize self-sustained fracture growth. The first is a buoyancy factor that compares the total released volume to the volume of a hydrostatically loaded radial fracture to determine whether buoyant growth occurs. The second number is the dimensionless viscosity of a radial fracture when buoyant effects become of order one. This dimensionless viscosity notably depends on the rate at which the fluid volume is released, indicating that both the total volume and release history impact self-sustained buoyant growth. We identify six well-defined propagation histories based on these two dimensionless numbers. Their growth evolves between distinct limiting regimes of radial and buoyant propagation, resulting in different fracture shapes. Our findings notably reveal two growth rates depending on the dominant energy dissipation mechanism (viscous flow vs fracture creation) in the fracture head. For finite values of material toughness, the toughness-dominated limit represents a late-time solution for all fractures in growth rate and head shape (possibly reached only at a very late time). The viscosity-dominated limit can appear at intermediate times. Our three-dimensional simulations confirm the predicted scalings. This contribution highlights the importance of the entire propagation and release history for accurate analysis of buoyant hydraulic fractures.

5.2 Introduction

This work investigates the growth of a planar three-dimensional (3D) hydraulic fracture (HF) from the release of a finite volume of fluid from a point source and its possible transition to a self-sustained buoyant fracture. Hydraulic fractures are tensile, fluid-filled fractures driven by the internal fluid pressure exceeding the minimum compressive in-situ stress (Detournay, 2016). Natural occurrences of HFs are related to the transport of magma through the lithosphere by magmatic intrusions (Rivalta et al., 2015; Spence et al., 1987; Lister and Kerr, 1991) or pore pressure increases due to geochemical reactions during the formation of hydrocarbon reservoirs (Vernik, 1994). One of the most frequent engineering applications of HFs is the production stimulation of hydrocarbon wells (Economides and Nolte, 2000; Smith and Montgomery, 2015; Jeffrey et al., 2013).

In the absence of buoyancy, the propagation of radial hydraulic fractures upon the end of the release (denoted as "shut-in" in industrial applications) has recently been analyzed in detail (see chapter 3). In an impermeable medium, the final radius of the HF solely depends on the material parameters and the total amount of fluid volume injected/released. However, the HF does not necessarily stop its growth directly upon the end of the release. When dissipation through viscous fluid flow is important at the end of the release, the propagation continues in a viscosity-dominated pulse regime before finally arresting at a radius independent of the release

rate. These theoretical findings derived in chapter 3 were recently verified experimentally by Tanikella et al. (2023).

When considering gravity, recent research has focused on deriving the limiting volume necessary for the emergence of a three-dimensional buoyant fracture (Dahm, 2000b; Davis et al., 2020; Salimzadeh et al., 2020; Smittarello et al., 2021). Neglecting fluid viscosity, Davis et al. (2020) identify a critical volume similar to previous two-dimensional (2D) predictions (Weertman, 1971). It is, however, impossible to constrain the ascent rate of the fracture without accounting for the effect of fluid viscosity (as discussed in Garagash and Germanovich (2014)). The consensus of these studies is that the resulting buoyant fracture features a head and tail structure (Lister and Kerr, 1991), where the head dominates the overall fracture behavior, but the tail dominates the ascent rate (Garagash and Germanovich, 2022) (see figure 5.1). Davis et al. (2023) estimate a maximum ascent velocity considering a viscosity-dominated tail. A similar solution has been derived by Garagash and Germanovich (2014) (see Garagash and Germanovich (2022) for details) for a finger-like fracture with a toughness-dominated head. In their work, they derive a three-dimensional (3D) head similar to the limiting volume of Davis et al. (2020). This fracture "head" is coupled to a tail of constant length, providing a late-time solution after the transition from radial to self-sustained buoyant propagation. Considering lubrication flow in the initially radially propagating fracture, Salimzadeh et al. (2020) performed a few simulations investigating the early phase of the transition to buoyant propagation. Equivalent to Davis et al. (2020) and Garagash and Germanovich (2014), a limiting value for the necessary volume released for a buoyant fracture to emerge is reported. All three minimal/critical volume release estimates have the same characteristic scale and only differ in prefactors. A combined study of the limiting volume, considering the emergence of buoyancy-driven fractures and their evolution towards their late-time characteristics, is not yet available.

5.3 Preliminaries

We investigate tensile (mode I) hydraulic fractures under the classical assumption of linear elastic fracture mechanics (LEFM) and laminar Newtonian lubrication flow (Detournay, 2016). A finite volume is released from a point source at depth into a linearly elastic and impermeable medium with uniform properties. The fracture orientation and stress state are equivalent to the one described in chapter 4 and sketched in figure 5.1. We omit the detailed discussion of the mathematical formulation (see section 4.3.1 of chapter 4 for details) as the only difference pertains to the history of the fluid release. We consider here a simple injection history where the fluid volume is released at a constant rate until the end of the release at time $t = t_s$ (the shut-in time), where the rate suddenly drops to zero. We denote the constant release rate during the block injection as Q_o such that the rate history is:

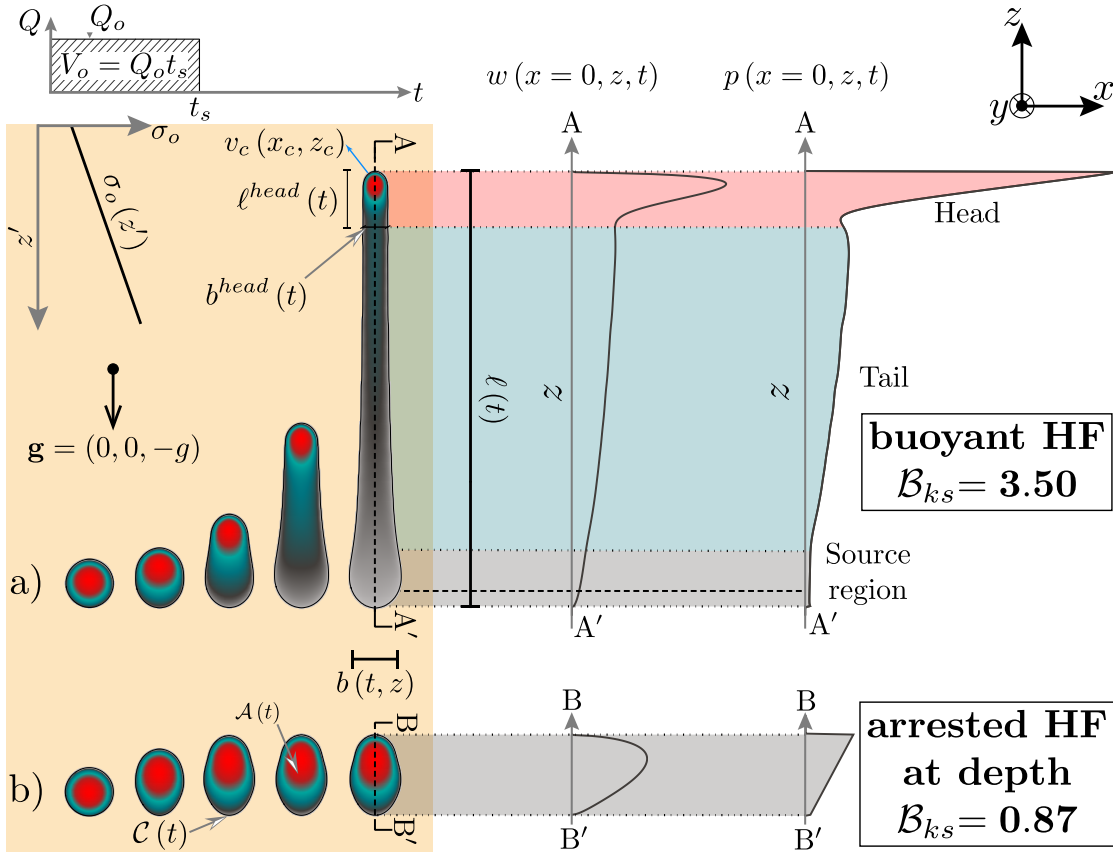


Figure 5.1: a) Buoyant self-sustained growth of a hydraulic fracture. b) Arrested hydraulic fracture at depth. Both fractures emerge from a finite fluid volume released from a point source through a block injection and propagate in a homogeneous linear elastic medium ($x|z$ plane) with the downwards oriented gravity vector \mathbf{g} (in $-z$) creating a linear confining stress $\sigma_o(z)$. Fracture area is denoted by $\mathcal{A}(t)$ with a closed front $\mathcal{C}(t)$ and a local normal velocity $v_c(x_c, z_c)$ (with $(x_c, z_c) \in \mathcal{C}(t)$). The fracture extent is defined by its local breadth $b(z, t)$ and total length $\ell(t)$.

$$Q(t) = \begin{cases} Q_o & t \leq t_s \\ 0 & t > t_s \end{cases}. \quad (5.1)$$

The coherent global volume balance in the case of an impermeable medium is

$$\mathcal{V}(t) = \int_{\mathcal{A}(t)} w(t, x, z) dx dz = \begin{cases} Q_o t & t < t_s \\ V_o = Q_o t_s & t \geq t_s \end{cases}, \quad (5.2)$$

where $V_o = Q_o t_s$ is the total volume of fluid released.

In the following, we combine scaling arguments and numerical simulations using the fully-coupled planar 3-D hydraulic fracture solver PyFrac (Zia and Lecampion, 2020). We refer the reader to Zia and Lecampion (2020); Peirce and Detournay (2008) and references therein for a detailed description of the numerical scheme. In short, the solver is a Python-based displacement discontinuity method combined with the implicit level set algorithm implemented using boundary elements. The documentation of the open-source code and examples of applications are available for download at PyFrac. We initiate the fracture according to the self-similar solution of a radial, viscosity-dominated fracture (see its definition in Savitski and Detournay (2002)) at a fixed time t_{init} . For this solution to be valid, we must ensure that the dimensionless numbers describing the transition from viscosity- to toughness-dominated ($\mathcal{K}_m(t)$ (5.4)) and the change from radial to buoyant propagation ($\mathcal{B}_k(t)$ and $\mathcal{B}_m(t)$ (5.9)) are all significantly smaller than one at $t = t_{init}$. We provide the time of initialisation and other parameters of the simulations in the shared data of this chapter. Note that we could equivalently initiate our simulations with a finite size, radial fracture with a radius smaller than the respective transition scales ℓ_{mk} , $\ell_{m\hat{m}}$, and $\ell_{k\hat{k}}$ (see Savitski and Detournay (2002) and chapter 4). The simulation would then automatically approach the self-similar, viscosity-dominated solution. Note that in any case, we need to ensure that $t_{init} \ll t_s$ or equivalently for a finite size fracture, $\ell_{init} \ll R_a$ (5.3).

5.3.1 Arrest of a finite volume radial hydraulic fracture without buoyancy

In the absence of buoyant forces, considering the limiting case of an impermeable medium, hydraulic fractures finally arrest after the end of the injection when reaching an equilibrium between the injected volume and the linear elastic fracture mechanics propagation condition. This problem was investigated in chapter 3. The fracture characteristics at arrest are independent of the shut-in time t_s . They only depend on the properties of the solid and the total amount of fluid released. For example, the arrest radius R_a (subscript a for arrest) is given by

$$R_a = \left(\frac{3}{8\sqrt{\pi}} \right)^{2/5} \left(\frac{E' V_o}{K_{Ic}} \right)^{2/5}, \quad (5.3)$$

Chapter 5. Three-dimensional buoyant hydraulic fractures: finite volume release

where $E' = E / (1 - \nu^2)$ is the plane-strain modulus with E the materials Young's modulus and ν its Poisson's ratio, and K_{Ic} the fracture toughness of the material.

Even though the arrest radius is independent of t_s , the growth history prior to arrest depends on it. In particular, the arrest is not necessarily immediately after the end of the release. This is notably the case when the hydraulic fracture propagates in the viscosity-dominated regime at the end of the release. The immediate arrest versus continuous growth is captured by the value of the dimensionless toughness at the shut-in time:

$$\mathcal{K}_{ms} = K_{Ic} \frac{t_s^{1/9}}{E'^{13/18} \mu'^{5/18} Q_o^{1/6}}. \quad (5.4)$$

where $\mu' = 12\mu$ and μ is the fracturing fluid viscosity. In (5.4), we have used the subscripts m and s to indicate a viscous scaling and the end of the release, respectively. If the fracture is viscosity-dominated ($\mathcal{K}_{ms} \ll 1$), it propagates in a viscosity-dominated pulse regime for a while until it finally arrests when reaching $R = R_a$. On the other hand, if fracture energy is already dominating ($\mathcal{K}_{ms} \gg 1$), the arrest is immediate upon shut-in. The viscosity-dominated pulse regime has been shown to emerge for $\mathcal{K}_{ms} \lesssim 0.3$ (for a detailed description of the viscosity-dominated pulse regime, see section 3.4.2 of chapter 3). Numerical estimation of the immediate arrest yields a value of $\mathcal{K}_{ms} \gtrsim 0.8$ (note that in chapter 3 we report a value of 2.5 due to an alternative definition of (5.4) using $K' = \sqrt{32/\pi} K_{Ic}$ instead of K_{Ic}).

5.3.2 Buoyant hydraulic fracture under a continuous release

In the case of a fluid release occurring at a constant volumetric rate Q_o , the fracture elongates along the orientation of the gravity vector. These buoyant forces are generated by the density difference between the solid and the fracturing fluid. To obtain the value of the buoyancy, we assume fractures propagating in vertical planes and the minimum in-situ horizontal stress as

$$\sigma_o(z) = \sigma_h(z) = \alpha \sigma'_v(z) + p_p(z) \quad (5.5)$$

with σ_h the minimum in-situ horizontal stress, σ'_v the effective vertical stress, α a lateral earth pressure coefficient, and p_p the pore pressure in the formation. Assuming now that the vertical stress is lithostatic $\sigma_v = \rho_s g z'$, and the formation fluid pressure hydrostatic $p_p = \rho_F g z'$, the gradient of the stress normal to the fracture plane is (in the coordinate system sketched in figure 5.1)

$$\nabla \sigma_o = (\alpha(\rho_s - \rho_F) + \rho_F) \mathbf{g} \quad (5.6)$$

where ρ_s is the solid and ρ_F the formation fluid density, g is the Earth's gravitational acceleration coefficient, and $\mathbf{g} = (0, 0, -g)$ the gravity vector. Using the net pressure ($p = p_f - \sigma_o$) in

the Poiseuille relation, we obtain the following expression

$$\mathbf{q}(x, z, t) = -\frac{w(x, z, t)^3}{\mu'} \left(\nabla p(x, z, t) + \Delta\gamma \frac{\mathbf{g}}{|\mathbf{g}|} \right) \quad (5.7)$$

$$\text{with: } \Delta\gamma = (\alpha(\rho_s - \rho_F) + \rho_F - \rho_f)g. \quad (5.8)$$

In equation (5.8), $\Delta\gamma$ is the effective buoyancy contrast of the system. A positive buoyancy will lead to a fracture elongation in the opposite direction of the gravity vector. A negative buoyancy will lead to propagation in the direction of the gravity vector. Without additional stresses (e.g. tectonic stresses), the lateral earth pressure coefficient can be approximated as $\alpha = \nu/(1 - \nu)$. In the following, we include any tectonic or other effects into α and assume, consistent with equation (5.8), that $\Delta\gamma = \text{cst}$. Note that the expression of $\Delta\gamma$ differs from the one in chapter 4 where we assumed a dry formation (e.g. $p_p = 0$). Two dimensionless buoyancies related either to the viscosity dominated (subscript m) or the toughness-dominated regime (subscript k) emerge (see chapter 4):

$$\mathcal{B}_m = \Delta\gamma \frac{Q_o^{1/3} t^{7/9}}{E'^{5/9} \mu'^{4/9}}, \quad \mathcal{B}_k = \Delta\gamma \frac{E'^{3/5} Q_o^{3/5} t^{3/5}}{K_{Ic}^{8/5}}. \quad (5.9)$$

These dimensionless buoyancies are related through the dimensionless viscosity of a radial fracture when buoyancy becomes of order $\mathcal{O}(1)$:

$$\mathcal{M}_{\hat{k}} = \mu' \frac{Q_o E'^3 \Delta\gamma^{2/3}}{K_{Ic}^{14/3}} \quad (5.10)$$

as

$$\mathcal{B}_k = \mathcal{B}_m^{27/35} \mathcal{M}_{\hat{k}}^{12/35}. \quad (5.11)$$

Similar to the dimensionless toughness at the end of the release \mathcal{K}_{ms} (5.4), $\mathcal{M}_{\hat{k}}$ defines if the transition from a radial to an elongated buoyant fracture occurs in the viscosity- ($\mathcal{M}_{\hat{k}} \gg 1$) or toughness-dominated ($\mathcal{M}_{\hat{k}} \ll 1$) phase of the radial hydraulic fracture propagation. A family of solutions emerges as a function of this dimensionless viscosity $\mathcal{M}_{\hat{k}}$ as discussed in detail in chapter 4. Notably, a limiting large toughness solution has been obtained in Garagash and Germanovich (2014) (see details in Garagash and Germanovich (2022)). This large toughness limit is observed for $\mathcal{M}_{\hat{k}} \leq 10^{-2}$ (see notably section 4.5 of chapter 4) and shows a buoyant finger-like fracture with a constant breadth and a fixed-volume head. These attributes, combined with a constant injection rate, lead to a linear growth rate of the buoyant fracture. In an intermediate range of values for $\mathcal{M}_{\hat{k}} \in [10^{-2}, 10^2]$, the fractures exhibit a uniform horizontal breadth and a finger-like shape. In this range of $\mathcal{M}_{\hat{k}}$, the prefactors (for

length, width, etc.) become dependent on the dimensionless viscosity $\mathcal{M}_{\hat{k}}$ (5.4). Particularly, an increase in fracture breadth and head volume is observed with increasing values of $\mathcal{M}_{\hat{k}}$. Even larger values of $\mathcal{M}_{\hat{k}} \geq 10^2$ generate fractures exhibiting a negligible toughness, buoyant solution at intermediate times, where the growth of the fracture is sub-linear. The breadth of these fractures increases for a while before reaching an ultimately constant value related to the non-zero fracture toughness value. The fracture's growth rate then becomes constant. Concurrently, the head and tail structure stabilizes. In the strictly zero-toughness limit, the breadth continuously increases, and the fracture height growth always remains sub-linear as a consequence of global volume balance.

5.3.3 Hydrostatically loaded radial fracture

The occurrence of the self-sustained buoyant growth of a finite volume fracture has been investigated by several authors from the point of view of the static linear elastic equilibrium of a radial fracture under a linearly varying load (Davis et al., 2020; Salimzadeh et al., 2020; Davis et al., 2023). Under the hypothesis of zero viscous flow, the net loading opening the fracture is equal to the hydrostatic fluid pressure minus the linearly varying background stress $\sigma_o(z)$. The elastic solution and the evolution of the stress intensity factor at the upper and lower tip are known analytically for this loading (Tada et al., 2000) (see section 2.2 of Davis et al. (2020) for a detailed derivation). Adopting a LEFM propagation condition, the stress-intensity factor (SIF) K_I at the upper end is set to the material fracture toughness K_{Ic} . On the other hand, the lower tip SIF is set to zero, allowing the fracture to close and liberate the volume necessary for further upward propagation. Enforcing the conditions of $K_I = K_{Ic}$ at the upper and $K_I = 0$ at the lower tip constrains the limiting volume to

$$V_{\text{limit}} \propto \frac{K_{Ic}^{8/3}}{E' \Delta \gamma^{3/5}} = V_{\hat{k}}^{\text{head}} \quad (5.12)$$

This minimal volume for buoyant propagation has been independently identified in recent contributions (Davis et al., 2020; Salimzadeh et al., 2020; Davis et al., 2023) and corresponds to the one of the toughness-dominated head of a buoyant hydraulic fracture in the case of a constant release (see Garagash and Germanovich (2014) and chapter 4).

If the volume of fluid released in the radial fracture is slightly larger than this value, the upper tip would have a stress intensity $K_I > K_{Ic}$, indicating excess energy leading to upward propagation. Similarly, the lower end would have $K_I < 0$ and the fracture would interpenetrate. Small perturbations of the released volume around this minimum would lead to either an arrest of the fracture (lower volume) or a departure of a buoyant fracture (larger volume). Note that when the fracture volume equals this minimal volume and fluid viscosity is neglected, the previous derivation fails to predict how the fracture will subsequently propagate. Only the introduction of fluid viscosity can resolve the physical limitation of this approach.

5.4 Arrest at depth vs. self-sustained propagation of buoyant hydraulic fractures

In addition, the previous derivation of the minimum volume for a buoyant self-sustained propagation assumes a perfectly radial shape until the entire fluid volume has been released. This approach is equivalent to considering buoyancy only at this moment. It does not cover cases where buoyant forces become non-negligible when the fracture is still propagating (whether this is the case during the release or after its end).

5.4 Arrest at depth vs. self-sustained propagation of buoyant hydraulic fractures

From the discussion of the arrest radius of a hydraulic fracture in the absence of buoyancy (see section 5.3.1) and the regimes of buoyant hydraulic fracture growth under a continuous release (see section 5.3.2), we can anticipate several scenarios for the emergence of a self-sustained buoyant finite volume fracture. The transition toward buoyancy-driven growth can occur during the release of fluid or the pulse propagation phase, when the propagation is viscosity-dominated at the end of the release. We investigate these different propagation histories in relation to the dimensionless buoyancies and dimensionless buoyant viscosity introduced in section 5.3 and discuss their relationship with the critical minimum volume (5.12).

5.4.1 Toughness-dominated at the end of the release

We first investigate the case where the fracture is toughness-dominated at the end of the release. In the absence of buoyancy, a constant fluid pressure establishes in the penny-shaped fracture, which immediately stops at its arrest radius R_a (see equation (5.3)). Due to the addition of buoyant effects, a linear pressure gradient develops and creates the configuration discussed above (see section 5.3.3). We anticipate that the total volume released must exceed $V_{\hat{k}}^{\text{head}}$ (5.12) for a buoyant fracture to emerge. Neglecting the temporal evolution, the comparison $V_o / V_{\hat{k}}^{\text{head}}$ is sufficient to assess the emergence of buoyant fractures. When considering a radial growth in time, the dimensionless buoyancy $\mathcal{B}_k(t)$ (5.9) indicates when buoyant forces become dominant. Estimating $\mathcal{B}_k(t)$ at the end of the release $t = t_s$, we obtain

$$\mathcal{B}_{ks} = \mathcal{B}_k(t = t_s) = \Delta\gamma \frac{E'^{3/5} Q_o^{3/5} t_s^{3/5}}{K_{Ic}^{8/5}} = \Delta\gamma \frac{E'^{3/5} V_o^{3/5}}{K_{Ic}^{8/5}} = \left(\frac{V_o}{V_{\hat{k}}^{\text{head}}} \right)^{3/5}. \quad (5.13)$$

From this last relation (5.13), we see that the condition of a dimensionless buoyancy at the end of the release $\mathcal{B}_{ks} > 1$ (under the hypothesis of a radial toughness-dominated fracture) is strictly equivalent to the condition of a released volume larger than the minimal volume for buoyant growth (5.12).

5.4.2 Viscosity-dominated at the end of the release $\mathcal{K}_{ms} \ll 1$

In contrast to toughness-dominated hydraulic fractures, radial viscosity-dominated fractures at the end of the release will continue to propagate in a viscous-pulse regime until they reach their arrest radius R_a (5.3) (see section 3.4.1 of chapter 3). During that post-release propagation phase, the fracture may become buoyant and continue its growth as a result. In addition, we need to check if it remains buoyant when it is already so at the end of the release. This can be done by estimating the dimensionless buoyancy of a radial viscous fracture $\mathcal{B}_m(t)$ (5.9) at the end of the release $t = t_s$:

$$\mathcal{B}_{ms} = \mathcal{B}_m(t = t_s) = \Delta\gamma \frac{Q_o^{1/3} t_s^{7/9}}{E'^{5/9} \mu'^{4/9}} = \Delta\gamma \frac{V_o^{1/3} t_s^{4/9}}{E'^{5/9} \mu'^{4/9}}. \quad (5.14)$$

A value of $\mathcal{B}_{ms} \geq 1$ indicates that the fracture has already transitioned to buoyant propagation when the release stops and is already elongated. On the other hand, if $\mathcal{B}_{ms} < 1$, buoyancy is not of primary importance at the end of the release, and the fracture still exhibits a radial shape.

Dominant buoyancy at the end of the release $\mathcal{B}_{ms} \geq 1$

In the case $\mathcal{B}_{ms} \geq 1$, the fracture is already buoyant at the end of the release. We must check if it remains buoyant or possibly arrests after the release ends. It is natural to compare the volume of the viscous head at the end of the release $V_{\hat{m}}^{\text{head}}(t = t_s)$ to the limiting volume (equation (5.12)). The time-dependent volume of a viscous head is given in equation (4.34) of chapter 4 and relates to equation (5.14) as

$$\mathcal{B}_{ms} = \left(\frac{V_o}{V_{\hat{m}}^{\text{head}}(t = t_s)} \right)^{2/3}. \quad (5.15)$$

Using the relationship of equation (5.11), we obtain the following relation with the minimal limiting volume:

$$\frac{V_o}{V_{\hat{k}}^{\text{head}}} = \left(\frac{V_o}{V_{\hat{m}}^{\text{head}}(t = t_s)} \right)^{6/7} \mathcal{M}_{\hat{k}}^{4/7}.$$

For a viscosity-dominated fracture, one necessarily has $\mathcal{M}_{\hat{k}} \geq 1$ and to be buoyant at the end of the release, we necessarily have $V_o \geq V_{\hat{m}}^{\text{head}}(t = t_s)$ as $\mathcal{B}_{ms} \geq 1$. As a result of the previous relations, we necessarily have $V_o \geq V_{\hat{k}}^{\text{head}}$, respectively $\mathcal{B}_{ks} \geq 1$ and the volume released is larger than the minimum required for a toughness-dominated radial fracture subjected to a linear pressure gradient to become buoyant. After the release ends, the viscous forces diminish in the head, ultimately becoming toughness-dominated. As a result, after the release,

5.4 Arrest at depth vs. self-sustained propagation of buoyant hydraulic fractures

as buoyancy is of order one, the condition $\mathcal{B}_{ks} \geq 1$ is always satisfied, and self-sustained buoyant growth will necessarily continue.

Viscosity-dominated fracture with negligible buoyant forces at the end of the release $\mathcal{B}_{ms} < 1$

If buoyancy forces are negligible at the end of the release, and the propagation is viscosity-dominated ($\mathcal{B}_{ms} < 1$ and $\mathcal{K}_{ms} \ll 1$), the finite volume fracture will continue to grow radially in a viscous-pulse regime for a while before it finally arrests. In the presence of buoyant forces, it may be possible that buoyancy takes over as a driving mechanism before the fracture arrests. To incorporate such a possible growth history into the analysis, we use a dimensionless buoyancy in such a radial viscous pulse regime:

$$\mathcal{B}_m^{[V]}(t) = \Delta\gamma \frac{V_o^{1/3} t^{4/9}}{E'^{5/9} \mu'^{4/9}} = \mathcal{B}_{ms} (t/t_s)^{4/9}, \quad (5.16)$$

where the superscript $[V]$ indicates that the scaling is related to a finite volume release (replacing Q_o by V_o/t in the continuous release expression). From chapter 3, the radial viscous pulse fracture stops propagating when it becomes toughness-dominated. The corresponding time scale for which $\mathcal{K}_m^{[V]}$ of a finite volume radial hydraulic fracture in the absence of buoyancy (see equation (3.10) in chapter 3) becomes of order one, and the fracture arrests is given by

$$t_{mk}^{[V]} = \frac{E'^{13/5} V_o^{3/5} \mu'}{K_{Ic}^{18/5}}. \quad (5.17)$$

It is thus possible to check if buoyancy is of order one at this characteristic time of arrest by estimating the value of the dimensionless buoyancy $\mathcal{B}_m^{[V]}(t)$ (5.16) at $t = t_{mk}^{[V]}$:

$$\mathcal{B}_m^{[V]}(t = t_{mk}^{[V]}) = \Delta\gamma \frac{E'^{3/5} V_o^{3/5}}{K_{Ic}^{8/5}} = \left(\frac{V_o}{V_{\hat{k}}^{\text{head}}} \right)^{3/5} = \mathcal{B}_{ks}. \quad (5.18)$$

Interestingly, this evaluation is strictly equivalent to the comparison of the limiting $V_{\hat{k}}^{\text{head}}$ with the total released volume V_o (see equation (5.13)). We conclude that regardless of the propagation history, the comparison of the released volume with the limiting volume for toughness-dominated buoyant growth is sufficient to characterize the emergence of a self-sustained buoyant hydraulic fracture. In what follows, we use the dimensionless buoyancy of a radial toughness-dominated finite volume hydraulic fracture \mathcal{B}_{ks} to quantify the emergence of self-sustained growth ($\mathcal{B}_{ks} > 1$). Similarly, the volume ratio $V_o/V_{\hat{k}}^{\text{head}} = \mathcal{B}_{ks}^{5/3}$ could also be used.

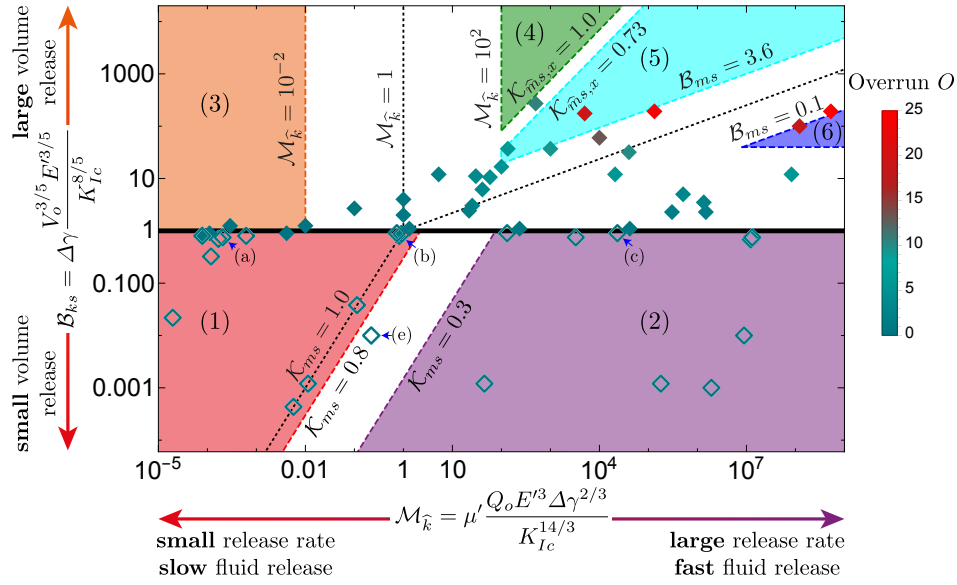


Figure 5.2: Structure of the solution for a finite volume release hydraulic fracture as a function of the dimensionless buoyancy \mathcal{B}_{ks} (5.13) and viscosity $\mathcal{M}_{\hat{k}}$ (5.10). Each symbol represents a simulation. Arrested fractures have empty symbols, and filled symbols indicate self-sustained buoyancy-driven pulses. Numbered areas of different colors delimit distinct propagation histories. The color of the symbols represents the value of the horizontal overrun O (5.22). We indicate the simulations presented in figure 5.3 via blue arrows.

5.4.3 Structure of the solution for a finite volume release

In the preceding subsections, the necessary and sufficient condition for the birth of a buoyant fracture $\mathcal{B}_{ks} \geq 1$ (see equation (5.13)) was derived. The fact that the birth (or not) of a buoyant hydraulic fracture solely depends on the total released volume and elastic parameters but is independent of how the volume is accumulated intrinsically derives from this statement. Furthermore, we discussed that the characteristics of self-sustained buoyant fractures depend additionally on the dimensionless viscosity $\mathcal{M}_{\hat{k}}$ (see equation (5.10)), and hence on the specifics of the release (how the volume got released). These two parameters combined encompass any possible configuration and thus form the parametric space of the entire problem (see figure 5.2).

First, the parametric space can be split into an upper half ($\mathcal{B}_{ks} \geq 1$) where self-sustained buoyant propagation occurs and a lower part ($\mathcal{B}_{ks} < 1$) where the fractures ultimately arrest at depth. We have numerically investigated this limit, where every symbol in figure 5.2 corresponds to a simulation. Empty symbols show simulations where the fracture ultimately arrests at depth, whereas filled symbols correspond to cases where self-sustained buoyant growth occurs. In general, figure 5.2 shows that the scaling argument that self-sustained buoyant growth occurs for $\mathcal{B}_{ks} \geq 1$ is correct without any prefactor. Only toughness-dominated fractures at the end of the release ($\mathcal{K}_{ms} \geq 0.8$ where no post-injection radial propagation occurs) sometimes lead to self-sustained buoyant growth for values of \mathcal{B}_{ks} slightly smaller than 1. We use a value

5.4 Arrest at depth vs. self-sustained propagation of buoyant hydraulic fractures

| Region | Limiting regimes encountered | Range of applicability | |
|----------------|---|--|--|
| 1 (red) | $M \rightarrow K \rightarrow K^{[V]}$ | $0.30 \mathcal{M}_{\hat{k}}^{3/2} \leq \mathcal{B}_{ks} < 1$ | $\mathcal{M}_{\hat{k}} \leq 2.23$ |
| 2 (purple) | $M \rightarrow M^{[V]} \rightarrow K^{[V]}$ | $\mathcal{B}_{ks} < 1$ | $76 \mathcal{B}_{ks}^{2/3} \leq \mathcal{M}_{\hat{k}}$ |
| 3 (orange) | $M \rightarrow K \rightarrow \hat{K} \rightarrow \hat{K}^{[V]}$ | $1 \leq \mathcal{B}_{ks}$ | $\mathcal{M}_{\hat{k}} \leq 10^{-2}$ |
| 4 (dark green) | $M \rightarrow \hat{M} \rightarrow \hat{K} \rightarrow \hat{K}^{[V]}$ | $\mathcal{M}_{\hat{k}}^{24/35} \leq \mathcal{B}_{ks}$ | $10^2 \leq \mathcal{M}_{\hat{k}}$ |
| 5 (light blue) | $M \rightarrow \hat{M} \rightarrow \hat{M}^{[V]} \rightarrow \hat{K}^{[V]}$ | $3.98 \mathcal{M}_{\hat{k}}^{12/35} \leq \mathcal{B}_{ks} \leq 0.40 \mathcal{M}_{\hat{k}}^{24/35}$ | $10^2 \leq \mathcal{M}_{\hat{k}}$ |
| 6 (dark blue) | $M \rightarrow M^{[V]} \rightarrow \hat{M}^{[V]} \rightarrow \hat{K}^{[V]}$ | $40 \leq \mathcal{B}_{ks} \leq 0.17 \mathcal{M}_{\hat{k}}^{12/35}$ | $8.25 \times 10^6 \leq \mathcal{M}_{\hat{k}}$ |

Table 5.1: The regions of figure 4.11 with their respective propagation history and the estimated limiting values of the dimensionless coefficients. The descriptions of the limiting regimes can be found in Savitski and Detournay (2002) for the M and K regimes, chapter 3 for the $M^{[V]}$ and $K^{[V]}$ regimes, chapter 4 for the \hat{M} and \hat{K} regimes, and in this chapter for the $\hat{M}^{[V]}$ and $\hat{K}^{[V]}$ regimes (see appendix 5.9.1 for a summary of the scalings).

of $\mathcal{B}_{ks} = 1$ as the limit for the birth of a self-sustained finite volume buoyant hydraulic fracture. This limit is close to the results obtained in previous contributions: $\mathcal{B}_{ks} \approx 0.90$ for Davis et al. (2020) and $\mathcal{B}_{ks} \approx 0.91$ for Salimzadeh et al. (2020). The equivalent value of \mathcal{B}_{ks} calculated from the semi-analytically derived head volume of a propagating toughness-dominated buoyant fracture by Garagash and Germanovich (2014) is significantly higher: $\mathcal{B}_{ks} \approx 1.26$.

The parametric space of figure 5.2 captures more than the limit between fractures that ultimately arrest and self-sustained buoyant pulses. We distinguish six well-defined regions, corresponding to several propagation histories visiting the limiting regimes of radial and buoyant growth: stagnant fractures with a toughness-dominated end of the release (region 1; bottom left - red, section 5.5), stagnant fractures with a viscosity-dominated end of the release (region 2; bottom right - purple, section 5.5), toughness-dominated buoyant fractures at the end of the release (region 3; top left - orange, section 5.6.1), viscosity-dominated buoyant fractures with a stabilized breadth at the end of the release (region 4; top centre - dark green, section 5.6.2), viscosity-dominated buoyant fractures without stabilization at the end of the release (region 5; top centre - light blue, section 5.6.2), and viscosity-dominated radial fractures at the end of the release (region 6; top right - dark blue, section 5.6.2). The distinction between regions 4 and 5 stems from the stagnation of lateral growth observed for viscosity-dominated buoyant hydraulic fractures under a constant release rate with a finite toughness (see notably section 4.6.1 and equation (4.33) of chapter 4) and will be detailed later. We define in table 5.1 the sequence and respective limiting regimes visited for every region of the parametric space with their estimated range of applicability as a function of the dimensionless numbers $\mathcal{M}_{\hat{k}}$ and \mathcal{B}_{ks} . The scales of the buoyant finite volume limiting regimes are listed in appendix 5.9.1. The characteristics of the propagation path of these different regions are described in the following sections.

5.5 Fractures arrested at depth $\mathcal{B}_{ks} < 1$

Fractures that arrest at depth do not show self-sustained propagation in the buoyant direction. In the absence of any form of material or stress heterogeneities and assuming an infinite impermeable elastic medium, a fracture will arrest only due to an insufficient volume being released: $\mathcal{B}_{ks} < 1$. The lower part of figure 5.2 distinguishes two propagation histories for arresting fractures: a region where the fracture is toughness-dominated at the end of the release (region 1) and one where it is viscosity-dominated (region 2). As described in section 5.3.1, the characteristics of radially arresting fractures are independent of the propagation history. In the cases where $\mathcal{B}_{ks} \ll 1$, the fracture has a stress intensity factor (SIF) K_I along the entire fracture front equal to the fracture toughness K_{Ic} (c.f. figures 5.3d) - f)). In other words, as long as the final radius of the fracture R_a (5.3) is small compared to the buoyancy length scale ℓ_b (Lister and Kerr, 1991), the fracture arrests radially, and the findings obtained in the absence of buoyancy are valid (see chapter 3 for this case).

For larger released volumes which are still insufficient for the start of self-sustained growth ($\mathcal{B}_{ks} \lesssim 1$), fracture elongation occurs before it finally arrests. The fracture footprints of figures 5.3a) - c) indicate such elongated shapes as the dimensionless buoyancy approaches 1. In line with this, the stress intensity factor is smaller than the material toughness in the lower part of the fracture. The final elongation of the fracture is more pronounced for lower values of the dimensionless viscosity \mathcal{M}_k . The continuous release case has shown that toughness- and viscosity-dominated transitions present a distinct evolution of their shape (see chapter 4). Therefore, it is not surprising that the shapes of the arrested fractures differ as a function of the dimensionless viscosity if the released volume approaches the limiting one.

5.6 Self-sustained finite volume buoyant fractures: $\mathcal{B}_{ks} > 1$

5.6.1 Toughness-dominated, buoyant fractures at the end of the release (region 3): $\mathcal{M}_k \ll 1$

When the released volume is sufficient to create a buoyant hydraulic fracture ($\mathcal{B}_{ks} > 1$), a set of possible propagation histories exists as function of the dimensionless viscosity \mathcal{M}_k . We first discuss toughness-dominated fractures, which, according to the arguments of sections 5.3.1 and 5.4 must have a transition from radial to buoyant when the release is still ongoing. This results in a well-established, finger-like buoyant fracture with a constant volume, toughness-dominated head at the end of the release. The head characteristics in the case of a continuous release were obtained from the assumption that $\ell^{\text{head}}(t) \sim b^{\text{head}}(t)$ and elasticity, toughness, and buoyant forces are dominating. If we additionally restrict these derivations by the finiteness of the total release volume, the resulting length, opening, and pressure scales remain unchanged (see equations (4.24) in chapter 4) but a time-dependent dimensionless viscosity emerges

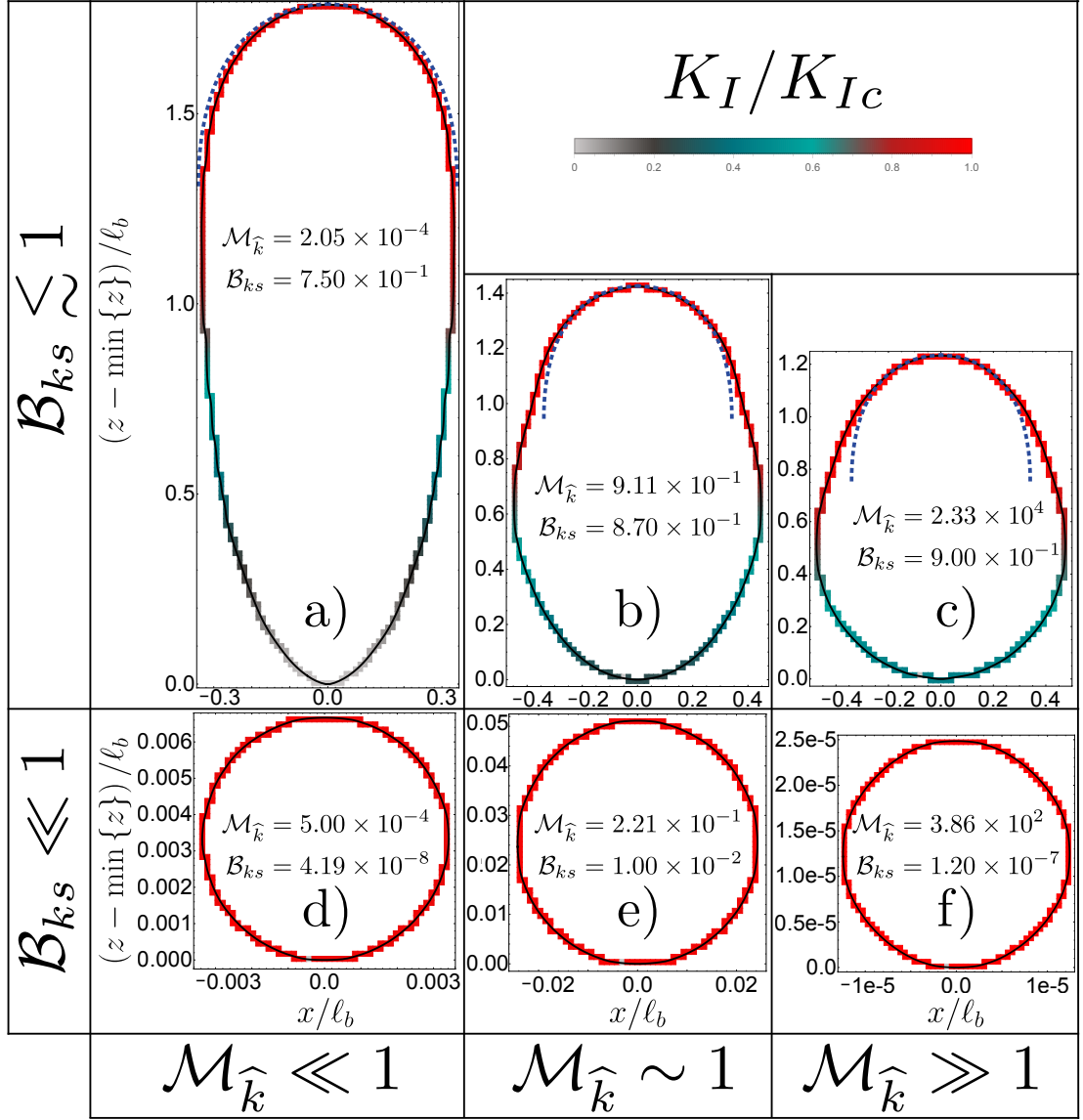


Figure 5.3: Final shape and stress intensity factors (SIF) along the front $\mathcal{C}(t)$ of ultimately arrested fractures at depth ($\mathcal{B}_{ks} < 1$) as a function of \mathcal{B}_{ks} and $\mathcal{M}_{\hat{k}}$. Colors indicate the ratio between the local stress intensity factor K_I and the material fracture toughness K_{Ic} from 0 (light grey) to 1 (red). The blue dashed lines in a) to c) correspond to the shape of an expanding head of a propagating toughness-dominated buoyant fracture (Garagash and Germanovich, 2014).

$$\mathcal{M}_{\hat{k}}^{[V]}(t) = \mu' \frac{V_o E'^3 \Delta \gamma^{2/3}}{K_{Ic}^{14/3} t} = \mathcal{M}_{\hat{k}} \frac{t_s}{t}. \quad (5.19)$$

The decreasing nature of $\mathcal{M}_{\hat{k}}^{[V]}$ with time indicates that the fracture head will necessarily become toughness-dominated at late time. Garagash and Germanovich (2014) similarly derived the finite volume limit and concluded that the head and tail breadths do not change compared to the continuous release case. Their solution is thus equivalently representative of any finite volume, buoyant hydraulic fracture with a finite toughness. We denote their result hereafter as the 3D $\hat{K}^{[V]}$ GG (2014) solution. For cases in the intermediate range of $\mathcal{M}_{\hat{k}} \in [10^{-2}, 10^2]$, we check how their head breadth approaches the 3D $\hat{K}^{[V]}$ GG (2014) solution at late time (e.g. $b^{head}(t \rightarrow \infty) = \pi^{-1/3} \ell_b$). We show in figure 5.4a) the evolution of one toughness-dominated simulation with $\mathcal{M}_{\hat{k}} = 10^{-2}$ and two fractures with an intermediate value of $\mathcal{M}_{\hat{k}} = 1$. The head breadth of the toughness-dominated fracture validates the limiting solution during the release (dark green line in figure 5.4a)) and shows no change after the release has ended. In contrast to this constant value of the head breadth, the simulations with an intermediate value of $\mathcal{M}_{\hat{k}}$ (light green and red lines in figure 5.4a)) have a maximum value exceeding the limiting breadth at the end of the release. Afterward, the head breadth gradually reduces and approaches the limiting 3D $\hat{K}^{[V]}$ GG (2014) solution. In the continuous release case, the limiting breadth is valid for $\mathcal{M}_{\hat{k}} \leq 10^{-2}$, using equation (5.19) we can thus estimate the time for the fracture to reach the limit as $t \left(\mathcal{M}_{\hat{k}}^{[V]}(t) = 10^{-2} \right) = 10^2 \mathcal{M}_{\hat{k}} t_s$ (see section 4.5 of chapter 4 for the derivation of the limit of 10^{-2}). For $\mathcal{M}_{\hat{k}} \in [10^{-2}, 10^2]$, the simulations presented in figure 5.4 the 3D $\hat{K}^{[V]}$ GG (2014) solution would be reached once $t \sim 100 t_s$. From the rate with which the breadth approaches the 3D $\hat{K}^{[V]}$ GG (2014) observed in figure 5.4a), this estimate seems reasonable. In fact, the fracture with $\mathcal{M}_{\hat{k}} = 1$ and $\mathcal{B}_{ks} = 2$ is already within 15% of the limiting solution at $t \sim 50 t_s$.

We derive the scaling of the viscosity-dominated tail of such a late-time solution using the assumption of a constant fracture breadth on the order of the breadth of the head $b \sim \ell_b = K_{Ic}^{2/3} / \Delta \gamma^{2/3}$ as

$$\ell_{\hat{k}}^{[V]}(t) = \frac{V_o^{2/3} \Delta \gamma^{7/9} t^{1/3}}{K_{Ic}^{4/9} \mu^{1/3}}, \quad b_{\hat{k}}^{[V]} = \frac{K_{Ic}^{2/3}}{\Delta \gamma^{2/3}} \equiv \ell_b \quad (5.20)$$

$$w_{\hat{k}}^{[V]}(t) = \frac{V_o^{1/3} \mu^{1/3}}{K_{Ic}^{2/9} \Delta \gamma^{1/9} t^{1/3}}, \quad p_{\hat{k}}^{[V]}(t) = E' \frac{\Delta \gamma^{5/9} V_o^{1/3} \mu^{1/3}}{t^{1/3} K_{Ic}^{8/9}}. \quad (5.21)$$

where we use $\hat{\cdot}$ to refer to a buoyant scaling. These scales are obtained from the continuous-release scales by replacing Q_o with V_o/t , and reveal a sub-linear growth of the fracture height according to a power law of the form $\ell(t) \sim t^{1/3}$. Note that these scales have been obtained by Garagash and Germanovich (2014) when deriving their 3D $\hat{K}^{[V]}$ GG (2014) solution. We present in figure 5.4b) the evolution of dimensionless fracture length $\ell(t)/\ell(t = t_s)$ as a function of

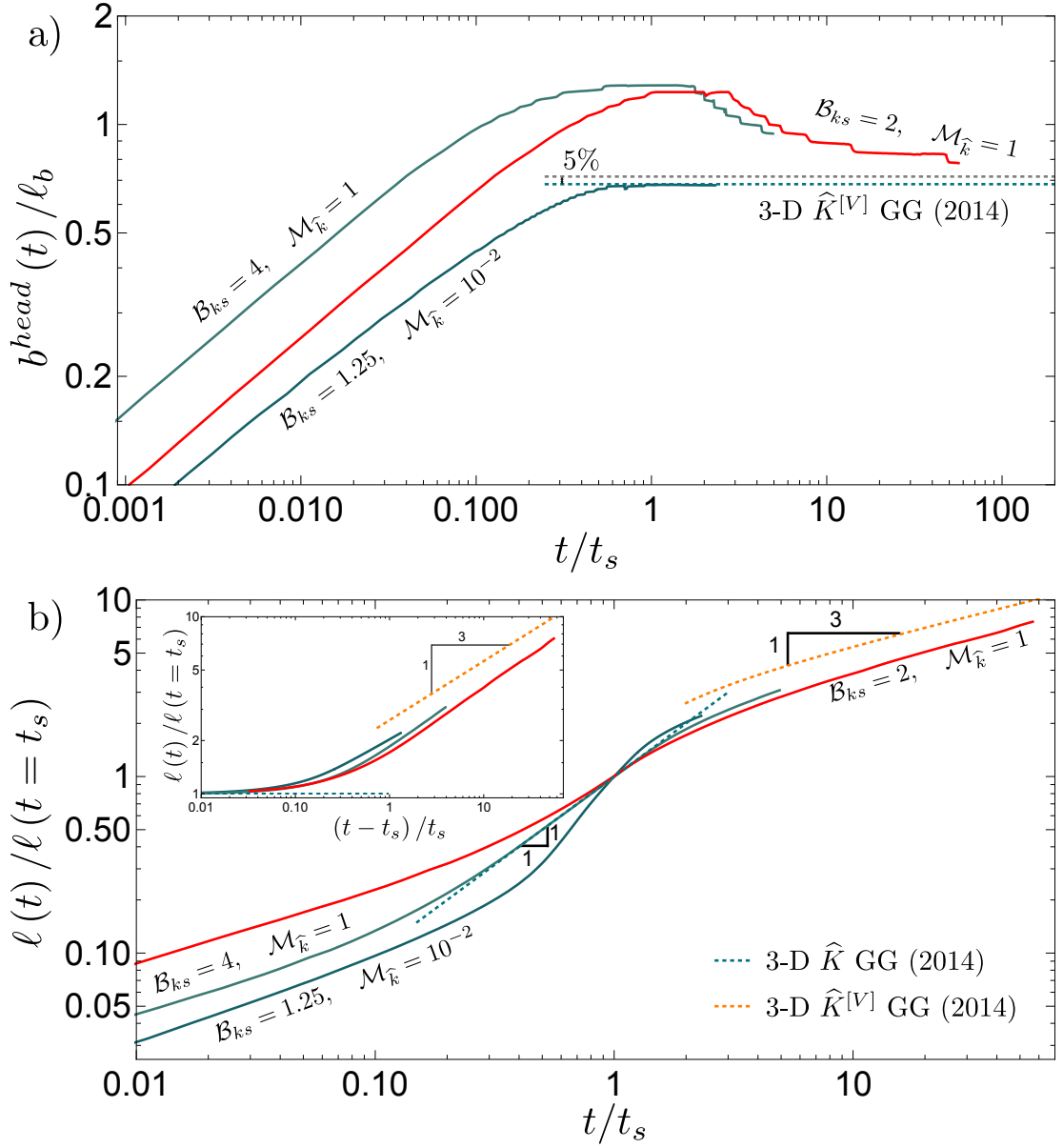


Figure 5.4: Toughness-dominated self-sustained buoyant fractures. Evolution of the dimensionless head breadth $b^{head}(t)/\ell_b$ (a) and fracture length $\ell(t)/\ell(t=t_s)$ (b) as a function of the dimensionless shut-in time t/t_s . The green-dotted line corresponds to the limiting 3D \hat{K} GG (2014) solution ($b^{head}(t \rightarrow \infty) = \pi^{-1/3}\ell_b$ in a), and the orange dashed line is the 3D $\hat{K}^{[V]}$ GG (2014) solution. The inset of figure (b) shows the same quantity on the y-axis with a shifted x-axis (e.g., $(t-t_s)/t_s$).

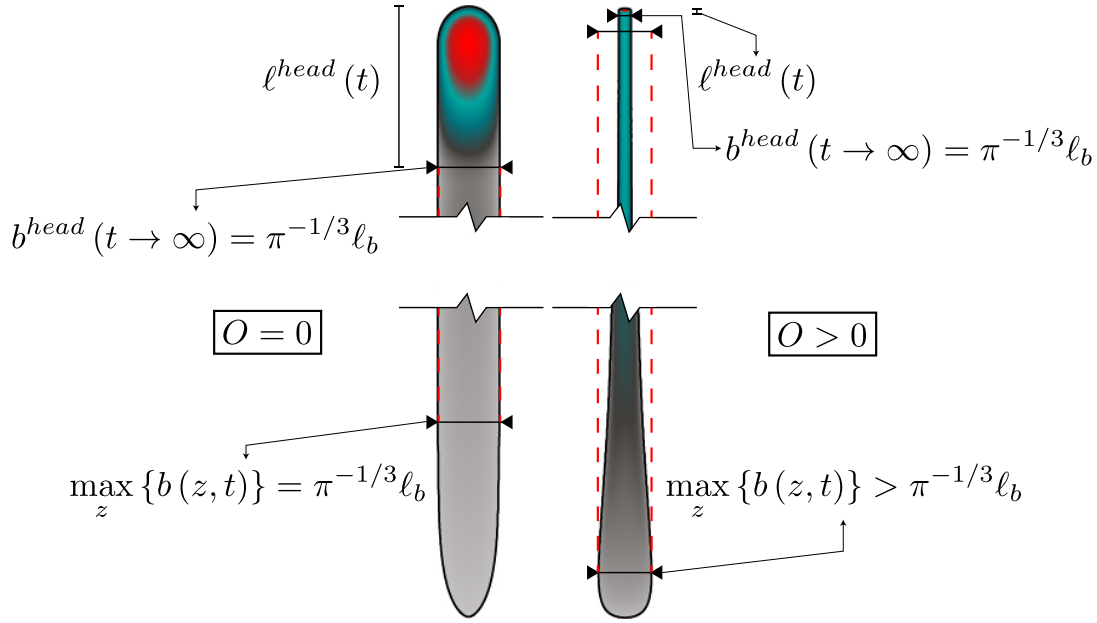


Figure 5.5: Illustration of the definition of the overrun (5.22). Left: example of a zero overrun (as obtained for toughness-dominated buoyant fractures at the end of the release - region 3). Right: example of an overrun with the maximum breadth larger than the limiting breadth of the 3-D $\hat{K}^{[V]}$ GG (2014) solution (Garagash and Germanovich, 2014, 2022).

the dimensionless time t/t_s . The dark green line with a 1 : 1 slope indicates the scaling-derived temporal power-law for a toughness-dominated buoyant hydraulic fracture under a continuous fluid release. The two simulations with low \mathcal{B}_{ks} (dark red and green) cannot reach this intermediate regime, as they are not propagating long enough in this \hat{K} -regime (see the discussion in section 4.5.4 of chapter 4). The simulation with $\mathcal{B}_{ks} = 4$ reaches this limit for about one order of magnitude in time before decelerating towards the late-time power law predicted by the scaling of equation (5.20). A similar deceleration is observed for the other two simulations without any of the simulations reaching the limiting $\ell(t) \sim t^{1/3}$ power-law. The orange dashed line indicates the 3D $\hat{K}^{[V]}$ GG (2014) for fracture length, which we would expect to be valid at late times. The inset of figure 5.4b) sets the time when the release ends as zero according to the hypothesis of Garagash and Germanovich (2014). This correction of the data highlights the tendency of the fracture length of all simulations to approach the limiting solution. A late-time validation of the solution can be expected as the relative difference between the predicted length and the simulation with $\mathcal{B}_{ks} = 2$ and $\mathcal{M}_{\hat{k}} = 1$ at the end of the simulation is only on the order of 23 %. These findings indicate that buoyant fractures with a finite toughness will have a late-time behavior akin to the 3D $\hat{K}^{[V]}$ GG (2014) solution. Even though this late-time behavior will be consistent, it also shows that the exact shape of the fracture will depend on both parameters, $\mathcal{M}_{\hat{k}}$ and \mathcal{B}_{ks} . Only the breadth close to the head, the head itself, and the growth rate will be equivalent to the 3D $\hat{K}^{[V]}$ GG (2014) solution. To get an idea of the overall fracture shape, we define a shape parameter called the overrun as

$$O = \frac{\max_{z,t} \{b(z,t)\} - \pi^{-1/3} \ell_b}{\pi^{-1/3} \ell_b}, \quad (5.22)$$

sketched in figure 5.5. This parameter defines how much the maximum lateral extent exceeds the late-time head breadth $\pi^{-1/3} \ell_b$. O has a lower bound of 0, reached for fully toughness-dominated fractures with $\mathcal{M}_{\hat{k}} \leq 10^{-2}$. This limit is validated by the simulation reported in this section with $\mathcal{M}_{\hat{k}} = 10^{-2}$ and $\mathcal{B}_{ks} = 1.25$ which effectively has an overrun of 0 (see figure 5.5). For the fractures in between the toughness and viscosity dominated limit of the continuous release with a uniform breadth (e.g., $\mathcal{M}_{\hat{k}} \in [10^{-2}, 10^2]$), the overrun cannot be predicted by scaling laws. From the observation of figure 4.8 of chapter 4, we can, however, derive that it will increase with increasing values of $\mathcal{M}_{\hat{k}}$. The overrun of the two simulations reported here is respectively 0.88 ($\mathcal{M}_{\hat{k}} = 1$ and $\mathcal{B}_{ks} = 4$) and 0.80 ($\mathcal{M}_{\hat{k}} = 1$ and $\mathcal{B}_{ks} = 2$). We display the overrun value for simulations that lead to a buoyant hydraulic fracture in figure 5.2. Within the region of the toughness-dominated fractures with a buoyant end of the release (region 1), the values are effectively 0. The overrun increases with the value of $\mathcal{M}_{\hat{k}}$ towards the viscosity-dominated domain (regions 4 to 6) and will be estimated using scaling arguments later (figure 5.5 sketches the concept for a fracture of region 5).

Numerical limitations

The fact that no simulations propagating for longer times - which would ultimately exhibit the 3D $\hat{K}^{[V]}$ GG (2014) solution - are reported deserves discussion. These simulations have multiple numerical challenges: their overall computational cost and the numerical treatment of closing cells at the bottom of the fracture, among others. We illustrate the computational cost by the example of a toughness-dominated buoyant hydraulic fracture. Such fractures accelerate around the transition from radial to buoyant before slowing down to the ultimately constant velocity. In chapter 4, we report that for their simulations, the acceleration terminates at a dimensionless time of approximately $t/t_{k\hat{k}} \approx 3$, where $t_{k\hat{k}}$ is the transition time from radial to buoyant (see equation (4.20) of chapter 4). Observation of figure 5.4b) shows that after the end of the release, additional time is required to transition to the late-time buoyant pulse solution. This figure gives an estimate of the time to reach the 3D $\hat{K}^{[V]}$ GG (2014) solution of $t \sim 100t_s$. An estimate of the fracture extent for a simulation with $\mathcal{M}_{\hat{k}} = 10^{-2}$ at this time, based on growth according to the power law of equation (5.20), gives $\ell \sim 1600\ell_b$. The computational cost can now be estimated by taking a discretization of approximately 44 elements per ℓ_b (see section 4.5.3 of chapter 4) and an approximation of the constant breadth of $b(t) \approx \pi^{-1/3} \ell_b$, yielding about 2×10^6 elements in the fracture. Our current implementation of PyFrac (Zia and Lecampion, 2020) can handle buoyant simulations covering up to 20 orders of magnitude in time and up to 15 orders of magnitude in space within about 4 weeks of computation time on a multithreaded Linux desktop system with twelve Intel@Core i7-8700 CPUs, using at most 30 GB of RAM, and arising to a discretization of up to 2×10^5 elements within the fracture footprint. It is worth noting that the simulation with $\mathcal{M}_{\hat{k}} = 1$ tends towards the predicted $\ell(t) \propto t^{1/3}$ propagation with a significant offset. This difference is related to the inherent assumption

of equation (5.20) that the total released volume is significantly larger than the volume of the head ($V^{head} \gg V_o$). The difference can thus be related to the ratio of the two volumes or equivalently to \mathcal{B}_{ks} (5.13). We show in the supplementary material (section 1.2) that reaching the solution to within 5% is only possible if $\mathcal{B}_{ks} \geq 12$. For all simulations presented in figure 5.4, the fracture height could only get within $\sim 17\%$ (for $\mathcal{B}_{ks} = 4$) of equation (5.20). Efficiently reaching the exact solution would require a toughness-dominated fracture $\mathcal{M}_{\hat{k}} \leq 10^{-2}$ with $\mathcal{B}_{ks} \geq 12$, which becomes even more challenging than the calculations presented previously.

An additional issue presents closing cells at the bottom of the fracture. As the opening continuously reduces (see $w_{\hat{k}}^{[V]}$ in equation (5.20)), and we do not allow for complete fracture healing, a minimum width activates (Zia and Lecampion, 2020) (the minimum width is considered fluid-filled, and we continue solving the width-averaged lubrication approximation for these cells). In the context of hydraulic fractures in rocks, such a minimum aperture relates to the roughness of the fracture. With the current system of closed, fluid-filled cells, two effects arise: First, elastic contact stress changes the stress distribution and the overall behavior. Second, some volume gets trapped, reducing the one available for fracture propagation. Both effects slow down propagation (Pezzulli, 2022). They further increase the non-linearity of the system, such that convergence is challenging, which leads to a breakdown of the simulation at late time $t \gg t_s$. A possible remedy would be removing these closed cells from the fracture domain and reallocating the fluid they contain.

5.6.2 Viscosity-dominated at the end of the release (regions 4 to 6): $\mathcal{M}_k \gg 1$

The difference between a buoyant or radial end of the release has been shown to depend on the dimensionless viscosity at the end of the release \mathcal{B}_{ms} (see equation (5.14), section (5.4.2)). An additional separation between two possible cases of buoyant fractures at the end of the release is required to accurately evaluate the emerging shape. In chapter 4 we have shown that whenever a finite fracture toughness is present (e.g., $K_{Ic} \neq 0$), lateral growth stabilizes within a finite time at $\max_{z,t} \{b(z, t)\} \propto \mathcal{M}_{\hat{k}}^{2/5} \ell_b$. The time of stabilization is related to a dimensionless lateral toughness $\mathcal{K}_{\hat{m},x}(t)$ (see their equation 6.1), which we can evaluate at the end of the release

$$\mathcal{K}_{\hat{m},x} = \mathcal{K}_{\hat{m},x}(t = t_s) = K_{Ic} \frac{\Delta\gamma^{1/8} t_s^{1/3}}{E^{19/24} V_o^{1/8} \mu^{1/3}} = \mathcal{M}_{\hat{k}}^{1/3} \mathcal{B}_{ks}^{25/72}. \quad (5.23)$$

A value of $\mathcal{K}_{\hat{m},x} \geq 1$ indicates that lateral growth has ceased, whereas a value below one means that the fracture is still growing laterally as $b \sim t^{1/4}$ (see equation (4.33) of chapter 4).

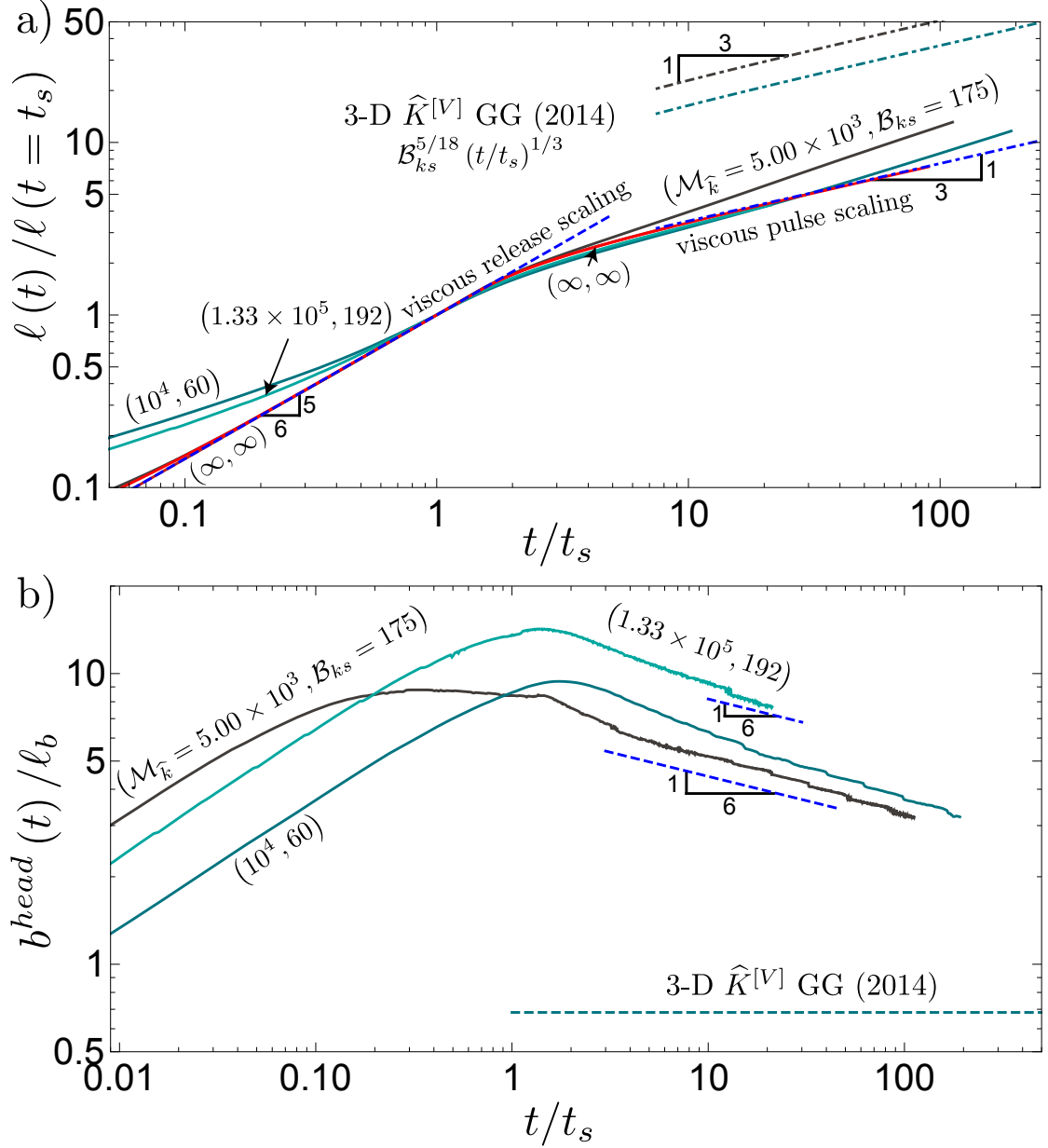


Figure 5.6: Evolution of fracture length $\ell(t)/\ell(t=t_s)$ (a) and head breadth $b^{head}(t)/\ell_b$ for viscosity-dominated buoyant non-stabilized fractures at the end of the release as a function of the dimensionless shut-in time t/t_s : $\mathcal{M}_{\hat{k}} \gg 1$, $\mathcal{B}_{ks} \geq 1$, $\mathcal{K}_{\hat{m},s} < 1$. Colored dashed-dotted lines in (a) show the corresponding late time, 3D $\hat{K}^{[V]}$ GG (2014) solution, the blue dashed line the continuous release buoyant scaling ($\ell(t)/\ell(t=t_s) \sim t^{5/6}$), the blue dashed-dotted line a numerical zero-toughness fit $\ell(t)/\ell(t=t_s) \approx 1.62 (t/t_s)^{0.33}$ (matching the $\hat{M}^{[V]}$ -scaling). The green dashed line in (b) indicates the late-time limit of the 3D \hat{K} GG (2014) solution for the corresponding simulation. The blue-dashed line indicates the scaling dependence in the $\hat{M}^{[V]}$ -scaling, $b^{head}(t) \sim t^{-1/6}$. Note that the two zero-toughness simulations differ by their value of \mathcal{B}_{ms} (100 for the dark red and 25 for the light red simulation).

Viscosity-dominated, buoyant fracture at the end of the release without laterally stabilized breadth (region 5): $\mathcal{B}_{ms} \geq 1$ and $\mathcal{K}_{\hat{m},s,x} \ll 1$

First, we consider the case of zero-fracturing toughness by developing a tail scaling. The principle hypotheses are buoyant forces, elasticity, and viscous energy dissipation at first order and an aspect ratio scaling like the respective lateral and horizontal fluid velocities ($\ell(t)/b(t) \sim v_z(t)/v_x(t)$)

$$\begin{aligned} \ell_{\hat{m}}^{[V]} &= \frac{V_o^{1/2} \Delta \gamma^{1/2} t^{1/3}}{E^{1/6} \mu^{1/3}}, & b_{\hat{m}}^{[V]} &= \frac{E^{1/4} V_o^{1/4}}{\Delta \gamma^{1/4}} \\ w_{\hat{m}}^{[V]} &= \frac{V_o^{1/4} \mu^{1/3}}{E^{1/12} \Delta \gamma^{1/4} t^{1/3}}, & p_{\hat{m}}^{[V]} &= \frac{E^{2/3} \mu^{1/3}}{t^{1/3}}. \end{aligned} \quad (5.24)$$

Note that Davis et al. (2023) presented the same scaling for fracture length. The finite volume inherently prevents the infinite lateral growth observed for a continuous release, and $b_{\hat{m}}^{[V]}$ is time-independent. Figure 5.6c) shows limited lateral growth for all simulations. It is interesting to note that the scaling predicts a fracture length evolution with a $\ell \sim t^{1/3}$ power-law, equivalent to the height evolution in the toughness-dominated case. Figure 5.6a) shows this evolution for various viscosity-dominated simulations. When $\mathcal{M}_{\hat{k}}$ is sufficiently large and $\mathcal{K}_{\hat{m},s} \ll 1$ (in other words, when the fracture is sufficiently far from lateral stabilization) the 1 : 3 slope predicted by the scaling of equation (5.24) emerges. However, the height growth quickly departs from the $t^{1/3}$ power-law. The reason is the time-dependent inflow rate of the head (derived from the scaling of equation (5.24))

$$\begin{aligned} \ell_{\hat{m}}^{head,[V]} = b_{\hat{m}}^{head,[V]} &= \frac{E^{11/24} V_o^{1/8} \mu^{1/6}}{\Delta \gamma^{5/8} t^{1/6}}, & w_{\hat{m}}^{head,[V]} &= \frac{V_o^{1/4} \mu^{1/3}}{E^{1/12} \Delta \gamma^{1/4} t^{1/3}} \\ p_{\hat{m}}^{head,[V]} &= \frac{E^{11/24} V_o^{1/8} \mu^{1/6} \Delta \gamma^{3/8}}{t^{1/6}}, & V_{\hat{m}}^{head,[V]} &= \frac{E^{5/6} V_o^{1/2} \mu^{2/3}}{\Delta \gamma^{3/2} t^{2/3}}, \end{aligned} \quad (5.25)$$

revealing a shrinking viscous head.

Considering now a finite fracture toughness, a dimensionless toughness can be obtained in the head

$$\mathcal{K}_{\hat{m}}^{[V]}(t) = K_{Ic} \frac{t^{1/4}}{E^{11/16} V_o^{3/16} \Delta \gamma^{1/16} \mu^{1/4}} = \mathcal{B}_{ks}^{5/48} \mathcal{M}_{\hat{k}}^{[V]}(t)^{-1/4} = \mathcal{B}_{ks}^{5/48} \mathcal{M}_{\hat{k}}^{-1/4} \left(\frac{t}{t_s} \right)^{1/4}. \quad (5.26)$$

Equation (5.26) indicates that the head will become toughness dominated at late times as

5.6 Self-sustained finite volume buoyant fractures: $\mathcal{B}_{ks} > 1$

$\mathcal{K}_{\hat{m}}^{[V]}(t)$ increases with time. From this observation, we anticipate that the region close to the propagating head will ultimately follow the 3D $\hat{K}^{[V]}$ GG (2014) head solution (see section 5.6.1) and derive the characteristic time scale of the transition

$$t_{\hat{m}\hat{k}}^{[V]} = \frac{E'^{11/4} V_o^{3/4} \Delta\gamma^{1/4} \mu'}{K_{Ic}^4}. \quad (5.27)$$

Evaluating the viscosity-dominated head scaling (see equations (5.25)) at this characteristic time gives the scales of the toughness-dominated head (see (5.20)). This observation implies that even though the shape further away from the head varies, the length scale $\ell(t)_{\hat{k}}^{[V]}$ becomes applicable. Relating the two length scales of buoyant fractures from a finite volume release

$$\ell_{\hat{k}}^{[V]}(t) = \mathcal{B}_{ks}^{5/18} \ell_{\hat{m}}^{[V]}(t) \quad (5.28)$$

shows that $\ell_{\hat{k}}^{[V]}(t) \geq \ell_{\hat{m}}^{[V]}(t)$ for a buoyant fracture (as $\mathcal{B}_{ks} \geq 1$). The observation of figure (5.6)a shows the fracture deviation from the lower, viscosity-dominated solution towards the upper, toughness-dominated solution (shown by dashed-dotted lines for two simulations). The observed faster growth in height originates in the narrowing of the tail, creating a lateral inflow from the stagnant parts of the fracture into a central tube of the fixed breadth predicted by the 3D $\hat{K}^{[V]}$ GG (2014) solution. We do not present a simulation that finishes the transition to the toughness-dominated regime due to its high computational cost (see the discussion in section 5.6.1).

In equation (5.22), we have introduced the overrun as a characteristic of the fracture shape. In the case of viscous fractures with a buoyancy-dominated, laterally non-stabilized end of the release, such overrun can be estimated from the viscous scaling as

$$O_{\hat{m}} = \frac{b_{\hat{m}}^{[V]} - \pi^{-1/3} \ell_b}{\pi^{-1/3} \ell_b} = \pi^{1/3} \frac{E'^{1/4} V_o^{1/4} \Delta\gamma^{5/12}}{K_{Ic}^{2/3}} - 1 = \pi^{1/3} \mathcal{B}_{ks}^{5/12} - 1. \quad (5.29)$$

The increase of the overrun with the value of the dimensionless buoyancy \mathcal{B}_{ks} is observable in figure 5.2.

Viscosity-dominated, buoyant fracture at the end of the release with laterally stabilized breadth (region 4): $\mathcal{B}_{ms} \geq 1$ and $\mathcal{K}_{\hat{m}s,x} \geq 1$

Lateral stabilization of buoyant, viscosity-dominated fractures occurs when the volume of the fracture head becomes constant, leading to two fixed points, the laterally stabilized breadth of $\max_{z,t} \{b(z,t)\} \sim \mathcal{M}_{\hat{k}}^{2/5} \ell_b$ and the constant volume, constant breadth head. The section of extending fracture breadth in between the two conserves its shape, creating a fracture where

Chapter 5. Three-dimensional buoyant hydraulic fractures: finite volume release

elongation concentrates within the zone of laterally stabilized breadth. From this observation, one can draw an analogy to a toughness-dominated buoyant fracture (see section 5.6.1). The scales of this equivalent toughness-dominated fracture are related through a factor of $\mathcal{M}_{\hat{k}}^{2/5}$, such that the behavior after the end of the release will be the same as presented in section 5.6.1, differing only by the starting point ($\mathcal{M}_{\hat{k}}^{2/5}$ instead of $\mathcal{M}_{\hat{k}}$).

Because the processes after the end of the release do not differ from toughness-dominated fractures, we omit a detailed discussion of this case hereafter and only list the difference in the shape parameter

$$O_{\hat{m}}^{stab} = \frac{\mathcal{M}_{\hat{k}}^{2/5} \ell_b - \pi^{-1/3} \ell_b}{\pi^{-1/3} \ell_b} = \pi^{1/3} \mathcal{M}_{\hat{k}}^{2/5} - 1. \quad (5.30)$$

The overrun in the non-stabilized case of viscosity-dominated fractures depends solely on the dimensionless buoyancy \mathcal{B}_{ks} and, as such, on the total released volume and elastic parameters. In contrast, the governing parameter of the stabilized case is the dimensionless viscosity $\mathcal{M}_{\hat{k}}$, and the history of the release (how the total volume gets accumulated) governs the overrun of the fracture.

Viscosity-dominated fracture with negligible buoyancy at the end of the release (Region 6):

$$\mathcal{B}_{ms} \ll 1$$

This type of fracture becomes buoyant in the pulse propagation phase as long as its dimensionless buoyancy \mathcal{B}_{ks} (see (5.13)) is larger than one. This transition from radial to buoyant propagation is characterized by the dimensionless buoyancy of the viscous pulse $M^{[V]}$ -scaling $\mathcal{B}_m^{[V]}(t)$ (see equation (5.16)) and has a characteristic transition time

$$t_{m\hat{m}}^{[V]} = \frac{E'^{5/4} \mu'}{V_o^{3/4} \Delta \gamma^{9/4}} = \mathcal{B}_{ks}^{-5/2} t_{\hat{m}\hat{k}}^{[V]}. \quad (5.31)$$

The corresponding transition length scale is equivalent to the constant breadth of a buoyant viscosity-dominated fracture $\ell_m^{[V]}(t = t_{m\hat{m}}^{[V]}) = \ell_{m\hat{m}}^{[V]} = b_{\hat{m}}^{[V]}$, indicating that the maximum breadth is reached at the transition. Figure 5.7d) shows that for an increasing dimensionless buoyancy \mathcal{B}_{ks} (see (5.13)), the growth of the maximal breadth continues (continuous lines) after transition but remains within the order of magnitude predicted by the scaling (5.24). Lateral growth ultimately tapers off at about $3\ell_{m\hat{m}}^{[V]}$ at $t \approx 10^3 t_{m\hat{m}}^{[V]}$. The expected overrun becomes equivalent to the case of a non-stabilized, buoyant viscosity-dominated end of the release (see equation (5.29)).

The scaling for these fractures is given by equations (5.24) and (5.25). Despite the distinct propagation histories, the late-time fracture footprint does not vary significantly (see figure 5.8). Similar to the case of a constant release, the fracture first becomes somewhat elliptical, with

a peak in pressure and opening appearing in the fracture head. Propagation then deviates to the buoyant direction with a continuously shrinking head, and no saddle point develops between the maximum lateral extent and the head. In the case of finite fracture toughness, an inflection point forms in this area, such that the evolution of the breadth towards the head becomes convex at the transition time $t_{\hat{m}\hat{k}}^{[V]}$ (see equation (5.27)). Note that the bottom end of the fractures in figure 5.7h), i) seem to be of uniform opening. This observation directly results from the numerical scheme with an activated minimum width.

When observing the evolution of the fracture length and head breadth, one observes that the simulations approach the 3D $\hat{K}^{[V]}$ GG (2014) solution for cases with a finite toughness. The breadth and length evolution of the 3D $\hat{K}^{[V]}$ GG (2014) in the viscous buoyant scaling (see equations (5.24) and (5.25)) depends on the value of \mathcal{B}_{ks} such that we only indicate one of the possible late-time solutions. We pick the one which is most likely to be reached, corresponding to the smallest value of \mathcal{B}_{ks} for the length and the largest for the breadth with dashed orange lines. The tendency towards those solutions is visible. Reaching them exactly is, however, associated with too high computational costs (see the discussion in section 5.6.1). The evolution of fracture opening and net pressure is plotted along the centreline (e.g., $x = 0$) in figures 5.7a) and b). The head is identified once it departs from the source before it subsequently shrinks. This shrinking makes the head volume negligible compared to the overall fluid volume after sufficient buoyant propagation. When this moment is reached, the fracture propagates in the viscosity-dominated regime (see also the nearly self-similar footprint reported in figure 5.12 of section 5.10.2). Section 5.10.2 shows that the opening along the centerline approaches the 2D solution of Roper and Lister (2005). An approximated solution may be possible when combining the zero toughness head (c.f. figure 4.7 of chapter 4) with the tail solution of Roper and Lister (2007) (see their equation (6.7)) but is left for further study.

5.6.3 Late time fracture shapes

The governing mechanisms delimiting the different regions of the parametric space of figure 5.2 give rise to different phenotypes of fracture shape. Figure 5.8 displays the late-time shape of buoyant fractures in the different regions (3-5) of the parametric space. Figure 5.8a) shows the characteristic shape of a toughness-dominated buoyant fracture at the end of the release (region 3). Their footprint is finger-like with a constant breadth and head volume. Already early in the propagation, the bulk of the released volume is located in the head (indicated by the color code). Except in the source region and for the expanding head, no change in breadth is observed, and the overrun O (see equation (5.22)) is zero. For fractures with a uniform breadth, not validating the toughness solution (e.g., $\mathcal{M}_{\hat{k}} \in [10^{-2}, 10^2]$ and $\mathcal{B}_{ks} \geq 1$, between regions 3 and 4), the bulk of the fluid volume is similarly in the head. One difference is the change in breadth observed close to the source region related to the end of the release, giving rise to a small, non-zero overrun. When the fractures are more viscosity-dominated (see figures 5.8c-e)), the overrun becomes more pronounced, and the opening distribution

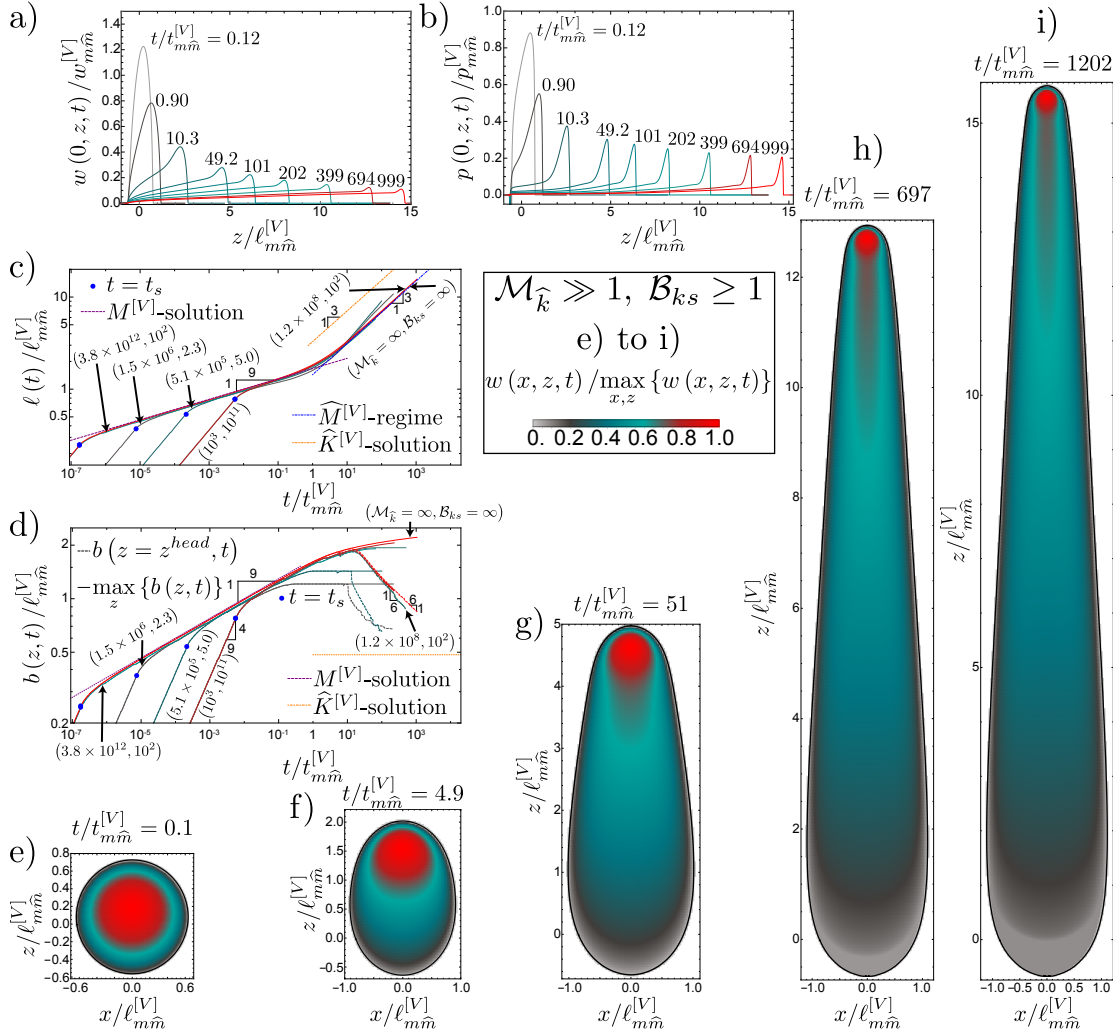


Figure 5.7: Viscosity-dominated fractures with negligible buoyancy at the end of the release: $\mathcal{B}_{ks} \geq 1$ and $\mathcal{B}_{ms} \ll 1$. a) Opening along the centerline $w(0, z, t) / w_{m\hat{m}}^{[V]}$ for $\mathcal{M}_{\hat{k}} = \infty$, $\mathcal{B}_{ks} = \infty$, and $\mathcal{B}_{ms} = 10^{-3}$ (zero-toughness case). b) Net pressure along the centerline $p(0, z, t) / p_{m\hat{m}}^{[V]}$ for the same case as in a). c) Fracture length $\ell(t) / \ell_{m\hat{m}}^{[V]}$ for large viscosity $\mathcal{M}_{\hat{k}} \in [5.1 \times 10^5, \infty]$ simulations. The blue dashed line is a fit of the zero-toughness simulation $\ell(t) \propto t^{0.33}$. d) Fracture breadth $b(t) / \ell_{m\hat{m}}^{[V]}$ (continuous lines) and head breadth $b^{head}(t) / \ell_{m\hat{m}}^{[V]}$ (dashed lines) for the same simulations. Purple dashed lines indicate the $M^{[V]}$ -solution (see section 3.4.2 of chapter 3), orange dashed lines the 3D $\hat{K}^{[V]}$ GG (2014) solution for the highest value of \mathcal{B}_{ks} . e - i) Evolution of the fracture footprint from radial e) towards the late time shape h) and i) for the zero-toughness simulation. For the definition of the transition scales $t_{m\hat{m}}^{[V]}$ see table 5.4.

5.6 Self-sustained finite volume buoyant fractures: $\mathcal{B}_{ks} > 1$

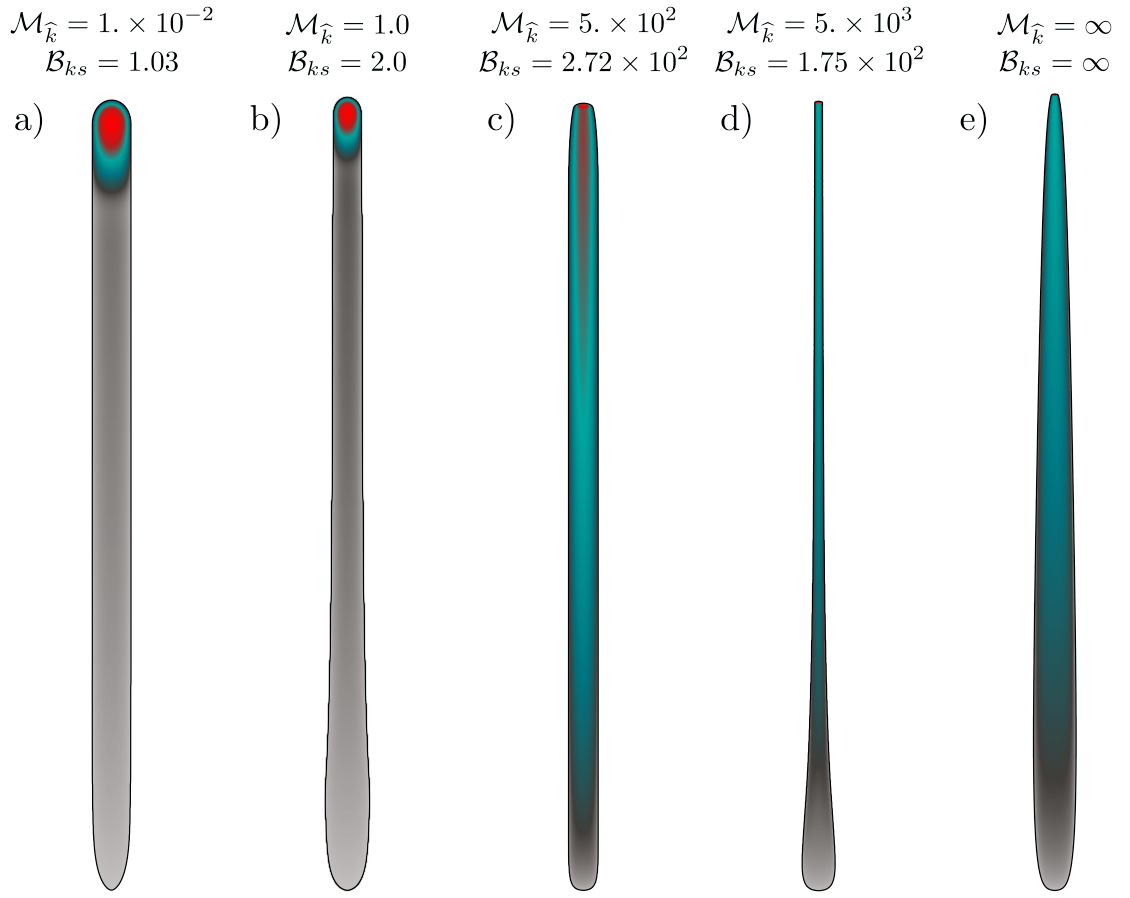


Figure 5.8: Phenotypes of possible buoyant hydraulic fractures of finite volume emerging from a point source ($\mathcal{B}_{ks} \geq 1$). a) Toughness-dominated finger-like fracture (region 3 in figure 5.1). b) Intermediate fracture with a stable breadth and negligible overrun. c) Viscosity-dominated buoyant end of the release with stabilized breadth (region 4 in figure 5.1). d) Viscosity-dominated buoyant end of the release without stabilized breadth (region 5 in figure 5.1). e) Zero-toughness case with a buoyant end of the release ($\mathcal{B}_{ms} = 10^2$). a) and b) are scaled by ℓ_b (Lister and Kerr, 1991), c) to e) by $\ell_{m\hat{m}}^{[V]}$ (see table 5.4).

is more homogeneous along the fracture length. For example, figure 5.8c) shows a viscosity-dominated, buoyant fracture with a stabilized breadth at the end of the release (region 4) with a barely visible head (light red area at the propagating edge). The red-colored part extending long into the tail shows that the tail opening is much closer to the head opening than in the toughness-dominated cases of figures 5.8a) and b). The particularity of this phenotype is its uniform breadth over a finite height due to lateral stabilization (associated with a finite fracture toughness value). Figure 5.8d) (region 5) emphasizes the approaching towards the late-time 3D $K^{[V]}$ GG (2014) solution of viscosity-dominated fractures by thinning the breadth along the fracture length towards its head. The head breadth of this simulation still exceeds the limiting solution by a factor of about 4.7, and the opening distribution along the fracture is still too homogeneous. In other words, a significant proportion of the volume remains in the tail (compare the grey color in figure 5.8a) with the green color in figure 5.8d)). The last phenotype in figure 5.8e) represents the case of a zero-toughness simulation with a buoyant end of the release. Comparing this shape to the zero toughness simulation with negligible buoyancy at the end of the release (c.f. figures 5.7h-i)) reveals no significant difference. All zero-toughness simulations, independent of the state at the end of the release, will show this particular shape. Only if a finite fracture toughness is present, the fracture will tend to the late-time 3D $K^{[V]}$ GG (2014) solution, and the shape will resemble figure 5.8d) (see also figure 1b) of Davis et al. (2023)).

5.7 Discussion

5.7.1 Implications for industrial treatments

We consider a single stage of a multistage fracturing treatment in a horizontal well, taking the fluid properties as the ones of slickwater (Economides and Nolte, 2000; Lecampion and Zia, 2019) with a density of $\rho_f \approx 1000 \text{ kg/m}^3$ and a viscosity of $\mu \approx 0.005 \text{ Pa}\cdot\text{s}$. We consider a relatively compliant rock with a Young's Modulus of $E \approx 10 \text{ GPa}$, a Poisson's ratio of $\nu \approx 0.1$, density of $\rho_s \approx 2300 \text{ kg/m}^3$, and fracture toughness $K_{Ic} \approx 2 \text{ MPa}\cdot\text{m}^{1/2}$. Assuming that the reservoir and fracturing fluids have similar densities ($\rho_F \approx \rho_f$), the effective density contrast (5.8) becomes $\Delta\gamma = \alpha(\rho_s - \rho_f)g$. Typical injection rates are on the order of $Q_o \approx 0.1 - 0.3 \text{ m}^3/\text{s}$ with a total fluid volume of $V_o \approx 1500 - 5700 \text{ m}^3$. With this set of material, fluid, and injection parameters, the critical volume for buoyant propagation as a function of the lateral earth pressure coefficient α reads $V_{lim}(\alpha) \approx 0.90\alpha^{-5/3}$ (5.12). For the fluid release with the smallest volume $V_o \approx 1500 \text{ m}^3$ to become buoyant, the lateral earth pressure coefficient must exceed $\alpha \gtrsim 0.012$. When using a lateral earth pressure coefficient at rest $\alpha = \nu / (1 - \nu) = 0.11$, the fracture becomes buoyant with a dimensionless buoyancy of $\mathcal{B}_{ks} \approx 9.51$ (5.13). It is necessary to reduce the horizontal stress gradient by about 90% (through tectonic relaxation or other processes) to prevent buoyant propagation under these conditions. Note that the corresponding dimensionless viscosity is on the order of $\mathcal{M}_{\hat{\kappa}} \approx 0.60 - 10.0$ (5.10) for the release rates considered. The emerging buoyant fractures are thus situated somewhere in between the toughness-dominated region 3 (section 5.6.1), and the viscosity-dominated regions 4 and

| | Unit | Exp. 1837 | Exp. 1945 | Exp. 1967 |
|-------------------------|----------------------------------|-----------------------|-----------------------|-----------------------|
| μ_f | $\text{Pa} \cdot \text{s}$ | 1.74×10^{-3} | 48×10^{-3} | 970×10^{-3} |
| E | Pa | 1345 | 426 | 944 |
| ν | | 0.5 | 0.5 | 0.5 |
| K_{Ic} | $\text{Pa} \cdot \text{m}^{1/2}$ | 23.1 | 7.3 | 16.2 |
| $\Delta\rho$ | $\text{kg} \cdot \text{m}^{-3}$ | 260 | 160 | 150 |
| V_o | m^3 | $2. \times 10^{-5}$ | $1. \times 10^{-5}$ | $1. \times 10^{-5}$ |
| Q_o | $\text{m}^3 \cdot \text{s}^{-1}$ | 1.23×10^{-7} | 8.33×10^{-7} | 1.11×10^{-7} |
| t_s | s | 162 | 12 | 90 |
| $\mathcal{M}_{\hat{k}}$ | | 1.20×10^{-3} | 1.11 | 0.76 |
| \mathcal{B}_{ks} | | 2.28 | 2.93 | 1.24 |
| \mathcal{B}_{ms} | | 57.7 | 3.85 | 1.49 |

Table 5.2: Material parameters and the released volume V_o are taken from table 3 of Davis et al. (2023) (based on the work of Smitarello (2019)). We extract the shut-in time from figure 5a of Davis et al. (2023) and calculate the release rate as $Q_o = V_o / t_s$.

5 (sections 5.6.2 and 5.6.2).

5.7.2 Comparison with experiments

We compare recent laboratory experiments with our scalings and numerical simulations. We use three sets of parameters from experiments performed by Smitarello (2019) and reported in Davis et al. (2023) (see table 5.2). The resulting dimensionless parameters are listed in table 5.2. These fractures appear to be toughness-dominated (experiment 1827) or in the transition with a uniform breadth (experiments 1945 and 1967). We report the evolution of fracture height with time in figure 5.9 (data of the experiments from figure 5a of Davis et al. (2023)). Along with the three experiments, we show our simulation closest to experiments 1945 and 1967 as well as the limiting solutions derived by Garagash and Germanovich (2014). The toughness-dominated experiment (exp. 1837) displays a linear fracture height growth with time, expected from the continuous release scaling. Surprisingly, the end of the release does not lead to a significant reduction in height growth (c.f. the simulation with $\mathcal{M}_{\hat{k}} = 10^{-2}$ in figure 5.4b)), which continues linearly until it reaches the top of the tank (end of the data stream). We expect this to be related to free-surface effects attracting the fracture, a hypothesis supported by observations of the other two experiments. The fractures of the other experiments grow without showing any scaling-based power laws. This behavior is typical for many laboratory experiments, which unfortunately appear to be “in-between” limiting regimes. Additionally, the extent of the hydraulic fractures created often suffers from detrimental effects associated with the finite size of the sample, making any comparison with theoretical and numerical predictions difficult. The fact that the release rate in laboratory experiments is often not constant presents an additional inconvenience. Indeed, at early time, the interplay between compressibility of the injection line and fracture initiation leads to a non-constant entering

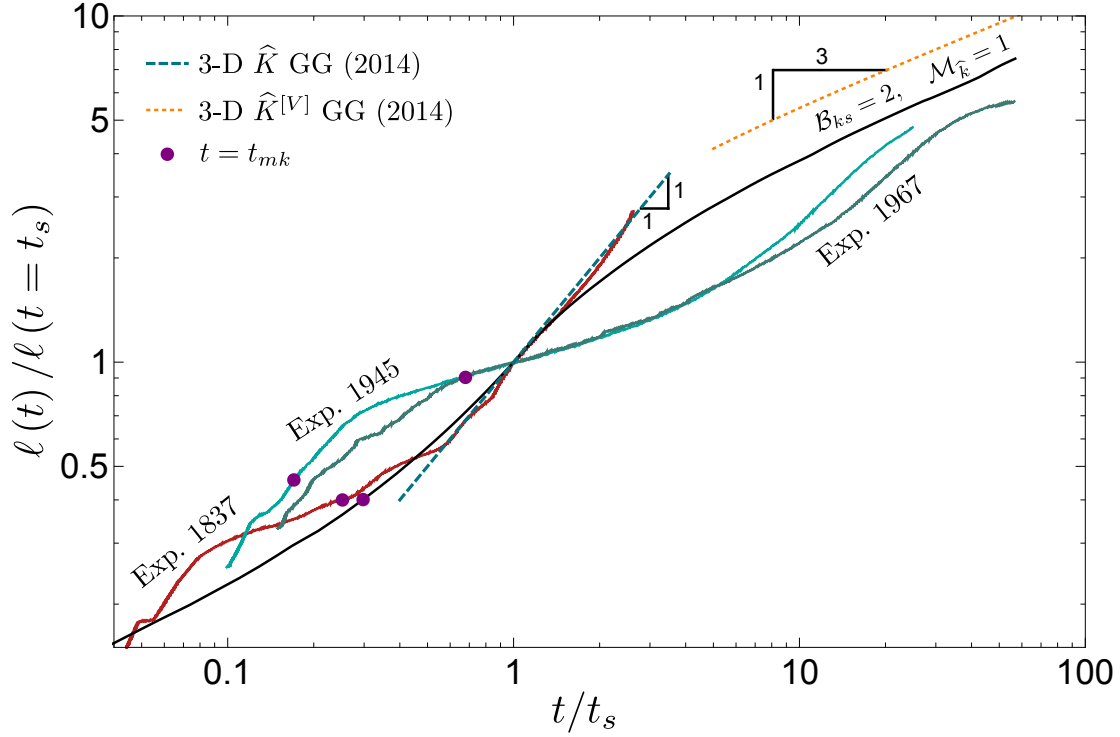


Figure 5.9: Fracture height evolution as a function of dimensionless time for the experiments listed in table 5.2. Data extracted from figure 5a of Davis et al. (2023) based on experiments reported in Smitarello (2019). The black line shows a simulation with similar dimensionless parameters to Exp. 1945 and Exp. 1967. Purple dots mark the moment when the fracture becomes toughness dominated (e.g., $t = t_{mk}$), and dashed lines indicate the limiting solutions derived by Garagash and Germanovich (2014) respectively (green for a continuous release, orange for the release of a finite volume).

flux (Lecampion et al., 2017). In addition, for many experiments related to buoyancy, the fluid is injected manually using a syringe which is likely the case here. Especially in viscosity-dominated fracture propagation regimes, this has a significant influence on fracture growth via $\mathcal{M}_{\hat{k}}$. Another possible effect is given by the "oriented" fluid release with a syringe from the bottom of the tank rather than perpendicular to the fracturing plane. Such a difference notably influences the early propagation phase, which should be radial and accurately reproduced (note that PyFrac has been shown to reproduce laboratory experiments of initially radial hydraulic fractures with success (Peruzzo, 2023; Zia and Lecampion, 2019)).

The complete parametric space characterizing 3D finite volume buoyant hydraulic fractures described in this paper should help in better designing experiments within probing well-defined propagation history.

5.8 Conclusions

We have shown that finite-volume hydraulic fractures are entirely characterized by a dimensionless buoyancy $\mathcal{B}_{ks} = \Delta\gamma E'^{3/5} V_o^{3/5} / K_{Ic}^{8/5}$ relating the total released V_o to the minimum volume necessary for self-sustained buoyant propagation $V_{\hat{k}}^{head} = K_{Ic}^{8/3} / (E' \Delta\gamma^{3/5})$: $\mathcal{B}_{ks} = (V_o / V_{\hat{k}}^{head})^{3/5}$, and a dimensionless viscosity $\mathcal{M}_{\hat{k}} = \mu' Q_o E'^3 \Delta\gamma^{2/3} / K_{Ic}^{14/3}$ representative of the ratio between the energy dissipation through viscous flow and the creation of new surfaces at the change from radial to buoyant propagation. Although the emergence (or not) of a self-sustained buoyant fracture solely depends on \mathcal{B}_{ks} , in other words, on the total volume released and material and fluid parameters, the details of the release (duration and injection rate) have a first-order impact on the shape and propagation rates of the fracture through the dimensionless viscosity $\mathcal{M}_{\hat{k}}$. Combining these two dimensionless numbers (\mathcal{B}_{ks} , $\mathcal{M}_{\hat{k}}$), reveals six regions corresponding to distinct propagation histories (see figure 5.2 and table 5.1).

For a finite value of the material fracture toughness ($K_{Ic} \neq 0$), the toughness-dominated pulse solution of Garagash and Germanovich (2014) characterizes the late-time buoyant head and the fracture breadth in its vicinity ($b^{head} = \pi^{-1/3} \ell_b$). Note that such a late-time solution may appear only at very late times and does not describe the complete fracture shape. In the zero-toughness case ($K_{Ic} = 0$), the fracture head continues to lose fluid such that its volume asymptotically approaches zero. Due to the finiteness of the released volume, the maximum lateral breadth stabilizes at a finite value even for the zero-toughness case. It is thus possible to relate the limiting breadth close to the head, given by the solution of Garagash and Germanovich (2014), to the stabilized maximum one. We define this parameter as the overrun O and derive its value for the different regions of the parametric space. Note that this parameter gives only an idea of the shape: a similar overrun does not imply that the fracture has the same overall shape. When the fracturing toughness is zero, the head breadth tends to zero (e.g., $\ell_b = 0 \rightarrow b^{head} = 0$), resulting in an infinite overrun. It is important to note that this does not imply unbounded lateral growth, as lateral growth is limited by the finite volume rather than fracture toughness.

The identified late-time behavior further fixes the late-time ascent rate to the toughness-dominated solution as $\dot{\ell}_{\hat{k}}^{[V]}(t) \sim V_o^{2/3} \Delta\gamma^{7/9} / (K_{Ic}^{4/9} \mu'^{1/3} t^{2/3}) \propto t^{1/3}$. An important observation is that the time power-law dependence of the ascent rate for a viscosity-dominated buoyant fracture is equivalent (e.g., $\dot{\ell}_{\hat{m}}^{[V]} \sim V_o^{1/2} \Delta\gamma^{1/2} / (E'^{1/6} \mu'^{1/3} t^{2/3}) \propto t^{1/3}$). During its history, a buoyant hydraulic fracture can first ascent in a viscosity-dominated manner as $\dot{\ell}_{\hat{m}}^{[V]}(t)$ and then transition to the limiting ascent rate dictated by the late toughness solution $\dot{\ell}_{\hat{k}}^{[V]}(t)$. The late-time ascent rate of the toughness limit is always faster (or at least equal) than the one of the viscosity-dominated limit ($\dot{\ell}_{\hat{k}}^{[V]}(t) = \mathcal{B}_{ks}^{5/18} \dot{\ell}_{\hat{m}}^{[V]}(t)$, with $\mathcal{B}_{ks} \geq 1$ for a self-sustained buoyant fracture). Fractures transitioning when the fluid release is still ongoing can show even higher velocities during their propagation history. Estimations or averaging of vertical growth rates must be done with great care and must necessarily account for both $\mathcal{M}_{\hat{k}}$ and \mathcal{B}_{ks} . In other words, the details of the release history (rate and duration) do significantly

Chapter 5. Three-dimensional buoyant hydraulic fractures: finite volume release

impact the ascent rate even long after the end of the release, implying that for realistic cases (as well as laboratory experiments), the detail of the release matter. Consequently, a more complicated evolution of the release (compared to the simple constant rate / finite duration) will undoubtedly impact the growth of buoyant fractures.

Notably, most parameter combinations for natural or anthropogenic hydraulic fractures would lead to self-sustained buoyant propagation between the well-distinct regions of the parametric space depicted in figure 5.2. Additionally, the time required to reach the late-time solution at the propagating edge and the fracture size when doing so naturally clash with sample sizes in the laboratory or the scales of heterogeneities in the upper lithosphere. We emphasize that even though theoretically buoyant fractures emerge (see 5.7.1), to our knowledge, nearly no cases of buoyant fractures from hydraulic fracturing treatments reaching the surface have been reported. We expect this to originate from the interaction with heterogeneities, fluid leak-off, confining stress jumps, and other possible arrest mechanisms not considered in this contribution.

Data availability statement. The data supporting this study's findings are openly available at [10.5281/zenodo.7788051](https://doi.org/10.5281/zenodo.7788051).

5.9 Appendix

5.9.1 Recapitulating tables of scales

We list all the characteristic scales used within this contribution in the following tables for completeness. A Wolfram Mathematica notebook containing their derivation and the different scalings is also provided as Supplementary Material.

5.10 Supplementary material

5.10.1 Approximated toughness-dominated solution $\hat{\mathbf{K}}^{[V]}$

The main hypotheses of the solution presented first in Garagash and Germanovich (2014), detailed in Garagash and Germanovich (2022) and termed in this contribution the 3D $\hat{\mathbf{K}}^{[V]}$ GG (2014) solution, do not differ from their constant-release counterparts. Both assume a toughness-dominated 3D buoyant fracture head with a finger-like tail far enough from the source point to feel any influence of it (e.g., large aspect ratios). The strictly hydrostatic net pressure in the head leads to a constant volume and geometry head. Due to the finite volume release, the net pressure in the tail is no longer uniform along its length. A 2D plane-strain approach with constant pressure is still possible along the horizontal cross-section.

| | <i>Radial</i> | | <i>Elongated</i> | |
|-----------------------|--|--|---|---|
| | $M^{[V]}$ | $K^{[V]}$ | $\hat{M}^{[V]}$ (tail) | $\hat{M}^{[V]}$ (head) |
| $\ell_*^{[V]}$ | $\frac{E^{1/9} V_o^{1/3} t^{1/9}}{\mu^{1/9}}$ | $\frac{E^{2/5} V_o^{2/5}}{K_{Ic}^{2/5}}$ | $\frac{V_o^{1/2} \Delta \gamma^{1/2} t^{1/3}}{E^{1/6} \mu^{1/3}}$ | $\frac{\Delta \gamma^{5/8} t^{1/6}}{E^{11/24} V_o^{1/8} \mu^{1/6}}$ |
| $b_*^{[V]}$ | $\ell_*^{[V]}$ | $\ell_*^{[V]}$ | $\frac{E^{1/4} V_o^{1/4}}{\Delta \gamma^{1/4}}$ | $\ell_*^{head, [V]}$ |
| $w_*^{[V]}$ | $\frac{V_o^{1/3} \mu^{2/9}}{E^{2/9} t^{2/9}}$ | $\frac{K_{Ic}^{4/5} V_o^{1/5}}{E^{4/5}}$ | $\frac{V_o^{1/4} \mu^{1/3}}{E^{1/12} \Delta \gamma^{1/4} t^{1/3}}$ | $\frac{V_o^{1/3} \mu^{1/3}}{K_{Ic}^{2/9} \Delta \gamma^{1/9} t^{1/3}}$ |
| $V_*^{[V]}$ | V_o | V_o | $V_o - V_*^{head, [V]}$ | $V_o - V_*^{head, [V]}$ |
| $p_*^{[V]}$ | $\frac{E^{2/3} \mu^{1/3}}{t^{1/3}}$ | $\frac{K_{Ic}^{6/5}}{E^{1/5} V_o^{1/5}}$ | $\frac{E^{2/3} \mu^{1/3}}{t^{1/3}}$ | $\frac{E' \Delta \gamma^{5/9} V_o^{1/3} \mu^{1/3}}{K_{Ic}^{8/9} t^{1/3}}$ |
| $\mathcal{B}_s^{[V]}$ | $\mathcal{K}_m^{[V]} = (t/t_{mk}^{[V]})^{5/18}$ | $\mathcal{M}_k^{[V]} = (t/t_{mk}^{[V]})^{-1}$ | $\mathcal{K}_{\tilde{m}}^{[V]} = \left(\mathcal{M}_{\tilde{k}}^{[V]} \right)^{-1/4}$ | $\mathcal{M}_{\tilde{k}}^{[V]} = \mu' \frac{V_o E'^3 \Delta \gamma^{2/3}}{K_{Ic}^{14/3} t}$ |
| | $\mathcal{B}_m^{[V]} = (t/t_{m\tilde{m}}^{[V]})^{4/9}$ | $\mathcal{B}_k^{[V]} = \Delta \gamma \frac{E^{3/5} V_o^{3/5}}{K_{Ic}^{8/5}}$ | | |

Table 5.3: Characteristic scales (and governing dimensionless parameters) in the different scalings.

Chapter 5. Three-dimensional buoyant hydraulic fractures: finite volume release

| | $t^{[V]}$ | $\ell_*^{[V]} = b_*^{[V]}$ | $w_*^{[V]}$ | $p_*^{[V]}$ |
|---|---|---|---|--|
| $M^{[V]} \rightarrow K^{[V]}$ | $t_{mk}^{[V]} = \frac{E'^{13/5} V_o^{3/5} \mu'}{K_{Ic}^{18/5}}$ | $\ell_{mk}^{[V]} = \frac{E'^{2/5} V_o^{2/5}}{K_{Ic}^{2/5}}$ | $w_{mk}^{[V]} = \frac{K_{Ic}^{4/5} V_o^{1/5}}{E'^{4/5}}$ | $p_{mk}^{[V]} = \frac{K_{Ic}^{6/5}}{E'^{1/5} V_o^{1/5}}$ |
| $M^{[V]} \rightarrow \hat{M}^{[V]}$ | $t_{m\hat{m}}^{[V]} = \frac{E'^{5/4} \mu'}{V_o^{3/4} \Delta\gamma^{9/4}}$ | $\ell_{m\hat{m}}^{[V]} = \frac{E'^{1/4} V_o^{1/4}}{\Delta\gamma^{1/4}}$ | $w_{m\hat{m}}^{[V]} = \frac{V_o^{1/2} \Delta\gamma^{1/2}}{E'^{1/2}}$ | $p_{m\hat{m}}^{[V]} = E'^{1/4} V_o^{1/4} \Delta\gamma^{3/4}$ |
| $\hat{M}^{[V]} \rightarrow \hat{K}^{[V]}$ (tail) | $t_{\hat{m}\hat{k}}^{[V]} = \frac{E'^{11/4} V_o^{3/4} \Delta\gamma^{1/4} \mu'}{K_{Ic}^4}$ | $\ell_{\hat{m}\hat{k}}^{[V]} = \frac{E'^{1/4} V_o^{1/4}}{\Delta\gamma^{1/4}}$ | $w_{\hat{m}\hat{k}}^{[V]} = \frac{K_{Ic}^{4/3}}{E' \Delta\gamma^{1/3}}$ | $p_{\hat{m}\hat{k}}^{[V]} = \frac{K_{Ic}^{4/3}}{E'^{1/4} V_o^{1/4} \Delta\gamma^{1/12}}$ |
| $\hat{M}^{[V]} \rightarrow \hat{K}^{[V]}$ (head) | | $\ell_{\hat{m}\hat{k}}^{head,[V]} = \ell_b = \frac{K_{Ic}^{2/3}}{\Delta\gamma^{2/3}}$ | $w_{\hat{m}\hat{k}}^{head,[V]} = w_{\hat{m}\hat{k}}^{[V]}$ | $p_{\hat{m}\hat{k}}^{head,[V]} = K_{Ic}^{2/3} \Delta\gamma^{1/3}$ |

Table 5.4: Transition scales between regimes. The transition scales of the $M^{[V]} \rightarrow K^{[V]}$ transition correspond to the $K^{[V]}$ -scales, and the transition scales of the $\hat{M}^{[V]} \rightarrow \hat{K}^{[V]}$ (head) to the $\hat{K}^{[V]}$ scales of the head, given respectively as the $K^{[V]}$ and $\hat{K}^{[V]}$ (head) in table 5.3.

Toughness-dominated head

This part of the fracture is strictly identical to the 3D \hat{K} GG (2014) solution, described in section 4.11.1.

Viscous tail

The tail only differs in its overall volume balance, which is given by

$$b \int_0^{\ell^{tail}} \bar{w}(z, t) dz = V_o - V^{head} \quad (5.32)$$

where the opening now depends on time and location. For all other details, we refer the reader to section 4.11.2.

With the hypotheses of the 3D \hat{K} GG (2014) at hand, one can obtain the similarity solutions for the propagating tail through the usual methods (see Spence et al. (1987); Lister (1990b); Spence and Turcotte (1990)). When casting the numerical solutions (with prefactors) presented by Garagash and Germanovich (2022) in our scaling, we obtain

$$\begin{aligned} \ell^{tail}(t) &\approx 2.60603 \frac{V_o^{2/3} \Delta\gamma^{7/9} t^{1/3}}{K_{Ic}^{4/9} \mu'^{1/3}} - 2.05837 \frac{K_{Ic}^{4/3} t^{1/3}}{E'^{2/3} \Delta\gamma^{1/3} \mu'^{1/3}} \\ &\approx 2.60603 \ell_{\hat{k}}^{[V]}(t) - 2.05837 \frac{K_{Ic}^{4/3} t^{1/3}}{E'^{2/3} \Delta\gamma^{1/3} \mu'^{1/3}} \end{aligned} \quad (5.33)$$

we substitute $\ell^{tail} = \gamma^{tail} \ell_{\hat{k}}^{[V]}(t = t_s)$ to obtain

$$\gamma^{tail} \approx 2.60603 \frac{Q_o^{1/3} t^{1/3}}{V_o^{1/3}} - 2.05837 \frac{K_{Ic}^{16/9} Q_o^{1/3} t^{1/3}}{E^{2/3} V_o \Delta \gamma^{10/9}} \quad (5.34)$$

and replace $t = \tau t_s$ to obtain

$$\gamma^{tail} \approx 2.60603 \tau^{1/3} \left(1 - 0.78985 \frac{K_{Ic}^{16/9}}{E^{2/3} V_o^{2/3} \Delta \gamma^{10/9}} \right) \approx 2.60603 \tau^{1/3} (1 - 0.78985 \mathcal{B}_{ks}^{-10/9}). \quad (5.35)$$

This equation shows we will reach the tail solution within a certain percentage. This difference, respectively the change in the prefactor, depends on the value of the dimensionless buoyancy \mathcal{B}_{ks} as

$$\varepsilon \tau^{1/3} = \gamma^{tail} \rightarrow \varepsilon = 1 - 0.78985 \mathcal{B}_{ks}^{-10/9} \quad (5.36)$$

where ε is the change in the prefactor to the tail scaling one obtains for the given parameter combination. To observe the scaling predicted by the $\hat{K}^{[V]}$ solution presented in the article (e.g. $\ell^{tail}(t) = 2.60603 \ell_{\hat{k}}^{[V]}(t)$) within an error of 5 %, we would need a dimensionless buoyancy of the order of

$$\mathcal{B}_{ks}^{\varepsilon=5\%} \geq 11.9872. \quad (5.37)$$

When applying this to figure 5.4b, we show with an orange dotted line the main trend

$$\gamma^{tail} \approx 2.60603 \tau^{1/3} \quad (5.38)$$

and omit the details of the dependency on \mathcal{B}_{ks} because only one simulation (the one showing the linear trend in the continuous release case) could effectively show these details. We hence report the exact prediction for this simulation only in figure 5.10 and observe a minimal error to the end of the simulation of about 24 %. If propagation continues, the error decreases further. To discuss why we do not report further ongoing simulations, we refer the reader to section 5.6.1.

We further get the scales of the opening and pressure of their solution, which are, respectively

$$\overline{w}(t) = 0.845257 \frac{V_o^{1/3} \mu^{1/3}}{K_{Ic}^{2/9} \Delta \gamma^{1/9} t^{1/3}} = 0.845257 w_{\hat{k}}^{[V]}(t) \quad (5.39)$$

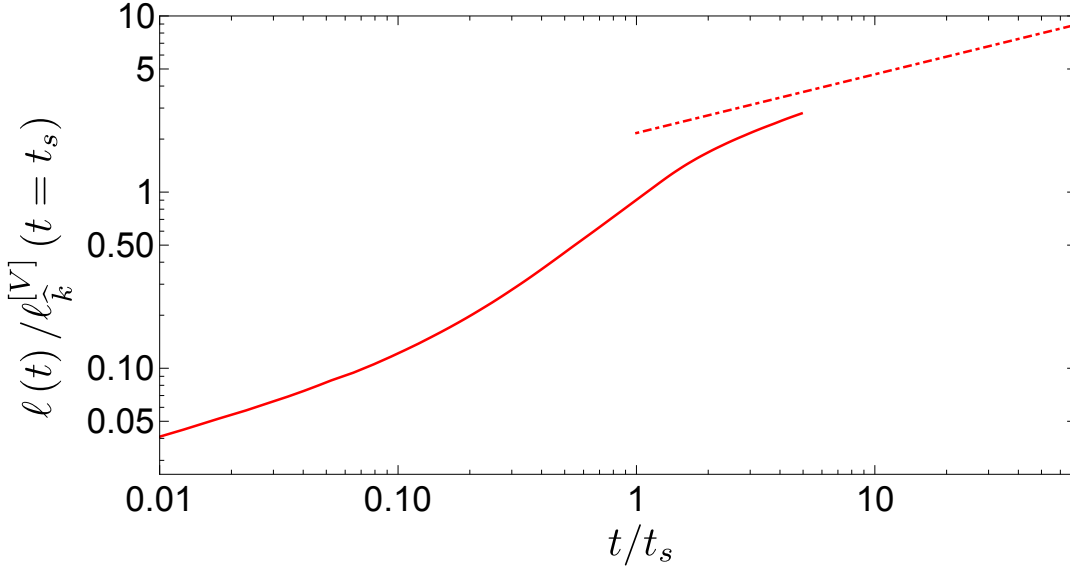


Figure 5.10: Height evolution of a toughness-dominated fracture together with the 3D $\hat{K}^{[V]}$ GG (2014) according to equation (5.35).

$$p(t) = 0.790216 \frac{E' V_o^{1/3} \Delta \gamma^{5/9} \mu^{1/3}}{K_{Ic}^{8/9} t^{1/3}} = 0.790216 p_{\hat{k}}^{[V]}(t). \quad (5.40)$$

More interesting to see is the evolution of the average opening and pressure with the coordinate z

$$\overline{w}(z, t) = 0.523599 \frac{\mu^{1/2}}{\Delta \gamma^{1/2} t^{1/2}} z^{1/2}. \xrightarrow{x=0} w(z, t) = \frac{2}{3} \frac{\mu^{1/2}}{\Delta \gamma^{1/2} t^{1/2}} z^{1/2} \quad (5.41)$$

$$p(z, t) = 0.489504 \frac{E' \Delta \gamma^{1/6} \mu^{1/2}}{K_{Ic}^{2/3} t^{1/2}} z^{1/2}. \quad (5.42)$$

In figure 5.10, we show the opening and pressure profile at the last time step of the simulation with $\mathcal{M}_{\hat{k}} = 1$ and $\mathcal{B}_{ks} = 2$ reported in figure 4) of the main article. One observes that the match obtained using equations (5.41) and (5.42) is very accurate.

Limit of applicability of the 3D $\hat{K}^{[V]}$ GG (2014) solution

This solution is only valid if the pressure in the tail does not allow for lateral expansion (e.g., the fracture breadth does not grow). In other terms, the pressure in the tail must at all times be $p(z, t) \leq K_{Ic} / \sqrt{0.782257 \ell_b}$. As the pressure in the tail reduces, this condition verifies at a

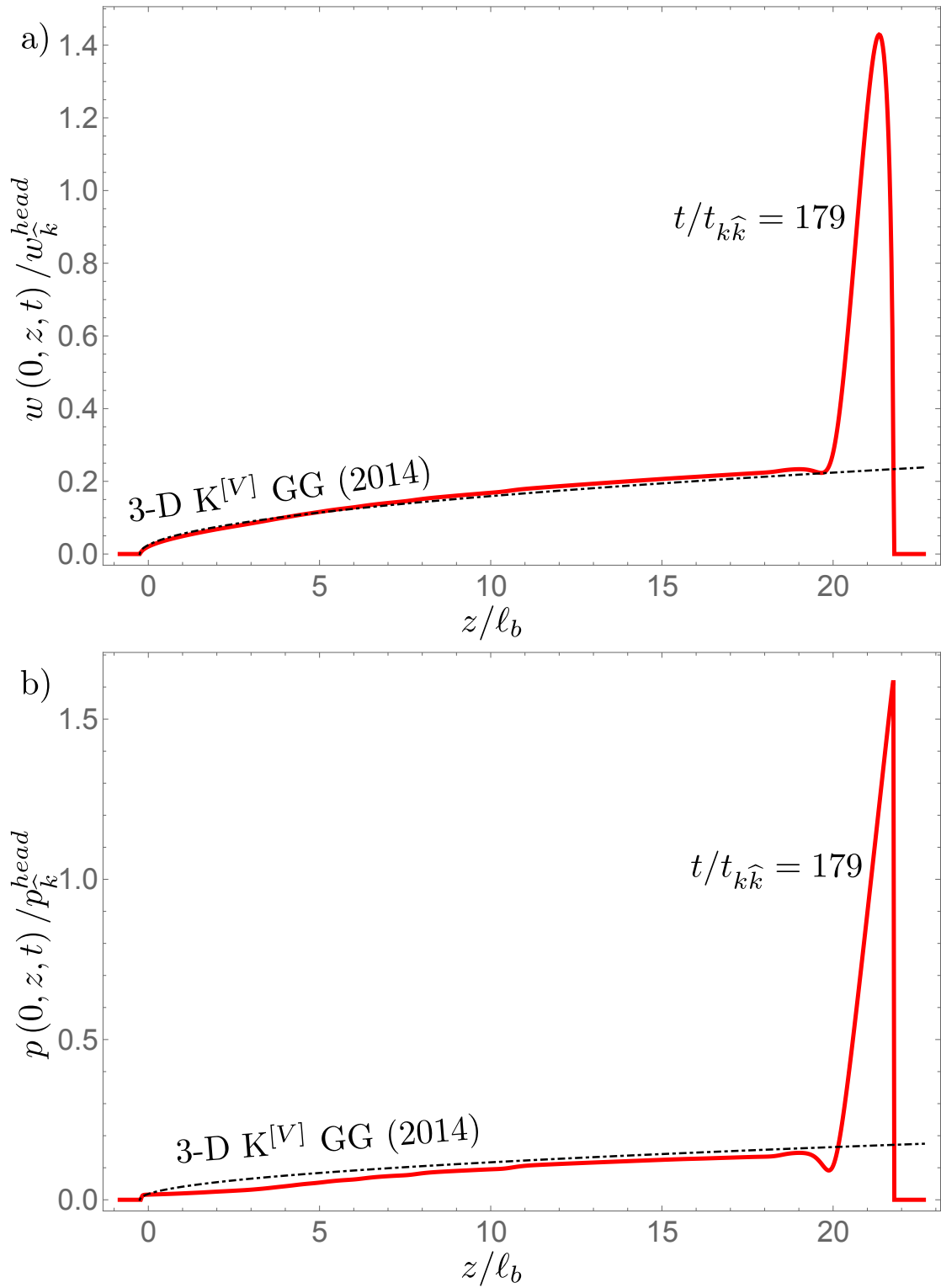


Figure 5.11: Opening (a) and pressure (b) along the centerline (e.g., $x = 0$) for a toughness-dominated simulation with $\mathcal{M}_{\hat{k}} = 1$ and $\mathcal{B}_{ks} = 2$ at $t/t_{k\hat{k}} = 179$. Black dashed-dotted lines show the tail solutions of equations (5.41) and (5.42).

given time during fracture propagation. Garagash and Germanovich (2014) derive this limit as

$$\frac{V_o/V_*}{t/t_*} < 0.352139 \quad (5.43)$$

which be transformed in a stabilization time of the form

$$t_{stab} = 0.545885 t_{\hat{m}\hat{k}}^{[V]} \mathcal{B}_{ks}^{5/12}. \quad (5.44)$$

The fact that lateral stabilization occurs later than the transition of the tail from viscosity- to toughness-dominated propagation (because $\mathcal{B}_{ks} \geq 1$ for buoyant fractures) explains why we have such a hard time showing simulations validating the toughness-dominated limit after being viscosity-dominated. Figure 5.6 shows this problem, and we sketch the computational cost implied in section 5.6.1.

5.10.2 Self-Similarity of the Zero-Toughness Solution

In section 5.4.2 of the main article, we mention that the evolution of a zero-toughness, finite volume, buoyant hydraulic fracture becomes nearly self-similar at a late time. This self-similarity is a function of the scales presented in equation (5.24)

$$\begin{aligned} \ell_{\hat{m}}^{[V]} &= \frac{V_o^{1/2} \Delta \gamma^{1/2} t^{1/3}}{E^{1/6} \mu^{1/3}}, & b_{\hat{m}}^{[V]} &= \frac{E^{1/4} V_o^{1/4}}{\Delta \gamma^{1/4}} \\ w_{\hat{m}}^{[V]} &= \frac{V_o^{1/4} \mu^{1/3}}{E^{1/12} \Delta \gamma^{1/4} t^{1/3}}, & p_{\hat{m}}^{[V]} &= \frac{E^{2/3} \mu^{1/3}}{t^{1/3}}. \end{aligned} \quad (5.45)$$

Figure 5.12 shows a simulation with $\mathcal{M}_{\hat{k}} = \mathcal{B}_{ks} = \infty$ and $\mathcal{B}_{ms} = 10^{-3}$ (e.g. transitioning from radial to buoyant in the viscosity-dominated pulse $M^{[V]}$ -regime) where we report all quantities scaled by the scaling of equation (5.45). Note that we use a shifted z coordinate \hat{z} as to have $\hat{z} = 0$ coinciding with the lowest point of the fracture.

The horizontal scale of the footprint is time-independent, whereas its vertical scale depends on time as $\ell_{\hat{m}}^{[V]} \propto t^{1/3}$. One observes that after the transition, the total height of the fracture (e.g., the highest point in the scaled simulation) no longer changes. Simultaneously, fracture propagation becomes akin to the scaling, as depicted in figure 5.7. Such is the case for times later than $t/t_{m\hat{m}}^{[V]} \gtrsim 10$, even though the footprint shape is still elliptical. During ongoing propagation, the shape becomes more and more avocado-like before approaching self-similarity for $t/t_{m\hat{m}}^{[V]} \gtrsim 800$. The resulting footprint is similar to the self-similar shape of a zero-toughness, continuous-release, buoyant hydraulic fracture (see figure 4.5), albeit elongated. As in this continuous release case, the nearly self-similar shape occurrence relates to the head volume becoming negligible compared to the total release volume. This effect is visible in figure 5.12b,

where the head to the right becomes smaller and no longer shows significantly more cross-section volume than the adjacent parts of the tail. The detail of the head becomes negligible when observing the overall shape, even though it still governs the propagation rate.

Similarly to the continuous release case, the footprint becomes flat around the centreline $x = 0$ (see figure 5.12a), indicating that the approximation of a 2D plain strain fracture at the centreline might be applicable. Roper and Lister (2007) sketched such a solution in section 6 of their article and derived the fracture height (see their equation (6.7)). Interestingly, this two-dimensional evolution is equivalent to the scaling for the toughness-dominated case of equation (5.41) but without a prefactor

$$w^{lister}(z, t) = \frac{\mu'^{1/2}}{\Delta\gamma^{1/2} t^{1/2}} z^{1/2}. \quad (5.46)$$

Scaling with $\Omega = w^{lister}(z, t) / w_{\hat{m}}^{[V]}$ and using the dimensionless coordinate $\hat{\zeta} = \hat{z} / \ell_{\hat{m}}^{[V]}$ we obtain

$$\Omega(\hat{\zeta}) = \sqrt{\hat{\zeta}} \quad (5.47)$$

shown as a blue dashed line in figure 5.12c. The match close to the source region is astonishing and holds even if the width constraint becomes activated close to the source point. In the proximity of the propagating head, the solution seems to deviate because of 3D effects. Nonetheless, combining the zero toughness head solution (c.f. figure 4.7 of chapter 4) with equation (5.47) could result in a complete description of zero toughness, buoyant, finite volume fractures.

Chapter 5. Three-dimensional buoyant hydraulic fractures: finite volume release

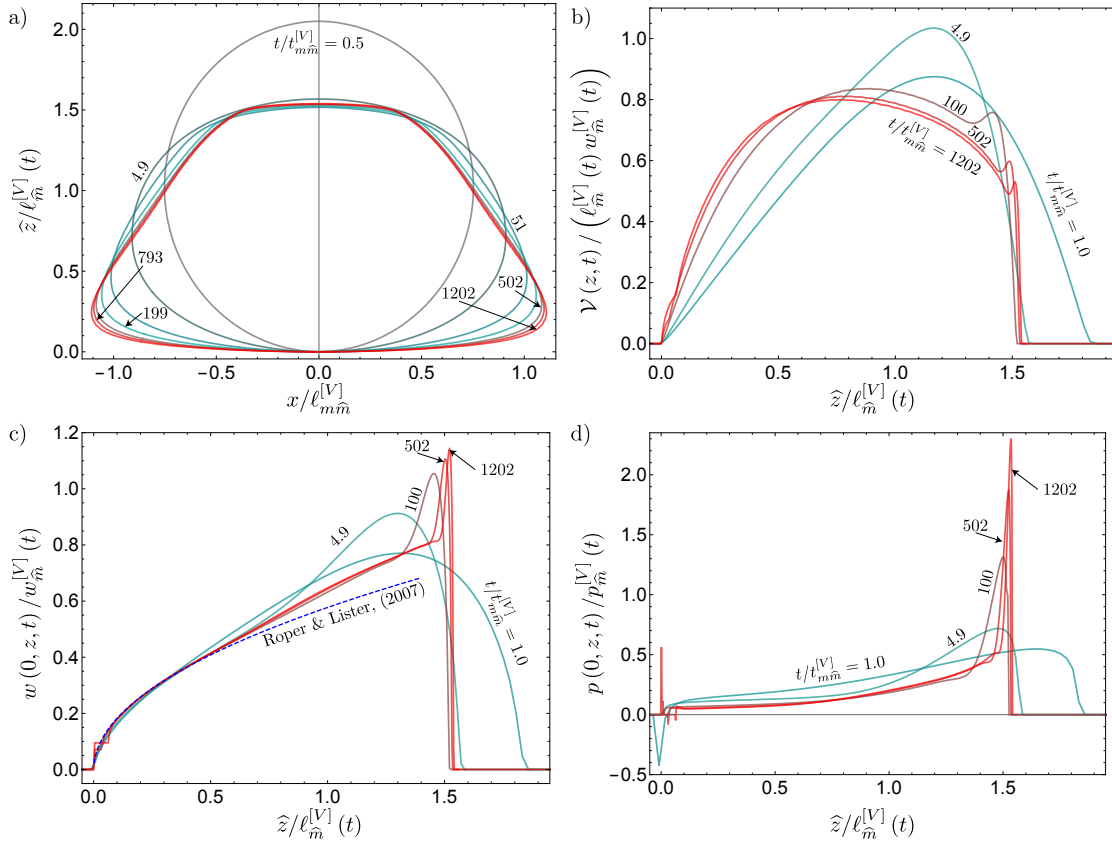


Figure 5.12: Footprint (a), cross-sectional volume (b), opening (c), and pressure (d) of a zero-toughness, finite volume buoyant hydraulic fracture scaled by the corresponding $\hat{M}^{[V]}$ -scaling (see equation (5.45), or equation (5.24)). The blue dashed line in c) indicates the solution presented by Roper and Lister (2007).

6 Effects of fluid leak-off or solidification on buoyant hydraulic fractures

This chapter is a manuscript currently prepared for submission to the Journal of Geophysical Research Letters (GRL).

Contributions

Andreas Möri has conceptualized the problem, performed a formal and scaling analysis, decided on the methodology, adapted the numerical solver, committed validation against known results, searched experiments for comparison, and developed the discussion. He further generated the visualizations, wrote the original draft, and edited and adapted the manuscript. Prof Brice Lecampion has assisted in clarifying the pulsation times, reviewed and helped to adjust figures and the writing, and acquired the funding for this study.

6.1 Abstract

Three-dimensional buoyant hydraulic fractures propagating through the lithosphere show large extents and migrate during long periods. The host formations are usually permeable, which is susceptible to generating leak-off-related effects to fracture propagation. Similarly, the emplacement of magmatic intrusions shows thermal effects due to the temperature difference between the fluid and the solid. We derive in this contribution the limiting late-time regime for buoyant hydraulic fractures under a continuous fluid release at a constant rate considering these two effects. We demonstrate that, under certain conditions, the two can be treated as a one-dimensional diffusion problem of matching time dependence. Through scaling arguments and numerical simulations, we demonstrate that the overall fracture propagation is akin to a global volume balance but shows a pulsating behavior when considering the typical head and tail structure of buoyant hydraulic fractures. Such a pulsating behavior observed in laboratory experiments may arrive even for a continuous fluid release with a constant release rate.

6.2 Introduction

We consider in this study three-dimensional (3D) planar hydraulic fractures propagating in the subsurface and investigate the phenomena of fluid leak-off and solidification. The problem of fluid leak-off (e.g., the loss of fracturing fluid into the surrounding porous media) has obtained a lot of interest in the literature. This interest stems from industrial applications, where the so-called fracturing efficiency describes how much of the injected fluid remains in the fracture. In other words, this quantity is an indicator of fracture opening.

The most commonly used model for fluid leak-off is the so-called Carter's model (named after Carter (1957)). This model assumes a porous solid surrounding the fracture governed by Darcy flow. Such a configuration leads to a 3D diffusion equation governing pore pressure and fluxes in the porous media. Additional complexity is added to the problem by the time dependence of the problem and the fact that the fluid pressure in the fracture is an inherent part of the problem. Carter's leak-off model uses several simplifications to overcome these complexities. Notably, it assumes only slightly permeable media, which holds for most deep geo-energy applications (Kovalyshen, 2010), such that the fracture propagates much faster than 3D diffusion can occur. In line with the assumption of deep reservoirs with low permeability, the excess fluid pressure (above the confining background stress) is supposed to be negligible. Combining these two major assumptions, Carter's leak-off model reduces to a pressure-independent, one-dimensional (1D) diffusion equation in which the leak-off velocity evolves as an inverse square-root dependence of the exposure time (e.g., $v_l \propto (t - t_o)^{-1/2}$). The effects of a Carter-like leak-off have been studied numerically for two-dimensional (2D) plane strain (Adachi and Detournay, 2008) and axisymmetric (penny-shaped) fractures (Mad-yarova, 2003). Extensions to the Carter leak-off model were proposed by Kovalyshen (2010). He performed a study using the complete 3D diffusion and showed that Carter's leak-off approx-

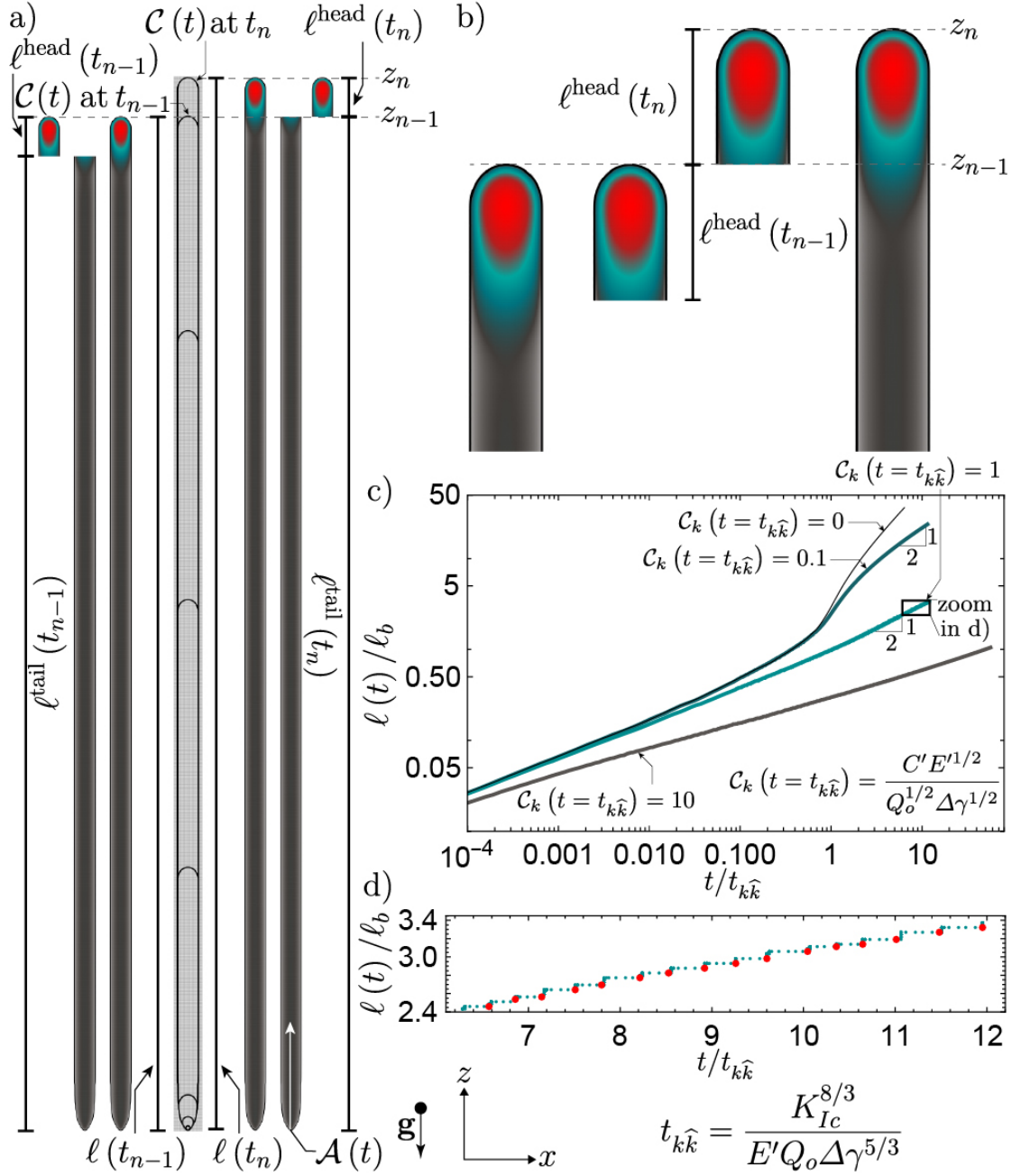


Figure 6.1: Sketch of a buoyant hydraulic fracture propagating within a permeable media. a) Sketch showing the change in total $\ell(t)$, head $\ell^{\text{head}}(t)$, and tail $\ell^{\text{tail}}(t)$ height in the interval $\Delta t = t_n - t_{n-1}$. The color code shows the fracture opening normalized by the maximum value. b) Zoom on the propagation at the head. The head's positions and the tail's beginning can be related to the coordinates z_n and t_{n-1} . c) Evolution of total fracture height $\ell(t)$ as a function of time for simulations with various leak-off coefficients at the transition from radial to buoyant propagation $\mathcal{C}_{\hat{k}}$. d) Zoom on the evolution of the simulation with $\mathcal{C}_{\hat{k}} = 1$, showing the pulsation of the fracture.

Chapter 6. Effects of fluid leak-off or solidification on buoyant hydraulic fractures

imation breaks down for highly permeable solids. A similar result was found by Kanin et al. (2020); Dontsov (2021), who assumed a pressure-dependent leak-off instead of complete 3D diffusion. Other studies investigated the circulation in a tip region (Detournay and Garagash, 2003), or water flooding treatments in weak permeable rocks (Gao and Detournay, 2020, 2021). All these contributions focused on propagating hydraulic fracture. The study of arresting or receding fractures has only recently obtained interest. In the framework of Carter's leak-off, we investigated in chapter 3 the arrest of fractures generated by a finite volume of fluid released. They showed that, albeit post-injection propagation is possible, fluid leak-off will always lead to an ultimate arrest of the fracture. The work presented in chapter 3 was extended by Peirce (2022) to account for the closure of axisymmetric fractures.

Interestingly, some indications can be derived from the investigation of solidifying magmatic intrusions. Instead of economic considerations, the interest in the solidification of dikes relates to their ability to reach the surface and become eruptive. In contrast to the evaluations of leak-off for non-buoyant fractures, the study of solidification considers already well-established buoyant fractures. Bruce and Huppert (1990) notably developed a model based on the initial presence of a finite width dike in 2D. To obtain the same time-dependence of the solidification front as for the Carter leak-off, they assumed an early-time behavior where the advection of the fluid is negligible, and the conduction diffusion equation governs the problem. If the temperature difference between the fluid at its source is minor compared to the far-field temperature of the host medium, Bruce and Huppert (1990) derive a solidification front moving inward at a rate with an inverse square-root dependence of the exposure time $v_s \propto (t - t_o)^{-1/2}$. Several studies used this, or similar, simplified approaches to derive limiting volumes for the ascent of magmatic intrusions (Turcotte and Schubert, 2002; Bruce and Huppert, 1989, 1990; Bruce, 1989; Carrigan et al., 1992; Delaney and Pollard, 1982; Petford et al., 1994; Rubin, 1993). These studies were similarly limited to early-time behavior and generally 2D geometries.

In this study, we investigate the influence of a Carter-like leak-off for buoyant hydraulic fractures and the early-time solidification of magmatic intrusions. We use scaling arguments and validate these using a 3D planar hydraulic fracture solver (PyFrac, (Zia and Lecampion, 2020)).

6.3 Data and methods

6.3.1 Mathematical formulation

Figure 6.1a sketches the problem considered in this contribution. A planar tensile hydraulic fracture is fed by a constant fluid inflow from a deep laying point source leading to vertical propagation. The propagation plane is enforced by the minimum in-situ stress $\sigma_o(z)$ acting horizontally (perpendicular to the vertical plane). Vertical propagation inherently means that the gravity vector is acting in-plane in the downward direction (in $-z$, see figure 6.1a).

Because we consider deep hydraulic fractures, the presence of a fluid lag can be neglected (see discussion in Garagash and Detournay (2000); Lecampion and Detournay (2007); Detournay (2016)). In this numerical model, the in-situ stress is assumed to vary linearly with depth akin to the weight of the overlaying rock (Heidbach et al., 2018; Cornet, 2015; Jaeger et al., 2007). The material within which the fracture propagates is modeled as a linear elastic medium with constant and uniform properties. Under these assumptions, we can relate the net loading on the fracture (e.g., the fluid pressure minus the in-situ stress $p(x, z, t) = p_f(x, z, t) - \sigma_o(z)$) to the fracture opening $w(x, z, t)$ as (Crouch and Starfield, 1983; Hills et al., 1996)

$$p(x, z, t) = p_f(x, z, t) - \sigma_o(z) = -\frac{E'}{8\pi} \int_{\mathcal{A}(t)} \frac{w(x', z', t)}{[(x' - x)^2 + (z' - z)^2]^{3/2}} dx' dz' \quad (6.1)$$

where we have denoted the fracture surface in the propagation plane as \mathcal{A} and introduced the materials plane-strain modulus $E' = E/(1 - \nu^2)$ (E is the materials Young's modulus and ν its Poisson's ratio). The model accounts for the fluid flow of an incompressible Newtonian fracturing fluid in the fracture under the hypothesis of lubrication flow (Batchelor, 1967). The corresponding width-averaged continuity equation reads

$$\frac{\partial w(x, z, t)}{\partial t} + \nabla \cdot (w(x, z, t) \mathbf{v}_f(x, z, t)) + \frac{2C_L}{\sqrt{t - t_o(x, y)}} = \delta(x) \delta(z) Q_o(t). \quad (6.2)$$

In equation (6.2) we have denoted the width averaged fluid velocity as $\mathbf{v}_f(x, z)$, the constant volumetric fluid release rate as Q_o , Carter's leak-off coefficient as C_L , and the leak-off initiation time, the time when the fracture arrives at a point (x, z) , as $t_o(x, z)$. The fluid exchange according to the third left-hand-side term of equation (6.2) assumes Carter leak-off (Carter, 1957; Howard and Fast, 1957), a model considering a one-dimensional diffusion perpendicular to the fracture under the condition that the fluid net pressure is much smaller than the in-situ stress. These assumptions hold for most hydraulic fractures at depth (see among others Kovalyshen (2010); Dontsov (2021)). In the framework of the thin film lubrication approximation, we can define the fluid flux along the fracture using Poiseuille's law

$$\begin{aligned} \mathbf{q}(x, z, t) &= w(x, z, t) \mathbf{v}_f(x, z, t) = -\frac{w(x, z, t)^3}{\mu'} (\nabla p_f(x, z, t) - \rho_f \mathbf{g}) \\ &= -\frac{w(x, z, t)^3}{\mu'} \left(\nabla p(x, z, t) + \Delta\gamma \frac{\mathbf{g}}{|\mathbf{g}|} \right). \end{aligned} \quad (6.3)$$

In the definition of Poiseuille's law, the constant and uniform fluid density is denoted as ρ_f , and we have used the equivalent parallel $\mu' = 12\mu_f$, which is a simple multiplication of the fluid viscosity μ_f . Were we changed from the fluid to the net pressure and accounted for the linear variation of the in-situ stress. $\Delta\gamma = \Delta\rho g = (\alpha\rho_s - \rho_f)g$ is the buoyancy of the system

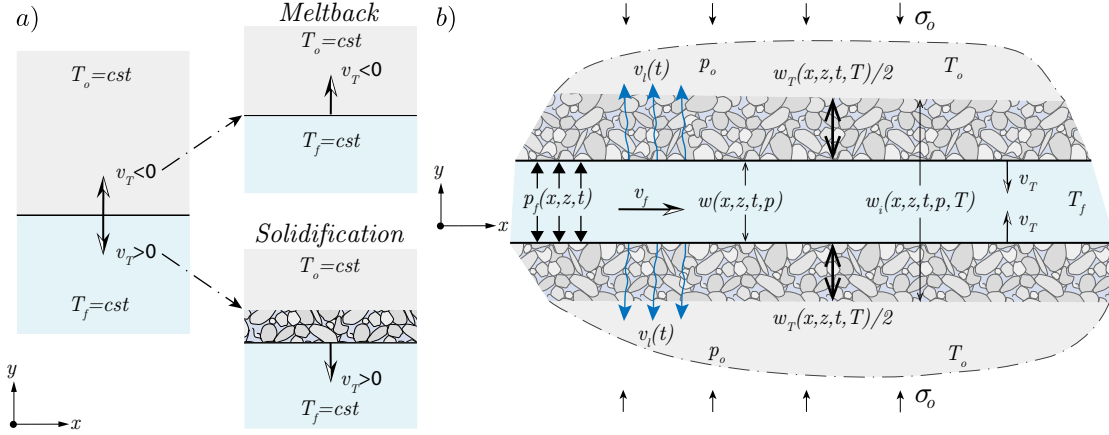


Figure 6.2: a) Sketch of a one-dimensional Stefan problem of a moving solidification boundary. The fracture can either melt the surrounding rock (meltback) such that the opening increases or the fluid solidifies, and the effective fracture opening for fluid flow reduces. b) Section of the considered problem where leak-off and solidification are considered. The fracture opening gets reduced due to the solidification of the fluid, whereas leak-off can still occur across the solidified boundary.

fluid-solid with α a lateral earth pressure coefficient and ρ_s the density of the solid. The driving mechanism of fracture propagation is the fluid release at the point source. We have thus to validate the volume balance of the system given by

$$Q_o t = \int_{\mathcal{A}(t)} w(x, z, t) dx dz + \int_{\mathcal{A}(t)} \int_t \frac{2C_L}{\tau - \tau_o} d\tau. \quad (6.4)$$

For stable fracture propagation in a linear elastic medium, we can use the linear elastic fracture mechanics (LEFM) approach to quasi-static equilibrium and obtain a propagation criterion of the form

$$(K_I(x_c, z_c) - K_{Ic}) v_c(x_c, z_c) = 0 \quad v_c(x_c, z_c) \geq 0 \quad K_I(x_c, z_c) \leq K_{Ic} \quad (6.5)$$

where v_c is fracture velocity normal to the fracturing front at any point laying on the fracture front (x_c, z_c) . Equation (6.5) states that when the fracture propagates $v_c > 0$, the stress intensity factor at the tip K_I must match the fracture toughness of the host media K_{Ic} .

The 3D planar-hydraulic fracture solver PyFrac (Zia and Lecampion, 2020) is used to solve the set of equations (6.1), (6.2), (6.4), and (6.5). This open-source code is a Python implementation of the implicit level set algorithm (ILSA) (Peirce and Detournay, 2008) tested in various regimes of hydraulic fracture growth (Peirce, 2015, 2016; Zia et al., 2018; Zia and Lecampion, 2020; Moukhtari et al., 2020) (see also chapters 3, 4, and 5).

6.3.2 Model for fluid solidification

When dealing with magmatic intrusions in the lithosphere, magma solidification becomes a process to consider. Solidification includes mass exchanges between the solid and the fluid, rheological changes of the latter, and thermally induced changes to the host rock. It is driven by two heat transfer processes, advection by the hot flowing magma along the dyke and convection from the magmatic body to the surrounding host rock. We restrict hereafter to conductive heat exchange between the fluid and the solid only (see figure 6.2 for a sketch of the problem) and assume Newtonian rheology for the magma. The last assumption is validated thanks to limited crystallization (Brandeis and Jaupart, 1986). We assume a laminar flow in the fracture (consistent with our base hypothesis), and shear heating effects are neglected. When we additionally make the hypothesis of a solid at a constant initial temperature T_o everywhere and a fluid remaining at a constant temperature T_f , the problem of solidification reduces to a one-dimensional Stefan problem (Stefan, 1891) (see i. e. Carslaw and Jaeger (1959) for its detailed solution). We make here the additional assumptions that the density of the solidified melt and the density of the fluid, as well as their melting temperature T_m and latent heat L , are equivalent. Under these assumptions, the velocity of the solidification front is given by

$$v_T = \lambda \sqrt{\frac{\kappa_f}{t}} \quad (6.6)$$

with λ the solution to

$$\lambda \pi^{1/2} = -\frac{e^{-\lambda^2}}{\text{Erfc}[\lambda] S_f} - \sqrt{\frac{\kappa_s}{\kappa_f}} \frac{e^{-\frac{\kappa_f}{\kappa_s} \lambda^2}}{\text{Erfc}[\lambda] S_s} \quad (6.7)$$

with the Stefan numbers

$$S_f = \frac{L}{c_f (T_f - T_m)}, \quad S_s = \frac{L}{c_s (T_m - T_o)} \quad (6.8)$$

where we have used the subscripts \cdot_s and \cdot_f to denote quantities of the fluid and solid respectively. κ_i is the thermal diffusivity and c_i the corresponding specific heat of the material. The problem thus depends on its Stefan numbers (6.8) and the respective ratio of the thermal diffusivity. In the case of solidification, one can assume that the thermal diffusivity and specific heat of the materials are equivalent (e.g., $\kappa_s = \kappa_f = \kappa$ and $c_s = c_f = c$), such that equation (6.7) reduces to

$$\pi^{1/2} \lambda e^{\lambda^2} = -\frac{1}{\text{Erfc}[\lambda] S_c} \quad (6.9)$$

with the Stefan number

$$S_c = \frac{L}{c (T_f - T_o)}. \quad (6.10)$$

Chapter 6. Effects of fluid leak-off or solidification on buoyant hydraulic fractures

Equation (6.9) gives solidification ($\lambda < 0$, see figure 6.2a) for all positive values of S_c .

Figure 6.2b shows a possible consideration of solidification for dikes in the framework of planar 3D hydraulic fractures. Denoting the total opening as w_t , the hydraulically and elastically relevant open channel height as w , and the part lost due to the solidification of the fluid as w_T . Rewriting now the conservation of mass (6.2) in the absence of fluid leak-off as

$$\frac{dw_t(p, T, x, z, t)}{dt} + \nabla \cdot (w(x, z, t) \mathbf{v}_f(x, z, t)) = \delta(x) \delta(z) Q_o(t). \quad (6.11)$$

Following the definitions of the three openings, we can rewrite the first term on the left-hand-side of equation (6.11) as

$$\begin{aligned} w_t(p, T, x, z, t) &= w(p, x, z, t) + w_T(T, x, z, t) \\ \frac{dw_t(p, T, x, z, t)}{dt} &= \frac{\partial w(p, x, z, t)}{\partial t} \Big|_{T=cst.} + \frac{\partial w_T(T, x, z, t)}{\partial t} \Big|_{p=cst.} \\ &= \frac{\partial w(p, x, z, t)}{\partial t} \Big|_{T=cst.} = -2\lambda \sqrt{\frac{\kappa}{t}}. \end{aligned} \quad (6.12)$$

Note that in equation (6.12), we have accounted for the direction of the solidification boundary and used equation (6.6). We also have a factor 2 appearing because equation (6.6) gives the velocity of a single solidification front. As sketched in figure 6.2, both boundaries solidify simultaneously such that the total reduction in opening is equivalent to twice the propagation of a single solidification front. The solidification will only begin once the fracture has arrived at the location evaluated. This moment has already been used in the definition of the fluid leak-off as t_o , which is not only the leak-off but also the solidification initiation time. Introducing now the total derivative (6.12) in the conservation of mass (6.11), we obtain the final expression for the case of fluid solidification as

$$\frac{\partial w(p, x, z, t)}{\partial t} + \nabla \cdot (w(x, z, t) \mathbf{v}_f(x, z, t)) - \frac{2\lambda \sqrt{\kappa}}{\sqrt{t - t_o(x, y)}} = \delta(x) \delta(z) Q_o(t). \quad (6.13)$$

Comparing equation (6.13) with equation (6.2) we observe that the leak-off and solidification terms show the same time-dependence and differ only by their prefactor. It is thus possible to define a general fluid mass loss coefficient C' as

$$C' = \begin{cases} 2C_L & \text{for fluid leak-off,} \\ -2\lambda \sqrt{\kappa} & \text{for solidification.} \end{cases} \quad (6.14)$$

In the expressions hereafter, we restrict our analysis to the values of C' (6.14) without referencing a specific mechanism generating the fluid mass loss.

6.3.3 Leaking/Solidifying buoyant hydraulic fracture

When considering a fully developed, buoyant hydraulic fracture, the characteristic head-tail structure shown in figure 6.1 emerges (see the derivations in chapters 4 and 5). In chapters 4 and 5, we have shown that the fracture tail governs the dynamics/ascent rate of such fractures, whereas their head dominates the shape. The respective regimes of the head and tail are related to the typical competition of energy dissipation mechanism in hydraulic fractures (Detournay, 2016). The characteristics of a hydraulic fracture are different if the energy dissipated by the viscous flow of the fluid (viscosity-dominated) exceeds the energy required to create new surfaces and vice-versa (toughness-dominated). Additional complexity arises when considering solidification or fluid exchange between the fracture and the solid. The fracture can either be storage- (most of the total released volume is in the fracture) or leak-off/solidification-dominated (most of the released fluid has been lost to the surrounding host rock or got solidified). We will refer hereafter to the leak-off/solidification-dominated case as the leak-off-dominated case only.

Global scaling

The scalings for storage-toughness-dominated buoyant fractures have been shown in table 4.3 and read

$$\begin{aligned} b_{\hat{k}} &= \frac{K_{Ic}^{2/3}}{\Delta\gamma^{2/3}}, & \ell_{\hat{k}}(t) &= \frac{Q_o^{2/3} \Delta\gamma^{7/9} t}{\mu'^{1/3} K_{Ic}^{4/9}}, \\ w_{\hat{k}}(t) &= \frac{Q_o^{1/3} \mu'^{1/3}}{K_{Ic}^{2/9} \Delta\gamma^{1/9}}, & p_{\hat{k}}(t) &= \frac{E' Q_o^{1/3} \Delta\gamma^{5/9} \mu'^{1/3}}{K_{Ic}^{8/9}} \end{aligned} \quad (6.15)$$

$$\mathcal{C}_{\hat{k}} = C' \frac{K_{Ic}^{2/9} \Delta\gamma^{1/9} t^{1/2}}{Q_o^{1/3} \mu'^{1/3}}, \quad (6.16)$$

where b_* is the scale of the lateral extent, ℓ_* the total length of the fracture, w_* is the scale of the overall average opening, and p_* the average pressure. Equation (6.16) defines a dimensionless leak-off coefficient. Its increasing function of time indicates that the overall fracture necessarily becomes leak-off-dominated at late time. Adopting the same scaling approach as in the storage-toughness-dominated case, we obtain the buoyant leak-off-toughness-dominated scalings enforcing that the second term on the right-hand-side of equation (6.4) dominates the overall volume balance. Considering then that the dynamics are given by viscous flow in the tail, we obtain the global scaling as

$$\begin{aligned}
 b_{\hat{k}} &= \frac{K_{Ic}^{2/3}}{\Delta\gamma^{2/3}}, \quad \ell_{\hat{k}}(t) = \frac{Q_o \Delta\gamma^{2/3} t^{1/2}}{C' K_{Ic}^{2/3}}, \\
 w_{\hat{k}}(t) &= \frac{Q_o^{1/2} \mu^{1/2}}{C'^{1/2} K_{Ic}^{1/3} \Delta\gamma^{1/6} t^{1/4}}, \quad p_{\hat{k}}(t) = \frac{E' Q_o^{1/2} \Delta\gamma^{1/2} \mu^{1/2}}{C'^{1/2} K_{Ic} t^{1/4}}
 \end{aligned} \tag{6.17}$$

where we have used the subscript $\hat{\cdot}$ to indicate a buoyant leak-off-dominated scaling. The scaling (6.17) indicates that leak-off/solidification significantly slows down fracture propagation in time. It is expected that buoyant hydraulic fractures either ascend due to the linear velocity prescribed by the storage-toughness-dominated scaling (see table 4.3) or with the square root dependence coming from equation (6.17), disregarding their structural details. For the discussion of this chapter, we retain these two scalings because we show in appendix 6.6.2 that the leak-off toughness-dominated scaling is the late-time scaling of all buoyant hydraulic fractures.

Head-Tail separation

We are focusing first on the specific case of storage-toughness-dominated buoyant hydraulic fractures. Chapter 4 has shown that such fractures have a head of constant shape and volume. The tail thus governs the dynamics of this fracture without any fluid exchange between the two. Moreover, the head volume is equivalent to the minimum volume necessary for buoyant propagation (see the discussion in section 5.4). When extending the approach to account for fluid leak-off/solidification, the head is expected to lose fluid mass such that the head volume would fall below the critical one, which would, as of the derivations of section 5.4, arrest the upward propagation. Due to the nature of the considered fluid loss depending solely on the exposure time, we investigate the amount of fluid lost by the head alone. As for a storage-toughness-dominated fracture, the propagation velocity of the fracture is constant (see equation 6.15), and the exposure time becomes constant. We highlight this by the observation of figure 6.1b where we show the movement of the head for a time step of $\Delta t = t_n - t_{n-1}$ corresponding to the advancement of the head of exactly its head length ℓ^{head} . Starting from the general form of a leak-off volume (see also the second right-hand-side term of equation (6.4))

$$\mathcal{V}_L^{\text{head}} \sim \int_t \int_x \int_z \frac{C'}{\sqrt{\tau - \tau_o}} d\xi d\zeta d\tau. \tag{6.18}$$

Performing a change of variable for the arrival and maximum exposure time. The former of the two results in a leak-off initiation time t_o as the solution to the equation

$$t_o \rightarrow z_{n-1} = \ell(t_o) + \ell^{\text{head}}(t_o). \tag{6.19}$$

Similarly, the head will be past this location at the time t_{max} when we have the condition

$$t_{max} \rightarrow z_{n-1} = \ell(t_{max}). \quad (6.20)$$

For the particular case of the toughness-, storage dominated fracture, we can define the exact dependences of τ and τ_o as

$$\ell_{\hat{k}}(t) = \frac{Q_o^{2/3} \Delta \gamma^{7/9} t}{K_{Ic}^{4/9} \mu^{1/3}} = v_{\hat{k}} t, \quad \ell_{\hat{k}}^{\text{head}} = \left(\frac{K_{Ic}}{\Delta \gamma} \right)^{2/3} = \ell_b \rightarrow \tau = \frac{\zeta}{v_{\hat{k}}}, \quad \tau_o = \frac{\zeta - \ell_b}{v_{\hat{k}}}. \quad (6.21)$$

In equation (6.21), we have made use of the constant fracture velocity $v_{\hat{k}}$. With these inclusions, the integral equation of the head leak-off volume (6.18) becomes

$$\mathcal{V}_L^{\text{head}} \sim \int_t \int_o^{b^{\text{head}}} \int_{v_{\hat{k}} t}^{v_{\hat{k}} t + \ell_b} \frac{C' v_{\hat{k}}^{1/2}}{\sqrt{\zeta - (\zeta - \ell_b)}} d\xi d\zeta d\tau = \frac{C' v_{\hat{k}}^{1/2}}{\ell_b^{1/2}} \int_t \int_o^{b^{\text{head}}} \int_{v_{\hat{k}} t}^{v_{\hat{k}} t + \ell_b} d\xi d\zeta d\tau. \quad (6.22)$$

Performing a dimensional analysis of equation (6.22), we obtain the scale of the leak-off volume of a propagating head as

$$\mathcal{V}_L^{\text{head}} \propto C' v_*^{1/2}(t) \ell_*^{\text{head}1/2}(t) b_*^{\text{head}}(t) t, \quad (6.23)$$

where we allow for the head breadth and length and for fracture velocity to be time-dependent. We further replaced the subscript characterizing this specific case with a placeholder. This generalization holds because the dependence is linked to the exposure time, which is always on the order of the time required for the fracture to propagate the distance of its head. The scaling of this time is thus inherently coming from the ratio between the distance to travel and the velocity (for a demonstration of the applicability, see appendix 6.6.1).

When introducing the scales of the storage-toughness-dominated buoyant hydraulic fracture (see equation (6.21) in equation (6.23)) we can see that the leak-off volume of the head increases linearly in time. In this case, no fluid exchange between the tail and head occurs such that the head is of a finite volume. This volume is reduced due to the fluid leak-off/solidification. At some point, it falls below the critical volume, and the fracture arrests. We hypothesize that also the fracture footprint no longer changes, meaning that the tail stops elongating simultaneously. From this, two effects arise: First, the exposure time of the arrested head increases, and second, fluid exchange between the tail and head immediately initiates. The former means that the leak-off rate of the head will now follow the classical square-root decrease of the fluid mass loss models, and the leak-off volume will only increase as $\mathcal{V}_L^{\text{head}} \propto t^{1/2}$. We observe from the fluid exchange between the head and tail that the released fluid directly feeds the head. For

the continuous release at a constant rate considered, the inflow to the head thus increases linearly in time such that the head should regain volume and resume propagation.

This argument indicates that, even if the release rate at the source is constant, a pulsating vertical growth should occur if the fracture head is at the critical volume for buoyant propagation. Such is the case if the fracture is either storage- or leak-off-toughness-dominated (for a demonstration of the second, see Appendix 6.6.1).

We have used until here the case of a buoyant storage-toughness-dominated hydraulic fracture for ease of illustration. The scaling analysis of the entire domain does, however, show that the late-time solution for buoyant hydraulic fractures will be a buoyant leak-off-toughness-dominated hydraulic fracture (see the argument for this in Appendix 6.6.2). The scaling and physical arguments in this late-time regime remain unchanged.

Note that these arguments clarify why a pulsation should be observable without specifying the timescale of the phenomenon. From a theoretical point of view, the volume of the head is precisely at the critical volume, and any fluid leak-off/solidification, no matter how small, should arrest the fracture. However, an arrest would immediately lead to a fluid exchange with the tail for which propagation should resume. The propagating fracture is thus oscillating around a stable equilibrium governed by the overall volume balance.

6.4 Results

Observing the pulsating behavior of buoyant hydraulic fractures is possible by running simulations in the toughness-dominated limits. The simulations differ in the importance of fluid leak-off at the transition from radial to buoyant propagation, characterized by the dimensionless leak-off coefficient at this moment

$$\mathcal{C}_k(t = t_{k\hat{k}}) = \frac{C' E^{1/2}}{Q_o^{1/2} \Delta^{1/2}}. \quad (6.24)$$

Figure 6.1c shows the evolution of the overall fracture height with time. This figure shows the zero leak-off case, which tends to the linear propagation at late time predicted by the scaling (6.21) for comparison. The simulations with intermediate and small leak-off ($\mathcal{C}_k(t = t_{k\hat{k}}) = 1.0$ respectively 0.1) tend to the square-root evolution in time predicted by (6.17). The simulation with high leak-off ($\mathcal{C}_k(t = t_{k\hat{k}}) = 10$) did not yet become buoyant. This effect comes simply from the excessive fluid mass loss to the medium, delaying the fracture volume from reaching the critical one.

In figure 6.1c, we cannot identify a pulsation but see that the overall behavior is validated. However, a zoom into the details of the overall height growth reveals a pulsating behavior of the fracture with $\mathcal{C}_k(t = t_{k\hat{k}}) = 1.0$ (6.24). We emphasize this behavior with a close-up view in figure 6.1d. We denote with red dots all moments when buoyant propagation resumes. One

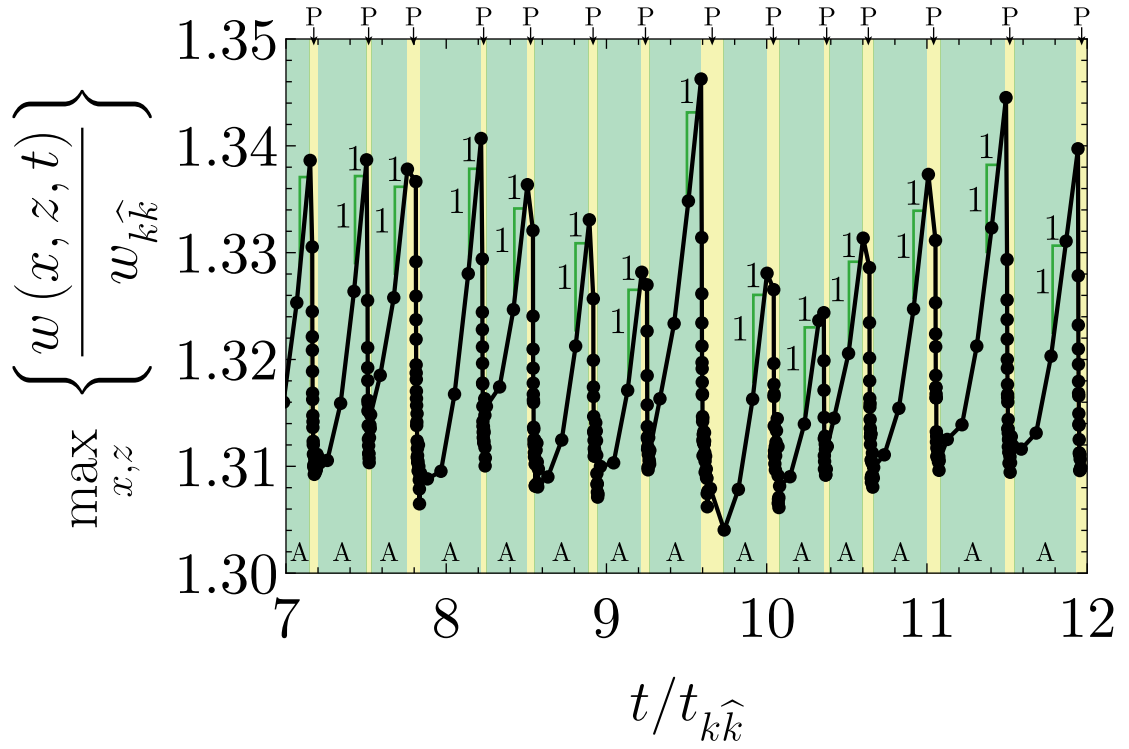


Figure 6.3: Dimensionless maximum opening of the head (equivalent to the maximum overall opening) $\max_{x,z} \left\{ \frac{w(x,z,t)}{w_{k\hat{k}}} \right\}$ with $w_{k\hat{k}} = \frac{K_{Ic}^{4/3}}{E'\Delta\gamma^{1/3}}$ as a function of dimensionless time $t/t_{k\hat{k}}$ (see figure 6.1 for a definition of $t_{k\hat{k}}$) for a simulation with $\mathcal{C}_k(t = t_{k\hat{k}}) = 1$. Black dots mark the reported evaluation points, and green edges indicate the approximate power law. A = Arrested phase, P = Propagation phase.

main observation of figure 6.1d is that the arrested phases, when fracture growth is stopped, are significantly larger than the propagation phases of the fracture. One also observes that the pulsation is fairly regular, meaning that one cycle composed of a propagation and arrest phase takes up approximately $(0.357 \pm 0.065) t_{k\hat{k}}$. As stated in section 6.3.3, this phenomenon is closely related to the head volume. The numerical evaluation of the head volume is challenging (see the discussion in section 4.11.3 of chapter 4), and the precision might be on the order of the accuracy of the evaluation method. A more suitable quantity to monitor is the maximum opening in the head because it is the maximum overall opening. Figure 6.3 shows the evolution of this quantity for the same time window as selected in figure 6.1d. The pulsating behavior is well reflected in the maximum opening, as peaks correspond to moments when the fracture starts to propagate and minima to the temporal arrest of the fracture. The head undergoes inflation (arrested phase) and deflation (propagation phase) cycles.

The spatial distribution of the opening changes is visualized in figure 6.4, where we plot the evolution of the fracture opening and pressure during the propagation and arrested phase between $t/t_{k\hat{k}} \in (11.0, 11.5)$ as a function of the tip based coordinate $\hat{z}(t) = -(z - \ell(t))$. During the propagation phase (figures 6.4a and b), the fracture opening effectively decreases in the head (from grey to red). This effect is subtle and only visible when watching closely (see the inset of figure 6.4a). The changes outside the maximum opening are negligible and even disappear for the tail. The changes to the pressure are also marginal. The only difference observed is that the linearity of the pressure gradient along the head gets lost, indicating that viscous effects become important and that propagation will cease (see the inverse curvature appearing at the propagating tip of figure 6.4b). When the evolution of the volume in the head is reversed (figures 6.4c and d), the opening increases again (red to green), and the pressure regains the linear gradient. One crucial observation is that neither the opening nor the pressure change significantly in the tail. If we recall, one assumption of the argument for pulsation was that when propagation ceases, the tail becomes of constant volume. The sections of figures 6.4 support this hypothesis, which can be explained with simple arguments. The breadth is stable from the beginning, and the opening of the tail does not change because its exposure time is long compared to the pulsation time, such that the leak-off velocity in this part of the fracture is negligible during the arrested phase. Finally, the length of the tail cannot change because it is limited by the neck (pressure depression between the head and tail), which would first need to be lifted. From all of these effects, we have that the opening of the head must necessarily change at the rate of the fluid release. Figure 6.3 indicates the linear increase in opening expected for a linear fluid release, and we observe a good match over nearly all of the cycles investigated.

6.5 Discussion and conclusion

We have considered in this contribution the propagation of buoyant hydraulic fractures subjected to fluid leak-off or solidification. We discussed arguments for why this type of fracture should present a pulsating behavior at late time. For our solidification model, fluid

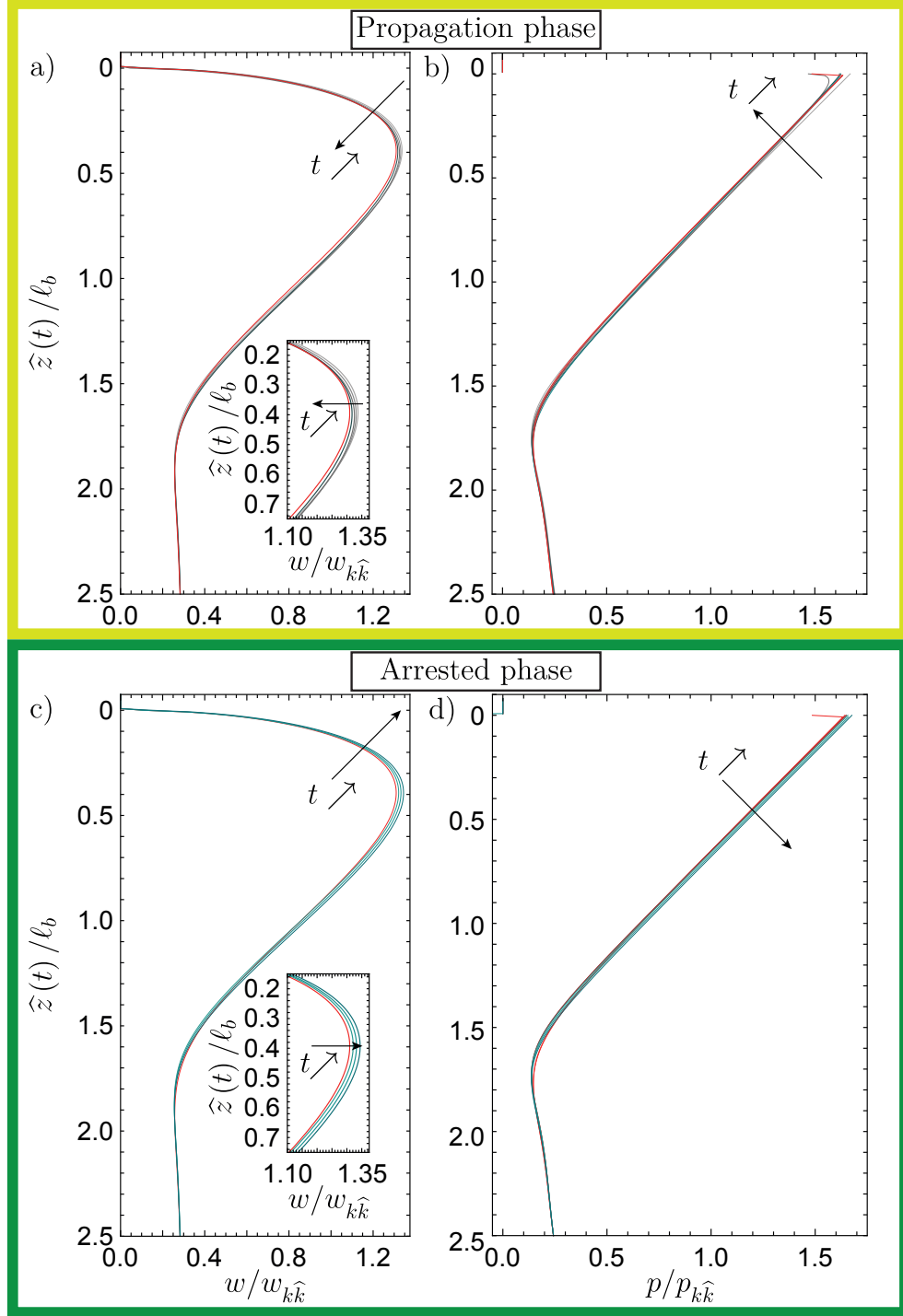


Figure 6.4: Opening and pressure evolution during propagation (a and b) and arrest (c and d) cycle for $\mathcal{C}_{\hat{k}} = 1$. a) and c) show the tip-based opening evolution. Insets emphasize the reduction (a) and increase (c) during the two stages. b) and d) show the corresponding pressure profiles. At the tip, the linearity disappears, causing the fracture to arrest. Insets show the oscillation of head volume (b)) and the head length (d)). Red dots mark the last moment of arrest before propagation occurs again.

Chapter 6. Effects of fluid leak-off or solidification on buoyant hydraulic fractures

leak-off is modeled using Carter's model, and we assume negligible convection along the fracture and fluid at a constant temperature. The fluid release is continuous in time, and all material properties are uniform and constant.

Using a three-dimensional planar hydraulic fracture solver, we simulated buoyant fractures subjected to fluid mass loss and observed pulsating behavior during their upward propagation. We then used physics-based scaling arguments to show that such pulsation should effectively occur for a continuous fluid release. Our scaling approach fails to predict the time scale of this phenomenon. The pulsating behavior can be explained from a toughness-dominated head with an original volume equal to the critical one necessary for buoyant propagation. The fluid leak-off/solidification depletes the head, bringing it to an arrest. During the arrested phase, the tail becomes of constant volume such that the entire released fluid can flow into the fracture head. Once the head becomes inflated above the critical volume again, propagation resumes. Our simulations show that minimal changes in head volume induce this behavior and that an overall volume balance predicts global behavior.

We cannot determine the pulsating cycles' duration or amplitude as of today. We can merely state that the pulsation occurs around the stable equilibrium given by the overall volume balance and highlight its relation to the pronounced head-tail structure of toughness-dominated buoyant hydraulic fractures. Nonetheless, the behavior demonstrated here numerically and explained by scalings has been observed in the laboratory experiments of Taisne and Tait (2011). These experiments investigate the solidification of various fluids injected in hydrogels. Further investigations are needed to clarify the behavior and define the limits of applicability of the pulsation phenomenon. We further envision comparing our findings with the Taisne and Tait (2011) experiments and seismic data recorded during the emplacement of dikes.

6.6 Appendix

6.6.1 Dimensionless leak-off coefficient \hat{K} -regime

We apply the derivations of section (6.3.3) to a buoyant hydraulic fracture with a toughness-dominated head and a leak-off-, viscosity-dominated tail with

$$\ell_{\hat{k}}(t) = \frac{Q_o \Delta \gamma^{2/3} t^{1/2}}{C' K_{Ic}^{2/3}} = B_{\hat{k}} t^{1/2}, \quad \ell_{\hat{k}}^{\text{head}} = \left(\frac{K_{Ic}}{\Delta \gamma} \right)^{2/3} = \ell_b \quad (6.25)$$

$$\tau = \left(\frac{\zeta}{B_{\hat{k}}} \right)^2, \quad \tau_o = \left(\frac{\zeta - \ell_b}{B_{\hat{k}}} \right)^2, \quad (6.26)$$

where $B_{\hat{k}}$ is a dimensional prefactor with the unit $\text{m/s}^{1/2}$.

If we include these scales in the integral equation (6.18), one obtains

$$\begin{aligned}
 \mathcal{V}_{lo}^{\text{head}} &\sim \int_t \int_0^{\ell_b} \int_{B_{\hat{k}} t^{1/2}}^{B_{\hat{k}} t^{1/2} + \ell_b} \frac{C' B_{\hat{k}}}{\sqrt{\zeta^2 - (\zeta - \ell_b)^2}} d\zeta d\xi d\tau \\
 &\sim \frac{C' B_{\hat{k}}}{\sqrt{\ell_b}} \int_t \int_0^{\ell_b} \int_{B_{\hat{k}} t^{1/2}}^{B_{\hat{k}} t^{1/2} + \ell_b} \frac{1}{\sqrt{2\zeta - \ell_b}} d\zeta d\xi d\tau.
 \end{aligned} \tag{6.27}$$

Integrating over ξ and ζ , and manipulating the equation

$$\mathcal{V}_{lo}^{\text{head}} \sim C' B_{\hat{k}}^{3/2} \sqrt{\ell_b} \int_t \sqrt{2\tau^{1/2} + \frac{\ell_b}{B_{\hat{k}}}} - \sqrt{2\tau^{1/2} - \frac{\ell_b}{B_{\hat{k}}}} d\tau \tag{6.28}$$

which we now integrate over time to obtain

$$\begin{aligned}
 \mathcal{V}_{lo}^{\text{head}}(t) &\sim C' B_{\hat{k}}^{3/2} \sqrt{\ell_b} \left\{ \frac{1}{5} \left[\left(2\sqrt{t} + \frac{\ell_b}{B_{\hat{k}}} \right)^{5/2} - \left(2\sqrt{t} - \frac{\ell_b}{B_{\hat{k}}} \right)^{5/2} \right] \right. \\
 &\quad \left. - \frac{\ell_b}{3B_{\hat{k}}} \left[\left(2\sqrt{t} - \frac{\ell_b}{B_{\hat{k}}} \right)^{3/2} + \left(2\sqrt{t} + \frac{\ell_b}{B_{\hat{k}}} \right)^{3/2} \right] \right\}.
 \end{aligned} \tag{6.29}$$

We know that reaching buoyant propagation requires $\ell(t) \gg \ell_b$ (e.g. $\sqrt{t} \gg \ell_b/B_{\hat{k}}$). This condition is equivalent to a late-time behavior, as shown in chapter 4, such that we can approximate equation (6.29) as

$$\mathcal{V}_{lo}^{\text{head}}(t) \sim C' B_{\hat{k}}^{3/2} \sqrt{\ell_b} \frac{2^{3/2}}{3} \frac{\ell_b t^{3/4}}{B_{\hat{k}}} \sim \frac{2^{3/2}}{3} C' B_{\hat{k}}^{1/2} \ell_b^{3/2} t^{3/4}. \tag{6.30}$$

Equation (6.30) is very similar to equation (6.23) and can be shown to be equivalent when dropping prefactors and using an alternative definition of $B_{\hat{k}}$

$$\mathcal{V}_{lo \hat{k}}^{\text{head}}(t) \sim C' \sqrt{v_{\hat{k}}(t)} \ell_b^{3/2} t \quad \text{with} \quad B_{\hat{k}} \sim v_{\hat{k}} t^{1/2}. \tag{6.31}$$

6.6.2 Transition from $\hat{\mathbf{M}}$ to $\hat{\mathbf{K}}$

Viscosity-dominated buoyant hydraulic fractures in impermeable media, respectively, in an isothermal system, differ from toughness-dominated fractures in the same configuration because of their ability to accumulate a fluid volume exceeding the minimum volume for propagation in their head (see the discussion in chapters 4 and 5 and table 4.3 for the scalings).

Chapter 6. Effects of fluid leak-off or solidification on buoyant hydraulic fractures

For a media subjected to fluid leak-off or solidification, this volume will be reduced during the propagation of the fracture. It is thus physically intuitive that the late-time solution would directly have the limiting volume for propagation, which forms the basis for the derivation of toughness-dominated scalings.

In sections 6.3.3 and 6.6.1, we have demonstrated that the pulsating propagation theoretically appears for both toughness-dominated cases. However, the overall behavior is always governed by the tail (storage- or leak-off-dominated). For this reason, we list the corresponding viscosity-dominated scalings in table 6.1 with their respective dimensionless coefficients. From the increasing nature of all dimensionless toughness and leak-off coefficients (head and tail), we can deduce that the late-time solution of buoyant hydraulic fractures from a continuous fluid release is necessarily leak-off, toughness-dominated.

| | <i>radial</i> | | <i>elongated</i> | |
|-----------------|---|---|---|---|
| | \mathbf{M} | $\tilde{\mathbf{M}}$ | $\hat{\mathbf{M}}$ (tail) | $\hat{\mathbf{M}}$ (head) |
| ℓ_* | $\frac{E^{1/9} Q_0^{1/3} t^{4/9}}{\mu^{1/9}}$ | $\frac{Q_0^{1/2} t^{1/4}}{C^{1/2}}$ | $\frac{Q_0^{1/2} \Delta \gamma^{1/2} t^{5/6}}{E^{1/6} \mu^{1/3}}$ | $\frac{Q_0^{2/3} \Delta \gamma^{1/3} t^{4/9}}{E^{2/9} \mu^{1/9} C^{2/3}}$ |
| b_* | ℓ_* | ℓ_* | ℓ_* | ℓ_* |
| w_* | $\frac{Q_0^{1/3} \mu^{2/9} t^{1/9}}{E^{2/9}}$ | $\frac{Q_0^{3/8} \mu^{1/4} t^{1/16}}{C^{1/8} E^{1/4}}$ | $\frac{Q_0^{1/4} \mu^{1/3}}{E^{1/12} \Delta \gamma^{1/4} t^{1/2}}$ | $\frac{Q_0^{1/3} \mu^{4/9}}{E^{1/9} \Delta \gamma^{1/3} C^{1/3} t^{5/18}}$ |
| p_* | $\frac{E^{2/3} \mu^{1/3}}{t^{1/3}}$ | $\frac{Q_0^{1/8} t^{3/16}}{C^{3/8} \mu^{1/4} E^{3/4}}$ | $\frac{t^{1/3}}{E^{1/24} Q_0^{1/8} \Delta \gamma^{3/8} \mu^{1/6}}$ | $\frac{w_*^{\text{tail}}}{C^{1/6} t^{5/36}}$ |
| \mathcal{P}_s | $\mathcal{K}_m = (t/t_{mk})^{1/9}$ | $\mathcal{K}_{\tilde{m}} = (t/t_{\tilde{m}\tilde{k}})^{1/16}$ | $\mathcal{K}_{\hat{m},x} = \mathcal{M}_{\hat{k}}^{-3/14} (t/t_{m\hat{m}})^{5/24}$ | $\mathcal{K}_{\hat{m}} = K_{Ic} \frac{C^{1/4} t^{5/24}}{E^{2/3} Q_0^{1/4} \mu^{1/3}}$ |
| | $\mathcal{B}_m = (t/t_{m\hat{m}})^{7/9}$ | $\mathcal{B}_{\tilde{m}} = (t/t_{\tilde{m}\hat{m}})^{7/16}$ | $\mathcal{C}_{\hat{m}}^{\text{tail}} = \left(t/t_{\hat{m}}^{\text{tail}} \right)^{7/12}$ | $\mathcal{K}_{\hat{m},x}^{\text{tail}} = K_{Ic} \frac{C^{1/6} \Delta \gamma^{1/6} t^{11/36}}{Q_0^{1/6} E^{7/9} \mu^{7/18}}$ |
| | $\mathcal{C}_m = (t/t_{m\hat{m}})^{7/18}$ | - | $\mathcal{C}_{\hat{m}} = (t/t_{\hat{m}\hat{m}})^{49/48}$ | |

Table 6.1: Characteristic scales (and governing dimensionless parameters \mathcal{P}_s) in the different leak-off/solidification-dominated scalings.

7 Arrest mechanisms of buoyant hydraulic fractures

This chapter is a modified version of a conference paper submitted to the 57th U.S. Rock Mechanics / Geomechanics Symposium, 2023 in Atlanta (ARMA23).

Möri, A., Peruzzo, C., Lecampion, B., and Garagash, D.I. (2023). Arrest Mechanisms of Buoyant Hydraulic Fractures. *57th U.S. Rock Mechanics / Geomechanics Symposium (ARMA23)*.

Contributions

Andreas Möri has conceptualized the problem, performed a formal and scaling analysis, decided on the methodology, adapted the numerical solver, generated the visualizations, and wrote the original draft. Carlo Peruzzo has derived the framework to study the energy budget of a semi-infinite hydraulic fracture, participated in the adaption of visualizations, and reviewed and edited the text in iterations with Andreas Möri. Brice Lecampion acted as supervisor, supported the conceptualization and methodology, supervised the formal and scaling analysis, acquired the funding, and reviewed and edited the text in iterations with Andreas Möri. Dmitry Garagash acted as supervisor, supported the conceptualization, assisted in the formal analysis, and reviewed the text in iterations with Andreas Möri. He further emphasized the approach of a fracture size-dependent toughness and gave valuable inputs on how to model it.

7.1 Abstract

Hydraulic fracturing (HF) treatments can form widespread fractures. Understanding their containment at depth is critical, given the positive buoyancy contrast between the fracturing fluid and the surrounding rock, promoting upward growth. We study arrest mechanisms for established buoyant HF, restricting our investigation to fully planar fractures. We show that changes in the fracturing toughness (K_{Ic}) (E , and ν remain unchanged) are inefficient in arresting buoyant HFs. A fracture size-dependent, apparent K_{Ic} can only prevent buoyant fractures from emerging but not stop their ascent. Sudden changes of K_{Ic} between layers need to be significant to arrest a buoyant HF $K_{Ic-2}/K_{Ic-1} \gtrsim 2-3$. Contrary, a stress barrier efficiently arrests buoyant fractures for stress contrasts as little as $\Delta\sigma \gtrsim 1.00$ (MPa). We further demonstrate that the interaction with a high-leak-off layer is more efficient in arresting fracture ascent than an equivalent uniform leak-off value. Moderate to high leak-off arrests fractures before they become buoyant or without significant uprise. All considered arrest mechanisms can stop the propagation of a buoyant HF, implying that combining several mechanisms will likely prevent buoyant HFs from reaching shallow formations or even the surface.

7.2 Introduction

Hydraulic fractures (HF) created through industrial treatments can have significant extents. Ensuring a safe operation and efficient exploitation of the targeted formation is only possible if the fracture remains contained at depth. In the absence of any heterogeneity, assuming a Newtonian fluid, an impermeable medium subjected to linear background stress, and a block injection, we have shown in chapter 5 that the containment depends on a single, dimensionless buoyancy \mathcal{B}_{ks} (see their equation (9)). It is possible to define a limiting volume, determining if the fracture arrests at depth or becomes buoyant (Davis et al., 2020; Salimzadeh et al., 2020). This limit for buoyant propagation is equivalent to $\mathcal{B}_{ks} \geq 1$. Here we investigate cases of buoyant fractures with $\mathcal{B}_{ks} \gg 1$ (see table 7.1) and will explore the effects of changes in the apparent fracturing toughness, stress barriers, and fluid leak-off will have on buoyant HF. Following chapter 5, we consider a block injection of a fluid with a viscosity μ at a constant rate Q_o until shut-in of the injection at t_s , giving a total injected volume of $V_o = Q_o t_s$. The medium is considered linear-elastic with a given value of the plain-strain modulus $E' = E/(1 - \nu^2)$, with E the materials Young's modulus and ν its Poisson's coefficient. We consider a linearly varying background stress with depth (e.g., $\sigma(z) \propto z$) and use constant values for the rock and fluid density. A buoyant force, caused by the difference of the two $\Delta\gamma = \Delta\rho g = (\rho_{solid} - \rho_{fluid})g$, with $g = 9.81 \text{ (m}\cdot\text{s}^{-2}\text{)}$ the earth gravitational acceleration, emerges, driving buoyant propagation. Note that we do not consider any density variation. The effect of any heterogeneity will be related to the dominating energy dissipation mechanism (viscosity- vs. toughness-dominated) when the fracture becomes buoyant and encounters heterogeneity. For a change in properties at a given distance from the injection point, the interaction will differ if the fracture reaches the jump during an ongoing injection or when shut-in has already occurred. All these possible interactions depend on an additional set of two dimensionless coefficients. The first is the

| | Set 1 | Set 2 |
|--|-------------------|-------------------|
| E' (GPa) | 20 | 30 |
| K_{Ic} (MPa·m ^{1/2}) | 1.5 | 1.0 |
| μ (Pa·s) | $5 \cdot 10^{-3}$ | 1.0 |
| $\Delta\rho$ (kg·m ⁻³) | 1700 | 1200 |
| Q_o (m ³ ·s ⁻¹) | 0.05 | 0.01 |
| V_o (m ³) | 135 | 27 |
| $\mathcal{M}_{\hat{k}}$ | 236 | $1.68 \cdot 10^5$ |
| \mathcal{B}_{ks} | 63.0 | 41.3 |
| \mathcal{D} | 12.5 | 12.9 |

Table 7.1: The two sets of parameters used within this study and their main dimensionless parameters.

dimensionless viscosity $\mathcal{M}_{\hat{k}}$ describing the dominant energy dissipation mechanism at the transition from radial to buoyant propagation (see equation (4.23) of chapter 4). This parameter alone governs the case of a constant rate, continuous release and characterizes together with \mathcal{B}_{ks} the release of a finite volume of fluid (see chapters 4 and 5). Combining these two coefficients is sufficient to describe any possible state of a buoyant fracture. Notably, values of $\mathcal{M}_{\hat{k}} \gg 1$ indicate viscosity-dominated and $\mathcal{M}_{\hat{k}} \ll 1$ toughness-dominated fractures at the transition from radial to buoyant. Finally, the case of a change in properties at a distance d (distance from the injection point to the change of properties, see figure 7.1) requires a dimensionless form of this distance. We achieve the dimensionless form using the buoyancy length scale $\ell_b = (K_{Ic}/\Delta\gamma)^{2/3}$ (Lister and Kerr, 1991) to obtain $\mathcal{D} = d/\ell_{b-1}$ (see table 7.1). According to chapter 5, we must ensure $\mathcal{D} \geq 3$ to have fully developed buoyant fractures.

We showcase the interaction with various arrest mechanisms according to table 7.2 for two sets of parameters (see table 7.1). The first set is considered an approximation of a crosslink gel injection into a sandstone. The second refers to a slickwater injection into a mudstone. For all simulations with a change in properties, we assume a distance to the layer of $d = 250$ (m). table 7.2 reports the considered material parameters or changes between solid one and solid two (see figure 7.1). We use PyFrac, an open-source, planar HF solver developed in our laboratory. The reader finds details in Zia and Lecampion (2020) and applications to buoyancy problems in chapters 4 and 5 of this thesis. We further use scaling arguments where we indicate the corresponding scalings with subscripts. The subscripts m and k refer to a viscosity- respectively, toughness-dominated scaling. Subscripts with a \sim indicate leak-off dominated scalings, a $\hat{\cdot}$, scalings with dominant buoyancy. Finally, we use an addition to the subscript of the form $-i$ with $i \in (o, 1, 2)$ referring either to a base value (e.g., o) or the corresponding material (e.g., $1, 2$).

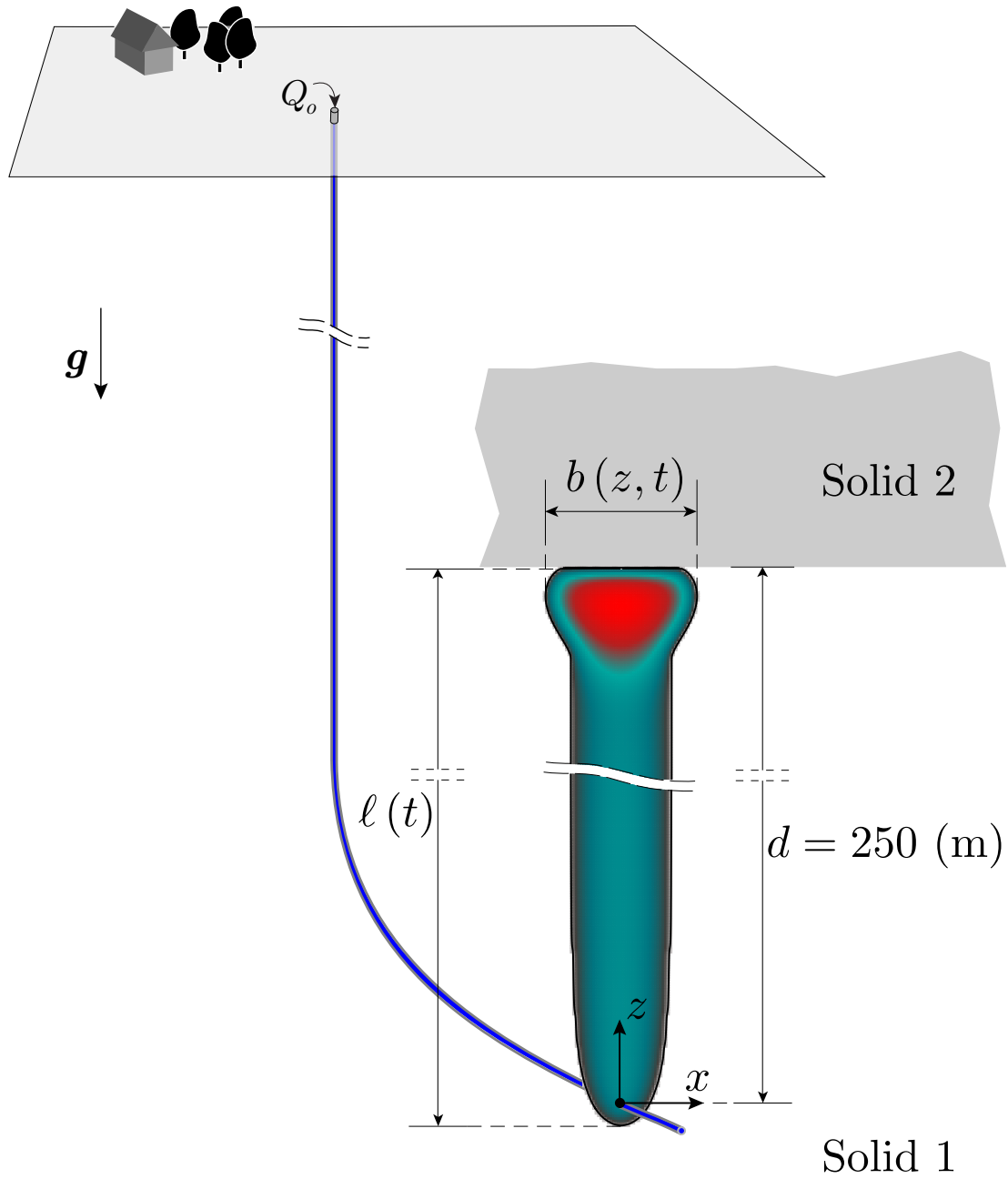


Figure 7.1: Sketch of the numerical simulation setup. We consider a block injection of fluid creating a planar three-dimensional fracture in the (x, z) -plane (point source at $(x, z) = (0, 0)$). The compressibility of the injection line and surface effects are neglected. All considered fluids are positively buoyant, so we study changes in solid properties at a distance $z = d$ from the source point.

| Section | | Modest | Max |
|------------------------------------|-----------------------------------|------------------|-------------------|
| Size-dependent K_{Ic} 7.3.1 | κ | 0.25 | 0.50 |
| | h (m) | 0.25 | 0.10 |
| Toughness jump 7.3.2 | K_{Ic-2}/K_{Ic-1} | 2.0 | 5.0 |
| Stress jump 7.4 | $\Delta\sigma$ (MPa) | 0.5 | 3.0 |
| Uniform leak-off 7.5.1 | C (m·s ^{-1/2}) | 10 ⁻⁶ | 10 ⁻¹⁰ |
| Jump in leak-off coefficient 7.5.2 | ΔC (m·s ^{-1/2}) | 10 ⁻⁶ | 10 ⁻¹⁰ |

Table 7.2: The two parameters, respectively, changes used throughout the paper.

7.3 Toughness heterogeneities

The first mechanism considered is a change in the apparent fracture toughness, respectively, the material fracture toughness because of a lithology change. In the former case, we restrict our investigation to a fracture size-dependent toughness (section 7.3.1) and neglect any effects on apparent toughness by the fracture velocity. To address lithology changes, we investigate a change in fracturing energy by varying only the fracturing toughness K_{Ic} between two layers.

7.3.1 Fracture size dependent toughness

Numerous field observations of anthropogenic fractures indicate that the apparent fracturing toughness felt by the propagating fracture might depend on its size (Rutledge et al., 2004; Mayerhofer et al., 2000; Garagash, 2023). We restrict our investigation here to a global apparent fracturing toughness by altering the property of the material without considering any local effects. The apparent fracturing toughness is adapted between time steps due to the fracture size of the previous iteration. More precisely, we change the overall fracturing toughness of the material as a function of the propagating part(s) of the front according to the law proposed by Liu et al. (2019)

$$K_{Ic-ap}(\ell_p, \kappa, h, K_{Ic-o}) = K_{Ic-o} \left(\frac{\ell_p}{h} \right)^\kappa \quad (7.1)$$

where K_{Ic-o} (MPa·m^{1/2}) is the fracturing toughness measured at the laboratory scale h (m), ℓ_p is the curvilinear length along the fracture front where the local velocity is not zero at the current time step, and κ the dimensionless exponent. Liu et al. (2019) used a similar approach and derived the characteristics of a radially propagating fracture where ℓ_p is proportional to the fracture radius. We investigate this problem using the planar three-dimensional (3D) hydraulic fracture solver PyFrac (Zia and Lecampion, 2020). Due to the discretization on a regular rectangular grid on the fracture plane, we have numerous front segments, and each is considered a straight line for which we calculate the normal velocity. For the transition from radial to buoyant propagation investigated in this work, the fracture propagation goes from axisymmetric to uni-directional. During this transition, various front segments alter

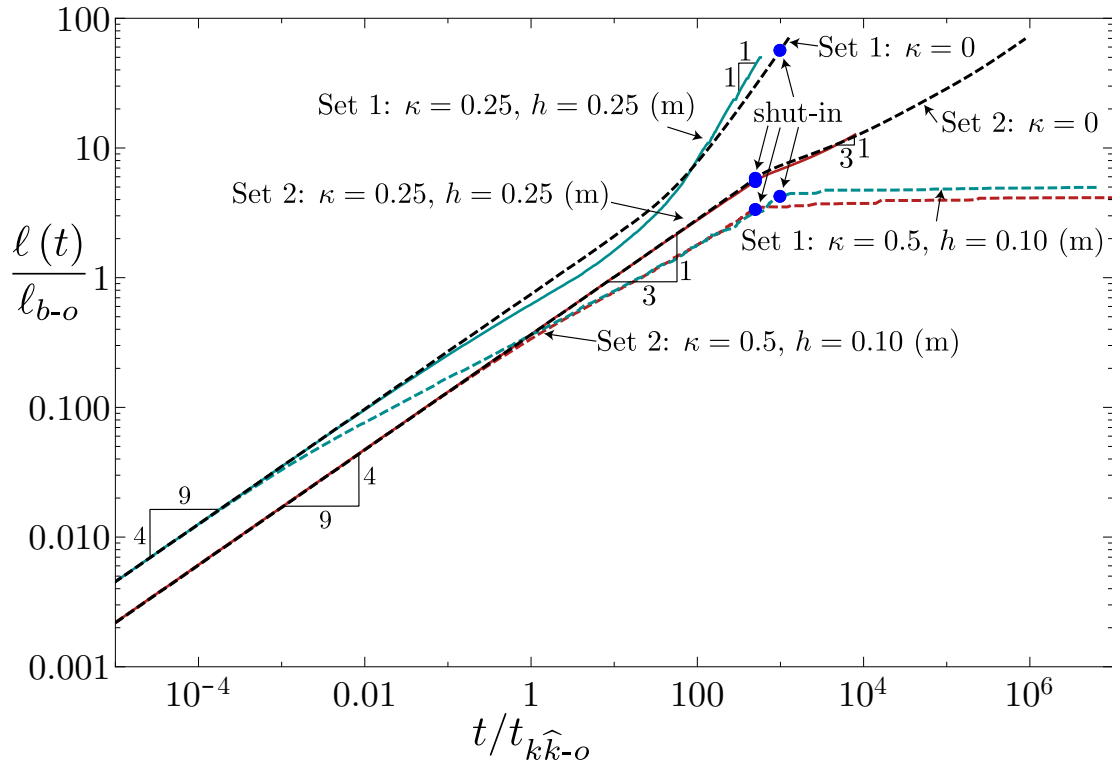


Figure 7.2: Evolution of scaled fracture height for simulations with a size-dependent apparent toughness. Green and red lines represent respectively set 1 (crosslink gel into sandstone) and set 2 (slickwater into mudstone), with continuous lines the modest property change and dashed lines the maximum one. Classical scaling laws like the $t^{4/9}$ of radial-viscosity-dominated propagation or the t^1 dependence for toughness-dominated buoyant fractures during the injection are indicated. Black dashed lines indicate the solution for a uniform, constant fracture toughness.

their state multiple times between propagation and arrest. Because we want to consider only the contribution of propagating parts of the fracture to the apparent fracturing toughness K_{Ic-ap} (7.1), the scheme is prone to show large fluctuations when we only count propagating segments of the front. This numerical effect can be reduced when introducing a maximum reduction of K_{Ic-ap} between two successive time steps. In the simulations shown in this work, we arbitrarily limit the reduction of K_{Ic-ap} to 5 % between two considered time steps. This artificial damping stabilizes our numerical code while allowing the fracture to follow the radial scalings (see the correct power-laws in figure 7.2 (Liu et al., 2019)). The validity of this approach and the sensibility to the reduction chosen remains to be validated in ongoing studies. We omit the scaling details herein (see Liu et al. (2019) for the radial case) and emphasize the possibility of the size-dependent toughness to arrest a fracture before it becomes buoyant. We obtain the equivalent dimensionless viscosity for a fracture size-dependent toughness of the form of equation (7.1) as

$$\mathcal{M}_{\hat{k}-eq} = \mu' \frac{h^{14\kappa/(3-2\kappa)} E'^3 \Delta\gamma^{14/(3-2\kappa)}}{K_{Ic-o}^{14/(3-2\kappa)}}. \quad (7.2)$$

One can obtain the scaling for a uniform toughness by setting $\kappa = 0$. Similar to equation (7.2), we derive an equivalent value of the dimensionless buoyancy \mathcal{B}_{ks} as

$$\mathcal{B}_{ks-eq} = \Delta\gamma \left(\frac{E'^{3-2\kappa} V_o^{3-2\kappa} h^{8\kappa}}{K_{Ic-o}^8} \right)^{\frac{1}{5+2\kappa}}. \quad (7.3)$$

We validate numerically that the conclusions of chapters 4 and 5 remain valid when using the adapted dimensionless coefficients (equations (7.2) and (7.3)) instead of the original ones (see notably figure 5.2 of chapter 5).

The modest and maximal values (see table 7.2) applied to the first parameter set (see table 7.1, crosslink gel injection into a sandstone) lead to fractures which are toughness-dominated at the transition ($\mathcal{M}_{\hat{k}-eq} = 0.51$ for the modest values and $\mathcal{M}_{\hat{k}-eq} = 2.06 \cdot 10^{-6}$ for the maximum values). We expect the maximum values to arrest the fracture at depth, as its dimensionless buoyancy becomes inferior to unity ($\mathcal{B}_{ks-eq} = 0.29$). For the modest variation, the emergence of a buoyant fracture is still expected ($\mathcal{B}_{ks-eq} = 4.68$). Figure 7.2 shows the evolution of the fracture height $\ell(t)$ of these fractures (green lines represent Set 1) and validates our prediction. Despite a delay in the emergence of the buoyant fracture (expected at $t/t_{k\hat{k}} \sim 1$ for a uniform K_{Ic} , see the black lines for the case with $\kappa = 0$), a self-sustained buoyant pulse emerges. The evolution of the apparent fracturing toughness in figure 7.3 further shows that during buoyant propagating K_{Ic-ap} tends to stabilize, as expected from the finger-like behavior of buoyant fractures (e.g., a constant breadth of the propagating front). During radial propagation, the apparent fracturing toughness continuously increases before fluctuating around a stable value. Note that the reported simulation has not yet reached shut-in, as the scaling does not indicate

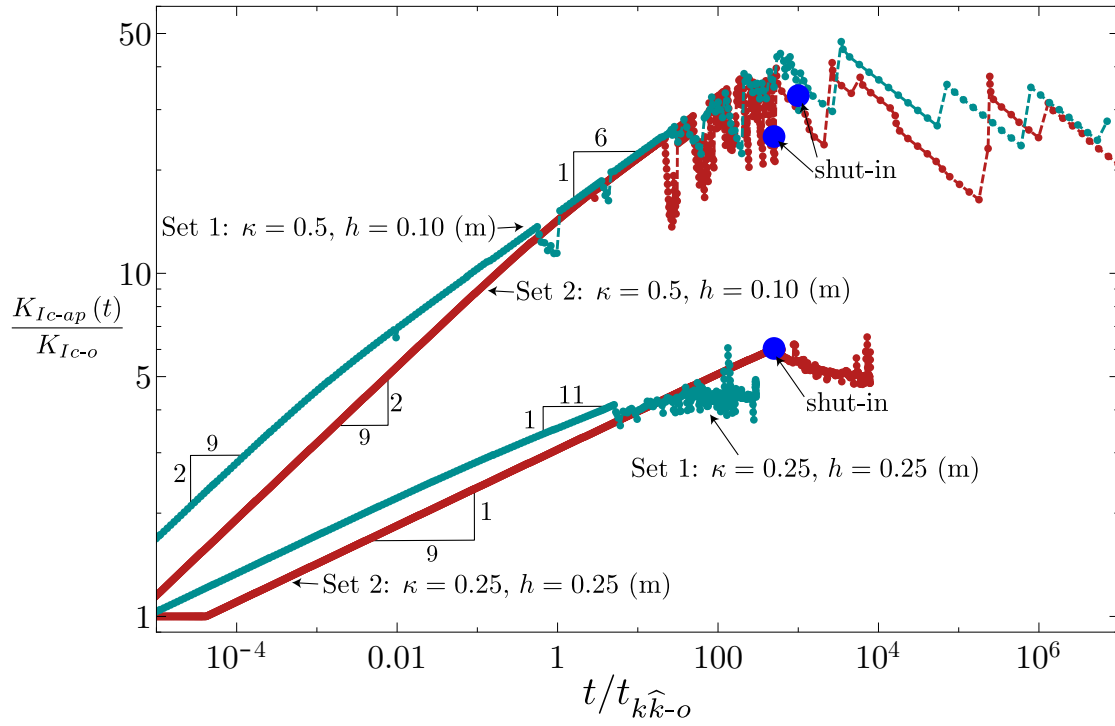


Figure 7.3: Evolution of scaled fracture-size dependent apparent toughness. The color code is equivalent to figure 7.2. Indicated power laws are derived from characteristic length scales of classical HF regimes in equation (7.1). For the becoming buoyant at late time (two lines with smaller slope, set 1 and set 2 with modest values), the toughness seems to become approximately stable with variations of the order of $\pm 15 - 20\%$.

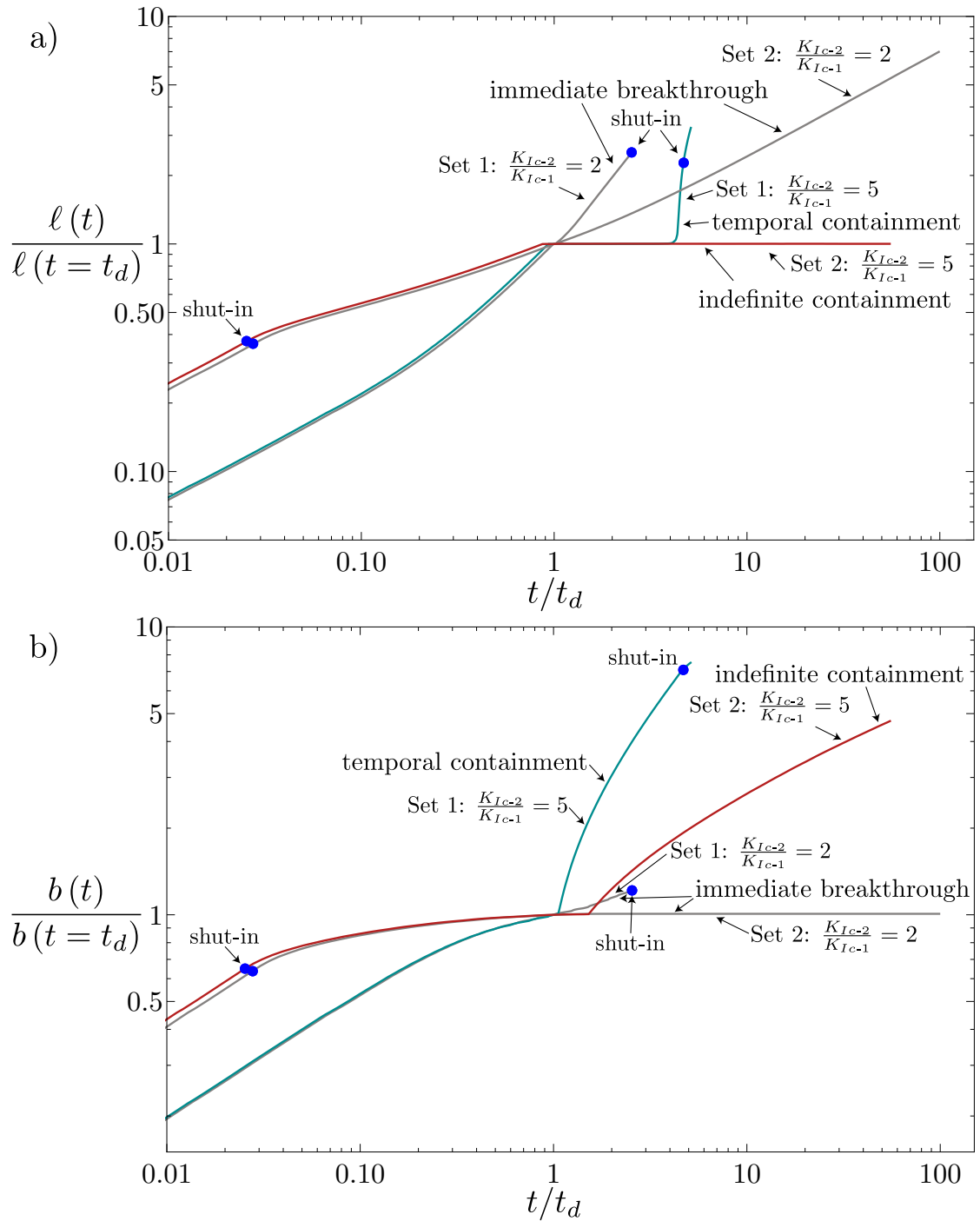


Figure 7.4: Evolution of fracture height (a) and maximum breadth (b) for simulations with a jump in fracture toughness. Grey lines show an immediate breakthrough (minimal spreading at the interface), turquoise lines a temporal containment (height growth stops temporarily before increasing again), and red lines an indefinite containment (the fracture arrests indefinitely at the interface).

any more changes to the fracture propagation; the conclusions remain valid. Additionally, the fracture height at shut-in would already extend beyond the scale of other heterogeneities like jumps in stress, toughness, or leak-off ($\ell(t = t_s) \approx 1.8$ (km)).

When studying the second set of parameters (slickwater injection into a mudstone), the modest version of the size-dependent toughness is not able to change the governing dissipation mechanism at the radial to buoyant transition from viscosity- to toughness-dominated ($\mathcal{M}_{\hat{k}-eq} = 381$). Only the more restrictive, maximum values are sufficient to change the governing energy dissipation mechanism ($\mathcal{M}_{\hat{k}-eq} = 1.67 \cdot 10^{-3}$). Similar to the first parameter set, the volume, in this case, becomes insufficient to create a buoyant fracture ($\mathcal{B}_{ks-eq} = 0.236$), whereas a self-sustained buoyant fracture is expected for the modest parameters ($\mathcal{B}_{ks-eq} = 3.45$). According to the evolution of the fracture height and the apparent fracturing toughness (see figures 7.2 and 7.3), the predictions are confirmed. The apparent fracturing toughness seems to decrease for the fractures that arrest, which is related to the numerical damping preventing a sudden drop in the fracturing toughness. At a very late time, one would expect the apparent toughness to reduce back to the initial value of K_{Ic-0} . This phenomenon poses the question of emerging buoyant fractures at late times. Our simulations do not show such behavior even at very late times, not reported within figures 7.2 and 7.3. From the observations of figures 7.2 and 7.3, we anticipate that the findings of chapter 5 remain valid through the use of the equivalent dimensionless coefficients of equations (7.3) and (7.2). A fracture size-dependent toughness of the form presented in equation (7.1) can thus prevent the emergence of a buoyancy-driven fracture but is not a mechanism that could arrest an already buoyant fracture.

7.3.2 Toughness jump

Unlike a size-dependent toughness, K_{Ic} might change abruptly between layers. We restrict our analysis to increases in the fracturing toughness from the injection layer (material 1 in figure 7.1) to the upper layer (material 2, $K_{Ic-2} > K_{Ic-1}$). The upper and lower limits of the toughness jump are chosen according to the compilation performed by Peruzzo and Lecampion (2023a) as $K_{Ic-2}/K_{Ic-1} = 2$ and $K_{Ic-2}/K_{Ic-1} = 5$. Peruzzo and Lecampion (2023a) have shown that in the absence of buoyancy, three scenarios are possible when injecting into a layer with K_{Ic-1} , contained between two layers of higher toughness K_{Ic-2} . The options consist of an *immediate breakthrough*, a *temporary containment*, or an *indefinite containment*. Similar behavior is expected for the presented case, where the scenario depends on the characteristics of the fracture when it encounters the interface between the two formations. Numerically, we characterize the moment when the fractures interact with the interface by the time passed since the fluid injection started when the fracture front reaches the upper layer denoted as t_d . Comparing t_d to the shut-in time of the fracture t_s , we decide whether the fracture encounters the heterogeneity when the injection is still ongoing (e.g., $t_d \leq t_s$) or when the injection has already ended (e.g., $t_d > t_s$). This distinction is necessary because it directly affects the governing mechanisms, fracture velocity, and characteristics of the buoyant head at first contact (for possible fracture states at contact, see chapters 4 and 5).

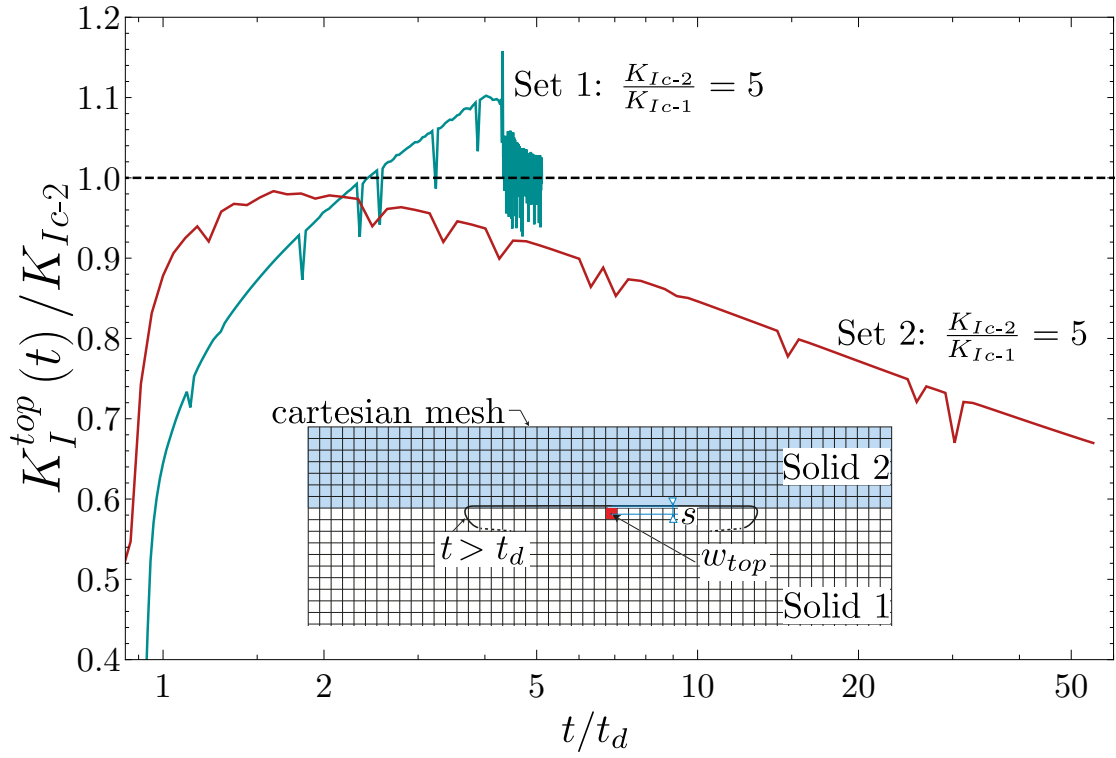


Figure 7.5: Evolution of the "local" energy release rate at the top front position on the fracture center line (see the inset for a definition) for toughness jump simulations. The color code is as defined in figure 7.4, and dashed horizontal lines indicate the modest (blue) and maximum (red) toughness jumps.

We investigate first the situation of a crosslink gel injection into a sandstone (Set 1), leading to a viscosity-dominated ($\mathcal{M}_{\hat{k}} = 236 > 1$) fracture encountering the heterogeneity during the injection ($t_d \approx 550$ (s) < 2700 (s) $= t_s$). Figure 7.4a shows that only for the case of $K_{Ic-2}/K_{Ic-1} = 5$ a containment is observed, whereas $K_{Ic-2}/K_{Ic-1} = 2$ leads to an *immediate breakthrough*. The observed containment of the higher toughness jump is a *temporary containment*. As observed in the case without gravity (Peruzzo and Lecampion, 2023a), the lateral expansion of the fracture leads to an increase in fracture opening at the center ($x = 0$), where the buoyant fracture originally encountered the interface. The stress intensity factor, initially below the higher fracture toughness K_{Ic-2} , increases with the opening increase. It is possible to estimate the stress intensity factor from an inversion of the classical LEFM square-root asymptote (Rice, 1968b) as $K_I^{top} = \sqrt{\pi/32E'} w_{top}/\sqrt{s}$, with w_{top} the numerical opening at a distance s from the front (at the ribbon cell (Zia and Lecampion, 2020)), obtained from the solution of the complete elastohydrodynamic system (e.g., also accounting for viscous effects, see the inset of figure 7.5 for a definition of w_{top} and s). When the local front velocity is non-zero (before reaching the interface or after breakthrough), K_I^{top} has no physical meaning as the use of the classical LEFM square-root asymptote (Rice, 1968b) is not correct. On the other hand, it measures the stress-intensity factor and can thus be compared to the fracturing toughness K_{Ic-i} for an arrested fracture at the point where K_I^{top} is evaluated. For the two contained fractures of figure 7.4 (maximum parameters on both sets), we show the evolution of K_I^{top}/K_{Ic-2} during their arrested time, where the evaluation has a meaning. Figure 7.4 shows that for the *temporarily arrested* fracture of the crosslink gel injection into a sandstone (green line), K_I^{top} is effectively below the fracturing toughness of solid 2 K_{Ic-2} , such that the fracture is not able to break through immediately. During the time when the fracture is arrested, K_I^{top} increases up to K_{Ic-2} . The breakthrough occurs at this instance, and the fracture becomes buoyant again (note that the "overshoot" is numerical and corresponds approximately to our numerical precision). Interestingly, lateral expansion does not stop after the breakthrough and continues at about the same rate (see figure 7.4b). The same observation holds for the fracture with an immediate breakthrough, where lateral propagation is also established. In both cases, a buoyant finger-like fracture rises from the breakthrough point in the higher toughness layer, showing a decreasing breadth towards the propagating head (see figure 7.6). After the breakthrough of a temporarily contained fracture, the fluid in the lower layer starts to concentrate in a channel at the interface with continued lateral extension at the lateral extremities as well as fracturing fluid flowing back from zones close to the breakthrough point into the central finger-like buoyant HF of the higher toughness layer. The opening distribution in the lower toughness layer is thus complex and uneven.

Different from the first set of a crosslink gel injection into sandstone, the second set encounters the heterogeneity once the injection has already ended ($t_d \approx 10^5$ (s) > 2700 (s) $= t_s$) as a viscosity-dominated fracture ($\mathcal{M}_{\hat{k}} = 1.68 \cdot 10^5 > 10^2$). Figure 7.4a shows that the minimum toughness jump of $K_{Ic-2}/K_{Ic-1} = 2$ cannot stop the buoyant propagation of the fracture. On the other hand, the high toughness jump (e.g., $K_{Ic-2}/K_{Ic-1} = 5$) creates an *indefinitely contained* fracture. Observation of figure 7.5 shows that the stress intensity factor at the propagating

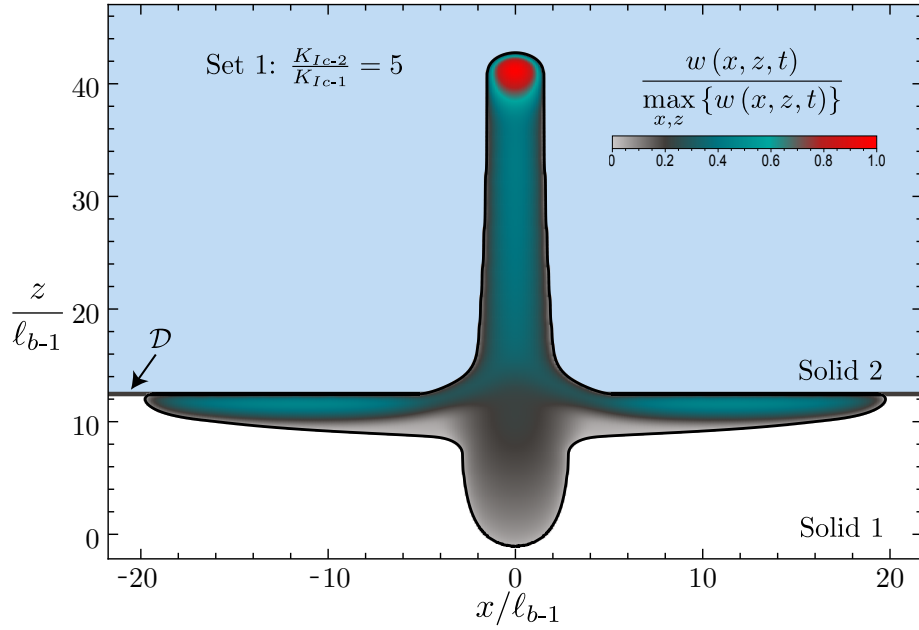


Figure 7.6: Footprint and opening distribution for the temporarily contained fracture of Set 1 and a toughness jump of $K_{Ic-2}/K_{Ic-1} = 5$ at $t/t_d = 5.11$. The buoyant HF in the upper layer after the breakthrough is finger-like. A combination of extension and fluid flow into the central buoyant HF generates a complex opening distribution in the low-toughness layer.

edge K_I^{top} (dark red line) never reaches the fracturing toughness of the upper layer K_{Ic-2} . The state of the fracture upon reaching the interface and the stress jump can explain this behavior. When the fluid injection has stopped when the fracture encounters the higher toughness layer, and the fracture accumulates volume at the interface, K_I^{top} increases. As soon as lateral propagation is favored, lateral spreading initiates. If, until this moment, no breakthrough occurred, the finite volume will spread out and reduce the opening, and hence K_I^{top} , at the point of contact on the layer. From then on, no more increase in K_I^{top} can occur if no additional fluid is released, leading to the observed indefinite containment. It is interesting to note that the same volume released directly into the higher toughness layer would have created a buoyant fracture (e.g., $\mathcal{B}_{ks-2} = 3.14 \geq 1$).

7.4 Stress jump

The case of a stress jump can be treated similarly to a toughness jump. Nonetheless, the mechanisms are slightly different, as the fracture must penetrate the higher confining stress layer to feel the change in normal stress. Recent developments based on the seminal work of Adachi et al. (2010) have shown that pure lateral extension is only possible for toughness-dominated fractures (Peruzzo and Lecampion, 2023b). In this regime, the fracture penetrates the higher stress level for a uniform depth from the interface (Peruzzo and Lecampion, 2023b). Different from this symmetrically contained case with uniform net pressure, we expect the

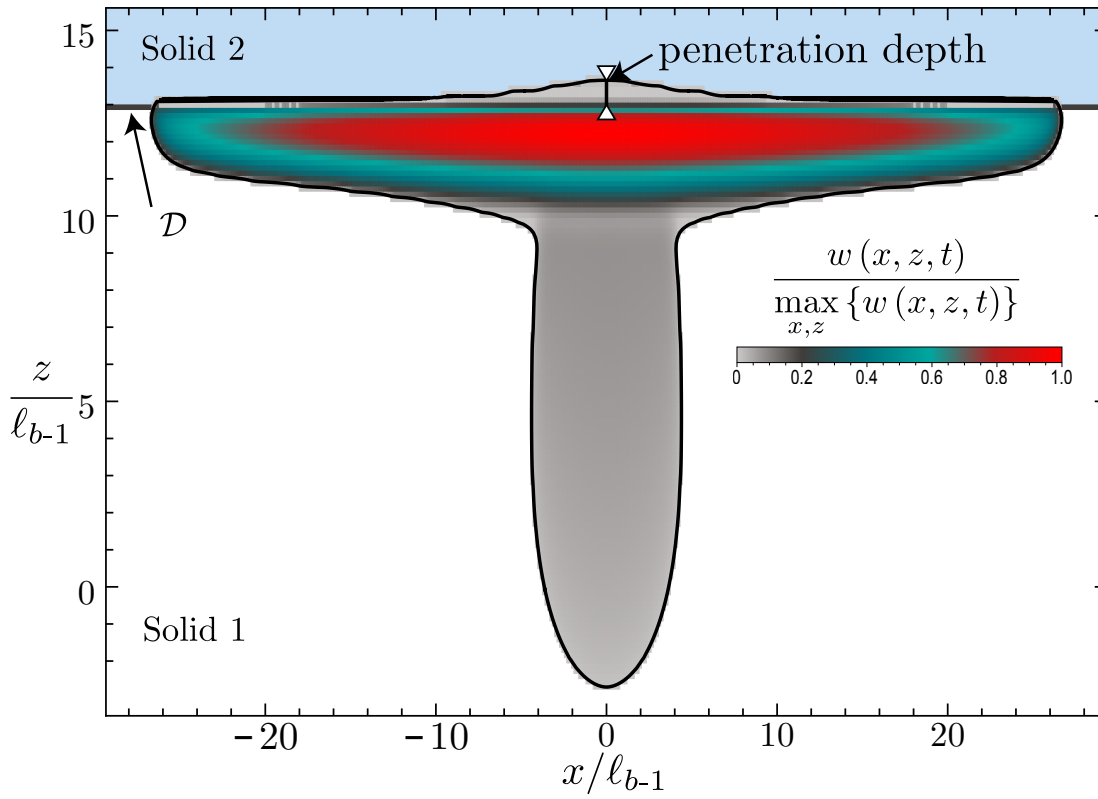


Figure 7.7: Footprint and opening distribution for an indefinitely contained fracture with $\Delta\sigma = 1.00$ (MPa) at $t/t_d = 156$. After a limited penetration into the upper layer, the fluid release ceases. The fracture concentrates in an elongated, nearly elliptical shape just below the interface of the stress jump.

asymmetry of the problem combined with an emerging linear pressure gradient from the background stress to lead to a penetration depth that decreases from the center to the edges of the lateral expansion along the interface. Comparing figure 7.7 and 7.6, this prediction is observed. Even though we expect the same outcomes for both jumps, the breakthrough in the stress jump case will be related to a penetration depth overcoming the buoyancy length scale. It is possible to perform an adimensionalization of the stress jump using the characteristic buoyancy pressure $\mathcal{S} = \Delta\sigma / (K_{Ic}^{2/3} \Delta\gamma^{1/3})$. The limiting value of the dimensionless stress jump \mathcal{S} for temporal or indefinite containment will, however, change in function of the state of the fracture upon reaching the stress jump (the values of \mathcal{M}_k , \mathcal{B}_{ks} , and \mathcal{D}). For ease of simplicity, we use hereafter the dimensional values of the stress jumps $\Delta\sigma$.

7.4.1 Simulations of modest and maximum cases

We perform the four simulations (two parametric sets, table 7.1 combined with two values of $\Delta\sigma$, table 7.2. Different from the case of a toughness jump (see section 7.3.2), we can only observe an *indefinite containment* and an *immediate breakthrough* (see figure 7.8a). In both cases, the higher stress jump of $\Delta\sigma = 3.0$ (MPa) arrests the fracture at depth. Nonetheless, a *transient containment* is theoretically possible. As indicated by figure 7.7, we define the penetration depth as the maximum distance (at the center $x = 0$) the fracture propagated into the high confinement layer, which we expect to increase continuously. Figure 7.8b shows that the evolution of the penetration depth is smooth for the simulations breaking through immediately and in jumps for the contained fractures. These jumps stem from the spatial discretization and not the physics of the problem. The definition of *temporal containment* and *immediate breakthrough* for a stress jump must be related to a timescale. As hypothesized, we expect the breakthrough when the penetration depth overcomes the buoyancy length scale ℓ_{b-1} . From this observation, we arbitrarily define a fracture as *temporarily contained* when the breakthrough occurs only after a time larger than $t \geq 2t_d$. Figure 7.8b clearly shows that for the lower stress jump, breakthrough occurs at a time $t < 2t_d$ such that we classify it as an *immediate breakthrough*. On the other hand, the higher stress jumps generate indefinitely contained fractures as the penetration depth never reaches ℓ_{b-1} .

7.4.2 Temporal containment for set 2

We numerically vary the stress jump between the limiting values of $\Delta\sigma = 0.5$, and 3.0 (MPa) to obtain the limit of temporal containment. Figure 7.9 shows the evolution of the penetration depth of these fractures. One observes that effectively a breakthrough occurs only when the penetration depth overcomes the buoyancy length scale $\ell_{b-1} = 19.3$ (m). The limiting stress jump to create temporal containment is about $\Delta\sigma = 0.80$ (MPa). The limiting stress jump to arrest the fracture is between $\Delta\sigma = 0.80$ (MPa) and $\Delta\sigma = 1.00$ (MPa), corresponding approximately to $\mathcal{S} \approx 4$.

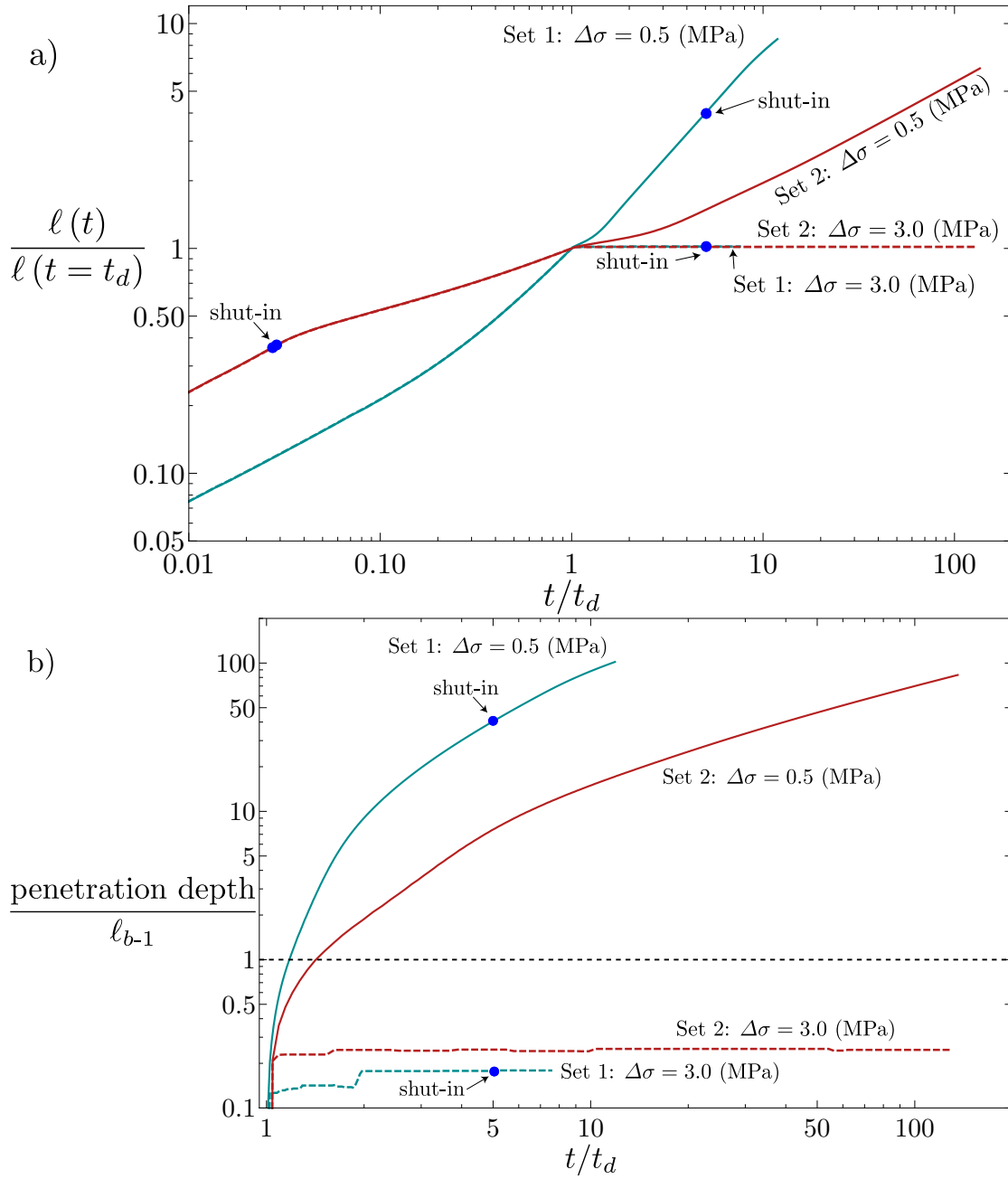


Figure 7.8: Evolution of fracture height (a) and penetration depth (b) for simulations encountering a stress jump. The color code is equivalent to the one described in figure 7.2. (b) Shows the expected behaviour derived from the analysis of figure 7.9 with no breakthrough if the penetration depth remains below ℓ_{b-1} .

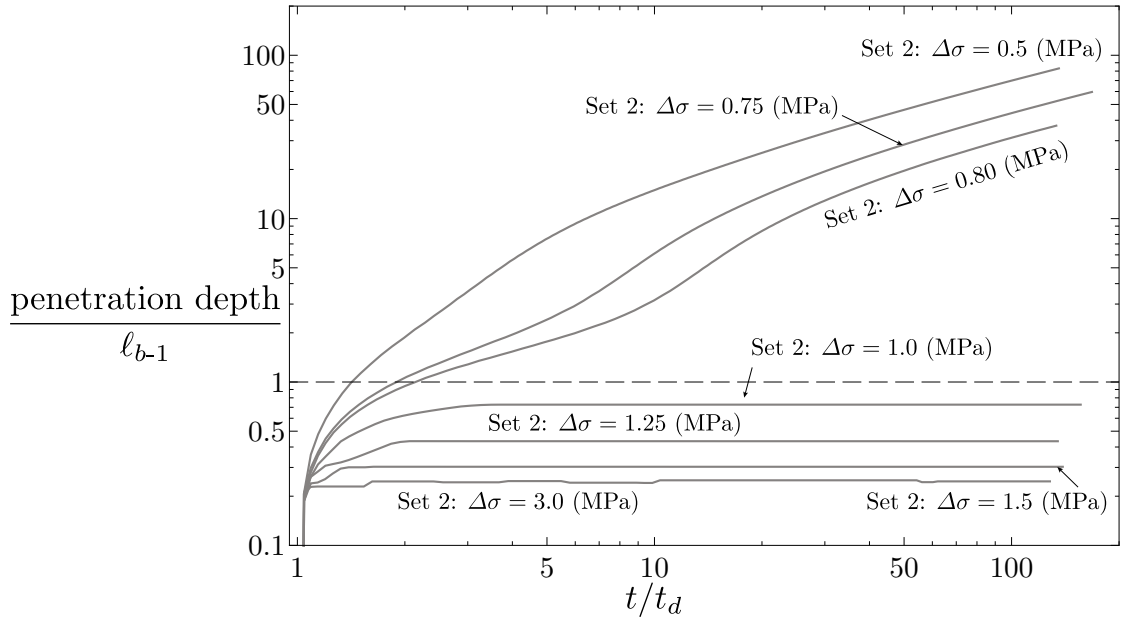


Figure 7.9: Evolution of the penetration depth for various stress jumps (corresponding to $\mathcal{S} \in (2.20, 13.2)$) applied to the second parameter set. This evaluation shows that breakthrough only occurs once the penetration depths overcome the buoyancy length scale ℓ_{b-1} .

7.5 Leak-off

The last arrest mechanism considered is fluid leak-off to the surrounding media. We assume the Carter leak-off model (Carter, 1957) (for a discussion of the model and its validity, see Lecampion et al. (2018); Kanin et al. (2020) and section 2.2.2) and consider two different scenarios. In the first scenario, the leak-off coefficient is constant in the entire domain consisting of one material only and denoted as C . Second, we investigate the configuration shown in figure 7.1, where Solid 1 is impermeable, and Solid 2 has a non-zero leak-off coefficient with a change in leak-off coefficient denoted as ΔC .

7.5.1 Uniform leak-off coefficient

When the injection consists of a finite volume release, a uniform leak-off will always lead to the arrest of the fracture. We thus focus on the capabilities of uniform leak-off to minimize its final height. The evolution of a radial fracture under a constant injection rate is well characterized by a rectangular propagation diagram, depending on only one dimensionless coefficient (Madyarova, 2003; Detournay, 2016; Dontsov, 2016). The case of a finite volume release was later described in chapter 3 and extended to the closure of the fracture by Peirce (2022) (based on Peirce and Detournay (2022)). We restrict our analysis to the possible arrest of the hydraulic fracture and neglect any phenomena occurring during closure. In chapter 3, we have shown that a radial fracture arrests immediately upon shut-in of the injection when it is leak-off or toughness-dominated. Our scaling analysis of the radial, leak-off dominated cases reveals that

a transition during an ongoing release is possible in all four limiting regimes. On the other hand, a buoyant fracture during a pulse propagation can only occur if the fracture is viscosity- and storage-dominated (see the discussion in chapter 3).

Studying first the crosslink injection into a sandstone, with a value of $\mathcal{M}_{\hat{k}} = 236 > 1$, the transition from radial to buoyant of this fracture will be viscosity-dominated. We check if the transition is in the viscosity-storage dominated regime or the viscosity-leak-off regime through the examination of the dimensionless leak-off coefficient at the transition

$$\mathcal{C}_m(t = t_{m\hat{m}}) = \frac{C' E'^{1/2}}{Q_o^{1/2} \Delta\gamma^{1/2}}, \text{ with } t_{m\hat{m}} = \frac{E'^{5/7} \mu'^{4/7}}{Q_o^{3/7} \Delta\gamma^{9/7}}. \quad (7.4)$$

For the material properties of Set 1 (see table 7.1) and the two different leak-off coefficients (see table 7.2) the corresponding values are $\mathcal{C}_m(t = t_{m\hat{m}}) = 9.80 \cdot 10^{-3}$ for $C = 10^{-6} \text{ (m}\cdot\text{s}^{-1/2})$ and $9.80 \cdot 10^{-7}$ for $C = 10^{-10} \text{ (m}\cdot\text{s}^{-1/2})$ respectively. In both cases, the transition is thus viscosity-storage dominated and happens during the release. Figure 7.10 shows that the influence of leak-off is negligible up to shut-in (indicated by the $\ell(t) \propto t^{5/6}$ power-law). The higher leak-off simulation (dashed line) then indicates a leak-off caused arrest of buoyant propagation. From the progression of height growth observed in figure 7.10, we can estimate this arrest at a final fracture extent of about $\ell_f / \ell_{m\hat{m}} \approx 55.0$, corresponding to $\ell_f \approx 2500 \text{ (m)}$ (see the caption of figure 7.10 for a definition of $\ell_{m\hat{m}}$). Such a fracture height is above the typical length scale of other heterogeneities, such as the ones presented herein. Uniform leak-off is thus not efficient in arresting fracture propagation at depth. We expect uniform leak-off to be efficient only if the fracture becomes leak-off dominated before the transition to buoyant propagation occurs. We perform an additional simulation with $C = 10^{-4} \text{ (m}\cdot\text{s}^{-1/2})$ which leads to a dimensionless leak-off coefficient of $\mathcal{C}_m(t = t_{m\hat{m}}) = 0.98$ arresting the fracture radially upon shut-in. The final extent of this fracture, arrested at depth, would be $\ell_f \approx 130 \text{ (m)}$.

As the second set of parameters also generates a fracture transitioning to buoyancy in the viscosity-dominated regime ($\mathcal{M}_{\hat{k}} = 1.68 \cdot 10^5$), we check again the dimensionless leak-off coefficient at the transition (see equation (7.4)) and obtain $\mathcal{C}_m(t = t_{m\hat{m}}) = 3.19 \cdot 10^{-2}$ for $C = 10^{-6} \text{ (m}\cdot\text{s}^{-1/2})$ and $3.19 \cdot 10^{-6}$ for $C = 10^{-10} \text{ (m}\cdot\text{s}^{-1/2})$ respectively. Different from the previous case, the shut-in occurs at about the time when the fracture becomes buoyant ($t_s / t_{m\hat{m}} = 0.51$). Prediction of an arrest at depth before becoming a buoyant fracture is thus difficult for this parameter set. Using numerical simulations (see figure 7.10), we observe that the high-leak-off coefficient stops the fracture close to the end of the release. The ongoing propagation of the high-leak-off fracture after shut-in (blue dots in figure 7.10) is solely related to the radial fracture becoming toughness-dominated (see section 3.4.3). Fracture arrest for this high leak-off occurs at about the same time as if the fracture would be perfectly radial (predicted arrest at $t / t_{m\hat{m}} \approx 12.1$). Observation of the fracture footprint at arrest (see figure 7.12a) reveals a nearly radial fracture with a maximum height of about $\ell_f \approx 204 \text{ (m)}$. The small leak-off coefficient tends to the finite volume, buoyant, viscosity-dominated fracture height

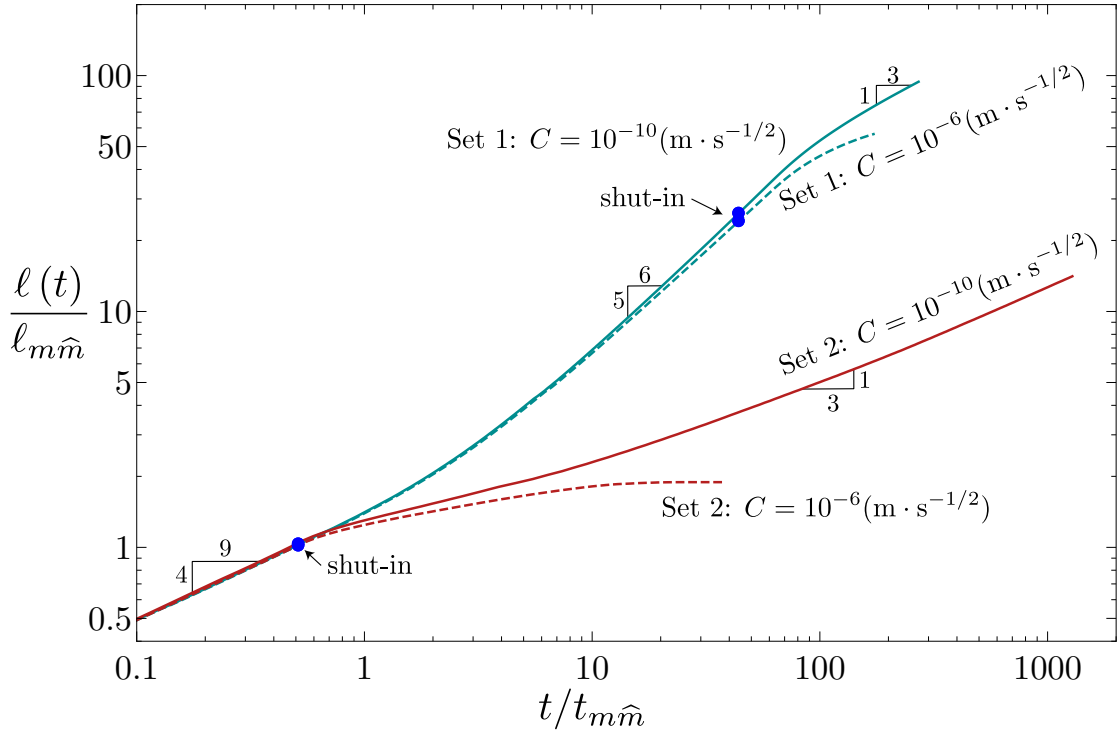


Figure 7.10: Fracture height evolution for simulations with a uniform leak-off coefficient as a function of $t/t_{m\hat{m}}$ with $\ell_{m\hat{m}} = E'^{5/7} \mu^{4/7} / (Q_o^{3/7} \Delta\gamma^{9/7})$. Color code as in figure 7.2.

growth before it accelerates towards the equivalent toughness-dominated fracture growth (at about $t/t_{m\hat{m}} \approx 100$). The expected arrest of the fracture (when becoming toughness, leak-off dominated) would occur at $t/t_{m\hat{m}} \approx 2.22 \cdot 10^6$ at a fracture length of about $\ell_f \approx 5.40$ (km) (corresponding to $\ell_f/\ell_{m\hat{m}} \approx 50.1$). This final height is again beyond the length scales of the different heterogeneities considered herein, and we expect a combination of effects to arrest the fracture before.

We can conclude from this section that uniform leak-off as an arrest mechanism is only efficient if it prevents the fracture from becoming buoyant in the first place. If the fracture becomes buoyant, the final fracture height becomes of the order of (km). We expect formations with a small leak-off coefficient to be arrested by different arrest mechanisms, limiting their buoyant growth.

7.5.2 Jump in leak-off intensity

The previous section revealed the limited capabilities of uniform leak-off to arrest a buoyant fracture. We now investigate a different mechanism, a change in the leak-off coefficient with an impermeable injection layer (Solid 1). The buoyant fracture then encounters a layer of higher leak-off (Solid 2), where the jumps in leak-off intensity are chosen in agreement with the uniform leak-off coefficients considered. A jump in leak-off intensity is only interesting

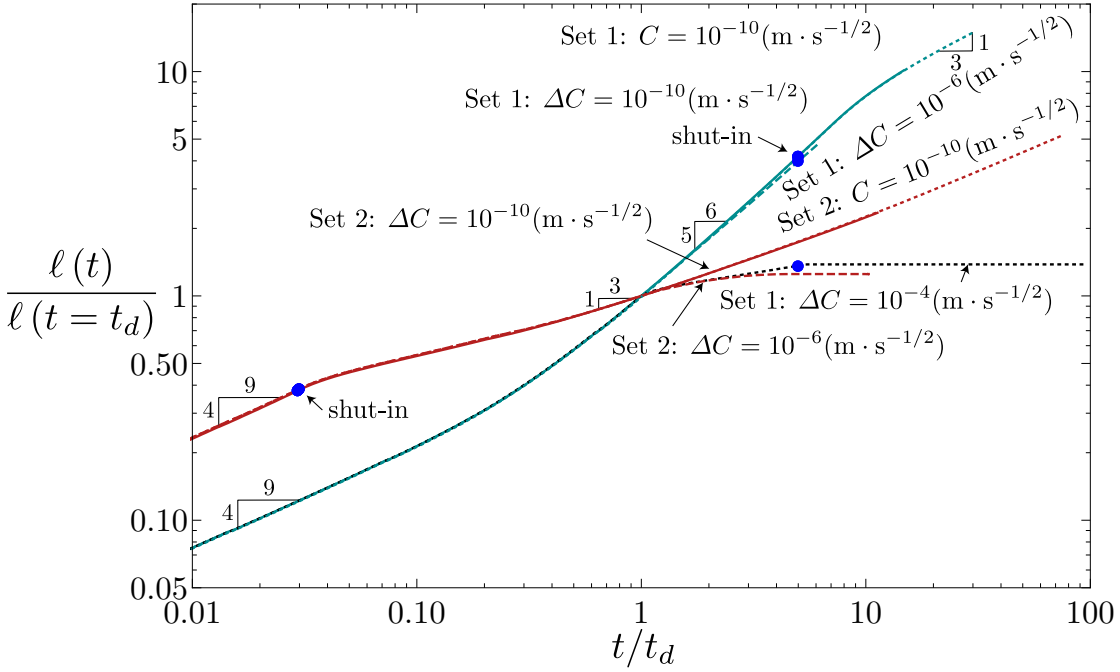


Figure 7.11: Fracture height evolution for simulations with a jump in leak-off coefficient. The dotted lines show the evolution for uniform leak-off simulations with $C = 10^{-10} \text{ (m} \cdot \text{s}^{-1/2})$. Color code as in figure 7.2.

if the fracture arrests "at the interface". If a fracture propagates long enough into the higher leak-off layer, the considerations will be equivalent to the uniform leak-off case of section 7.5.1. Considering still a distance of $d = 250 \text{ (m)}$, we found that the contact is buoyant, viscosity-dominated, and when the injection is still ongoing for Set 1 and buoyant, viscosity-dominated in a pulse regime for Set 2.

Figure 7.11 shows that for the crosslink gel injection into sandstone, the influence of a jump in leak-off coefficient does not differ from the effect of uniform leak-off. For comparison, we plot in dotted lines the equivalent simulation with uniform leak-off for $C = 10^{-10} \text{ (m} \cdot \text{s}^{-1/2})$ to emphasize this point. Because leak-off will only act once the fracture has passed into the upper layer, the final fracture extent for the jump is slightly larger due to the delayed effect of leak-off. Because we have negligible leak-off-related effects, we consider the encountering of an even higher leak-off layer with $\Delta C = 10^{-4} \text{ (m} \cdot \text{s}^{-1/2})$. The corresponding simulation (black dashed line in figure 7.11) shows that this increased leak-off can arrest the fracture within about 100 (m) of the interface. Compared to the total height of 130 (m) when the same coefficient is used in the uniform case, the jump is more efficient in arresting the fracture even though the total fracture height at arrest is more extensive (375 (m)).

The slickwater injection is shown in figure 7.11. This figure shows that fracture growth for these parameters rapidly stops if $\Delta C = 10^{-6} \text{ (m} \cdot \text{s}^{-1/2})$. The final fracture height of this simulation arises to $\ell_f = 366 \text{ (m)}$, which is about 1.8 times the size obtained for the uniform leak-off case,

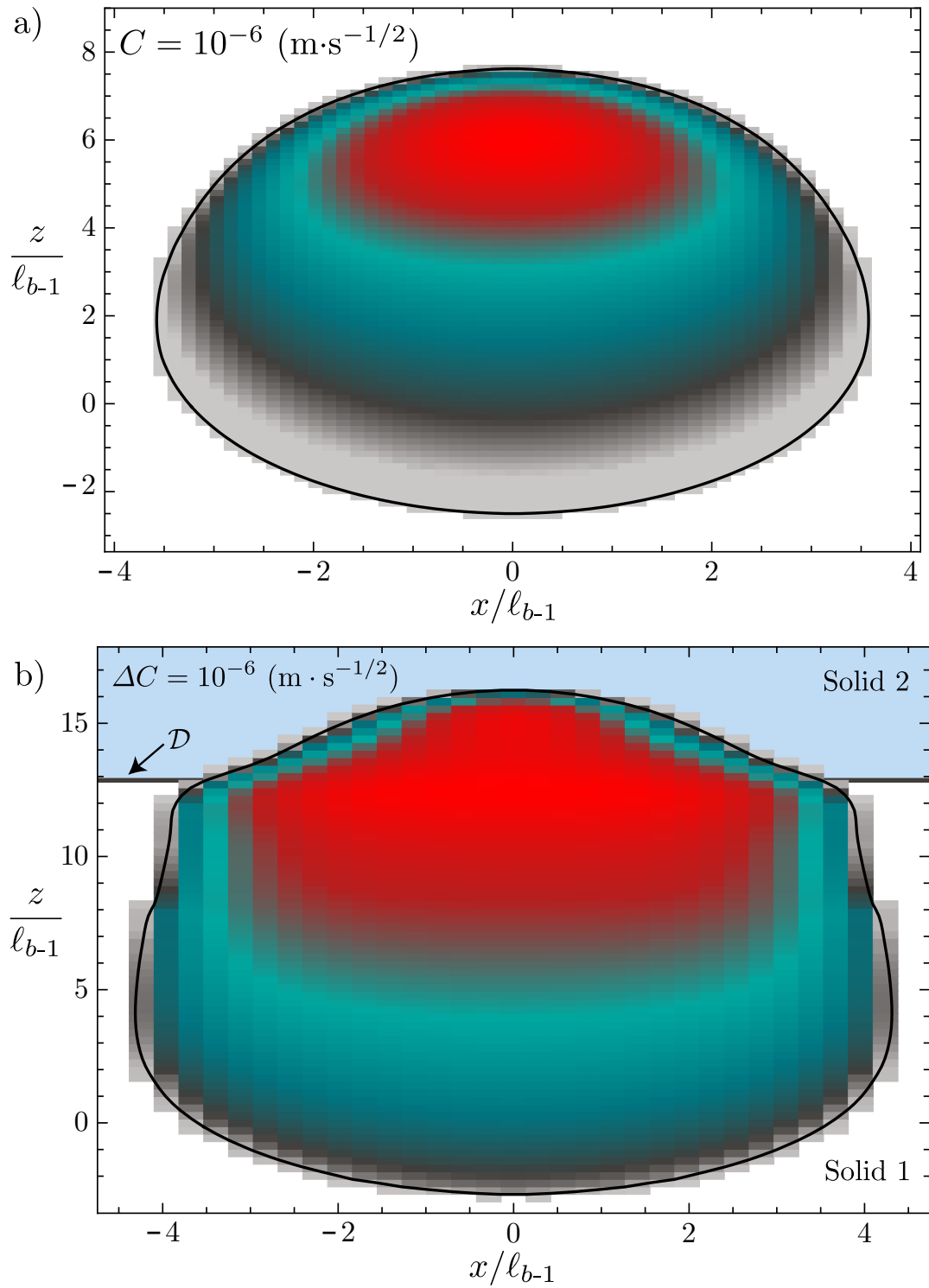


Figure 7.12: Arrested fracture footprint with opening distribution before closure for a uniform (a) and a jump (b) in leak-off coefficient. The figures use parameter Set 2 and a leak-off coefficient $C = \Delta C = 10^{-6} \text{ (m} \cdot \text{s}^{-1/2})$.

whereas the penetration depth is only about 65 (m). Compared to the arrested size in the case of uniform leak-off (e.g., 204 (m)), the jump is more efficient than continuous leak-off. The lower jump in leak-off intensity is not distinguishable from the continuous release case (continuous and dotted red lines in figure 7.11).

Jumps in leak-off intensity seem to arrest a fracture only if an equivalent, uniform value would arrest the emerging fracture before it becomes buoyant. In these cases, we then observe that the jump is more efficient. This statement refers to a smaller penetration depth when compared to the final height of a fracture with the same uniform leak-off coefficient. Observation of figure 7.12, where figure a) shows the arrested footprint of the fracture with uniform leak-off and figure b) the same for a jump in leak-off intensity validates this statement. The fractured part entering the high leak-off layer is negligible compared to the total size of the fracture in the uniform case, indicating that this heterogeneity of leak-off is more efficient.

7.6 Conclusions

We have shown through observation of numerical 3D planar simulations that various arrest mechanisms can stop buoyant hydraulic fractures. Through a scaling analysis, we derive that a fracture size-dependent, apparent fracturing toughness (see equation (7.1)) can prevent a fracture from becoming buoyant but not stop it if it is already buoyant. Interestingly, a jump in fracturing toughness between two layers (e.g., $K_{Ic-2}/K_{Ic-1} > 1.0$) proves to be a possible arrest mechanism, even when the total released volume would theoretically be sufficient to create a buoyant hydraulic fracture in the upper level (e.g. $\mathcal{B}_{ks-2} \geq 1$). Our simulations show that the required jump to arrest a fracture is significant and that an *indefinite containment*, a *immediate breakthrough*, and a *temporal containment* are possible. The most efficient way of arresting an already buoyant fracture is when it encounters a positive stress contrast (e.g., $\Delta\sigma > 0.0$). For the parametric sets considered within this study, a stress contrast of the order of $\Delta\sigma \sim 1.0$ (MPa) is sufficient to create an *indefinite containment* (e.g., $\mathcal{S} \approx 3 - 4$). The leaking of fluid into the surrounding environment will always lead to an ultimate arrest of a finite volume injection. We distinguish between an arrest at depth before the fracture becomes buoyant in the uniform leak-off case or at the interface to a different, higher leak-off layer and the final arrest reached when the fracture evolves as a buoyant hydraulic fracture. We find that the same values of leak-off are necessary to arrest a fracture when a higher leak-off layer is encountered or when leak-off is uniform. Generally, modest leak-off values (e.g., $C \sim 10^{-6}$ (m·s^{-1/2})) can arrest fractures within a reasonable final height and even prevent buoyant propagation. A single, high leak-off layer (e.g., $C \sim 10^{-4}$ (m·s^{-1/2})) is very efficiently arresting the fractures considered within a few meters of penetration into it. Our investigation has considered all effects separately. Most likely, a combination of several of these mechanisms occurs, arresting buoyant fractures. Even though the volumes of hydraulic fracturing treatments are usually sufficient to initiate the emergence of buoyant hydraulic fractures, we show that these fractures rarely present significant uprise due to a series of possible arrest mechanisms.

Conclusions and Perspectives **Part IV**

8 Conclusions and perspectives

8.1 Main contributions

In this thesis, we have studied the buoyant propagation of planar three-dimensional hydraulic fractures from a scaling and numerical perspective. In detail, we have investigated the transition from radial/axisymmetric to uni-directional buoyant propagation of hydraulic fractures created by a fluid release from a point source.

In the first step, we clarified the behavior of radial hydraulic fractures when the released fluid volume is finite. We could notably show that in impermeable media, the final arrested size, opening, and pressure distribution solely depend on the total volume of fluid released and the fluid and material parameters. The exact history of the release (e. g. the release rate and duration) do not influence the final fracture characteristics. However, large release rates can lead to significant propagation of the fracture even after the end of the fluid release. On the other hand, when the host medium of the fracture is permeable, the final arrested fracture characteristics are no longer unique for the same fluid volume released. This phenomenon arises due to the time dependence of the fluid leak-off into the surrounding media. It remains possible to predict the final extent and shape for any finite volume release may the host medium be impermeable or permeable. The necessary condition for such a prediction is the knowledge of the fracturing fluid and host rock properties, total fluid volume released, and leak-off rate.

The knowledge of the behavior of finite volume radial hydraulic fractures was a necessary pre-requisite to answer the first research questions addressed in this thesis. To understand the emergence and shape of buoyant hydraulic fractures, we first restricted ourselves to a continuous fluid release (e. g. the released volume is infinite) in an impermeable media. Under these circumstances, all fluid releases become buoyant self-sustained fractures. We studied their late-time behavior and the transition from radial to buoyant propagation. Our study confirmed the typical head and tail structure of buoyant fractures previously observed in two-dimensional (2D) studies. We demonstrated that this problem depends on a single dimensionless number defining a family of solutions. This dimensionless number is the

Chapter 8. Conclusions and perspectives

ratio between the energy dissipation rate by the viscous flow in the fracture, and the energy dissipated to create new surfaces when the fracture becomes buoyant. It measures the energy split in the fracture's head and defines the resulting characteristics of the entire fracture. The tail is always dominated by the viscous fluid flow inside and governs the vertical propagation velocity of buoyant hydraulic fractures. The emerging family of solutions has two limiting regimes. In the viscosity-dominated limit where the fracture resistance of the material is negligible, the fracture grows laterally *ad vitam eternum* at a sub-linear velocity, and the fracture head becomes unimportant to the problem at late times. The other limit has no solution for a strictly zero fluid viscosity. However, a toughness-dominated regime with a fixed horizontal fracture breadth and a constant vertical propagation velocity exists. This toughness-dominated limit shows significant acceleration around the transition from radial to buoyant propagation and requires long propagation distances and times to establish its finger-like shape fully. We showed that most natural occurrences and industrial applications fall within the boundaries of these limiting regimes. On the other hand, laboratory experiments often suffer from boundary effects and unsteady release rates and can not be allocated to one of these two limiting regimes.

Combining the first two studies, we answered the question of when a hydraulic fracture becomes buoyant by investigating finite volume releases. We remained in the framework of an impermeable media and notably showed that the emergence of buoyant hydraulic fractures is linked to another dimensionless number. Using scaling arguments, we derived the uniqueness of the emergence condition and verified our theoretical considerations through a series of numerical simulations. The answer to the question about the characteristic shape of finite-volume buoyant hydraulic fractures requires the combination of the two dimensionless numbers mentioned previously. We could delimit several "regions" within which the combined set of the two would lead to similar propagation histories of the emerging self-sustained fractures. We further demonstrated that various combinations of numbers could lead to comparable late-time behavior, making the interpretation of field data difficult.

Defining the limits when buoyant hydraulic fractures emerge and studying their characteristics has revealed that a significant range of conditions should favor buoyant propagation, especially for typical industrial configurations. Nonetheless, observations of anthropogenic buoyant fractures are rare. We thus used our knowledge of the different characteristics and vertical propagation velocities of buoyant hydraulic fractures to study the effect of possible arresting mechanisms. A particular interest was put on fluid leaking off to the surrounding medium, respectively, solidification of magmatic intrusions. Our numerical simulations revealed a pulsating advancement of buoyant hydraulic fractures subjected to fluid mass loss (leak-off or solidification). Based on this observation, we performed a physics-based scaling analysis, which gave a rationale for why such behavior could exist even for a fluid release at a continuous rate. We could further show that considering a size-dependent fracture toughness of the material is a very inefficient mechanism to arrest propagating buoyant hydraulic fractures. Our evaluations show that the most efficient arrest mechanisms of buoyant hydraulic fractures are jumps in the minimum in-situ stress (so-called stress barriers) and a depletion of the fracture

head associated with fluid mass loss by leak-off or solidification. To a lesser extent, changes in the fracturing toughness can also limit the vertical propagation of buoyant hydraulic fractures.

8.2 Perspectives

The developments presented in this thesis pave the way for other research questions. In particular, the following research questions could be addressed:

- The post-injection propagation of finite volume radial hydraulic fractures could be investigated experimentally. This point has already partially been investigated for an impermeable media (see the recent work of Tanikella and Dressaire (2022); Tanikella et al. (2023)) but remains open to be explored when leak-off is prominent.
- The available experimental data on the limiting regimes of buoyant hydraulic fractures due to a continuous fluid release still needs to be increased. Notably, most existing experiments suffer from boundary effects, and the difficulty in generating a constant fluid release rate must be resolved. Further, they are generally in an intermediate or toughness-dominated regime. It would thus be interesting to perform experiments in the viscous limit of buoyant hydraulic fractures to validate our findings.
- Similarly, experimental validation of the finite volume regimes and the limit on the critical volume for buoyant fractures to emerge could be beneficial to support the theory.
- A series of experiments investigating the solidification of buoyant hydraulic fractures exists (Taisne and Tait, 2011). These experiments show the same pulsation as observed in the numerical simulations. It would be interesting to compare them with numerical simulations to prove that the analogy between fluid leak-off and magma solidification is applicable. In this regard, a study on the limitations of the underlying simplifying assumptions should be performed theoretically, and additional experimental and numerical data should be collected.
- All considerations within this thesis treat an infinite medium. For questions related to ascending magmatic intrusion, the incorporation of topographical loads and the free surface remain to be investigated. These considerations are notably important when comparing the developed theoretical and numerical findings to field data of magmatic intrusions and laboratory experiments.
- Our developments have been limited to one point source. This limitation restricts the modeling of complex systems like the plumbing systems of volcanic edifices. It remains to be clarified how buoyant hydraulic fractures interact and how they differ if they do not originate from a single point source. Such considerations notably become important when applying the theory to dehydrating slabs in subduction zones. The

Chapter 8. Conclusions and perspectives

accumulation of fluid in such cases starts from a sub-critically growing flaw by an inflow of overpressurized formation fluid. Modeling such a process would also require the development of pressure-dependent leak-off type fluid exchange with the host media.

- We have yet to explore the transition from vertical to lateral dike at a neutral buoyancy line or due to changes in material properties. Theoretical developments to study such processes are of potential interest to understand the lateral emplacement of magmatic intrusions. The lateral emplacement often occurs in the form of sills which are laterally growing intrusions with a horizontal plane of propagation. With the current model, such a mechanism can not be studied as the plane of propagation is prescribed. Modeling the transition from dike (vertical propagation) to sill intrusions (horizontal propagation) would thus require an extension to the current numerical solver to account for propagation in a plane perpendicular to the originating dyke at the neutral buoyancy line.
- The limitations of lubrication flow and Newtonian fluids are non-negligible, especially when applications for magma migration are considered. Extending the present considerations to non-Newtonian fluids and multi-phase flows would be of significant scientific interest.

Bibliography

- Abé, H., Keer, L. M., and Mura, T. (1976). Growth rate of a penny-shaped crack in hydraulic fracturing of rocks 2. *J. Geophys. Res.*, 81:6292–6298.
- Adachi, J. I. and Detournay, E. (2008). Plane strain propagation of a hydraulic fracture in a permeable rock. *Eng. Fract. Mech.*, 75(16):4666–4694.
- Adachi, J. I., Detournay, E., and Peirce, A. P. (2010). Analysis of the classical pseudo-3D model for hydraulic fracture with equilibrium height growth across stress barriers. *Int. J. Rock Mech. Min. Sci.*, 47:625–639.
- Adachi, J. I., Detournay, E., and Savitski, A. A. (2001). Simulation of hydraulic fracturing using an explicit moving mesh algorithm. In *Proceedings of the 2001 U.S. Rock Mechanics/Geomechanics Symposium*, volume All Days of U.S. Rock Mechanics/Geomechanics Symposium. ARMA-01-0243.
- Adachi, J. I. and Peirce, A. P. (2008). Asymptotic analysis of an elasticity equation for a finger-like hydraulic fracture. *J. Elast.*, 90(1):43–69.
- Adachi, J. I., Siebrits, E., Peirce, A. P., and Desroches, J. (2007). Computer simulation of hydraulic fractures. *Int. J. Rock Mech. Min. Sci.*, 44(5):739–757.
- Adams, J. and Rowe, C. (2013). Differentiating applications of hydraulic fracturing. In *ISRM International Conference for Effective and Sustainable Hydraulic Fracturing*, volume All Days of ISRM International Conference for Effective and Sustainable Hydraulic Fracturing.
- Advani, S. H., Lee, T. S., and Lee, J. K. (1990). Three-dimensional modeling of hydraulic fractures in layered media: part I- finite element formulations. *J. Energy Resour. Technol. Trans. ASME*, 112(1):1–9.
- Alm, O., Jaktlund, L.-L., and Shaoquan, K. (1985). The influence of microcrack density on the elastic and fracture mechanical properties of Stripa granite. *Phys. Earth Planet. Inter.*, 40(3):161–179. Special Issue Experiments in Solid State Physics Relevant to Lithospheric Dynamics.
- Anderson, D. G. (1965). Iterative procedures for nonlinear integral equations. *J. ACM*, 12(4):547–560.

Bibliography

- Anderson, T. L. (2017). *Fracture mechanics: fundamentals and applications*. CRC press.
- Atkinson, B. K. (1984). Subcritical crack growth in geological materials. *J. Geophys. Res.: Solid Earth*, 89(B6):4077–4114.
- Atkinson, B. K. (1987). *Fracture mechanics of rock*. Elsevier.
- Barbati, A. C., Desroches, J., Robisson, A., and McKinley, G. H. (2016). Complex fluids and hydraulic fracturing. *Annu. Rev. Chem. Biomol. Eng.*, 7:415–453.
- Barenblatt, G. I. (1962). The mathematical theory of equilibrium cracks in brittle fracture. *Adv. Appl. Mech.*, VII:55–129.
- Barree, R. D. and Mukherjee, H. (1996). Determination of pressure dependent leakoff and its effect on fracture geometry. In *Proceedings SPE Annual Technical Conference and Exhibition*, Denver, Colorado, USA. SPE 36424.
- Batchelor, G. K. (1967). *An Introduction to Fluid Dynamics*. Cambridge Mathematical Library. Cambridge University Press, Cambridge, UK.
- Bonnet, M. (1999). *Boundary integral equation methods for solids and fluids*. John Wiley & Sons.
- Boone, T. J. and Ingraffea, A. R. (1990). A numerical procedure for simulation of hydraulically-driven fracture propagation in poroelastic media. *Int. J. Numer. Anal. Methods Geomech.*, 14(1):27–47.
- Brandeis, G. and Jaupart, C. (1986). On the interaction between convection and crystallization in cooling magma chambers. *Earth Planet. Sci. Lett.*, 77(3):345–361.
- Bruce, P. M. (1989). *Thermal convection within the Earth's crust*. PhD thesis, University of Cambridge.
- Bruce, P. M. and Huppert, H. E. (1989). Thermal control of basaltic fissure eruptions. *Nature*, 342(6250):665–667.
- Bruce, P. M. and Huppert, H. E. (1990). Solidification and melting along dykes by the laminar flow of basaltic magma. *Magma transport and storage*, pages 87–101.
- Bunger, A. P. and Detournay, E. (2007). Early-time solution for a radial hydraulic fracture. *J. Eng. Mech. - ASCE*, 133(5):534–540.
- Bunger, A. P. and Detournay, E. (2008). Experimental validation of the tip asymptotics for a fluid-driven crack. *J. Mech. Phys. Solids*, 56:3101–3115.
- Bunger, A. P., Detournay, E., and Garagash, D. I. (2005a). Toughness-dominated hydraulic fracture with leak-off. *Int. J. Fract.*, 134(2):175–190.

- Bunger, A. P., Detournay, E., and Jeffrey, R. G. (2005b). Crack tip behavior in near-surface fluid-driven fracture experiments. *C. R. Mècanique*, 333:299–304.
- Bunger, A. P., Gordeliy, E., and Detournay, E. (2013). Comparison between laboratory experiments and coupled simulations of saucer-shaped hydraulic fractures in homogeneous brittle-elastic solids. *J. Mech. Phys. Solids.*, 61(7):1636–1654.
- Bunger, A. P., Jeffrey, R. G., and Detournay, E. (2004). Toughness-dominated near-surface hydraulic fracture experiments. In Yale, D., Willson, S., and Abou-Sayed, A., editors, *Gulf Rocks 2004 – Proc 6th North American Rock Mechanics Symposium*, Houston. Paper No 468.
- Bunger, A. P., Jeffrey, R. G., and Detournay, E. (2005c). Application of scaling laws to laboratory-scale hydraulic fractures. In *Alaska Rocks 2005, The 40th US Symposium on Rock Mechanics (USRMS)*. ARMA/USRMS 05-818.
- Bunger, A. P., Jeffrey, R. G., and Detournay, E. (2008). Evolution and morphology of saucer-shaped sills in analog experiments. In Thompson, K. and Petford, N., editors, *Structure and Emplacement of High-Level Magmatic Systems*, volume 302, pages 107–118. Geological Society, London.
- Bunger, A. P., Jeffrey, R. G., and Zhang, X. (2011). Experimental investigation of the interaction among closely spaced hydraulic fractures. In *Proceedings 45th U.S. Rock Mechanics Symposium*, San Francisco, CA, USA. Paper No. 11-318.
- Bunger, A. P., Lau, H., Wright, S., and Schmidt, H. (2023). Mechanical model for geomechanical pumped storage in horizontal fluid-filled lenses. *Int. J. Numer. Anal. Methods Geomech.*, 47(8):1349–1372.
- Byerly, D. W. and Knowles, S. W. (2017). Tennessee “Marble”: a potential “Global Heritage Stone Resource”. *International Union of Geological Sciences*, 40(4):325–331.
- Carrigan, C. R., Schubert, G., and Eichelberger, J. C. (1992). Thermal and dynamical regimes of single- and two-phase magmatic flow in dikes. *J. Geophys. Res.: Solid Earth*, 97(B12):17377–17392.
- Carslaw, H. and Jaeger, J. (1959). *Conduction of heat in solids*. Oxford Univ Press.
- Carter, E. D. (1957). Optimum fluid characteristics for fracture extension. In Howard, G. and Fast, C., editors, *Drilling and Production Practices*, pages 261–270. American Petroleum Institute, Tulsa, OK.
- Castillo, J. L. (1987). Modified fracture pressure decline analysis including pressure-dependent leakoff. In *Proceedings SPE Low Permeability Reservoirs Symposium*, pages 273–281, Denver, Colorado, USA. SPE 16417.
- Chang, E. and Firoozabadi, A. (2000). Gravitational Potential Variations of the Sun and Moon for Estimation of Reservoir Compressibility. *SPE Journal*, 5(04):456–465.

Bibliography

- Charles, R. J. (1958a). Static fatigue of glass. i. *J. Appl. Phys.*, 29(11):1549–1553.
- Charles, R. J. (1958b). Static fatigue of glass. ii. *J. Appl. Phys.*, 29(11):1554–1560.
- Chen, H., Liu, H., Zhang, S., and Feng, Y. (2020). Smart thermoviscosifying polymer for improving drag reduction in slick-water hydrofracking. *Fuel*, 278:118408.
- Ciezboka, Jordan. and Courtier, James. and Wicker, Joe. (2018). Hydraulic Fracturing test site (HFTS)-project overview and summary of results (SPE 2937168). In *Unconventional Resources Technology Conference, Houston, Texas, 23-25 July 2018*, pages 1331–1339. Society of Exploration Geophysicists, American Association of Petroleum Geologists, Society of Petroleum Engineers.
- Cornet, F. H. (2015). *Elements of Crustal Geomechanics*. Cambridge University Press, Cambridge, UK.
- Crouch, S. L. and Starfield, A. M. (1983). *Boundary element methods in solid mechanics*. George Allen & Unwin.
- Cruse, T. A. (1996). BIE fracture mechanics analysis: 25 years of developments. *Computational Mechanics*, 18(1):1–11.
- Dahm, T. (2000a). Numerical simulations of the propagation path and the arrest of fluid-filled fractures in the earth. *Geophys. J. Int.*, 141(3):623–638.
- Dahm, T. (2000b). On the shape and velocity of fluid-filled fractures in the Earth. *Geophys. J. Int.*, 142(1):181–192.
- Dai, C. and Zhao, F. (2019). *Oilfield Chemistry*. Springer.
- Daneshy, A. A. (1978). Hydraulic Fracture Propagation in Layered Formations. *Soc. Pet. Eng. J.*, 18(01):33–41.
- Davis, T., Bagnardi, M., Lundgren, P., and Rivalta, E. (2021). Extreme curvature of shallow magma pathways controlled by competing stresses: Insights from the 2018 sierra negra eruption. *Geophys. Res. Lett.*, 48(13):e2021GL093038.
- Davis, T., Rivalta, E., and Dahm, T. (2020). Critical fluid injection volumes for uncontrolled fracture ascent. *Geophys. Res. Lett.*, 47(14):e2020GL087774.
- Davis, T., Rivalta, E., Smittarello, D., and Katz, R. F. (2023). Ascent rates of 3-D fractures driven by a finite batch of buoyant fluid. *J. Fluid Mech.*, 954:A12.
- De Marsily, G. (1986). Quantitative Hydrogeology. Technical report, Paris School of Mines, Fontainebleau, France.
- De Pater, H., Desroches, J., Groenenboom, J., and Weijers, L. (1996). Physical and numerical modeling of hydraulic fracture closure. *SPE Production & Facilities*, 11(02):122–128.

- Delaney, P. T. and Pollard, D. D. (1982). Solidification of basaltic magma during flow in a dike. *Am. J. Sci.*, 282(6):856–885.
- Delaney, P. T., Pollard, D. D., Ziony, J. I., and McKee, E. H. (1986). Field relations between dikes and joints: Emplacement processes and paleostress analysis. *J. Geophys. Res.: Solid Earth*, 91(B5):4920–4938.
- Desroches, J., Detournay, E., Lenoach, B., Papanastasiou, P., Pearson, J. R. A., Thiercelin, M., and Cheng, A. H.-D. (1994). The crack tip region in hydraulic fracturing. *Proc. R. Soc. A: Math. Phys. Eng. Sci.*, 447(1929):39.
- Desroches, J. and Thiercelin, M. (1993). Modelling the propagation and closure of micro-hydraulic fractures. *Int. J. Rock Mech. Min. Sci. & Geom. Abstr.*, 30(7):1231–1234.
- Detournay, E. (2004). Propagation regimes of fluid-driven fractures in impermeable rocks. *Int. J. Geomech.*, 4(1):35 – 45.
- Detournay, E. (2016). Mechanics of hydraulic fractures. *Annu. Rev. Fluid Mech.*, 48:311–339.
- Detournay, E., Cheng, A.-D., Roegiers, J.-C., and McLennan, J. (1989). Poroelasticity considerations in In-Situ stress determination by hydraulic fracturing. *Int. J. Rock Mech. Min. Sci. & Geom. Abstr.*, 26(6):507 – 513.
- Detournay, E. and Cheng, A. H.-D. (1991). Plane strain analysis of a stationary hydraulic fracture in a poroelastic medium. *Int. J. Solids Struct.*, 27(13):1645–1662.
- Detournay, E., Cheng, A. H.-D., and McLennan, J. D. (1990). A poroelastic PKN hydraulic fracture model based on an explicit moving mesh algorithm. *ASME J. Ener. Res. Tech.*, 112:224–230. pdf.
- Detournay, E. and Garagash, D. I. (2003). The near-tip region of a fluid-driven fracture propagating in a permeable elastic solid. *J. Fluid Mech.*, 494:1–32.
- Detournay, E. and Peirce, A. P. (2014). On the moving boundary conditions for a hydraulic fracture. *Int. J. Eng. Sci.*, 84:147–155.
- Dobson, P. and Houseworth, J. (2013). Inventory of Shale Formations in the US, Including Geologic, Hydrological, and Mechanical Characteristics. Technical report, Lawrence Berkeley National Lab. (LBNL), Berkeley, CA (United States).
- Dontsov, E. and Peirce, A. P. (2015a). A non-singular integral equation formulation to analyse multiscale behaviour in semi-infinite hydraulic fractures. *J. Fluid Mech.*, 781:R1.
- Dontsov, E. and Peirce, A. P. (2017). A multiscale implicit level set algorithm (ILSA) to model hydraulic fracture propagation incorporating combined viscous, toughness, and leak-off asymptotics. *Comput. Methods Appl. Mech. Eng.*, 313:53–84.

Bibliography

- Dontsov, E. V. (2016). An approximate solution for a penny-shaped hydraulic fracture that accounts for fracture toughness, fluid viscosity and leak-off. *R. Soc. Open Sci.*, 3(12):160737.
- Dontsov, E. V. (2017). An approximate solution for a plane strain hydraulic fracture that accounts for fracture toughness, fluid viscosity, and leak-off. *Int. J. Fract.*, pages 1–17.
- Dontsov, E. V. (2021). An efficient computation of leak-off induced poroelastic stress for a hydraulic fracture. *J. Mech. Phys. Solids.*, 147:104246.
- Dontsov, E. V. and Peirce, A. P. (2015b). An enhanced pseudo-3D model for hydraulic fracturing accounting for viscous height growth, non-local elasticity, and lateral toughness. *Eng. Fract. Mech.*, 142:116–139.
- Economides, M. J. and Nolte, K. G. (2000). *Reservoir Stimulation*. John Wiley & Sons.
- Entov, V. M., Chekhonin, E. M., Detournay, E., and Thiercelin, M. (2007). Fracture Propagation in High-Permeability Rocks: The Key Influence of Fracture Tip Behavior. In *SPE Hydraulic Fracturing Technology Conference and Exhibition*, volume All Days of SPE Hydraulic Fracturing Technology Conference and Exhibition. onePetro.
- Erdogan, F., Gupta, G. D., and Cook, T. (1973). Numerical solution of singular integral equations. In *Methods of analysis and solutions of crack problems*, pages 368–425. Springer.
- Etiope, G., Schoell, M., and Hosgörmez, H. (2011). Abiotic methane flux from the chimaera seep and tekirova ophiolites (turkey): Understanding gas exhalation from low temperature serpentinization and implications for mars. *Earth Planet. Sci. Lett.*, 310(1):96–104.
- Froger, J. L., Fukushima, Y., Briole, P., Staudacher, T., Souriot, T., and Villeneuve, N. (2004). The deformation field of the august 2003 eruption at piton de la fournaise, reunion island, mapped by asar interferometry. *Geophys. Res. Lett.*, 31(14).
- Fukushima, Y., Cayol, V., and Durand, P. (2005). Finding realistic dike models from interferometric synthetic aperture radar data: The february 2000 eruption at piton de la fournaise. *J. Geophys. Res.: Solid Earth*, 110(B3).
- Fukushima, Y., Cayol, V., Durand, P., and Massonnet, D. (2010). Evolution of magma conduits during the 1998–2000 eruptions of piton de la fournaise volcano, réunion island. *J. Geophys. Res.: Solid Earth*, 115(B10).
- Furst, S., Maccaferri, F., and Pinel, V. (2023). Modeling the shape and velocity of magmatic intrusions, a new numerical approach. *J. Geophys. Res.: Solid Earth*, 128(3):e2022JB025697.
- Gao, Y. and Detournay, E. (2020). A poroelastic model for laboratory hydraulic fracturing of weak permeable rock. *J. Mech. Phys. Solids.*, 143:104090.
- Gao, Y. and Detournay, E. (2021). Fracture toughness interpretation from breakdown pressure. *Eng. Fract. Mech.*, 243:107518.

- Garagash, D. and Detournay, E. (1998). Similarity solution of a semi-infinite fluid-driven fracture in a linear elastic solid. *Comptes Rendus de l'Académie des Sciences - Series IIB - Mechanics-Physics-Chemistry-Astronomy*, 326(5):285–292.
- Garagash, D. I. (2000). Hydraulic fracture propagation in elastic rock with large toughness. In Girard, J., Liebman, M., Breeds, C., and Doe, T., editors, *Rock Around the Rim [Proceedings of the 4th North American Rock Mechanics Symposium, Seattle]*, pages 221–228. Rotterdam, Balkema.
- Garagash, D. I. (2006a). Plane-strain propagation of a fluid-driven fracture during injection and shut-in: asymptotics of large toughness. *Eng. Fract. Mech.*, 73(4):456–481.
- Garagash, D. I. (2006b). Propagation of a plane-strain fluid-driven fracture with a fluid lag: early-time solution. *Int. J. Solids Struct.*, 43:5811–5835.
- Garagash, D. I. (2009). Scaling of physical processes in fluid-driven fracture: perspective from the tip. In Borodich, F., editor, *IUTAM Symposium on Scaling in Solid Mechanics*, volume 10 of *IUTAM Bookseries*, pages 91–100, Dordrecht. Springer.
- Garagash, D. I. (2023). Propagation of Elongated Fluid-Driven Fractures. *In preparation*.
- Garagash, D. I. and Detournay, E. (2000). The tip region of a fluid-driven fracture in an elastic medium. *J. Appl. Mech.*, 67:183–192.
- Garagash, D. I., Detournay, E., and Adachi, J. I. (2011). Multiscale tip asymptotics in hydraulic fracture with leak-off. *J. Fluid Mech.*, 669:260–297.
- Garagash, D. I. and Germanovich, L. N. (2014). Gravity driven hydraulic fracture with finite breadth. In Bajaj, A., Zavattieri, P., Koslowski, M., and Siegmund, T., editors, *Proceedings of the Society of Engineering Science 51st Annual Technical Meeting*. West Lafayette: Purdue University Libraries Scholarly Publishing Service.
- Garagash, D. I. and Germanovich, L. N. (2022). Notes on propagation of 3d buoyant fluid-driven cracks. arXiv:2208.14629.
- Geertsma, J. and De Klerk, F. (1969). A rapid method of predicting width and extent of hydraulically induced fractures. *J. Pet. Technol*, 21(12):1571–1581.
- Germanovich, L. N., Garagash, D. I., Murdoch, L., and M., R. (2014). Gravity-driven hydraulic fractures. In *AGU Fall Meeting Abstracts*, volume 2014, pages H53C–0874.
- Germanovich, L. N. and Murdoch, L. C. (2010). Injection of solids to lift coastal areas. *Proc. R. Soc. A: Math. Phys. Eng. Sci.*, 466(2123):3225–3252.
- Gíslason, S. R., Sigurdardóttir, H., Aradóttir, E. S., and Oelkers, E. H. (2018). A brief history of carbfix: Challenges and victories of the project's pilot phase. *Energy Procedia*, 146:103–114. Carbon in natural and engineered processes: Selected contributions from the 2018 International Carbon Conference.

Bibliography

- Gordeliy, E. and Detournay, E. (2011). Displacement discontinuity method for modeling axisymmetric cracks in an elastic half-space. *Int. J. Sol. Struct.*, 48(19):2614–2629.
- Green, G. (1854). An Essay on the Application of mathematical Analysis to the theories of Electricity and Magnetism. *Journal für die reine und angewandte Mathematik (Crelles Journal)*, 1854(47):161–221.
- Griffith, A. A. (1921). VI. The phenomena of rupture and flow in solids. *Philosophical transactions of the royal society of london. Series A, containing papers of a mathematical or physical character*, 221(582-593):163–198.
- Gu, H. and Leung, K. H. (1993). 3d numerical simulation of hydraulic fracture closure with application to minifracture analysis. *J. Pet. Technol*, 45(03):206–255.
- Guéguen, Y. and Palciauskas, V. (1994). Introduction to the Physics of Rock.
- Guha Roy, D., Singh, T. N., Kodikara, J., and Talukdar, M. (2017). Correlating the Mechanical and Physical Properties with Mode-I Fracture Toughness of Rocks. *Rock Mech. Rock Eng.*, 50(7):1941–1946.
- Guillot, D. and Dunand, A. (1985). Rheological Characterization of Fracturing Fluids by Using Laser Anemometry. *Soc. Pet. Eng. J.*, 25(01):39–45.
- Hagen, G. H. L. (1839). Über die Bewegung des Wassers in engen cylindrischen Röhren. In *Poggendorf's Annalen der Physik und Chemie*, volume 46, pages 423–42.
- Haimson, B. and Fairhurst, C. (1969). In-situ stress determination at great depth by means of hydraulic fracturing. In *The 11th U.S. Symposium on Rock Mechanics (USRMS)*, pages 559–584, Berkeley, Ca.
- Haimson, B. C. and Cornet, F. H. (2003). Isrm suggested methods for rock stress estimation-part 3: Hydraulic fracturing (hf) and/or hydraulic testing of pre-existing fractures (htpf). *Int. J. Rock Mech. Min. Sci.*, 40(7-8):1011–1020.
- Hall, H. N. (1953). Compressibility of Reservoir Rocks. *J. Pet. Technol*, 5(01):17–19.
- Heidbach, O., Rajabi, M., Cui, X., Fuchs, K., Müller, B., Reinecker, J., Reiter, K., Tingay, M., Wenzel, F., Xie, F., Ziegler, M. O., Zoback, M.-L., and Zoback, M. (2018). The World Stress Map database release 2016: Crustal stress pattern across scales. *Tectonophysics*, 744:484–498.
- Heimisson, E. R., Hooper, A., and Sigmundsson, F. (2015). Forecasting the path of a laterally propagating dike. *J. Geophys. Res.: Solid Earth*, 120(12):8774–8792.
- Heimpel, M. and Olson, P. (1994). Chapter 10 Buoyancy-Driven Fracture and Magma Transport through the Lithosphere: Models and Experiments. In Ryan, M. P., editor, *Magmatic Systems*, volume 57 of *International Geophysics*, pages 223–240. Academic Press.

- Hellström, G. and Larson, S. (2001). Seasonal thermal energy storage –the hydrock concept. *Bull. Eng. Geol. Environ.*, 60(2):145–156.
- Hills, D. A., Kelly, P. A., Dai, D. N., and Korsunsky, A. M. (1996). *Solution of crack problems: the distributed dislocation technique*, volume 44 of *Solid Mechanics and its Applications*. Kluwer Academic Publ., Dordrecht.
- Howard, G. C. and Fast, C. R. (1957). Optimum fluid characteristics for fracture extension. *Drilling and Production Practice*, pages 261–270.
- Howarth, R. W. and Jacobson, M. Z. (2021). How green is blue hydrogen? *Energy Sci. Eng.*, 9(10):1676–1687.
- Hubbert, M. K. and Willis, D. (1957). Mechanics of hydraulic fracturing. *Trans. Am. Inst. Min. Eng.*, 210:153–158.
- Huppert, H. E. and Sparks, R. S. J. (1981). The fluid dynamics of a basaltic magma chamber replenished by influx of hot, dense ultrabasic magma. *Contrib. Mineral. Petrol.*, 75(3):279–289.
- Huttrer, G. W. (2021). Geothermal Power Generation in the World 2015-2020 Update Report. In *World Geothermal Congress 2020+1*.
- Ioakimidis, N. and Theocaris, P. (1980). The practical evaluation of stress intensity factors at semi-infinite crack tips. *Eng. Fract. Mech.*, 13(1):31 – 42.
- Irwin, G. R. (1957). Analysis of Stresses and Strains Near the End of a Crack Traversing a Plate. *J. Appl. Mech.*, 24(3):361–364.
- Ito, G. and Martel, S. J. (2002). Focusing of magma in the upper mantle through dike interaction. *J. Geophys. Res.*, 107(B10):2223.
- Jaeger, J. C., Cook, N. G. W., and Zimmerman, R. W. (2007). *Fundamentals of Rock Mechanics*. Blackwell Publishing, 4 edition.
- Janiszewski, M., Kopaly, A., Honkonen, M., Kukkonen, I., Uotinen, L., Siren, T., and Rinne, M. (2016). Feasibility of underground seasonal storage of solar heat in finland. In Jian, Z., editor, *International Conference on Geo-mechanics, Geo-energy and Geo-resources: Conference Proceedings*, volume 236 of *International Conference on Geo-mechanics, Geo-energy and Geo-resources: Conference Proceedings*, pages 959 – 965. Monash University.
- Jeffrey, R. G., Bungler, A. P., Lecampion, B., Zhang, X., Chen, Z., van As, A., Allison, D., De Beer, W., Dudley, J., Siebrits, E., et al. (2009). Measuring hydraulic fracture growth in naturally fractured rock. In *SPE Annual Technical Conference and Exhibition*. SPE 124919.
- Jeffrey, R. G., Chen, Z., Mills, K. W., and Pegg, S. (2013). Monitoring and Measuring Hydraulic Fracturing Growth During Preconditioning of a Roof Rock over a Coal Longwall Panel. In *ISRM International Conference for Effective and Sustainable Hydraulic Fracturing*, number

Bibliography

- 019 in ISRM-ICHF-2013-019, page 22, Brisbane, Australia. ISRM, International Society for Rock Mechanics and Rock Engineering.
- Jiang, S., Mokhtari, M., Borrok, D., and Lee, J. (2018). Improving the total organic carbon estimation of the eagle ford shale with density logs by considering the effect of pyrite. *Minerals*, 8(4).
- Kanin, E. A., Dontsov, E. V., Garagash, D. I., and Osipov, A. A. (2020). A radial hydraulic fracture with pressure-dependent leak-off. *J. Mech. Phys. Solids.*, 143:104062.
- Kanin, E. A., Garagash, D. I., and Osipov, A. A. (2019). The near-tip region of a hydraulic fracture with pressure-dependent leak-off and leak-in. *J. Mech. Phys. Solids.*
- Kanninen, M. F. and Popelar, C. H. (1985). *Advanced Fracture Mechanics*, volume 15 of *The Oxford Engineering Science Series*. Oxford University Press, Oxford UK.
- Kear, J., White, J., Bunger, A. P., Jeffrey, R., and Hessami, M.-A. (2013). Three dimensional forms of closely-spaced hydraulic fractures. In Bunger, A. P., McLennan, J., and Jeffrey, R., editors, *Effective and Sustainable Hydraulic Fracturing*, chapter 34. IntechOpen, Rijeka.
- Kefi, S., Lee, J., Pope, T., Sullivan, P., Nelson, E., Hernandez, A., Olsen, T., Parlar, M., Powers, B., and Roy, A. (2004). Expanding applications for viscoelastic surfactants. *Oilfield Rev*, 16(4):10–23.
- Kelemen, P., Aines, R., Bennett, E., Benson, S., Carter, E., Coggon, J., de Obeso, J., Evans, O., Gadikota, G., Dipple, G., Godard, M., Harris, M., Higgins, J., Johnson, K., Kourim, E., Lafay, R., Lambart, S., Manning, C., Matter, J., Michibayashi, K., Morishita, T., Noël, J., Okazaki, K., Renforth, P., Robinson, B., Savage, H., Skarbek, R., Spiegelman, M., Takazawa, E., Teagle, D., Urai, J., and Wilcox, J. (2018). In situ carbon mineralization in ultramafic rocks: Natural processes and possible engineered methods. *Energy Procedia*, 146:92–102. Carbon in natural and engineered processes: Selected contributions from the 2018 International Carbon Conference.
- Kelemen, P. B., Matter, J., Streit, E. E., Rudge, J. F., Curry, W. B., and Blusztajn, J. (2011). Rates and mechanisms of mineral carbonation in peridotite: Natural processes and recipes for enhanced, in situ CO₂ capture and storage. *Annu. Rev. Earth Planet. Sci.*, 39(1):545–576.
- Khrstianovic, S. and Zheltov, Y. (1955). Formation of vertical fractures by means of highly viscous fluids. In *Proc., 4th World Petroleum Congress*, volume II, pages 579–586, Rome.
- Kiruja, J., Guinto, H., Ramirez, M., Bona, P., van den Boomen, R., Colvin, A., van Nieuwenhuijzen, A., and van der Voet, E. (2023). Global geothermal market and technology assessment. Technical report, IRENA and IGA.
- Kovalyshen, Y. (2010). *Fluid-Driven Fracture in Poroelastic Medium*. PhD thesis, University of Minnesota, Minneapolis, MN.

- Lai, C., Zheng, Z., Dressaire, E., Wexler, J. S., and Stone, H. A. (2015). Experimental study on penny-shaped fluid-driven cracks in an elastic matrix. *Proc. R. Soc. A*, 471(2182):20150255.
- Lancellotta, R., Flora, A., and Viggiani, C. (2017). *Geotechnics and Heritage: Historic Towers*. CRC Press.
- Larson, E. E. and Strangway, D. W. (1969). Magnetization of the spanish peaks dike swarm, colorado, and shiprock dike, new mexico. *J. Geophys. Res. (1896-1977)*, 74(6):1505–1514.
- Larsson, S. Aa. Fridh, B. and Haag, O. (1985). Hydrock - heat storage in bedrock. construction of heat exchanger surfaces by means of hydraulic fracturing; the hydrock-method.
- Lebedys, A., Akande, D., Coënt, N., Elhassan, N., Escamilla, G., Arkhipova, I., and Whiteman, A. (2022). Renewable capacity statistics 2022. Technical report, IRENA.
- Lecampion, B., Bunger, A. P., and Zhang, X. (2018). Numerical methods for hydraulic fracture propagation: A review of recent trends. *J. Nat. Gas Eng.*, 49:66–83.
- Lecampion, B. and Desroches, J. (2015). Simultaneous initiation and growth of multiple radial hydraulic fractures from a horizontal wellbore. *J. Mech. Phys. Solids.*, 82:235–258.
- Lecampion, B., Desroches, J., Jeffrey, R., Bunger, A. P., and Burghardt, J. (2015). Initiation versus breakdown pressure of transverse hydraulic fracture: theory and experiments. In *13th ISRM International Symposium on Rock Mechanics*, Montreal.
- Lecampion, B., Desroches, J., Jeffrey, R. G., and Bunger, A. P. (2017). Experiments versus theory for the initiation and propagation of radial hydraulic fractures in low permeability materials. *J. Geophys. Res. Solid Earth*, 122:1239–1263.
- Lecampion, B. and Detournay, E. (2007). An implicit algorithm for the propagation of a hydraulic fracture with a fluid lag. *Comput. Methods Appl. Mech. Eng.*, 196:4863–4880.
- Lecampion, B. and Zia, H. (2019). Slickwater hydraulic fracture propagation: near-tip and radial geometry solutions. *J. Fluid Mech.*, 880:514–550.
- Lenoach, B. (1995). The crack tip solution for hydraulic fracturing in a permeable solid. *J. Mech. Phys. Solids.*, 43(7):1025–1043.
- Lhomme, T. (2005). *Initiation of Hydraulic Fractures in Natural Sandstones*. PhD thesis, Delft University.
- Lister, J. R. (1990a). Buoyancy-driven fluid fracture: similarity solutions for the horizontal and vertical propagation of fluid-filled cracks. *J. Fluid Mech.*, 217:213–239.
- Lister, J. R. (1990b). Buoyancy-driven fluid fracture: the effects of material toughness and of low-viscosity precursors. *J. Fluid Mech.*, 210:263–280.
- Lister, J. R. and Kerr, R. C. (1991). Fluid-mechanical models of crack propagation and their application to magma transport in dykes. *J. Geophys. Res. Solid Earth*, 96(B6):10049–10077.

Bibliography

- Liu, D. and Lecampion, B. (2022a). Laboratory investigation of hydraulic fracture growth in zimbabwe gabbro. *J. Geophys. Res.: Solid Earth*, 127(11):e2022JB025678. e2022JB025678 2022JB025678.
- Liu, D. and Lecampion, B. (2022b). *Measurements of the Evolution of the Fluid Lag in Laboratory Hydraulic Fracture Experiments in Rocks*, chapter 2, pages 11–23. John Wiley & Sons, Ltd.
- Liu, D., Lecampion, B., and Blum, T. (2020). Time-lapse reconstruction of the fracture front from diffracted waves arrivals in laboratory hydraulic fracture experiments. *Geophys. J. Int.*, 223(1):180–196.
- Liu, D., Lecampion, B., and Garagash, D. I. (2019). Propagation of a fluid-driven fracture with fracture length dependent apparent toughness. *Eng. Frac. Mech.*, 220:106616.
- Lu, G., Gordeliy, E., Prioul, R., and Bunger, A. (2017). Modeling initiation and propagation of a hydraulic fracture under subcritical conditions. *Comput. Methods Appl. Mech. Eng.*, 318:61 – 91.
- Luo, X. R., Wang, S. Z., Jing, Z. F., and Wang, Z. G. (2014). Experimental Research on Rheological Properties of Slick Water Mixed with CO₂ System. In *Materials, Manufacturing Engineering and Information Technology*, volume 910 of *Adv. Mat. Res.*, pages 95–100. Trans Tech Publications Ltd.
- Maccaferri, F., Bonafede, M., and Rivalta, E. (2010). A numerical model of dyke propagation in layered elastic media. *Geophys. J. Int.*, 180(3):1107–1123.
- Maccaferri, F., Bonafede, M., and Rivalta, E. (2011). A quantitative study of the mechanisms governing dike propagation, dike arrest and sill formation. *J. Volcanol. Geotherm. Res.*, 208(1):39–50.
- MacDonald, R., Wilson, L., Thorpe, R. S., and Martin, A. (1988). Emplacement of the Cleveland Dyke: Evidence from Geochemistry, Mineralogy, and Physical Modelling. *J. Petrol.*, 29(3):559–583.
- Madyarova, M. (2003). Fluid-driven penny-shaped fracture in permeable rock. Master's thesis, University of Minnesota, Minneapolis, MN, USA.
- Massonnet, C. (1965). *Numerical use of integral procedure*, pages 198–235. Wiley, New York.
- Mayerhofer, M. J., Walker, R. N. J., Urbancic, T., and Rutledge, J. T. (2000). East Texas Hydraulic Fracture Imaging Project: Measuring Hydraulic Fracture Growth of Conventional Sandfracs and Waterfracs. *Proc. - SPE Annu. Tech. Conf. Exhib.*, All Days:SPE–63034–MS.
- McGrail, B. P., Schaef, H. T., Spane, F. A., Horner, J. A., Owen, A. T., Cliff, J. B., Qafoku, O., Thompson, C. J., and Sullivan, E. C. (2017). Wallula basalt pilot demonstration project: Post-injection results and conclusions. *Energy Procedia*, 114:5783–5790. 13th International

- Conference on Greenhouse Gas Control Technologies, GHGT-13, 14-18 November 2016, Lausanne, Switzerland.
- Medlin, W. and Masse, L. (1984). Laboratory experiments in fracture propagation. *SPE Journal*, 24(03):256–268.
- Mogilevskaya, S. and Nikolskiy, D. (2014). The use of complex integral representations for analytical evaluation of three-dimensional bem integrals—potential and elasticity problems. *Q. J. Mech. Appl. Math.*, 67(3):505–523.
- Mogilevskaya, S. G. (2014). Lost in translation: Crack problems in different languages. *Int. J. Solids Struct.*, 51(25):4492–4503.
- Mohammadnejad, T. and Andrade, J. E. (2016). Numerical modeling of hydraulic fracture propagation, closure and reopening using XFEM with application to in-situ stress estimation. *Int. J. Numer. Anal. Methods Geomech.*, 40(15):2033–2060.
- Moukhtari, F. E. and Lecampion, B. (2018). A semi-infinite hydraulic fracture driven by a shear thinning fluid. *J. Fluid Mech.*, 838:573–605.
- Moukhtari, F. E., Lecampion, B., and Zia, H. (2020). Planar hydraulic fracture growth perpendicular to the isotropy plane in a transversely isotropic material. *J. Mech. Phys. Sol.*, 137:103878.
- Nara, Y., Morimoto, K., Hiroyoshi, N., Yoneda, T., Kaneko, K., and Benson, P. M. (2012). Influence of relative humidity on fracture toughness of rock: Implications for subcritical crack growth. *Int. J. Solids Struct.*, 49(18):2471–2481.
- Noël, C., Baud, P., and Violay, M. (2021). Effect of water on sandstone’s fracture toughness and frictional parameters: Brittle strength constraints. *Int. J. Rock Mech. Min. Sci.*, 147:104916.
- Nolte, K. G. (1979). Determination of fracture parameters from fracturing pressure decline. In *Proc. SPE Annual Technical Conference and Exhibition, Las Vegas*. SPE 8341.
- Nordgren, R. P. (1972). Propagation of vertical hydraulic fractures. *Soc. Pet. Eng. J.*, 253:306–314.
- O’Keeffe, N. J., Huppert, H. E., and Linden, P. F. (2018). Experimental exploration of fluid-driven cracks in brittle hydrogels. *J. Fluid Mech.*, 844:435–458.
- Osselin, F., Soullain, C., Fauguerolles, C., Gaucher, E. C., Scaillet, B., and Pichavant, M. (2022). Orange hydrogen is the new green. *Nature Geoscience*, 15(10):765–769.
- Papanastasiou, P. (2000). Hydraulic fracture closure in a pressure-sensitive elastoplastic medium. *Int. J. Fract.*, 103(2):149–161.
- Pattyn, F. (2018). The paradigm shift in antarctic ice sheet modelling. *Nature Communications*, 9(1):2728.

Bibliography

- Pedersen, R., Sigmundsson, F., and Einarsson, P. (2007). Controlling factors on earthquake swarms associated with magmatic intrusions; constraints from iceland. *J. Volcanol. Geotherm. Res.*, 162(1):73–80.
- Peirce, A. P. (2015). Modeling multi-scale processes in hydraulic fracture propagation using the implicit level set algorithm. *Comput. Methods Appl. Mech. Eng.*, 283:881–908.
- Peirce, A. P. (2016). Implicit level set algorithms for modelling hydraulic fracture propagation. *Philos. Trans. A Math. Phys. Eng. Sci.*, 374(2078):20150423.
- Peirce, A. P. (2022). The arrest and recession dynamics of a deflating radial hydraulic fracture in a permeable elastic medium. *J. Mech. Phys. Solids*, 166:104926.
- Peirce, A. P. and Detournay, E. (2008). An implicit level set method for modeling hydraulically driven fractures. *Comput. Methods Appl. Mech. Eng.*, 197(33-40):2858–2885.
- Peirce, A. P. and Detournay, E. (2022). Multiscale tip asymptotics for a deflating hydraulic fracture with leak-off. *J. Fluid Mech.*, 947:A17.
- Peltier, A., Staudacher, T., and Bachèlery, P. (2007). Constraints on magma transfers and structures involved in the 2003 activity at piton de la fournaise from displacement data. *J. Geophys. Res.: Solid Earth*, 112(B3).
- Perkins, T. K. and Kern, L. R. (1961). Widths of hydraulic fractures. *J. Pet. Technol*, 222:937–949.
- Peruzzo, C. (2023). *Three-dimensional hydraulic fracture propagation in homogeneous and heterogeneous media*. PhD thesis, EPFL thesis # 10105, Lausanne. Available at <http://infoscience.epfl.ch/record/302100>.
- Peruzzo, C. and Lecampion, B. (2023a). How long a planar 3D hydraulic fracture remains contained by two layers of larger toughness. *In preparation*.
- Peruzzo, C. and Lecampion, B. (2023b). The Energy Balance of Fluid Driven Fractures. *In preparation*.
- Peruzzo, C., Lecampion, B., and Zia, H. (2021). Improved fracture front reconstruction in planar 3D fluid driven fractures simulation. In *14th World Congress on Computational Mechanics (WCCM XIV) and 8th European Congress on Computational Methods in Applied Sciences and Engineering (ECCOMAS 2020)*.
- Petford, N., Lister, J. R., and Kerr, R. C. (1994). The ascent of felsic magmas in dykes. *Lithos*, 32(1):161–168.
- Pezzulli, E. (2022). *Simulating hydraulic fracture propagation in crustal processes*. PhD thesis, ETH Zürich.
- Poiseuille, J. L. M. (1838). Ecoulement des liquides. In *Extraits des Proces-Vérbaux des Séances Pendant l'Année 1838*, pages 1–3, 77–81, Paris. Société Philomatique de Paris.

- Prinzhofer, A., Tahara Cissé, C. S., and Diallo, A. B. (2018). Discovery of a large accumulation of natural hydrogen in bourakebougou (mali). *Int. J. Hydrog. Energy*, 43(42):19315–19326.
- Ramstad, R. K., Hilmo, B. O., Brattli, B., and Skarphagen, H. (2007). Ground source energy in crystalline bedrock-increased energy extraction using hydraulic fracturing in boreholes. *Bull. Eng. Geol. Environ.*, 66(4):493–503.
- Reches, Z. and Fink, J. (1988). The mechanism of intrusion of the inyo dike, long valley caldera, california. *J. Geophys. Res.: Solid Earth*, 93(B5):4321–4334.
- Rice, J. R. (1968a). A path independent integral and the approximate analysis of strain concentration by notches and cracks. *J. Appl. Mech.*, 35:379–386.
- Rice, J. R. (1968b). Mathematical analysis in the mechanics of fracture. In H. Liebowitz, editor, *Fracture: An Advanced Treatise*, volume 2, chapter 3, pages 191–311.
- Rice, J. R. (1972). Some remarks on elastic crack-tip stress fields. *Int. J. Sol. Struct.*, 8:751–758.
- Ripepi, N., Gill, B., Chen, C. and Karmis, M., Keles, C., and Schlosser, C. (2023). Field Laboratory for Emerging Stacked Unconventional Plays in Central Appalachia. Technical report, Virginia Center for Coal and Energy Research, USDOE, United States.
- Rivalta, E., Böttinger, M., and Dahm, T. (2005). Buoyancy-driven fracture ascent: Experiments in layered gelatine. *J. Volcanol. Geotherm. Res.*, 144(1):273–285.
- Rivalta, E., Taisne, B., Bunger, A. P., and Katz, R. F. (2015). A review of mechanical models of dike propagation: Schools of thought, results and future directions. *Tectonophysics*, 638:1–42.
- Roper, S. M. and Lister, J. R. (2005). Buoyancy-driven crack propagation from an over-pressured source. *J. Fluid Mech.*, 536:79–98.
- Roper, S. M. and Lister, J. R. (2007). Buoyancy-driven crack propagation: the limit of large fracture toughness. *J. Fluid Mech.*, 580:359–380.
- Roult, G., Peltier, A., Taisne, B., Staudacher, T., Ferrazzini, V., and Di Muro, A. (2012). A new comprehensive classification of the piton de la fournaise activity spanning the 1985–2010 period. search and analysis of short-term precursors from a broad-band seismological station. *J. Volcanol. Geotherm. Res.*, 241-242:78–104.
- Rubin, A. M. (1993). Tensile fracture of rock at high confining pressure: implications for dike propagation. *J. Geophys. Res.: Solid Earth*, 98(B9):15919–15935.
- Ruddy, I., Andersen, M. A., Pattillo, P. D., Bishlawi, M., and Foged, N. (1989). Rock Compressibility, Compaction, and Subsidence in a High-Porosity Chalk Reservoir: A Case Study of Valhall Field. *J. Pet. Technol.*, 41(07):741–746.

Bibliography

- Rutledge, J. T., Phillips, W. S., and Mayerhofer, M. J. (2004). Faulting induced by forced fluid injection and fluid flow forced by faulting: An interpretation of hydraulic-fracture microseismicity, carthage cotton valley gas field, texas. *Bulletin of the Seismological Society of America*, 94(5):1817–1830.
- Salimzadeh, S., Zimmerman, R. W., and Khalili, N. (2020). Gravity Hydraulic Fracturing: A Method to Create Self-Driven Fractures. *Geophys. Res. Lett.*, 47(20):e2020GL087563.
- Savic, M. (1995). *Ultrasonic scattering from a hydraulic fracture: Theory, computation and experiment*. PhD thesis, Delft University of Technology.
- Savitski, A. and Detournay, E. (2002). Propagation of a penny-shaped fluid-driven fracture in an impermeable rock: asymptotic solutions. *Int. J. Solids Struct.*, 39(26):6311–6337.
- Schmidt, H., Wright, S., Mauroner, C., Lau, G., Hill, B., Zhou, G., and Bunger, A. P. (2023). Geomechanical Pumped Storage in Hydraulic Fractures. In *SPE Hydraulic Fracturing Technology Conference and Exhibition*, volume Day 3 Thu, February 02, 2023 of *SPE Hydraulic Fracturing Technology Conference and Exhibition*.
- Schwartz, B., Elsworth, D., and Marone, C. (2019). Relationships between mechanical and transport properties in Marcellus shale. *Int. J. Rock Mech. Min. Sci.*, 119:205–210.
- Senseny, P. E. and Pfeifle, T. W. (1984). Fracture Toughness Of Sandstones And Shales. In *U.S. Rock Mechanics/Geomechanics Symposium*, volume All Days of *U.S. Rock Mechanics/Geomechanics Symposium*. ARMA-84-0390.
- Sethian, J. A. (1999). *Level set methods and fast marching methods: evolving interfaces in computational geometry, fluid mechanics, computer vision, and materials science*, volume 3. Cambridge university press.
- Settari, A. and Cleary, M. P. (1984). Three-dimensional simulation of hydraulic fracturing. *J. Pet. Technol.*, 36(07):1177–1190.
- Sigmundsson, F., Hooper, A., Hreinsdóttir, S., Vogfjörð, K. S., Ófeigsson, B. G., Heimisson, E. R., Dumont, S., Parks, M. and Spaans, K., Gudmundsson, G. B., Drouin, V., Árnadóttir, T., Jónsdóttir, K., Gudmundsson, M. T., Högnadóttir, T., Fridriksdóttir, H. M., Hensch, M., Einarsson, P., Magnússon, E., Samsonov, S., Brandsdóttir, B., White, R. S., Ágústsdóttir, T., Greenfield, T., Green, R. G., Hjartardóttir, Á. R., Pedersen, R., Bennett, R. A., Geirsson, H., La Femina, P. C., Björnsson, H., Pálsson, F. and Sturkell, E., Bean, C. J., Möllhoff, M., Braidon, A. K., and Eibl, E. P. S. (2015). Segmented lateral dyke growth in a rifting event at bárðarbunga volcanic system, iceland. *Nature*, 517(7533):191–195.
- Simonson, E. R., Abou-Sayed, A. S., and Clifton, R. J. (1978). Containment of massive hydraulic fractures. *SPE Journal*, 18(1):27–32.
- Smitarello, D. (2019). *Propagation des intrusions basaltiques*. PhD thesis, Université Grenoble Alpes.

- Smith, M. B. and Montgomery, C. T. (2015). *Hydraulic Fracturing*. CRC press.
- Smittarello, D., Cayol, V., Pinel, V., Peltier, A., Froger, J.-L., and Ferrazzini, V. (2019). Magma propagation at piton de la fournaise from joint inversion of insar and gnss. *J. Geophys. Res.: Solid Earth*, 124(2):1361–1387.
- Smittarello, D., Pinel, V., Maccaferri, F., Furst, S., Rivalta, E., and Cayol, V. (2021). Characterizing the physical properties of gelatin, a classic analog for the brittle elastic crust, insight from numerical modeling. *Tectonophysics*, 812:228901.
- Snæbjörnsdóttir, S. Ó., Sigfússon, B., Marieni, C., Goldberg, D., Gislason, S. R., and Oelkers, E. H. (2020). Carbon dioxide storage through mineral carbonation. *Nat. Rev. Earth Environ.*, 1(2):90–102.
- Sneddon, I. N. (1946). The distribution of stress in the neighbourhood of a crack in an elastic solid. *Proc. Roy. Soc. series A*, 187(1009):229–260.
- Sneddon, I. N. (1951). *Fourier Transforms*. McGraw-Hill, New York NY.
- Spence, D. A. and Sharp, P. W. (1985). Self-similar solutions for elastohydrodynamic cavity flow. *Proc. R. Soc. A: Math. Phys. Eng. Sci.*, 400(1819):289–313.
- Spence, D. A., Sharp, P. W., and Turcotte, D. L. (1987). Buoyancy-driven crack propagation: a mechanism for magma migration. *J. Fluid Mech.*, 174:135–153.
- Spence, D. A. and Turcotte, D. L. (1985). Magma-driven propagation of cracks. *J. Geophys. Res. Solid Earth*, 90(B1):575–580.
- Spence, D. A. and Turcotte, D. L. (1990). Buoyancy-driven magma fracture: A mechanism for ascent through the lithosphere and the emplacement of diamonds. *J. Geophys. Res. Solid Earth*, 95(B4):5133–5139.
- Spera, F. J., Borgia, A., Strimple, J., and Feigenson, M. (1988). Rheology of melts and magmatic suspensions: 1. design and calibration of concentric cylinder viscometer with application to rhyolitic magma. *J. Geophys. Res.: Solid Earth*, 93(B9):10273–10294.
- Stefan, J. (1891). Über die Theorie der Eisbildung, insbesondere über die Eisbildung im Polarmeere. *Annalen der Physik*, 278(2):269–286.
- Stringfellow, W. T. and Dobson, P. F. (2020). Retrospective on recent doe-funded studies concerning the extraction of rare earth elements & lithium from geothermal brines (final report). Technical report.
- Stringfellow, W. T. and Dobson, P. F. (2021). Technology for the recovery of lithium from geothermal brines. *Energies*, 14(20).
- Tada, H., P.C., P., and Irwin, G. (2000). *The Stress Analysis of Cracks Handbook*. ASME Press, 3rd edition.

Bibliography

- Taisne, B. and Tait, S. (2009). Eruption versus intrusion? Arrest of propagation of constant volume, buoyant, liquid-filled cracks in an elastic, brittle host. *J. Geophys. Res. Solid Earth*, 114(B6).
- Taisne, B. and Tait, S. (2011). Effect of solidification on a propagating dike. *J. Geophys. Res.: Solid Earth*, 116(B1).
- Taisne, B., Tait, S., and Jaupart, C. (2011). Conditions for the arrest of a vertical propagating dyke. *Bull. Volcanol.*, 73(2):191–204.
- Tanikella, S. S. and Dressaire, E. (2022). Axisymmetric displacement flows in fluid-driven fractures. *J. Fluid Mech.*, 953:A36.
- Tanikella, S. S., Sigallon, M. C., and Dressaire, E. (2023). Dynamics of fluid-driven fractures in the viscous-dominated regime. *Proc. R. Soc. A: Math. Phys. Eng. Sci.*, 479(2271):20220460.
- Ting, T. C.-T. (1996). *Anisotropic elasticity: theory and applications*. Number 45. Oxford University Press on Demand.
- Tsai, V. and Rice, J. R. (2010). A model for turbulent hydraulic fracture and application to crack propagation at glacier beds. *J. Geoph. Res. - Earth Surface*.
- Turcotte, D. L. and Schubert, G. (2002). *Geodynamics*. Cambridge University Press, second edition.
- van Dam, D. B., de Pater, C. J., and Romijn, R. (2000). Analysis of hydraulic fracture closure in laboratory experiments. *SPE Production & Facilities*, 15(03):151–158.
- van Eijs, R. M. H. E. and van der Wal, O. (2017). Field-wide reservoir compressibility estimation through inversion of subsidence data above the Groningen gas field. *Netherlands Journal of Geosciences*, 96(5):117–129.
- Vandamme, L. and Curran, J. H. (1989). A three-dimensional hydraulic fracturing simulator. *Int. J. Numer. Methods Eng.*, 28:909–927.
- Vernik, L. (1994). Hydrocarbon-generation-induced microcracking of source rocks. *Geophysics*, 59(4):555–563.
- Viesca, R. C. and Garagash, D. I. (2018). Numerical methods for coupled fracture problems. *J. Mech. Phys. Solids*, 113:13–34.
- Villeneuve, N., Neuville, D. R., Boivin, P., Bachèlery, P., and Richet, P. (2008). Magma crystallization and viscosity: A study of molten basalts from the piton de la fournaise volcano (la réunion island). *Chemical Geology*, 256(3):242–251.
- Walker, H. F. and Ni, P. (2011). Anderson acceleration for fixed-point iterations. *SIAM Journal on Numerical Analysis*, 49(4):1715–1735.
- Wan, R. (2011). *Advanced well completion engineering*. Golf Professional Publishing.

- Wang, S. and Dempsey, J. (2011). A cohesive edge crack. *Eng. Frac. Mech.*, 78(7):1353–1373.
- Warpinski, N. R., Lorenz, J. C., Branagan, P. T., Myal, F. R., and Gall, B. L. (1993). Examination of a cored hydraulic fracture in a deep gas well (includes associated papers 26302 and 26946). *SPE Production & Facilities*, 8(03):150–158.
- Weertman, J. (1971). Theory of water-filled crevasses in glaciers applied to vertical magma transport beneath oceanic ridges. *J. Geophys. Res.*, 76(5):1171–1183.
- Weinberger, R., Lyakhovsky, V., Baer, G., and Agnon, A. (2000). Damage zones around en echelon dike segments in porous sandstone. *J. Geophys. Res.: Solid Earth*, 105(B2):3115–3133.
- Winner, R. A., Lu, G., Prioul, R., Aidagulov, G., and Bunger, A. P. (2018). Acoustic emission and kinetic fracture theory for time-dependent breakage of granite. *Eng. Fract. Mech.*, 199:101–113.
- Wolfram Research, I. (2020). Mathematica, Version 12.1.
- Wrobel, M., Mishuris, G., and Piccolroaz, A. (2017). Energy release rate in hydraulic fracture: can we neglect an impact of the hydraulically induced shear stress? *International Journal of Engineering Science*, 111:28–51.
- Wu, R., Bunger, A. P., Jeffrey, R. G., and Siebrits, E. (2008). A comparison of numerical and experimental results of hydraulic fracture growth into a zone of lower confining stress. In *The 42nd US Rock Mechanics Symposium (USRMS)*, pages ARMA–08–267. American Rock Mechanics Association.
- Xing, P., Yoshioka, K., Adachi, J. I., El-Fayoumi, A., and Bunger, A. P. (2017). Laboratory measurement of tip and global behavior for zero-toughness hydraulic fractures with circular and blade-shaped (PKN) geometry. *J. Mech. Phys. Solids*, 104:172–186.
- Zanganeh, B., Clarkson, C. R., and Hawkes, R. V. (2017). Reinterpretation of fracture closure dynamics during diagnostic fracture injection tests. In *SPE Western Regional Meeting*, page 18, Bakersfield, California. Society of Petroleum Engineers.
- Zgonnik, V. (2020). The occurrence and geoscience of natural hydrogen: A comprehensive review. *Earth-Science Reviews*, 203:103140.
- Zia, H. and Lecampion, B. (2019). Explicit versus implicit front advancing schemes for the simulation of hydraulic fracture growth. *Int. J. Numer. Anal. Meth. Geomech.*, 43(6):1300–1315.
- Zia, H. and Lecampion, B. (2020). PyFrac: A planar 3D hydraulic fracture simulator. *Comput. Phys. Commun.*, 255:107368.
- Zia, H., Lecampion, B., and Zhang, W. (2018). Impact of the anisotropy of fracture toughness on the propagation of planar 3D hydraulic fracture. *Int. J. Fracture*, 211(1-2):103–123.

Andreas Möri

Swiss Institute of Technology Lausanne (EPFL), EPFL – ENAC – IIC – GEL

Station 18, Lausanne, Switzerland, CH-1015

☎ (+41)(0) 79 564 02 12 • 📠 (+41)(0) 21 693 44 70

✉ andreas.mori@epfl.ch, andreas.mori92@gmail.com

ORCID: 0000-0002-7951-1238

EDUCATION

Doctor of Science (Ph.D.)

August 2019 – expected July 2023

Geo-Energy Laboratory (GEL) at the *Swiss Institute of Technology Lausanne (EPFL)* in the *Doctoral Program of Mechanics (EDME)* supervised by *Prof. Dr. Brice Lecampion*. Focus on hydraulic fractures in rock.

Master of Science (MSc)

September 2017 – July 2019

MSc in *Civil Engineering* of EPFL. Specialization in *Geotechnical Engineering* with a certificate in *Structural Engineering*. Master thesis in numerical modelling of *Slope Stability*.

Bachelor of Science (BSc)

September 2013 – July 2016

BSc in *Civil Engineering* of EPFL.

EXPERIENCE

Doctoral Assistant

August 2019 – to date

Geo-Energy Laboratory (GEL) at EPFL.

○ Research Projects

- Active developer of the open-source, fully coupled hydraulic fracture simulator **PyFrac** (boundary element method).
- Active developer of a **Mathematica**-based **Gauss-Chebyshev** scheme to solve boundary integral equations in hydraulic fracture problems.
- Studying the effect of shut-in, buoyant forces, and possible arrest mechanisms on hydraulic fractures.
- Investigating poroelastic effects around the tip region of a propagating hydraulic fracture.

○ Teaching Assistant

- Bachelor's (2) and Semester project during Master's (5) supervision
- Teaching assistant in **Computational Geomechanics** during the fall semesters from 2019 to 2021.
- Teaching assistant in **Geotechnical Engineering** during the spring semesters from 2019 to 2022.

Research collaborator

July 2018 – August 2018

Geo-energy Laboratory (GEL) at EPFL. Study of shear fault activation by stress transfer.

Editorial assistance

July 2018

Editorial work on the third edition of **Stahlbau (TGC Band 10)** at the RESSLAB at EPFL.

Teaching assistant

February 2018 – June 2019

Assistance in **Design of Steel Structures** at EPFL for the spring semesters of 2018 and 2019.

Head of Construction Site

July 2016 – July 2017

Internship as **head of construction site and technical calculator** at **Marti Bern AG**.

Teaching Assistant

September 2014 – June 2015

Teaching assistance in the first-year courses for all faculties in **Calculus 1** (fall semester) and **Calculus 2** (spring semester).

OTHER ACTIVITIES

Representation of Doctoral Students

August 2020 – to date

Representation of doctoral Students in the tender for new food trucks at EPFL. Also a member of the **Catering Commission** of EPFL representing all mid-level academics.

Handball Referee

August 2010 – to date

Official referee of the Swiss Handball Association.

December 2021 – December 2022

Treasurer of Doctoral Student Association

Treasurer of EPFL's doctoral students' association PolyDoc.

EDME Doctoral Student Representative

March 2020 – March 2022

Representative of doctoral students associated with the Doctoral Program of Mechanics (EDME).

Treasurer of Student Association

September 2015 – July 2016

Treasurer of **Travel GC**, the association organizing and financing the study trip of civil engineering bachelor students.

LANGUAGES

German: native language

French: proficient

English: proficient Course in Academic Writing Level C1 passed with a Grade of 6 (Excellent).

Spanish: beginner

SOFTWARE SKILLS

Very good knowledge: MS Office, LaTeX, MATHEMATICA

Advanced knowledge: C++, Python, MATLAB, Adobe Illustrator

Basic knowledge: Java, VBA, GIS, SQL, CAD, FEniCS

PUBLICATIONS

Journal Articles.....

Möri, A. and B. Lecampion (2023). "Three-dimensional buoyant hydraulic fractures: finite volume release". In: *Submitted to the Journal of Fluid Mechanics*, arXiv: 2304.00907.

Möri, A. and B. Lecampion (2022). "Three-dimensional buoyant hydraulic fractures: constant release from a point source". In: *Journal of Fluid Mechanics* 950, A12. doi: 10.1017/jfm.2022.800.

Möri, A. and B. Lecampion (2021). "Arrest of a radial hydraulic fracture upon shut-in of the injection". In: *International Journal of Solids and Structures* 219-220, pp. 151–165. doi: 10.1016/j.ijsolstr.2021.02.022.

Möri, A., C. Peruzzo, B. Lecampion, and D. Garagash (2024). "Arrest mechanisms of Buoyant hydraulic fractures". In: *In preparation*.

Möri, A. and B. Lecampion (2023). "Buoyant Hydraulic Fractures with fluid leak-off". In: *In preparation*.

Peruzzo, C., **A. Möri**, and B. Lecampion (2023). "The energy budget of hydraulic fractures". In: *In preparation*.

Talebkeikhah, M., **A. Möri**, B. Lecampion, A. Peirce, and E. Detournay (2023). "Numerical modelling of the recession and closure of planar three-dimensional hydraulic fractures: Contact-based vs. asymptotic-informed schemes". In: *In preparation*.

Möri, A. and B. Lecampion (2023). "A fully coupled Boundary Integral Method for Steadily Moving Hydraulic Fractures in Poroelastic Media". In: *In preparation*.

Möri, A. and B. Lecampion (2024). "Tip Asymptotes of Hydraulic Fractures in Poroelastic Media". In: *In preparation*.

Peer-Reviewed Conference Papers.....

Möri, A., C. Peruzzo, B. Lecampion, and D. I. Garagash (2023). “Arrest Mechanisms of Buoyant Hydraulic Fractures”. In: *57th U.S. Rock Mechanics / Geomechanics Symposium*. American Rock Mechanics Association (ARMA). 25–28 June, Atlanta, Georgia, USA.

Conference Abstracts.....

Talks

Möri, A., C. Peruzzo, B. Lecampion, and D. I. Garagash (2023). “Arrest Mechanisms of Buoyant Hydraulic Fractures”. In: *57th U.S. Rock Mechanics / Geomechanics Symposium*. American Rock Mechanics Association (ARMA). 25–28 June, Atlanta, Georgia, USA.

Möri, A. and B. Lecampion (2023). “Magmatic Intrusions From a Hydraulic Fracture Modeling Perspective (Sollicited Talk)”. In: *European Geoscience Union General Assembly 2023*. European Geoscience Union (EGU). 23–28 April, Wien, Austria.

Möri, A., C. Peruzzo, and B. Lecampion (2022). “The Transient Phase of Planar, Three-Dimensional Buoyant Hydraulic Fractures Emerging from a Point Source”. In: *8th European Congress on Computational Methods in Applied Sciences and Engineering, ECCOMAS Congress 2022*. 5 – 9 June, Oslo, Norway.

Möri, A. and B. Lecampion (2020). “Transition from a radial to a 3D buoyancy-driven hydraulic fracture”. In: *18th Swiss Geoscience Meeting (SGM 2020)*. Platform of Geosciences of the Swiss Academy of Sciences (SCNAT). 6–7 September, Zürich (Online), Switzerland.

Posters

Möri, A., D. Garagash, and B. Lecampion (2023). “Transition from Vertical to Lateral Diking at the Neutral Buoyancy Line”. In: *European Geoscience Union General Assembly 2023*. European Geoscience Union (EGU). 23–28 April, Wien, Austria.

Möri, A. and B. Lecampion (2021). “Limiting Regimes of a Three-Dimensional Buoyant Hydraulic Fracture Emerging from a Point Source”. In: *AGU Fall Meeting 2021*. American Geophysical Union. 13–17 December, New orleans, LA, USA.

Möri, A., B. Lecampion, and H. Zia (2020). “Fully-coupled 3D modelling of magmatic dike Propagation – finite pulse release from a point source”. In: *European Geoscience Union, General Assembly (EGU 2020)*. European Geoscience Union. 4–8 May, Online.

Möri, A., B. Lecampion, and F. Ciardo (2019). “Fluid injection driven, a-seismic fracture growth with remote nucleation on heterogeneous fault”. In: *SCCER-SoE Annual Conference (2019)*. Swiss Competence Center for Energy Research and Supply of Energy. 3–4 September, Lausanne, Switzerland.

Möri, A., B. Lecampion, and F. Ciardo (2019). “A-seismic fracture growth driven by fluid injection and remote nucleation of dynamic rupture in a weaker part of the fault”. In: *Third Schatzalp Workshop on Induced Seismicity, SED 2019*. Swiss Seismological Service. 5–8 March, Davos, Switzerland.

Outreach / Invited Talks / Seminars.....

Möri, A. and B. Lecampion (2023). “Magmatic Intrusions From a Hydraulic Fracture Modeling Perspective (Sollicited Talk)”. In: *European Geoscience Union General Assembly 2023*. European Geoscience Union (EGU). 23–28 April, Wien, Austria.

Möri, A. and B. Lecampion (2023). “Birth and Ascent of Buoyant Hydraulic Fractures”. In: *MCE Seminar Talk*. Californian Institute of Technology (Caltech). 21 June, Pasadena, USA.

Möri, A. and B. Lecampion (2022). *3D Buoyancy-Driven Propagation of Hydraulic Fractures and their Applications to Magmatic Plumbing Systems*. Focus on VIPS Blog. Volcanic & Igneous Plumbing Systems (VIPS).

Lecampion, B., **A. Möri,** C. Peruzzo, and H. Zia (2022). “The birth and death of buoyant hydraulic fractures”. In: *Swiss Mech Seminar Series*. ETH Zürich. 14 April, Online.